

Ontwikkeling van vervormbare optische  
en opto-elektronische tactiele sensoren

Development of Conformable Optical  
and Optoelectronic Based Tactile Sensors

Jeroen Missinne

Promotoren: prof. dr. ir. J. Vanfleteren, dr. ir. G. Van Steenberge  
Proefschrift ingediend tot het behalen van de graad van  
Doctor in de Ingenieurswetenschappen: Elektrotechniek

Vakgroep Elektronica en Informatiesystemen  
Voorzitter: prof. dr. ir. J. Van Campenhout  
Faculteit Ingenieurswetenschappen en Architectuur  
Academiejaar 2011 - 2012



ISBN 978-90-8578-472-2  
NUR 959  
Wettelijk depot: D/2011/10.500/75



Universiteit Gent  
Faculteit Ingenieurswetenschappen en Architectuur  
Vakgroep Elektronica en Informatiesystemen

Promotoren: prof. dr. ir. J. Vanfleteren  
dr. ir. G. Van Steenberge

Centrum voor Microsysteemtechnologie (CMST)  
Vakgroep Elektronica en Informatiesystemen  
Technologiepark 914A  
B-9052 Zwijnaarde

Tel.: +32-9-264.53.50  
Fax.: +32-9-264.53.74

Examencomissie: prof. dr. ir. L. Taerwe – Voorzitter  
prof. dr. ir. P. Van Daele – Secretaris  
prof. dr. ir. F. Berghmans  
prof. dr. ir. D. Reynaerts  
prof. dr. P. Dubruel  
prof. dr. ir. G. Roelkens  
prof. dr. ir. A. Dietzel

Dit werk kwam tot stand in het kader van een aspirantenmandaat van het FWO-Vlaanderen (Fonds Wetenschappelijk Onderzoek – Vlaanderen).



Proefschrift ingediend tot het behalen van de graad van  
Doctor in de Ingenieurswetenschappen: Elektrotechniek  
Academiejaar 2011-2012



# Dankwoord

Na 4 jaar bestuderen van optische sensoren, ligt het er eindelijk, 'het doctoraat'. Bij de start, jaar 1, kon ik me deze fase niet inbeelden, maar nu is het dus zo ver en dat is enkel maar mogelijk geweest door de hulp van velen.

Als eerste wil ik graag mijn promotor Jan Vanfleteren, en daarnaast ook Peter Van Daele bedanken. Zij hebben mij met een interessant onderzoeksonderwerp kunnen overtuigen om aan een doctoraat te beginnen. Ze hebben mij bovendien toegelaten om zelfstandig mijn onderzoek te verrichten, maar waren ook altijd beschikbaar als ik vragen had over de praktische kant en de organisatie van de vele aspecten van het doctoraat. Peter, bedankt ook voor de uitstap naar Yosemite Park en de vele reistips!

Bedankt aan André Van Calster voor het leiden van CMST, hij heeft altijd het beste met ons voorgehad en zijn inspanningen hebben geleid tot wat CMST vandaag is: een onderzoeksgroep met uitstekende infrastructuur en bovenal een goede werksfeer met talrijke teambuilding activiteiten.

In het bijzonder wil ik co-promotor Geert Van Steenberge bedanken, die mij uitstekend heeft begeleid doorheen al de technische uitdagingen. Dit heeft me veel inspiratie gegeven en heeft rechtstreeks een impact gehad op de resultaten in dit proefschrift. Toch zijn vele ideeën er niet zo maar gekomen, ze zijn het resultaat van een goede samenwerking, talrijke brainstorm sessies en discussies met het hele optische team. Als ik daar nog de vele geslaagde social events en de uitstekende sfeer bij bedenkt, dan mag ik terecht ook Bram, Erwin, Peter, Sandeep en Steven bedanken (in alfabetische volgorde). Rik, hoewel onze beide doctoraten verschillende onderwerpen beslaan, waren er toch vele gelijkenissen en we hebben dan ook goed kunnen samenwerken. Bedankt voor alle hulp!

Onze bureau is altijd een beetje een mobiele duiventeel geweest, maar we hebben het er denk ik wel goed gehad. Daarom, bedankt aan zij die er nu nog zitten: Amir, David, Rik, Thomas, Sandeep, Sanjeev, Sheila, en zij die er net niet meer zitten of af en toe nog zitten: Benoit, Jindrich, Tom. Ik meen alvast dat we het extra diploma van 'verhuizer' verdienen. Ook bedankt aan mijn aanspreekpunten van 'de meetruimte': Ann en Jindrich. Door al dat optische werk, begon mijn kennis van de elektronica toch stilaan wat af te brokkelen, en heb ik het ten zeerste geapprecieerd dat ik beroep kon doen op jullie kennis ter zake.

Bedankt aan An voor de hulp bij het platen, Björn om mijn veel te kleine componenten te willen proberen plaatsen, David de SEM'er en chemie-enthousiast,

Dieter voor de kennis van dunne film technieken en die ook te willen toepassen op mijn vele substraten, Filip omdat je bijna al onze technische tekeningen in praktijk kan omzetten, Peter voor de vele hulp in de cleanroom en Steven voor je kennis en hulp bij het talrijke laserwerk.

Vele collega's hebben mijn doctoraatsonderzoek ook aangenamer gemaakt door de ondersteunende taken op zich te nemen: Katrien voor de hulp bij de administratie; Peter om onze IT-infrastructuur werkende te houden; Inge om te zorgen voor de netheid in onze gebouwen, het EIP en drijvende kracht Nadine, bedankt om toe te zien op onze veiligheid!

Er zijn nog een hoop andere mensen binnen CMST die mij op een of andere manier geholpen en mij een aangename tijd bezorgd hebben. Te veel om op te noemen, maar allemaal bedankt. Ik heb de vriendschappelijke en goede werksfeer ten zeerste kunnen appreciëren!

Bedankt aan de jury om mijn proefschrift kritisch te willen evalueren. Mijn bijzondere dank gaat nogmaals uit naar de leden van de leescommissie, u heeft ondanks de drukke agenda's, mij toch een grondige feedback en nuttige bemerkingen bezorgd.

Bedankt aan alle externe collega's die door de goede samenwerking tot dit doctoraat hebben bijgedragen. Collega's van B-Phot, en in het bijzonder Jürgen Van Erps en Christof Debaes voor de hulp en goede raad bij de vele optische metingen. Collega's van 'de S4', Kenny Adesanya en Tim Van Gijsegheem en collega's van de KUL, Eleonora Ferraris en Yan Chunxiao en vele anderen voor de samenwerking tijdens FAOS. Verder zijn er nog heel wat collega's die ik niet bij naam genoemd heb, maar mij toch geholpen hebben en op een of andere manier tot dit proefschrift hebben bijgedragen. Bedankt allemaal!

Bedankt aan al mijn medestudenten en vrienden, jullie hebben ervoor gezorgd dat ik mij ook af en toe eens kon ontspannen: de legendarische loop-uitstapjes, nog legendarischere reisjes naar verre (n)oorden, weekendjes, oudjaar festiviteiten, roadtrips, interessante café conversaties en nog veel meer. In het bijzonder mijn huisgenootjes voor de juridische goede raad en interessante klimaat tips, bedankt! Ook Tim en andere (buitenlandse) vrienden die ik niet zo veel meer zie, ik ben jullie niet vergeten en 't is altijd tof om jullie terug te zien!

Ten slotte maar heel in het bijzonder wil ik mijn familie, en in de eerste plaats mijn ouders bedanken, zij zijn voor mij belangrijker dan wie ook en hebben mij steeds alle mogelijkheden en steun gegeven.

Bedankt ook aan u, lezer, dat u mijn werk leest, want u leest uiteraard ook verder dan dit dankwoord, toch?

*Gent, december 2011  
Jeroen Missinne*

# Table of Contents

<b>Dankwoord</b>	<b>i</b>
<b>List of Tables</b>	<b>vi</b>
<b>List of Figures</b>	<b>viii</b>
<b>List of Acronyms</b>	<b>xvii</b>
<b>Samenvatting</b>	<b>xix</b>
<b>Summary</b>	<b>xxv</b>
<b>1 Introduction</b>	<b>1</b>
1.1 Artificial skin: a sixth sense? . . . . .	1
1.1.1 The concept of “artificial skin” . . . . .	2
1.1.2 Applications of artificial skin . . . . .	3
1.2 Recent trends in tactile sensing technology . . . . .	11
1.2.1 Flexible and conformable sensor substrates . . . . .	11
1.2.2 Progress toward artificial skin . . . . .	12
1.3 Problem statement and objectives . . . . .	16
1.4 Research trajectory and structure of this book . . . . .	17
References . . . . .	19
<b>2 Stretchable optical materials</b>	<b>29</b>
2.1 Introduction . . . . .	29
2.2 Silicone chemistry . . . . .	30
2.3 Optical properties . . . . .	32
2.3.1 Refractive index . . . . .	32
2.3.2 Optical absorption . . . . .	35
2.4 Mechanical properties . . . . .	37
2.4.1 Elastic properties of PDMS . . . . .	37
2.5 Processing properties . . . . .	39
2.5.1 Material preparation and processing conditions . . . . .	40
2.5.2 Microfabrication related properties . . . . .	41

2.5.3	Adhesion related issues . . . . .	41
2.6	Conclusions . . . . .	44
	References . . . . .	45
<b>3</b>	<b>Stretchable waveguides for conformable optical sensors</b>	<b>49</b>
3.1	Introduction . . . . .	49
3.2	“Hybrid” waveguides . . . . .	50
3.2.1	Fabrication of “hybrid” waveguides . . . . .	50
3.2.2	Modeling of waveguide bends . . . . .	55
3.2.3	Applicability and Evaluation . . . . .	57
3.3	Micro-patterning of PDMS . . . . .	58
3.3.1	Traditional optical polymer processing techniques . . . . .	58
3.3.2	Soft-lithography . . . . .	60
3.3.3	PDMS waveguide fabrication in literature . . . . .	63
3.4	Fabrication of PDMS based waveguides . . . . .	64
3.4.1	Fabrication of a master mold . . . . .	64
3.4.2	Process flow 1: embossing based patterning . . . . .	69
3.4.3	Process flow 2: MIMIC based process . . . . .	72
3.5	Characterization of stretchable waveguides . . . . .	75
3.5.1	Introduction . . . . .	75
3.5.2	Optical propagation losses . . . . .	76
3.5.3	Optical bending losses . . . . .	79
3.5.4	Optical behavior under mechanical elongation . . . . .	80
3.6	Conclusions . . . . .	86
	References . . . . .	87
<b>4</b>	<b>Polymer waveguide based sensing</b>	<b>93</b>
4.1	Introduction . . . . .	93
4.2	Concept for a waveguide based tactile sensor . . . . .	95
4.2.1	Sensor operation principle . . . . .	95
4.2.2	Optical coupling mechanisms . . . . .	95
4.3	Waveguide based sensor architecture design . . . . .	97
4.3.1	Sensor based on evanescent field coupling . . . . .	97
4.3.2	Sensor based on coupling through mechanical contact . . . . .	99
4.4	Technology platform for waveguide sensors . . . . .	102
4.4.1	Polymer waveguides on deformable substrates . . . . .	102
4.4.2	Fabrication of mechanical support structures . . . . .	102
4.4.3	Micro-bonding techniques . . . . .	106
4.5	Functional testing of the fabricated prototype . . . . .	107
4.6	Conclusions . . . . .	109
	References . . . . .	110

<b>5</b>	<b>Optoelectronics based sensing: tactile shear sensor</b>	<b>113</b>
5.1	Introduction	113
5.2	Optical sensor principle	114
5.2.1	Selecting a transducer material	115
5.2.2	Implementation of the sensor principle	115
5.2.3	Ultra-thin flexible shear sensor	116
5.3	Optical sensor architecture design	117
5.3.1	One dimensional shear sensor architecture	119
5.3.2	Modifications toward an $(x, y)$ -shear sensor design	123
5.3.3	True $(x, y)$ -shear sensor design	126
5.3.4	Alternative sensor implementations	130
5.3.5	Shear sensor implementation in reflection	133
5.4	Mechanical sensor architecture design	133
5.4.1	Mechanical model in Comsol	134
5.4.2	Mechanical simulation results	135
5.4.3	Conclusions	140
5.5	Fabrication process	141
5.5.1	Embedding optoelectronics	141
5.5.2	Fabricating the shear sensor	143
5.5.3	Fabrication process evaluation and results	147
5.5.4	Fabrication process improvements	150
5.6	Conclusions	152
	References	153
<b>6</b>	<b>Tactile shear sensor characterization</b>	<b>157</b>
6.1	Introduction	157
6.2	Characterization of embedded optoelectronics	158
6.2.1	1x4 multimode VCSEL array chip	158
6.2.2	1x4 100 $\mu\text{m}$ $\varnothing$ photodiode array chip	160
6.2.3	250 $\mu\text{m}$ square photodiode chip	161
6.2.4	Validation of the sensor simulation model	161
6.3	Sensor functional testing	165
6.3.1	First generation sensor	166
6.3.2	Second generation sensor	171
6.3.3	Third generation sensor	172
6.3.4	Parameters potentially interfering with sensor operation	176
6.4	Conclusions	179
	References	179
<b>7</b>	<b>Conclusions and final remarks</b>	<b>181</b>
7.1	Main contributions to the field of tactile sensors	181
7.1.1	Objective 1: "Developing unobtrusive sensors"	181

---

7.1.2	Objective 2: “Exploring optical sensing principles for tactile sensors” . . . . .	183
7.1.3	Objective 3: “Focus on the shear stress component in tactile force sensing” . . . . .	184
7.2	Outlook and recommendations for future work . . . . .	184
<b>A</b>	<b>Appendix: Dissemination</b> . . . . .	<b>187</b>
A.1	Research context and related projects . . . . .	187
A.2	Research dissemination . . . . .	188
A.2.1	Journal papers . . . . .	188
A.2.2	Proceedings of international conferences . . . . .	189
A.2.3	Other international conferences, without proceedings . . . . .	190
A.2.4	Proceedings of national conferences . . . . .	191
A.2.5	Other publications . . . . .	191
A.2.6	The following patent has been filed . . . . .	191
	References . . . . .	191

## List of Tables

1.1	Overview of the properties of mechanoreceptors in the fingertips. . .	5
1.2	Tactile sensing requirements for different applications. . . . .	10
1.3	Overview of the properties of piezoresistive tactile sensors in literature. . . . .	13
1.4	Overview of the properties of conductive polymer based tactile sensors in literature. Since the sensor response is not always linear, sensitivities are typically difficult to define and they are therefore not included in this table. . . . .	14
1.5	Overview of the properties of capacitive tactile sensors in literature.	14
1.6	Overview of the properties of optical tactile sensors in literature. . .	15
2.1	Refractive index $n_d$ (at 589 nm) of different optical PDMS types, measured using an Abbe refractometer (21 °C). . . . .	34
2.2	Thermo-optic coefficient $\frac{dn}{dT}$ (at 589 nm) of different optical PDMS types compared with traditional optical materials. . . . .	34
2.3	Viscosity and working time of different silicones after mixing the 2 parts. . . . .	41
3.1	Process parameters for fabricating $50\ \mu\text{m} \times 50\ \mu\text{m}$ “hybrid” waveguides with Truemode core (parameters for Epocore waveguides are mentioned between parentheses if different). All process steps are performed on a sacrificial glass substrate. . . . .	51
3.2	Parameters used for the non-sequential ray tracing simulations. . .	55
3.3	Summary of possible PDMS patterning techniques. . . . .	62
3.4	Process parameters for fabricating $50\ \mu\text{m}$ SU-8 structures on a silicon wafer. . . . .	67
3.5	Tolerances on nominal $50\ \mu\text{m}$ SU-8 layer thickness. . . . .	67
3.6	Process parameters for fabricating arrays of $50\ \mu\text{m} \times 50\ \mu\text{m}$ multimode PDMS waveguides using the embossing technique with LS-6943 as core material and Sylgard®184 as cladding. See Figure 3.9.	68

3.7	Process parameters for fabricating arrays of $50\ \mu\text{m} \times 50\ \mu\text{m}$ multi-mode PDMS waveguides using the capillary channel filling technique with LS-6257 as core material and Sylgard®184 as cladding. See Figure 3.13. . . . .	73
3.8	Parameters corresponding with the different bending loss configurations (see Figure 3.18). . . . .	79
3.9	Measured bending loss for the configurations depicted in Figure 3.18 (average of the population $\pm$ standard deviation). Both waveguide array samples with LS-6257 and OE-6520 core material were tested (cladding: Sylgard®184) . . . . .	80
4.1	Process parameters for fabricating $50\ \mu\text{m} \times 50\ \mu\text{m}$ “hybrid” waveguides with EpoCore as core material and Truemode for the spacer structures (2 layer lithographic process). All process steps are performed on a sacrificial glass substrate. . . . .	103
5.1	Performance measures for 2 configurations based on square photodiodes. . . . .	130
5.2	Geometrical parameters used for constructing the mechanical model in Comsol Multiphysics. . . . .	135
5.3	Mechanical properties of the materials used for the simulation model in Comsol Multiphysics. . . . .	135
5.4	Laser ablation parameters used for opening contact pads by removing polymer layers on top of a $1\ \mu\text{m}$ thin copper layer. . . . .	145
6.1	Beam divergence angles calculated from the goniometric radiometer data. . . . .	163

# List of Figures

1.1	The concept of artificial skin as proposed by Lumelsky et al.: a deformable substrate with a matrix of sensors that can be wrapped around irregular objects. . . . .	2
1.2	(a) Robotic hand with tactile sensors for handling fragile objects (Courtesy of The Shadow Robot Company [5]). (b) Prototype of a robot for assistance of elderly people (Courtesy of Edsinger, A., MIT [6, 7]). . . . .	4
1.3	DaVinci®surgical system at AZ Sint-Lucas, Ghent, Belgium. A surgeon is operating remotely using robotic arms. . . . .	6
1.4	“Harmony®Vacuum Management System” from Otto Bock equipped with a vacuum pump to regulate the pressure in the socket. . . . .	8
2.1	Formula for “siloxane” and “polydimethylsiloxane” (PDMS): if “R” is “CH <sub>3</sub> ” in the basic siloxane unit, then it is named polydimethylsiloxane. . . . .	30
2.2	Different Siloxane polymers and corresponding nomenclature. . . . .	31
2.3	Cure mechanism of a 2-part addition-cure PDMS system. . . . .	31
2.4	Refractive index vs. wavelength of different optical silicones. . . . .	33
2.5	Optical absorption vs. wavelength (25 °C) of Nusil LS-6943 material. . . . .	35
2.6	Optical absorption vs. wavelength of Nusil LS-6257 material. Graph adopted from the datasheet [10]. . . . .	36
2.7	Typical plot of the applied force versus length change of a PDMS specimen following a tensile test. . . . .	38
2.8	Layer thickness versus spin speed curves for Sylgard®184 and PV-6010. . . . .	40
3.1	Process flow for fabricating “hybrid” waveguides. The temporary glass substrate is not show in the picture. . . . .	52
3.2	Cross-section of the profile of a spin-coated layer of PDMS on a 2” square glass substrate. . . . .	53

3.3	Cross-section of $50\ \mu\text{m} \times 50\ \mu\text{m}$ Truemode waveguides patterned on top of Sylgard®184 PDMS cladding. The visible dirt particles were generated when cutting using a razor blade. . . . .	54
3.4	System geometry for the bend loss simulation: a straight waveguide section is followed by 4 successive $90^\circ$ bend sections. The collecting efficiency of a detector is analyzed after each section. .	54
3.5	Collecting efficiency of a detector in function of the number of $90^\circ$ bends. The slope of the linear regression through these points determines the bending loss per $90^\circ$ bend. The different curves correspond with different bending radii. . . . .	56
3.6	Bending loss in function of bending radius for Epocore waveguides surrounded by air and by a Sylgard®184 cladding respectively. . . . .	56
3.7	Preliminary test for laser ablating LS-6946 PDMS using a KrF Excimer laser (wavelength 248 nm): optical profiler scan of an ablated $200\ \mu\text{m}$ wide and $8\ \mu\text{m}$ deep groove. . . . .	61
3.8	One dimensional cross-section of an X,Y-WYKO optical profile scan. The structure height is resolved accurately, but the nearly vertical sidewalls cannot be detected precisely by the optical profiler (the data shown is interpolated). However, it can be seen that the structure is approximately $50\ \mu\text{m}$ wide. . . . .	68
3.9	Process flow for patterning PDMS waveguides based on embossing. . . . .	69
3.10	Importance of a well-controlled embossing process. (a) Deformation due to excessive embossing pressure. (b) Desired structures with optimum embossing parameters. (c) Residual layer is not completely pressed away when too little pressure is applied. . . .	70
3.11	A cross-section of finished $50\ \mu\text{m} \times 50\ \mu\text{m}$ PDMS multimode waveguides with Sylgard®184 as cladding and LS-6943 as core material ( $125\ \mu\text{m}$ waveguide pitch). . . . .	71
3.12	Light guiding in $50\ \mu\text{m} \times 50\ \mu\text{m}$ PDMS multimode waveguides with Sylgard®184 as cladding and LS-6943 as core material. . . .	71
3.13	Process flow for patterning PDMS waveguides based on micro-molding in capillaries. See 3.7 for process parameters . . . . .	72
3.14	Cross-section of PDMS waveguides formed by capillary filling of channels (cladding: Sylgard®184 and core: LS-6257). The inset shows a magnified view of the middle waveguide in the array. . .	74
3.15	Setup for performing optical cut-back measurements. Input and output fibers are actively aligned with the sample using high precision motorized stages. . . . .	76
3.16	Optical attenuation of PDMS waveguides based on LS-6943 core and Sylgard®184 cladding (embossing process flow). . . . .	77

3.17	Optical attenuation of PDMS waveguides based on LS-6257 core and Sylgard®184 cladding (capillary filling process flow). . . . .	78
3.18	The different bending loss configurations and corresponding actual bending radius $r$ . . . . .	79
3.19	Process for passively aligning optical fibers in front of the PDMS waveguides formed by capillary filling. . . . .	81
3.20	Optical profiler scan of the 2 layered SU-8 structures: grooves for aligning the fibers passively in front of the waveguides (different designs). . . . .	83
3.21	Optical fibers aligned in front of the PDMS waveguides formed by capillary filling. . . . .	83
3.22	Configuration for stretching the waveguides . . . . .	84
3.23	Custom-built setup for stretching the waveguides . . . . .	84
3.24	Influence of waveguide elongation on detected optical power at the waveguide output (5 measurements). A trendline was fitted through the measured values. . . . .	85
4.1	Illustrated principle of the sensor based on light coupling between crossing waveguides. . . . .	95
4.2	Evanescence wave optical power coupling proof-of-principle demonstrator. Light is sent into a bottom waveguide and when pressure is exerted on the layer structure, the distance between the 2 waveguide layers decreases and light is coupled to a waveguide in the top layer. . . . .	96
4.3	Optical power coupling through mechanical contact. (a) shows the setup: 2 layers of waveguides separated by a thin foil with openings. The bottom waveguide layer is located under the foil and can therefore not be seen. (b) In rest, no light is coupled but when pressure is exerted (c), light is coupled from the input waveguide to the output waveguide. . . . .	96
4.4	Coupling coefficient in function of the separation distance for transfer of optical power between Truemode or Epocore waveguides, separated with a PDMS or air gap and crossing under an angle of $30^\circ$ . . . . .	98
4.5	Schematic representation of the sensor structure based on mechanical contact coupling. Two layers of waveguides patterned on a PDMS substrate are separated by mechanical "spacer" structures and are crossing under an angle. . . . .	100
4.6	Simplified geometry adopted for the mechanical simulations. Left: 3D view of the simulation model with 2 waveguides crossing under an angle and separated by an air gap. Right: cross-sectional view of the simulation model. . . . .	100

4.7	Result of the mechanical simulation: after a certain threshold pressure is exerted on the sensor, the waveguides are in contact and the contact area increases rapidly with increasing pressure. . . . .	101
4.8	Schematically illustrated process flow for fabricating waveguides and support structures or “spacers” on a layer of PDMS. . . . .	104
4.9	A microscopic view of the cross-section of a substrate with waveguides and spacer structures. . . . .	105
4.10	Light stays confined and is not escaping into the top part of the spacer owing to its lower refractive index. . . . .	105
4.11	Process flow for micro-bonding 2 waveguide samples. . . . .	106
4.12	Result of joining the 2 waveguide layers. (a) Cross-section of top waveguides bonded to spacers. (b) Top view of the 2 layers crossing under an angle. The dark crossing points are locations where top waveguides and spacers are bonded while on the clear crossing points a lower and upper waveguide is crossing. . . . .	107
4.13	Coupled optical power in function of applied pressure (increasing $\uparrow$ and decreasing $\downarrow$ pressure). For the second measurement, the tip was realigned to test repeatability. . . . .	108
5.1	Schematic representation of different implementations of the shear sensor “light emitter” and “detector”, (a) using a physical light source and detector directly or (b) using a “source” and “detector” waveguide. . . . .	116
5.2	The principle of the optical shear sensor relies on the changing optical coupling between a light source and a detector depending on the lateral displacement, and hence the shear stress. . . . .	117
5.3	An example of the 2-dimensional functions $\Phi_d$ and $PD(x, y)$ (for an arbitrarily chosen $d$ and $\phi$ ) . . . . .	119
5.4	Simulation showing the influence of the vertical VCSEL-to-photodiode distance on the sensor characteristics. . . . .	120
5.5	Simulation showing the influence of the VCSEL driving current on the sensor characteristics. . . . .	121
5.6	Simulation showing the influence of the layer thickness change caused by a normal pressure. . . . .	122
5.7	Two-dimensional sensor response. For $(0, 0)$ , the VCSEL and detector are perfectly aligned. . . . .	123
5.8	Configuration of the detector chip with half covered photodiodes in order to obtain an $(x, y)$ -sensitive sensor topology (large blue circle: detector; small red circle: VCSEL; brown rectangle: metal cover layer). . . . .	123
5.9	Two-dimensional sensor response. The red dot indicates the initial VCSEL location, $(0, 0)$ , i.e. when the sensor is not loaded. . . . .	124

5.10	Cross-section of the graph in Figure 5.9, as indicated by the dotted lines. The cross-sections show the sensor response to lateral displacement in 2 orthogonal directions $x$ and $y$ . The red dot indicates the initial VCSEL location. . . . .	125
5.11	Different configurations for obtaining a shear sensor sensitive to $(x, y)$ -variations. . . . .	126
5.12	Sensor response for configuration 1; the dashed contour corresponds with the location of the photodiode and the red dot indicates the initial location of the VCSEL. . . . .	128
5.13	Cross-section of the sensor response in Figure 5.12 in the direction of $\chi = \pm 90^\circ$ and the corresponding linear fit within the sensor dynamic range. . . . .	129
5.14	Sensor response for configuration 2; the dashed contour corresponds with the locations of the photodiodes $PD_1$ and $PD_2$ and the red dot indicates the initial location of the VCSEL. . . . .	130
5.15	Cross-section of the sensor response shown in Figure 5.14 in the direction of $\chi = 0^\circ$ and the corresponding linear fit within the sensor dynamic range. . . . .	131
5.16	Schematic representation of alternative shear sensor implementations. . . . .	132
5.17	Meshing of the model: a “mapped” mesh constructed with blocks was used instead of the standard tetraedric mesh, not to disturb the symmetry in the structure. . . . .	134
5.18	Deformation of the shear sensor stack (model cross-section). . . . .	136
5.19	Lateral displacement in function of the applied shear stress. . . . .	137
5.20	Influence of the normal pressure on the lateral displacement of the transducer layer. . . . .	138
5.21	The influence of the transducer layer length $l$ on the lateral displacement. . . . .	139
5.22	The influence of the material shear modulus on the lateral displacement. . . . .	140
5.23	Process flow for embedding optoelectronic components. . . . .	141
5.24	Additional steps to fabricate the shear sensor. . . . .	143
5.25	Finalized flexible shear sensor sample. . . . .	144
5.26	Aligning two ultra-thin optoelectronic packages using a modified mask aligner setup. . . . .	146
5.27	Contact pad, opened with $\text{CO}_2$ laser and surface cleaned with KrF Excimer laser (a). After dissolving the protective PVA layer (in water) (b). Releasing the ultra-thin optoelectronic chip package from the temporary carrier (c). Final result: flexible shear sensor consisting of a VCSEL and photodiode package with a PDMS layer in between (d). . . . .	147
5.28	First generation technology. . . . .	148

5.29	Second generation technology. . . . .	149
5.30	Third generation technology. . . . .	150
5.31	Eliminating internal mechanical stresses using PI2611 embedding material. . . . .	151
6.1	Magnified view of the ULM-Photonics 1x4 VCSEL chip. . . . .	158
6.2	Electrical characteristics of the 4 VCSELs in an embedded array chip: current in function of the voltage over the component (IV-curve). . . . .	159
6.3	Optoelectronic characteristics of the 4 VCSELs in an embedded array chip: emitted optical power in function of current through the component (LI-curve). . . . .	159
6.4	Optoelectronic characteristics of an embedded PD chip: photocurrent in function of incident optical power (LI-curve). . . . .	160
6.5	Magnified view on the different bare die photodiodes used. . . . .	161
6.6	Measured VCSEL far field beam profile: cross-sections in two orthogonal directions (solid and dotted line), projected on a plane at 200 $\mu\text{m}$ from the VCSEL, for different VCSEL driving currents. (f) was measured with a different gain, meaning that intensity values cannot be compared with the other graphs. . . . .	162
6.7	Simulation showing the influence of the VCSEL-to-photodiode vertical distance $d$ on the sensor characteristics, using the actual VCSEL radiation pattern as input (VCSEL driving current: 5 mA). . . . .	164
6.8	Simulation showing the influence of the VCSEL driving current on the sensor characteristics, using the actual VCSEL radiation pattern as input (VCSEL-to-photodiode distance: 200 $\mu\text{m}$ ). . . . .	164
6.9	Simulation showing the two-dimensional shear sensor response, using the actual VCSEL radiation pattern as input (VCSEL driving current: 5 mA, VCSEL-to-photodiode distance $d=500 \mu\text{m}$ ). . . . .	165
6.10	First setup for testing the sensor response. . . . .	166
6.11	Sensor response (i.e. photodiode current) versus displacement for different VCSEL driving currents. . . . .	167
6.12	Sensor response (i.e. photodiode current) versus displacement for different sensor points on the array chip. VCSEL driving current: 5 mA. . . . .	167
6.13	Setup for testing the sensor response in function of an applied shear force. . . . .	169
6.14	Sensor response (i.e. photodiode current) versus displacement for different VCSEL driving currents: comparison between the simulated and measured data. . . . .	170
6.15	Sensor response (i.e. photodiode current) versus applied shear force for different VCSEL driving currents: comparison between the simulated and measured data. . . . .	170

---

6.16	Measured sensor response to lateral displacement in 2 orthogonal directions $x$ and $y$ (second generation sensor). . . . .	172
6.17	Setup for testing the third generation, $(x, y)$ -shear sensor. . . . .	173
6.18	Sensor response (i.e. photodiode current) in function of displacement for $\chi$ -values from $-90^\circ$ to $90^\circ$ in $10^\circ$ increments. . . . .	174
6.19	Slope of the sensor response in function of the direction of displacement, as defined by the value of $\chi$ . . . . .	175
6.20	Sensor response (i.e. photodiode current) in function of displacement for $\chi=90^\circ$ . . . . .	176
6.21	(a) Sensor configuration for measuring shear stresses. (b) Sensor configuration for measuring bending of a substrate. . . . .	177
6.22	Measured sensor response (in rest, i.e. no shear stress applied) in function of operating temperature (increasing (++) and decreasing (-) temperature). . . . .	178



# List of Acronyms

CCD	Charge Coupled Device
CMST	Centre for Microsystems Technology
CTE	Coefficient of Thermal Expansion
DI	De-ionized Water
EMI	ElectroMagnetic Interference
FAOS	Flexible Artificial Optical Skin (IWT funded project)
FR4	Fiber Reinforced board material
GaAs	Gallium(III)Arsenide
IC	Integrated Circuit
IMEC	Interuniversitair Micro-elektronica Centrum
IPA	Isopropyl Alcohol
LED	Light Emitting Diode
MEMS	Microelectromechanical Systems
MIS	Minimal Invasive Surgery
NA	Numerical Aperture
PCB	Printed Circuit Board
PD	Photodiode
PDMS	Polydimethylsiloxane
PEN	Polyethylene Naphthalate
PET	Polyethylene Terephthalate
PI	Polyimide
PSD	Position sensitive detector
PVA	Polyvinylalcohol
rh	Relative Humidity
RIE	Reactive Ion Etching
Rms	Root mean square
rpm	revolutions per minute

SEM	Scanning Electron Microscope
SMD	Surface Mount Device
SMT	Surface Mount Technology
SU-8	Negative Photoresist from MicroChem
TM	Trademark
UV	Ultra Violet
VCSEL	Vertical-Cavity Surface-Emitting Laserdiode
WYKO	Non-contact optical profilometer from Veeco
YAG	Yttrium Aluminium Garnet

# Samenvatting

Dankzij de recente technologische vooruitgang zijn onderzoekers er in geslaagd om enkele menselijke zintuigen na te bootsen: camera's en microfoons zijn bijvoorbeeld wijd verspreide technische hulpmiddelen. Bovendien is het met behulp van gas sensoren of andere chemische sensoren mogelijk om de menselijke smaak- en reukzin kunstmatig te implementeren of zelfs uit te breiden. Daarentegen is het moeilijker om het vijfde menselijke zintuig na te bootsen, namelijk de huid met tastzin, omdat het een gedistribueerd karakter heeft en een zeer groot en vervormbaar orgaan is. Om die reden wordt heel wat onderzoek gedaan om de ultieme "artificiële" of "kunstmatige" huid te ontwikkelen. In de wereld van sensoren wordt zo een kunstmatige huid gezien als een dunne, vervormbare folie met een groot aantal sensoren, te vergelijken met de menselijke huid.

Een dergelijke kunstmatige huid heeft zeer veel mogelijke toepassingen in de robotica en biomedische sector. De meest spraakmakende toepassing is ongetwijfeld het voorzien van een kunstmatige tastzin bij robots of gebruikers van prothesen. Bovendien kunnen deze mechanisch vervormbare sensorfolies gebruikt worden voor tal van andere toepassingen die nood hebben aan een hoge dichtheid sensoren op een onregelmatig of bewegend oppervlak. Momenteel wordt er bijvoorbeeld onderzoek verricht naar slimme beenprothesen die het comfort van de patiënt drastisch kunnen verhogen. Ze doen dit door nadelige effecten zoals wrijving en te grote drukken actief tegen te gaan en dit afhankelijk van de specifieke belastingen die veroorzaakt worden door verschillende activiteiten. Zo een systeem kan natuurlijk enkel goed werken als de te compenseren belasting effectief kan opgemeten worden door middel van sensoren. Hiervoor zou een artificiële huid uitermate geschikt zijn omdat die "ongemerkt" tussen het been en de prothese kan aangebracht worden. Voor deze en vele andere toepassingen is niet enkel het meten van druk, maar ook het meten van schuifspanning van belang aangezien deze schuifspanningen voorkomen wanneer wrijving of effecten van slip optreden. Beide categorieën kunnen beschouwd worden als "tactiele sensoren" of "tastsensoren".

De sleutel tot het maken van kunstmatige huid is de integratie van sensoren in geschikte, vervormbare materialen. Bovendien mogen deze sensoren niet merkbaar aanwezig zijn in de toepassingen. Dat wil zeggen dat ze dun, effen, vervormbaar moeten zijn en zonder uitstekende elementen. Bij gebruik in een prothese bijvoor-

beeld, kunnen te grote of niet-efven sensoren de huid irriteren en op die manier wonden veroorzaken, hetgeen men net wil tegengaan met “slimme prothesen”

Tot nu toe werd er het meeste onderzoek verricht naar elektrische sensoren voor gebruik in kunstmatige huid, hoewel deze soms minder nauwkeurig en gevoelig aan elektromagnetische interferentie (EMI) zijn. De werking van een veel gebruikte elektrische sensor, namelijk de capacitieve sensor, wordt bijvoorbeeld beïnvloed door strooicapaciteit. Dit is een ongunstig effect aangezien het menselijke lichaam zich zelf als een strooicapaciteit gedraagt en zo de sensor kan verstoren. Bovendien is het net de bedoeling om deze kunstmatige huid met sensoren dicht bij het lichaam te gebruiken. Optische sensoren daarentegen hebben niet te lijden onder deze nadelige invloeden en kunnen dus mogelijk performanter zijn voor deze toepassing.

Daarom is de doelstelling van deze doctoraatsthesis het onderzoek naar nieuwe types optische sensor principes die kunnen resulteren in de ontwikkeling van optische tactiele sensoren en bovendien geschikt zijn om te integreren in vervormbare materialen. Aangezien er veel toepassingen voor zijn en maar weinig beschikbare oplossingen, werden naast druksensoren ook schuifspanningssensoren onderzocht. Twee soorten sensor principes werden beschouwd, een gebaseerd op optische golfgeleiders en een tweede gebaseerd op ingebedde opto-elektronische componenten. Golfgeleider gebaseerde sensoren hebben het voordeel dat ze volledig optisch zijn en dus geen elektrische signalen nodig hebben om te functioneren. Dit kan interessant zijn in gevoelige of explosieve omgevingen waar elektrische signalen niet toegelaten zijn. Een nadeel is wel dat deze sensoren aangestuurd moeten worden met externe lichtbronnen en detectoren. Opto-elektronische sensoren daarentegen, vereisen geen extra componenten want ze maken rechtstreeks gebruik van detectoren en lichtbronnen om grootheden op te meten, maar ze vergen dus wel elektrische signalen voor hun werking. Beide types sensoren vereisen ook specifieke materialen voor hun goede werking. Het belangrijkste materiaal dat hiervoor gebruikt werd is “silicone” of correcter geformuleerd “Polydimethylsiloxane” (PDMS), omwille van zijn geschikte mechanische en optische eigenschappen. Zoals beschreven in Hoofdstuk 2, is PDMS uitrekbaar, sterk, gemakkelijk in gebruik en daarom uitermate geschikt als basismateriaal voor kunstmatige huid. Bovendien bestaan er verschillende types PDMS van optische kwaliteit die een welbepaalde brekingsindex bezitten en optisch transparant zijn. Hierdoor is PDMS niet enkel geschikt als drager materiaal, maar ook om de optische structuren zelf, zoals golfgeleiders, te creëren.

Het onderzoek naar golfgeleider gebaseerde sensoren is beschreven in Hoofdstuk 3 en 4. Om de kunstmatige huid ook echt vervormbaar te maken, moeten de sensoren en tevens de gebruikte golfgeleiders rekbaar gemaakt worden. De verschillende technieken om dergelijke golfgeleiders te vervaardigen zijn beschreven in Hoofdstuk 3, waarbij de focus lag op  $50\ \mu\text{m} \times 50\ \mu\text{m}$  multimodale structuren.

Een eerste techniek is gebaseerd op het principe van rekbaar elektronica: een niet-rekbaar materiaal wordt als een meanderende baan ingekapseld in een rekbaar drager. Dit principe werd gevalideerd door een technologisch proces te ontwikkelen om "EpoCore" en "Truemode" optische polymeren in te kapselen in PDMS. Op die manier wordt een rekbaar optische structuur bekomen waarvan het optisch polymeer het kernmateriaal, en de PDMS errond de mantel van de golfgeleider vormt. Deze techniek heeft als voordeel gebaseerd te zijn op traditioneel gekende processen en daardoor makkelijk uitvoerbaar te zijn. Door een harder en brozer polymeer in het zachtere PDMS in te kapselen zal de mechanische sterkte en betrouwbaarheid van de golfgeleiders echter beperkt zijn.

Om deze reden werd een tweede techniek geïntroduceerd die enkel gebruik maakt van PDMS om golfgeleiders te maken. Hierbij werden de kern en mantel van de golfgeleider gevormd door 2 types transparante PDMS met verschillende brekingsindex. Deze ontwikkelde golfgeleiders werden uitgebreid optisch en mechanisch gekarakteriseerd: optische propagatie verliezen lager dan 0.14 dB/cm en buigingsverliezen lager dan 0.08 dB per gebogen centimeter (kromtestraal 3.9 mm) werden opgemeten. Bovendien werd ook nagegaan wat de invloed is van mechanische rek op de optische propagatie verliezen in de golfgeleiders. Na metingen bleek dat het uitrekken van de golfgeleiders geen aanleiding gaf tot extreme verliezen, maar het verlies beperkt bleef tot gemiddeld 0.19 dB per 10% rek. Bovendien was het zo dat het grootste deel van deze opgemeten extra verliezen waarschijnlijk te wijten zijn aan de meetmethode, eerder dan aan extra verliezen in de golfgeleiders zelf.

In hoofdstuk 4 wordt bekeken hoe deze golfgeleiders gebruikt kunnen worden om tastgevoelige sensoren te ontwikkelen. Hiervoor werd een principe onderzocht dat gebaseerd is op druk afhankelijke licht transfer tussen 2 lagen golfgeleiders. De golfgeleiders worden in een matrix-configuratie geschikt zodat elk kruispunt overeenkomt met een sensor punt. Aangezien de golfgeleiders zeer klein worden gemaakt, kan men op deze manier een hoge dichtheid sensoren bekomen. De werking van dit sensor principe werd uitvoerig gemodelleerd en gevalideerd door een prototype te construeren. Op basis daarvan werd echter bekomen dat deze specifieke sensor een aan/uit gedrag vertoont en bovendien enkel druk en geen schuifspanning kan detecteren. Uit deze resultaten werd geconcludeerd dat dit golfgeleider gebaseerd ontwerp niet rechtstreeks bruikbaar is om toe te passen als tastsensor.

Daarom werden ook andere technieken onderzocht om tastsensoren te ontwikkelen, namelijk gebaseerd op opto-elektronische componenten. Aan het Centrum voor Microsysteem Technologie (CMST) werd voorheen reeds een technologie ontwikkeld om Vertical-Cavity Surface-Emitting Laser (VCSEL) en fotodiode chips te verdunnen en in te kapselen in zeer dunne polymeer folies (totale dikte  $\approx 40 \mu\text{m}$ ). Deze folies kunnen zeer klein en flexibel gemaakt worden en bovendien werd binnen het CMST reeds aangetoond dat deze technologie bruikbaar is

om toe te passen in druk én schuifspanningssensoren. Dit maakt deze technologie uitermate geschikt als bouwstenen om artificiële huid te ontwikkelen. De nadruk van dit doctoraatsonderzoek lag op het ontwikkelen van de schuifspanningssensoren terwijl een ander doctoraatsonderzoek aan het CMST zich focust op de druksensoren.

Het ontwerp en realisatie van deze sensoren is gedetailleerd beschreven in Hoofdstuk 5. Het werkingsprincipe van de sensor is gebaseerd op het variërende optisch vermogen opgevangen door een detector, wanneer zijn relatieve zijdelingse verschuiving ten opzichte van een lichtbron verandert. Wanneer de lichtbron en detector perfect uitgelijnd zijn, is het gedetecteerde optische vermogen maximaal maar wanneer ze zijdelings verschoven worden ten opzichte van elkaar, neemt het vermogen invallend op de detector af. Zo een sensor detecteert in feite verplaatsingen. Nu is het echter zo dat schuifspanningen en verplaatsingen in materialen gekoppeld zijn aan elkaar en gebaseerd hierop kan dus een vervormbaar materiaal gebruikt worden om schuifspanning om te vormen naar detecteerbare zijdelingse verplaatsing. Hiervoor werd een transparant type PDMS, Sylgard®184, geselecteerd omwille van zijn lage mechanische modulus hetgeen aanleiding geeft tot een zeer gevoelige sensor.

Een theoretisch sensor model werd ontwikkeld om op basis daarvan geschikte optische en mechanische ontwerpparameters te selecteren. Voor de huidige sensoren werd de optimale laagdikte voor het omvormer materiaal vastgelegd op 180  $\mu\text{m}$ . Er is ook aangetoond dat een sensor met gewenste gevoeligheid en dynamisch bereik kan bekomen worden door keuze van een omvormer materiaal met geschikte mechanische eigenschappen. In dit hoofdstuk worden verschillende generaties sensoren besproken. Met het initiële sensor ontwerp kon enkel de grootte van een schuifspanning opgemeten worden en daarom werd bovendien een verbeterd ontwerp ontwikkeld dat toelaat om ook de richting van de schuifspanning te bepalen. Voor dit finale ontwerp werden een of meerdere vierkante photodiodes gebruikt, in combinatie met 2 VCSELs, een voor metingen van variaties in de  $x$ -richting en de andere voor metingen in de  $y$ -richting.

De karakterisering van de verschillende generaties sensoren is beschreven in Hoofdstuk 6. Eerst werden de opto-elektronische componenten zelf opgemeten om als feed-back te dienen ter validatie van het sensor model. Vervolgens werd de eerste generatie schuifspanningssensoren gekarakteriseerd met als doel de haalbaarheid van de sensor technologie aan te tonen. Deze metingen laten zien dat het gedrag van de sensor overeenkomt met de gesimuleerde waarden. Het dynamisch bereik van de sensor was ongeveer 100  $\mu\text{m}$  uitgedrukt in zijdelingse verplaatsing, ofwel 5 N uitgedrukt in schuifspanning. De gevoeligheid in het lineair gebied was  $-350 \mu\text{A N}^{-1}$  of  $-7 \mu\text{A kPa}^{-1}$ .

Het finale ontwerp biedt de mogelijkheid om ook de richting van de schuifspanning te bepalen en werd daarom uitgemeten in functie van de oriëntatie van een aangelegde zijdelingse verplaatsing. Deze uitgevoerde metingen toonden inder-

daad aan dat dit ontwerp geschikt is om de grootte en richting van een schuifspanning te bepalen. Door de verschillende opbouw van deze vierkante fotodiodes was het binnen de termijn van deze thesis nog niet aangetoond om deze componenten te integreren in een flexibele dunne folie. Momenteel wordt er echter onderzoek verricht binnen het CMST om dit in de toekomst wel mogelijk te maken.

Het werk wordt besloten in hoofdstuk 7 en de resultaten worden er getoetst aan de vooropgestelde objectieven. Bovendien worden enkele onderwerpen voor verder onderzoek gesuggereerd. Het is duidelijk dat er nog heel wat mogelijkheden zijn om de voorgestelde schuifspanningssensor en ook een veelheid van andere aspecten binnen het domein van de artificiële huid sensoren verder te ontwikkelen.



## Summary

Owing to recent technological advances, researchers were able to mimic several of the human sense organs artificially: cameras and microphones are widely available to support vision and hearing capabilities while gas sensors and other biosensors can be used to artificially implement the human smell and taste organs. However, the human touch organ or “skin” is much more difficult to imitate due to its distributed character; this is therefore a subject of intensive research. In the research domain of sensors, an “artificial skin” is considered to be a thin, deformable foil with a large number of sensors, comparable to the human skin.

Such an artificial skin-like sensor foil has numerous potential applications in the robotic and biomedical community. The most appealing is probably the possibility of providing robots or physically disabled people with an artificial sense of touch. Additionally, these deformable sensor patches can be used for several other applications requiring high-density sensors on an irregularly shaped or moving surface. As an example, research is currently being performed toward smart limb prosthetics that can increase the comfort of an amputee by adapting the conditions in the prosthetic socket depending on the detected physical loading situation. The benefits of such devices would drastically increase when appropriate artificial skin based sensors would be available to register these loading conditions, so that a closed-loop control system can be implemented. In several of the above-mentioned applications, not only pressure sensing (“normal stress”), but also shear stress sensing is important, especially for prosthetics, since this enables detection of friction or slippage effects.

The key to constructing artificial skin is integrating sensors in appropriate, deformable skin-like materials. Furthermore, these integrated sensors should be unobtrusive, i.e. “not noticed” by the application or user and therefore need to be thin, flat, deformable and without protrusions. When used in prosthetic sockets, for example, bulky or non-flat sensors may protrude in the patient’s skin and cause injury.

The focus of the former and current research in the field of artificial skin is mainly on electrical sensors, that may however be less accurate and susceptible to electromagnetic interference (EMI). For example, the operation of capacitive sensors is influenced by stray capacitance. This situation is most unfavorable since the

human body acts as a stray capacitance and the artificial skin with sensors is often used in proximity with the human body, influencing the sensor operation. Systems based on optical sensing principles do not suffer from these negative effects and potentially offer a better performance for operation in contact with the human body.

Therefore, the objective of this PhD dissertation is to investigate new types of optical sensing principles resulting in tactile sensors that are suitable for integration in deformable skin materials. Because of the large number of potential applications but low availability of prototypes or commercial products, shear stress tactile sensors were investigated, in addition to pressure tactile sensors. Two types of sensing principles were investigated, the first based on optical waveguides and the second based on embedded optoelectronic components. Waveguide based sensors have the advantage of being fully optical avoiding electrical signals in the sensing region but require to be coupled with external light sources and detectors. On the contrary, optoelectronic based sensors directly employ light sources and detectors for measuring a physical quantity but need electrical signals to operate. Both categories of sensors require dedicated materials for their operation. The key material used for these unobtrusive sensors is Polydimethylsiloxane (PDMS) because of its mechanical and optical properties, as described in Chapter 2. PDMS is stretchable, strong, easily processable and therefore ideally suited as a base material for creating artificial skin. Furthermore, there exist several types of optical grade PDMS formulations with a well-defined refractive index and a high optical transparency. Therefore, PDMS is not only suited as a substrate, but even to create micro-optical structures, such as waveguides.

The work on waveguide based sensors is described in Chapter 3 and 4. To make the artificial skin truly unobtrusive, the sensor assembly needs to be stretchable and therefore the used waveguides also need to be made stretchable. Different techniques to fabricate such stretchable waveguides are described in Chapter 3 and the focus was on  $50\ \mu\text{m} \times 50\ \mu\text{m}$  multimodal structures.

A first technique is based on the principle of stretchable electronics, i.e. a non-stretchable material is patterned as a meandering track and embedded in a stretchable material. This principle was validated by establishing a technology to embed "EpoCore" and "Truemode" optical polymers in PDMS so that the optical polymer serves as the waveguide core and the PDMS as the cladding. The advantage of this technology is that it is based on traditional printed circuit board fabrication techniques and therefore easily applicable. However, due to the use of a harder and more brittle polymer in a soft and highly stretchable rubber, the mechanical strength and reliability of the waveguides is limited.

Therefore, a second technique was introduced using 2 types of PDMS with a different refractive index for the waveguide core and cladding. These waveguides were extensively characterized and optical propagation losses down to 0.14 dB/cm and bending losses down to 0.08 dB per bent centimeter (3.9 mm

bending radius) were found, comparable to values reported in literature for optical polymer multimode waveguides. Furthermore, the influence of the optical propagation loss due to stretching of the waveguides was found to be limited (an average of 0.19 dB per 10% elongation). Moreover, the main part of the observed losses are believed to be attributed to coupling issues at the waveguide interface during the measurements rather than due to the elongation of the waveguides.

Chapter 4 describes how these waveguides can be employed to construct tactile sensors. Therefore, the principle of using pressure dependent light coupling between 2 layers of waveguide arrays, as in a matrix configuration, was investigated. Each crossing point of 2 waveguides on a different layer serves as a sensing point. Such a configuration enables very high sensor densities since the waveguides can be made very small. The sensor operation was extensively modeled and validated by fabricated proof-of-principle demonstrators. However, it was found that this sensing principle exhibits an on/off behavior and furthermore, only normal forces and no shear forces could be measured. From these results, it was concluded that this waveguide based coupling technique is not easily applicable for constructing a tactile sensor.

Therefore, alternative techniques for constructing tactile sensors, based on optoelectronic components, were established. At the Centre for Microsystems Technology (CMST), a technology was previously developed to embed Vertical-Cavity Surface-Emitting Lasers (VCSELs) and photodiodes in very thin polymer foils ( $\approx 40 \mu\text{m}$  thin). These optoelectronic foils can be made very small and flexible and it was shown that the same technology can be used to construct both tactile pressure and shear sensors so that they are ideally suited as building blocks for constructing artificial skin. Although an optoelectronic pressure sensor is also being developed at CMST, this dissertation only focuses on the development of the shear sensor.

The design and fabrication of the sensor is detailed in Chapter 5. The sensor operation principle is based on the changing optical power captured by a detector when its relative lateral position to a light source varies. When the light source and detector are perfectly aligned, the detected optical power is maximum. However, when the light source and detector are increasingly misaligned, the optical power incident to the detector decreases. This is actually an implementation of a displacement sensor. However, shear stresses and displacements in materials are linked meaning that a transducer material applied between the light source and detector can be used to convert the mechanical shear stress into displacements that can be measured. A transparent PDMS, Sylgard®184 was selected as transducer material because of its low modulus, resulting in a highly sensitive device.

Based on a constructed sensor model, optical and mechanical design parameters were selected. The optimum transducer layer thickness between the VCSEL and photodiode was found to be  $180 \mu\text{m}$  and it was demonstrated that the de-

sired shear sensor sensitivity and dynamic range can be obtained by selecting a (transparent) transducer material with appropriate mechanical properties. Furthermore, the basic sensor principle was extended to construct a device capable of detecting the shear stress direction in addition to its magnitude. The final design was based on using one or more square photodiodes in combination with 2 VCSELs, one for detecting changes in the  $x$ -direction and the other for detecting changes in the  $y$ -direction.

The characterization of the different shear sensor generations is described in Chapter 6. First, the used optoelectronic components were characterized and the acquired characteristics were used as feed-back to validate the sensor model. Then, the first generation shear sensor was characterized to prove the technological feasibility of constructing a flexible shear sensor. It was found that the sensor response, i.e. the current from the photodiode in function of the applied lateral displacement or shear force, was as expected. This sensor was only able to measure the magnitude of the shear force due to the symmetrical sensor build-up and the used round photodiode. The dynamic sensor range was about  $100\ \mu\text{m}$  in terms of displacement or  $5\ \text{N}$  in terms of shear force, and the maximum sensitivity was  $-350\ \mu\text{A N}^{-1}$  or  $-7\ \mu\text{A kPa}^{-1}$ .

The final sensor design that is also able to detect the direction of shear force was tested in function of the angle of lateral displacement. It was shown that this design is suited to detect both the shear force magnitude and direction. However, due to the different layout of the photodiodes it is more difficult to embed these components in flexible foils and therefore, some technological development is still needed to make this version of the sensor also mechanically flexible and to fully characterize it.

Chapter 7 concludes this dissertation by comparing the achievements with the initial objectives. Furthermore, some topics for future work are suggested. It is clear that there are still numerous opportunities for further developing the proposed shear sensor concept and several other topics from this emerging field of artificial skin-like tactile sensors.

# 1

## Introduction

*The beginning is the most important part of the work*  
–Plato

### **1.1 Artificial skin: a sixth sense?**

---

Some people are convinced they have a sixth sense and believe to have a connection with the unconsciousness or the spiritual world so that they are able to receive extra information related to a situation, next to information from the 5 basic senses. Imagine we can create such a sixth sense artificially using advanced technology. If we equip the human body with all sorts of sensors, they can provide valuable information. Firefighters, for example, are often working in dangerous situations and are exposed to heat, smoke or other chemical substances and limited view. Their working conditions would drastically improve if they would be fitted with an artificial sense organ that can measure temperature, gas, chemicals, proximity of objects etc. and is integrated in clothing, gloves or directly on the skin.

In the medical sector, true artificial skin with a sense of touch, could ultimately replace the human skin in case of serious injuries or on prostheses. Although you rather expect to encounter such applications in science fiction movies, work is in progress to fabricate “skins” with sensors, that behave similarly compared to the human skin and could be used to equip robots with a sense of touch. Providing

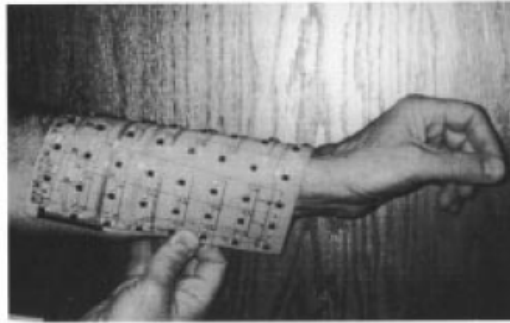


**Figure 1.1** – The concept of artificial skin as proposed by Lumelsky et al.: a deformable substrate with a matrix of sensors that can be wrapped around irregular objects (Courtesy of V. Lumelsky, Robotics Laboratory, University of Wisconsin-Madison [2]).

robots with this ability to feel is important when they have to operate in unstructured environments, in contact with other robots or humans. The robots that are programmed to assemble our cars, execute a series of fixed procedures, but when robots need to interact with humans they require recording the changing environment to act appropriately.

### 1.1.1 The concept of “artificial skin”

The concept of artificial skin and possible implementation strategies have been presented explicitly for the first time on a DARPA workshop in 1999 [1]. In a follow-up article, Lumelsky et al. have described the numerous applications and required technology [2]. To produce artificial skin, several basic components are required. Firstly, similarly to the human skin, a flexible and stretchable base layer or substrate is needed that can be wrapped around an irregular or moving surface, wrinkled and deformed without breaking and without hindering the movement of the surface on which it is applied, i.e. the skin needs to be unobtrusive. Therefore, new materials different than the rigid traditional printed circuit boards or silicon wafers have to be used for fabricating or embedding the sensors. Generally, a distinction is made between flexible and stretchable “substrates”. Stretchable substrates can be wrapped around a randomly shaped object, while flexible substrates can only be wrapped around a cylindrical object. Figure 1.1 shows a first prototype of surface mounted sensors on a flexible Kapton foil, as presented by Lumelsky.

The second basic requirement is a surface with a large number of sensors. The exact number and density of the sensors depends on the application, but at least an array with several sensing points is needed for distributed measurements. As a comparison, there are 241 sensing elements per square centimeter present in the

human fingertips.

Finally, there are some practical requirements that are related to the read-out and processing of the sensor data. Preferably, the driving electronics are small, low-power and integrated in the substrate itself. Furthermore, it can be questioned what the maximum number of sensors is that a system, for example a robot, can process before its response time becomes unacceptable. This response time to react to the sensor signals depends both on the readout speed of the sensors themselves and on the processing power of the system, meaning that these parameters directly limit the possible number of sensors. However, the specific topology for collecting and processing sensor data can also have a significant impact on the performance of the system. When all the sensors are directly connected to a central processor, it will be overloaded with data and the system becomes too slow. Instead, inspired by biological skin, some researchers propose to process the sensor data locally and then send only the relevant data to the central processor [3]. Additionally, such a distributed read-out and data processing would allow to cut the skin to the desired shape without destroying its functionality.

Combining all these proposed “requirements” is challenging, but considerable progress has recently been made and current technologies are increasingly approaching the realization of a true artificial skin.

### 1.1.2 Applications of artificial skin

Flexible or stretchable tactile sensor sheets have numerous applications. Not only they can be used to equip robots with a sensitive skin, but also in several other applications that require measuring mechanical stresses unobtrusively on larger surfaces. Furthermore, the stress acting on a surface has a component perpendicular and components parallel to the surface. The perpendicular component is observed as pressure while the parallel component is experienced as shear stress or friction. The focus on detecting pressure or shear stress or both, the range of detectable stress, sensitivity and resolution depends on the specific application. In the following text, several typical applications are discussed and correspondingly the requirements for the tactile sensors are formulated.

#### Providing robots with a sense of touch

For operating robots in unstructured environments, tactile sensors are needed. Camera vision systems are useful, but providing robots with a real sense of touch is leading to major breakthroughs. Furthermore, tactile sensors provide direct information, require less data processing and measurements are independent of environmental conditions such as lighting.

Manipulation of delicate objects –often pictured as “picking up an egg without breaking it”– can only be performed when a robotic hand is able to apply suf-

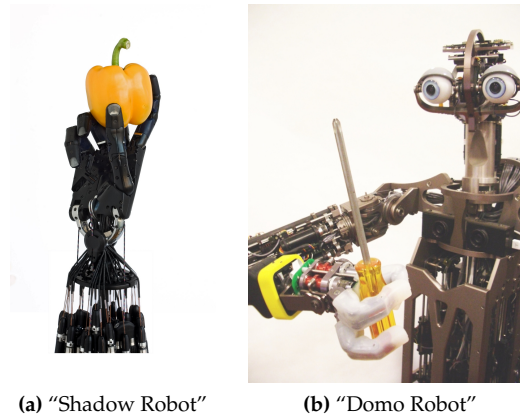


**Figure 1.2** – (a) Robotic hand with tactile sensors for handling fragile objects (Courtesy of The Shadow Robot Company [5]). (b) Prototype of a robot for assistance of elderly people (Courtesy of Edsinger, A., MIT [6, 7]).

ficient force, enough to grab the object but without breaking it. This can be achieved with pressure sensors, but shear stress sensors would additionally provide information related to slippage of the object [4]. Next to grasping, robots need to be able to sense contact for a safe interaction with humans, other robots or the environment.

These robots with a sense of touch have numerous applications as domestic robots for the assistance of elderly people, medical assistant robots or production site robots. Figure 1.2a shows a robotic hand equipped with artificial muscles and tactile sensors for the handling of delicate objects and Figure 1.2b shows the Domo Robot, a domestic robot being developed at MIT for the assistance of elderly people.

Requirements for robotic skin-like tactile sensors are difficult to define because they usually depend on the specific application. However, many researchers consider the properties of the human skin sensors (“mechanoreceptors”) as a reference for specifying ideal artificial tactile sensors. Therefore, these human tactile sensing properties have been investigated extensively [8, 9, 10].

An estimated number of  $241\text{ cm}^{-2}$  mechanoreceptors are present in the fingertips and about  $58\text{ cm}^{-2}$  in the palm of the hand. Furthermore, there are several types of receptors with different sensory functions and properties: Pacinian corpuscles and Meissner’s corpuscles are fast adapting while Merkel cells and Ruffini corpuscles are slow adapting receptors. The fast-adapting (FA) receptors respond when external stimuli are applied or removed, and the slow-adapting (SA) receptors remain activated as long as the stimuli are applied. Furthermore, type I re-

**Table 1.1** – Overview of the properties of mechanoreceptors in the fingertips. Adapted from [11].

	Pacinian Corpuscle	Ruffini Corpuscle	Merkel Cells	Meissner's Corpuscle
Type	FA II	SA II	SA I	FA I
Adaptation Rate	Fast	Slow	Slow	Fast
Spatial point to point resolution (mm)	10+	7+	0.5	3-4
Stimuli Frequency (Hz)	40-500+	100-500+	0.4-3	3-40

ceptors are found in the upper layers of the skin and have a well-defined, smaller receptive field while type II receptors are found deeper in the skin and therefore have a more diffuse, but larger receptive field [4]. Table 1.1 lists the most important properties of these receptors inside a human fingertip.

The spatial resolution of touch depends on the location across the body and furthermore on the type of mechanoreceptors. This parameter is commonly defined as the two-point spatial resolution, being the smallest separation at which one can distinguish if two different points are touched. For example, a human can resolve 2 points separated by 1 mm on the fingertips [11] and 30 mm on the abdomen.

The temporal resolution also depends on the type of mechanoreceptors and in general, humans are able to detect vibrations up to 700 kHz. Particularly the Pacinian receptors are specialized in detecting these high-frequency vibrations.

Based on these properties of the human mechanoreceptors, several research groups have formulated design hints when constructing sensor arrays for robotic in-hand manipulation [4, 11]. The point-to-point spatial resolution of such tactile sensors should be 1 mm on the fingertips and 5 mm in the palm of the hand. Furthermore, they should be sensitive to forces ranging from 0.1 N to 10 N with a 0.01 N resolution and a response time of 1 ms. Additionally, it is beneficial to be capable of detecting shear forces in order to compensate slippage. These shear forces resulting from slippage are not larger than the normal forces applied for grasping [12, 13, 14].

### Remote minimal invasive surgery

Minimal invasive surgery (MIS) has recently been introduced and enables operating through small incisions which results in less pain and reduced risk of complications for the patient. In MIS, a patient is operated by a robot which is remotely controlled by a surgeon. Based on visual information from a camera system, the



**Figure 1.3** – DaVinci® surgical system at AZ Sint-Lucas, Ghent, Belgium. A surgeon is operating remotely using robotic arms.

surgeon manipulates joysticks and the resulting signals are interpreted by a computer and serve as an input to drive the robotic arms operating the patient. Since the surgeon is not in direct contact with the patient but operates the tools from a distance, this offers possibilities for remote surgery of highly specialized operations that can only be performed by a few doctors around the globe.

Currently, a limitation of this innovative system is the lack of tactile feedback since the visual feedback is not sufficient to make surgical decisions in some cases, e.g. to decide where to cut. In traditional operations, a surgeon can rely on his own tactile organs to locate tumors or blood vessels for example. This technique of scanning the tissue to detect harder regions is named “palpation” and widely used in medicine. For example, the majority of all tumors can be detected by palpation and therefore mimicking the human tactile sense on a robotic finger would be highly beneficial for this purpose.

As described above, the requirements for such a tactile device are formulated according to the human tactile sense, and for MIS in particular on the properties of the mechanoreceptors in the fingertips. Johnson and Phillips have demonstrated that the human finger can distinguish between 2 points when not located closer than approximately 1 mm [11]. When the palpation is performed on a soft tissue, a detectable pressure range from 10-40 kPa is required [15], but a range of 10-100 kPa is recommended to provide a safe margin. For this application, high-density pressure sensing is more important than being able to detect shear stress. Furthermore, a sensor accuracy of  $\pm 10\%$  is sufficient, comparable to the human skin. Finally, the necessary read-out frequency of the sensors depends on the speed of palpation. This speed is typically smaller than  $120 \text{ mm s}^{-1}$ . Peine et al. determined that the bandwidth required corresponding with this speed is 30 Hz for 2 mm resolution and hence 60 Hz for 1 mm resolution when the data is to be

indicated on a tactile display [16]. However, to perceive textures, frequencies up to 500 Hz and above are needed [17].

Such “tactile displays” replicate tactile information so that a human finger, when touching the display, feels similar tactile sensations to those originating during actual palpation or touching of objects. A first approach aims to recreate the object being touched, for example using an array of moving pins comparable to an electronic version of the Braille system. Another approach relies on the application of lateral skin deformation, as presented by Hayward et al. [18, 19].

### Shoe sole stress distribution for sports or orthopedics

Being able to record the plantar stress distribution (i.e. the stress distribution on a foot sole [20]) of a patient is essential for clinical gait analysis. This subdivision of medical science describes the human gait patterns e.g. for diagnosing different disorders. Therefore, the stresses on individual parts of the foot need to be determined, meaning that a distributed sensing device is required so that not only the average stress value, but also peak values can be recorded. This is important because peak stresses higher than a certain value can result in the formation of pressure ulcers [21, 22]. Furthermore, it is shown that not only pressure, but also shear stresses have an important contribution to the plantar stresses and excessive values can lead to blood flow occlusions [23]. Moreover, shear and pressure stresses are rarely occurring separately but rather simultaneously, however usually one effect dominates over the other.

In sports, there is similar interest for such sensor systems. Detection of the stresses acting on the feet of a sportsman provides valuable information for a customized shoe design or personalized training schemes.

There are several possible types of sensor systems to record this plantar stress data. A first type are the force platforms; these systems provide 3-dimensional force information acting on the foot, can be very fast but do not allow to obtain stress distributions on the shoe sole itself. Instead, pressure distribution platforms are able to record these distributions, but are typically limited to pressure measurements. Due to their limited size, they need to be embedded in a walkway to provide a warming-up period and generate a normal walking situation at the time the actual sensor surface is reached. Furthermore, the system is mainly limited to barefoot measurements since the shoe may mask valuable information.

In-shoe systems directly record the stress at the foot-shoe interface and offers an ideal solution when investigating the influence of different shoes on the plantar stress distribution. Such a system allows recording repeated steps and can potentially be used for monitoring in-situ, outside the lab. Since they are embedded in the shoe, unobtrusive sensor foils are required to avoid interfering with normal activity such as walking or running. Therefore, these sensor systems need to be thin, flexible and without protrusions that can hurt the foot.



**Figure 1.4** – “Harmony®Vacuum Management System” from Otto Bock equipped with a vacuum pump to regulate the pressure in the socket. Courtesy of Otto Bock [33]

For in-shoe measurements, the readout bandwidth can be smaller than for tactile sensing, i.e. 10 Hz for normal walking and up to 200 Hz during more strenuous activities would be sufficient [24]. The size of the individual sensors in the matrix need to be small enough in order to distinguish between different areas of interest on the foot sole. Furthermore, a single sensor measures the average pressure over its whole surface and therefore large sensors may underestimate actual peak pressures. Davis et al. suggested that the individual sensors should be smaller than  $6.4 \text{ mm} \times 6.2 \text{ mm}$  to limit peak pressure underestimation [25].

The resulting pressure values are typically much higher than for palpation and depending on the type of activity. Peak pressure values up to 200 and 1000 kPa typically occur during stance and walking respectively. In more extreme conditions, these values may increase up to 2000-3000 kPa [24, 26, 27, 28, 29].

Commercially available sensing foils (such as F-scan [30] and Xsensor [31]) are only able to detect pressure or normal stresses, but no shear stresses. Additionally, measuring the shear stress distribution can reveal important information. Several studies have indicated relations between the location of peak shear stress and foot ulcers or skin breakdown, for example for diabetic patients [21, 22, 32]. These studies recorded peak shear stress values ranging from 30 kPa up to 300 kPa depending on the foot conditions, location and the type of activity.

### Smart prosthetics

Although (lower limb) prosthetics are becoming increasingly more advanced, there is still a significant discomfort for wearers of these devices resulting from interfacial stresses between the amputee stump and the prosthetic socket. Excessive stresses can lead to pressure ulcers, which are areas of local tissue breakdown

in skin and/or underlying tissue. These ulcers are painful, difficult to treat and reduce patient mobility. Preventing high interfacial stresses and the resulting formation of pressure ulcers can dramatically increase the quality of life of millions of amputees.

Relieving these stresses can be accomplished by fitting the prosthetic socket to a specific user and loading conditions, depending on the type of activities. The socket can be custom-made for the patient following a series of tests in the laboratory, e.g. using camera systems to observe patient-prosthesis interaction.

However, the actual exerted stresses can only be recorded accurately using sensor systems applied in the socket. For example, the ideal prosthesis design can be studied using a prototype socket with embedded sensors. The stresses occurring can then be recorded for various activities, potentially even outside the lab if the system is equipped with a transmitter or data logger. Based on the recorded stress distribution, the socket can be fit so that stress is relieved in the critical regions. When a best-fit socket is designed for a patient, it can significantly improve the comfort and reduce stresses, but the performance can only be optimized “on average”, meaning that for certain activities the socket will perform well, while for other activities another design would perform better.

In the ideal situation, the socket would be self-adjusting depending on the situation. This can only be achieved when the prosthesis is equipped with an actuator system to influence the conditions in the socket. A common problem causing phenomenon that designers of prostheses have been facing is the changing volume of the residual limb on the long and short term [34, 35]. To reduce this disadvantageous effect, vacuum assisted sockets have been developed [36, 37]. A commercial example is the “Harmony® Vacuum Management System” from Otto Bock (see Figure 1.4) which uses a vacuum pump to pull air out of the socket for a better fit.

Further optimization of such a system can be achieved by equipping the prosthesis with sensors to monitor the actual stress values. Depending on this measured data, an actuator (e.g. vacuum pump) can control the conditions in the socket continuously to achieve the optimum situation during various types of activities.

This ideal concept can only be achieved when sensors are integrated in the socket. Therefore, they need to be very thin, flexible and without protrusions. Several commercial sensors capable of measuring pressure distributions are available, but show limitations. They are unable to comply with the highly curved and complicated socket geometry, exhibit sensor protrusions causing stress peaks and can only detect normal stresses and not distinguish shear stresses [38, 39, 40]. Sanders et al. suggested that these shear stresses play an important role [41] and that shear stresses of 23 kPa may lead to skin breakdown [42]. However, only few studies have investigated the effect of shear stresses due to a lack of adequate sensors.

The typical required dynamic sensing range is again highly dependent on the specific patient and situation. During normal walking, peak pressures in the socket up to 150 kPa were recorded by Beil et al. [36], but stresses can be much higher during strenuous activities. On the other hand, Sanders et al. reported on interfacial pressures up to about 200-250 kPa and resulting shear stresses up to 50 kPa occurring in the socket [43, 44].

As a summary, for use in prosthetic sockets, highly compliant, thin and unobtrusive sensors are needed. In the ideal case, they need to be able to distinguish between and detect pressure and shear, since both types of stresses never occur isolated from each other. Pressure sensors need a sensing range of several hundreds of kPa, shear sensors a range of about 100 kPa and need to be able to detect the shear direction. Furthermore, these shear stresses are accompanied by skin deformations of a few centimeters that have to be taken into account for the sensor design. Additionally, the sensors need to exhibit a sufficient data acquisition rate (300-500 Hz) to record rapid changes during strenuous activities.

## Conclusion

The previous discussion only mentions the most appealing applications, but there are numerous other that would benefit from artificial skin-like tactile pressure and/or shear sensors. These applications are mainly situated in the medical community where various stresses at the interface with the human body need to be monitored. The required sensor characteristics vary over a wide range for all these different situations, but the sensors needed for these applications have one specific requirement in common being mechanical flexibility and geometrical shape. True unobtrusive sensors without protrusions are needed which are thin, flexible or ideally stretchable to be wrapped around curved and moving surfaces.

**Table 1.2** – Tactile sensing requirements for different applications.

	In-hand manipulation (Robotics)	Palpation (MIS)	Stress distribution (Shoe sole)	Interfacial forces (Prosthetics)
Spatial acuity (“resolution”)	1 mm (finger) 5 mm (palm)	1 mm	<6 mm	several cm
Readout bandwidth (Hz)	1000	500	200	300-500
Max. pressure/force	10 N	100 kPa	100 kPa- >1000 kPa	300 kPa
Pressure/force resolution	0.01 N	0.5 kPa	n/a*	n/a
Max. shear	10 N	n/a	100 kPa	100 kPa
Shear resolution	0.01 N	n/a	n/a	n/a

\* n/a: This field is not applicable or no explicit data is available.

As a general conclusion, several concrete specifications for sensors corresponding with the above-mentioned applications are summarized in Table 1.2.

## 1.2 Recent trends in tactile sensing technology

---

### 1.2.1 Flexible and conformable sensor substrates

As discussed and illustrated above for several applications, sensor systems will only be serving as “true artificial skin” when mechanically compliant and therefore, considerations about the substrate are very important. The sensors can be fabricated directly on a suitable substrate, or alternatively can be embedded in such a substrate material afterward.

Traditional printed circuit boards (“FR-4”) or silicon wafer substrates are rigid and therefore completely incompatible with the concept of skin. On the other hand, flexible substrates can be bent but only be wrapped around cylindrical surfaces. Therefore, an increasing amount of research is focusing on stretchable substrates which can cover irregularly shaped objects. To obtain a stretchable “sensor skin”, the sensors themselves can be made stretchable or alternatively non-stretchable islands with sensors can be incorporated in the skin and connected with stretchable interconnections. For example, the shear sensors developed in the scope of this work (see Chapter 5 and 6), are very small, thin and flexible, so that they are ideally suited for embedding in such stretchable skin materials.

These required interconnections are either optical (e.g. waveguides, fibers) or electrical (e.g. metal or conductive polymer tracks), depending on the sensing mechanism. Electrical sensors logically require electrical connections and several groups are performing research on these “stretchable electronic interconnections”. The copper tracks can for example be shaped as meanders [45, 46, 47] or wavy structures [48, 49] and embedded in an elastic material so that the entire composition becomes stretchable.

However, in this dissertation, the focus is on optical sensors. Depending on the location where this optical sensor signal is converted into an electrical signal (close to the sensing region or away from the sensing region), the sensors are connected either with electrical or optical interconnections. Such optical interconnections allow to link optical sensors directly without converting the optical signal into an electrical signal. This can be advantageous in situations where electrical currents are undesired, such as in the human body. Instead, the optical sensor signals are transported –this can be several centimeters or several meters– so that the conversion from optical to electrical signals can be performed outside the sensitive region.

Therefore, research was also performed toward such stretchable optical interconnections as described in Chapter 3, while the properties of the used materials are

discussed in Chapter 2.

### 1.2.2 Progress toward artificial skin

Several types of tactile sensors (pressure, shear or combined sensors) have been reported in literature. The earlier work was mainly based on silicon micromachining techniques that were traditionally used for MEMS (Microelectromechanical Systems) fabrication [50, 51]. However, the silicon substrate is very brittle and therefore not suited for constructing flexible sensor sheets. More recently, there has been a shift toward flexible polymer based sensors, using for example polyimide, parylene or PDMS substrates.

This section gives an overview of a number of tactile sensors as reported in literature. Both shear stress and pressure sensors were investigated. For preparing the overview of pressure or normal stress sensors, only papers presenting arrays of multiple elements were reviewed, since typically a matrix of sensors is needed for tactile sensing. However, regarding shear stress sensors, also single element solutions were included due to limited work reported on arrays of shear sensors. In the tables accompanying this section, details on both pressure and shear sensors are listed simultaneously, since often sensors are reported to measure both pressure and shear stress. The reported tactile sensors are mainly based on (piezo-)resistive, capacitive and recently also optical fiber or waveguide based sensing principles.

#### Resistive sensors

An overview of the functional properties of various piezoresistive sensors is given in Table 1.3. These sensors are based on the piezoresistive effect (e.g. in semiconductors) and are therefore typically very sensitive and linear. They are fabricated using well established MEMS techniques and can have small sizes and high spatial resolution. Furthermore, they can easily be integrated with electronics or other MEMS. However, the sensor elements are very fragile and therefore need appropriate packaging, which can significantly increase the total sensor size. Additionally, they may potentially suffer from temperature variations and the required micromachining processes are complex and rather expensive.

A slightly different resistive sensing approach relies on strain gauges mounted on deformable membranes, fabricated on polymer substrates instead of silicon wafers, to introduce mechanical flexibility [60, 61].

Another type of resistive sensors is based on conductive polymers, for example highly deformable rubbers. Depending on the pressure applied onto the polymer, the resistance varies. When conductive rubber polymers are used, the sensors are inherently flexible, robust and low-cost large area fabrication techniques can be applied. However, their sensing range and accuracy is lower. Furthermore, de-

**Table 1.3** – Overview of the properties of piezoresistive tactile sensors in literature.

Technology	Size of 1 sensor [mm]	Sensor count	Load [type]: [range]	Sensitivity
Silicon bulk micromachining, PDMS technology [52]	7x3.5	1	Shear: 7 kPa	50 mV kPa <sup>-1</sup>
Silicon bulk micromachining, PDMS technology [53]	10x10x1	1	Shear: 4 N	0.0036 N <sup>-1</sup> up to 0.0067 N <sup>-1</sup>
Silicon bulk micromachining, PDMS technology [54]	20x20x1.5	1	Shear: ±5 kPa	0.001 30 kPa <sup>-1</sup>
Advance silicon etching (ASE) [50]	2.3x2.3x1.3	1	Normal: 2.5 N; Shear: 0.4 N	0.054 N <sup>-1</sup>
Silicon bulk micromachining [51]	3x3x0.3	1	Shear: 1.4 N	0.13 $\frac{\text{mV}}{\text{mA MPa}}$
CMOS fabrication process [55]	4x4	4x8	Normal: 50 N; Shear: ±10 N	Normal: 0.013 V N <sup>-1</sup> ; Shear: 0.0023 V N <sup>-1</sup>

pending on the mechanical polymer behavior, the sensors may suffer from significant non-linearities or hysteresis. Since the rubbers conduct in all directions, the use of these type of sensors is mainly restricted to pressure sensing (see Table 1.4) [56, 57, 58, 59]. Although, some work has been reported on slip detection using conductive rubber [62].

### Capacitive sensors

Capacitive sensing may result in repeatable and linear sensor behavior immune to temperature variations. Nevertheless, they are susceptible to electromagnetic interference (EMI), stray capacitance (e.g. the human body) or cross-talk between sensing elements, all influencing the sensor operation. There is also a trade-off between the capacitor dimensions and the resulting sensor size. Larger capacitors result in a higher sensitivity, but large sensor dimensions and therefore potentially low spacial resolution. Furthermore, some capacitive sensors fabricated using thin metal layers in combination with highly deformable PDMS material may easily be damaged under large stresses.

**Table 1.4** – Overview of the properties of conductive polymer based tactile sensors in literature. Since the sensor response is not always linear, sensitivities are typically difficult to define and they are therefore not included in this table.

Technology	Size of 1 sensor [mm]	Sensor count	Load [type]: [range]
PI, PDMS technology [56]	2.54x2.54	32x32	Normal: 30 kPa
PI technology [57]	≈0.6x0.6	8x8	Normal: ≈300 kPa*
PI technology, screen printing [58]	2.54x2.54	16x16	Normal: ≈400 kPa*
Custom, PDMS technology [59]	1x1 or 2x2	8x8	Normal: 450 kPa

\*Interpreted from the measured or plotted data.

**Table 1.5** – Overview of the properties of capacitive tactile sensors in literature.

Technology	Size of 1 sensor [mm]	Sensor count	Load [type]: [range]	Sensitivity
Silicon bulk micromachining, PDMS technology [63]	2x2x1.112	8x8	3 directions: 10 mN (131 kPa)	Normal: 2.9%/mN; Shear: 2.5%/mN-x 3.0%/mN-y
PCB technology [64]	3.5x1.5x5	1	Shear: ±4 N	1.967 fF N <sup>-1</sup>
PI, PDMS technology [65]		1	Shear; Normal	not mentioned
PDMS technology [66, 67, 68]	10x10	1	Normal: 320 kPa; Shear: 70 kPa	varies
PDMS technology [69, 70]	8x8	8x8	Normal: 300 mN*; Shear: ±108 mN	Normal: 0.95%/mN; Shear: 1.67%/mN
PDMS technology [71]	64 mm <sup>2</sup>	multiple	Normal: 20 kPa	0.55 kPa <sup>-1</sup>
PDMS technology [72]	1x1	16x16	Normal: 40 mN (250 kPa)	3%/mN

\*Interpreted from the measured or plotted data.

### Optical sensors

Currently, most of the research is focusing on electrical tactile sensors, as noticed from the above discussion. However, electrical sensors have some disadvantages. They are susceptible to electromagnetic interference (EMI) and especially capacitive sensors are sensitive to parasitic effects influencing the sensor operation. An example of such an effect may be a stray capacitance caused by nearby conductors or the human body which can also be considered as a capacitor. Since artificial skin would often be used close to, or in contact with the human body, this situation is not desirable and serious errors may occur caused by the influence of the body on the sensor.

Furthermore, electrical sensors require electrical currents to operate, while in critical situations, electrical isolation is required for example inside the human body

**Table 1.6** – Overview of the properties of optical tactile sensors in literature.

Technology	Size [mm]	Sensor count	Load [type]: [range]	Sensitivity
Custom assembly (CCD) [73]	(large)	(multi)	Normal: 1.8 N; Shear: 2.2 N	0.270 mm N <sup>-1</sup> up to 0.511 mm N <sup>-1</sup>
SU-8 and PDMS (Fabry-Perot based**) [74]	1.5x1.5x0.4	1	Shear	(0.065 Pa resolution)
PDMS embedding (fiber bend loss) [75]	≈20x20	2x2	Normal; Shear	
PDMS waveguide (waveguide bend loss) [76]	2x2	4x4	Normal: 0.3 N up to 0.5 N	(Normal: 0.027 N resolution)
Fiber embedding (Bragg grating) [77]	10x10x3	1	Normal: 500 kPa; Shear: ±100 kPa	Normal: 2.2 $\frac{\text{pm}}{\text{kPa}}$ ; Shear: 4.35 pm kPa <sup>-1</sup> ; (5 kPa resolution)
Fiber embedding (Bragg grating) [78]	3.75x2x1	1	Shear: 40 N	66 pm N <sup>-1</sup>
Fiber embedding (Bragg grating) [79]	min. 5x5	3x3	Normal: 5 N	≈0.4 nm N <sup>-1</sup> *

\*Interpreted from the measured or plotted data.

\*\*This sensor was actually constructed to measure flow shear stress, but the principle is worth mentioning.

or in highly explosive environments. When using a fully optical sensor, no electrical currents need to be conducted to the sensing region which may drastically increase safe operation. Optical systems can also be more compact and lighter since no heavy electrical conductors are required. In modern airplanes and cars for example, several electrical interconnections are being replaced by lighter optical interconnections (e.g. silica or plastic optical fibers). Furthermore, sensors based on interferometry or gratings are very sensitive, although they currently need expensive and bulky read-out equipment.

There have been a number of optical sensors reported based on a variety of sensing principles such as interferometry [74], (fiber Bragg) gratings [77, 78], intensity based [75, 76] or camera based mechanisms [73], see Table 1.6 for a comparison. Compared to their electrical counterparts, optical sensors are not susceptible to EMI and have potentially a large dynamic range and multiplexing abilities. For use in prostheses or MIS, an optical sensing principle is desirable to eliminate electromagnetic interference that may occur for example when the human body interacts with a capacitive sensor.

This dissertation focuses both on fully optical, and optoelectronic systems. As opposed to fully optical sensors, optoelectronic sensors still require electrical currents for operation. However, the sensor principle itself is optical and therefore much less susceptible to electromagnetic interference compared to for example a capacitive sensor. Nevertheless, the electrical wires for connecting the sensor can still pick up interfering signals but this effect is much less influencing the sensor operation than the “fully electrical situation” where the sensor principle itself is sensitive to interference. Chapter 3 and 4 of this dissertation deal with fully optical structures, while in Chapter 5 and 6, an optoelectronic sensor is developed.

### **1.3 Problem statement and objectives**

---

From the above discussion, it is clear that the main challenge researchers are facing is incorporating sensors in appropriate skin-like materials that are thin, flexible and for several applications also stretchable. A high-density of sensors, such as present on the human finger tips is also still difficult to implement with the current technologies. Furthermore, most of the existing solutions are based on electrical sensing principles and therefore sensitive to electromagnetic interference (EMI) or exhibit reduced accuracy. Additionally, the majority of researchers is focusing on tactile pressure sensors, but there is also an increasing demand for tactile shear sensors.

All these aspects clearly reflect a very broad range of research and therefore this dissertation will mainly focus on certain distinct objectives:

- *Objective 1: “unobtrusive sensors”*. The fabrication of stretchable sensors or flexible sensors that can be embedded in stretchable skin materials aiming at maximum integration of all required sensor components. These sensors should be so thin and compact that they are not noticed, or so-called “unobtrusive sensors”.
- *Objective 2: “optical/optoelectronic sensors”*. Developing miniature optical/optoelectronic sensors to simultaneously allow for high accuracy, reduced EMI sensitivity and high sensing densities.
- *Objective 3: “focus on shear sensors”*. Next to investigating new schemes for pressure sensing, the focus is on shear sensing to address the emerging range of (medical) applications.

To achieve these goals, both generic technological work was performed and these technologies were applied for the construction and evaluation of 2 optical sensing principles. The technological work performed within the scope of this dissertation also resulted in establishing a platform that can serve as a basis for constructing optical tactile sensors. Therefore, the following research was performed in the field of micro-optics:

- Integration of polymer optical waveguides and other structures in mechanically stretchable sheets.
- Development of stretchable optical waveguides using stretchable PDMS materials.
- Combining optoelectronics embedding technologies in flexible foils with stretchable PDMS materials to obtain optical sensors

This technological work was combined with an exploration of several sensing principles leading to a concrete implementation and evaluation of 2 types of sensors:

- A fully optical high-density waveguide based pressure sensor.
- An ultra-thin miniature optoelectronic shear sensor.

## 1.4 Research trajectory and structure of this book

---

Within the “CMST” research group several technologies for fabricating optical tactile sensors are being investigated. They can mainly be split up in the following categories: fiber based, waveguide based or optoelectronics based sensors.

All these technologies have advantages and disadvantages and the best alternative is selected based on the application. Fiber and waveguide based sensors are fully optical and can operate in harsh situations or environments where electrical signals are not allowed. On the other hand, optoelectronic sensors are easier to integrate, since they do not require additional components for driving and reading out the waveguides.

Regardless of the different technologies that are pursued, the focus at the CMST research group is on miniaturization of optical sensors with the ultimate goal of completely integrating all necessary components in flexible and stretchable skin materials. These activities started with research performed toward the development of fiber-based and waveguide-based optical tactile sensors. In this scope, research was performed toward implementing waveguide based artificial sensor skin (as reported in this dissertation) and furthermore a technology was developed for packaging optoelectronic components for driving and read-out of these optical sensors, within the PhD of Erwin Bosman [80]. Therefore, thinned optoelectronic components were embedded in very thin polymer foils making them ideally suited for incorporating in flexible or stretchable skin materials, together with the optical sensors.

This technology for embedding optoelectronic components in flexible foils not only proved to be usable for driving optical fiber or waveguide sensors, but also resulted in establishing a technology platform for the creation of a next generation of optical microsystems and sensors. In this context, a tactile shear sensor was developed within the scope of this dissertation and a flexible optoelectronic VCSEL-based tactile pressure sensor is being developed within the scope of the PhD research of Bram Van Hoe [81].

Therefore, this dissertation contains both contributions detailing basic technological work paving the path for optical sensor development, and contributions describing 2 sensors that were implemented within that context. This book is divided in 7 chapters. After this *Introduction Chapter*, the mechanical and optical properties of the required materials are described in *Chapter 2*. *Chapter 3* describes the technological work performed on high-density multimode optical waveguides on stretchable substrates and in *Chapter 4*, part of this technology was used for examining a tactile sensor based on 2 layers of crossing waveguides. *Chapter 5* and *6* describe the research results on a novel sensing principle for measuring tactile shear stresses using optoelectronics embedded in thin flexible polymer foils. Finally, the conclusions and a discussion on the future work is formulated in *Chapter 7*.

---

## References

---

- [1] V. Lumelsky, M. Shur, and S. Wagner, "Sensitive Skin Workshop, Arlington, Virginia," *NSF, DARPA Sensitive Skin Workshop Report*, pp. 1–129, oct 1999.
- [2] V. Lumelsky, M. Shur, and S. Wagner, "Sensitive skin," *Sensors Journal, IEEE*, vol. 1, no. 1, pp. 41–51, jun 2001.
- [3] J. A. Paradiso, J. Lifton, and M. Broxton, "Sensate media - multimodal electronic skins as dense sensor networks," *BT Technology Journal*, vol. 22, pp. 32–44, 2004, 10.1023/B:BTTJ.0000047581.37994.c2. [Online]. Available: <http://dx.doi.org/10.1023/B:BTTJ.0000047581.37994.c2>
- [4] H. Yousef, M. Boukallel, and K. Althoefer, "Tactile sensing for dexterous in-hand manipulation in robotics-a review," *Sensors and Actuators A: Physical*, vol. 167, no. 2, pp. 171 – 187, 2011, solid-State Sensors, Actuators and Microsystems Workshop. [Online]. Available: <http://www.sciencedirect.com/science/article/pii/S0924424711001105>
- [5] The Shadow Robot Company. (accessed 2011) Shadow Robot Company. [Online]. Available: <http://www.shadowrobot.com>
- [6] A. Edsinger. (accessed 2011) Domo Robot Research Project. [Online]. Available: [http://people.csail.mit.edu/edsinger/domo\\_research.htm](http://people.csail.mit.edu/edsinger/domo_research.htm)
- [7] A. Edsinger-Gonzales and J. Weber, "Domo: a force sensing humanoid robot for manipulation research," in *Humanoid Robots, 2004 4th IEEE/RAS International Conference on*, vol. 1, nov. 2004, pp. 273 – 291 Vol. 1.
- [8] J. G. Rocha and S. Lanceros-Mendez, *Sensors: Focus on Tactile Force and Stress Sensors*. InTech, 2008.
- [9] A. Vallbo and R. Johansson, "Properties of cutaneous mechanoreceptors in the human hand related to touch sensation," *Human neurobiology*, vol. 3, no. 1, pp. 3–14, 1984.
- [10] K. O. Johnson, "The roles and functions of cutaneous mechanoreceptors," *Current Opinion in Neurobiology*, vol. 11, no. 4, pp. 455 – 461, 2001. [Online]. Available: <http://www.sciencedirect.com/science/article/pii/S0959438800002348>
- [11] K. O. Johnson and J. R. Phillips, "Tactile spatial resolution. i. two-point discrimination, gap detection, grating resolution, and letter recognition," *Journal of Neurophysiology*, vol. 46, no. 6, pp. 1177–1192, 1981. [Online]. Available: <http://jn.physiology.org/content/46/6/1177.short>

- [12] T. Maeno, S. Hiromitsu, and T. Kawai, "Control of grasping force by detecting stick/slip distribution at the curved surface of an elastic finger," in *Robotics and Automation, 2000. Proceedings. ICRA '00. IEEE International Conference on*, vol. 4, 2000, pp. 3895–3900 vol.4.
- [13] R. Howe, I. Kao, and M. Cutkosky, "The sliding of robot fingers under combined torsion and shear loading," in *Robotics and Automation, 1988. Proceedings., 1988 IEEE International Conference on*, apr 1988, pp. 103–105 vol.1.
- [14] M. Tremblay and M. Cutkosky, "Estimating friction using incipient slip sensing during a manipulation task," in *Robotics and Automation, 1993. Proceedings., 1993 IEEE International Conference on*, may 1993, pp. 429–434 vol.1.
- [15] V. Maheshwari and R. F. Saraf, "High-resolution thin-film device to sense texture by touch," *Science*, vol. 312, no. 5779, pp. 1501–1504, 2006. [Online]. Available: <http://www.sciencemag.org/content/312/5779/1501.abstract>
- [16] W. Peine, P. Wellman, and R. Howe, "Temporal bandwidth requirements for tactile shape displays," in *Sixth Annual Symposium on Haptic Interfaces for Virtual Environment and Teleoperator Systems, ASME International Mechanical Engineering Congress and Exposition, Dallas, 1997*, pp. 107–113.
- [17] K.-U. Kyung, S.-W. Son, D.-S. Kwon, and M.-S. Kim, "Design of an integrated tactile display system," in *Robotics and Automation, 2004. Proceedings. ICRA '04. 2004 IEEE International Conference on*, vol. 1, april-1 may 2004, pp. 776–781 Vol.1.
- [18] V. Hayward and J. M. Cruz-hernandez, "Tactile display device using distributed lateral skin stretch," 2000, pp. 1309–1314.
- [19] K. Drewing, M. Fritschi, R. Zopf, M. O. Ernst, and M. Buss, "First evaluation of a novel tactile display exerting shear force via lateral displacement," *ACM Trans. Appl. Percept.*, vol. 2, pp. 118–131, April 2005. [Online]. Available: <http://doi.acm.org/10.1145/1060581.1060586>
- [20] D. Rosenbaum and H.-P. Becker, "Plantar pressure distribution measurements. technical background and clinical applications," *Foot and Ankle Surgery*, vol. 3, no. 1, pp. 1–14, 1997. [Online]. Available: <http://dx.doi.org/10.1046/j.1460-9584.1997.00043.x>
- [21] M. Yavuz, A. Erdemir, G. Botek, G. B. Hirschman, L. Bardsley, and B. L. Davis, "Peak plantar pressure and shear locations," *Diabetes Care*, vol. 30, no. 10, pp. 2643–2645, October 2007. [Online]. Available: <http://care.diabetesjournals.org/content/30/10/2643.short>
- [22] M. J. Mueller, D. Zou, K. L. Bohnert, L. J. Tuttle, and D. R. Sinacore, "Plantar stresses on the neuropathic foot during barefoot walking," *Physical*

- Therapy*, vol. 88, no. 11, pp. 1375–1384, November 2008. [Online]. Available: <http://ptjournal.apta.org/content/88/11/1375.abstract>
- [23] M. Zhang, A. Turner-Smith, and V. Roberts, “The reaction of skin and soft tissue to shear forces applied externally to the skin surface,” *ARCHIVE: Proceedings of the Institution of Mechanical Engineers, Part H: Journal of Engineering in Medicine 1989-1996 (vols 203-210)*, vol. 208, no. 48, pp. 217–222, 1994.
- [24] S. Urry, “Plantar pressure-measurement sensors,” *Measurement Science and Technology*, vol. 10, no. 1, p. R16, 1999. [Online]. Available: <http://stacks.iop.org/0957-0233/10/i=1/a=017>
- [25] B. L. Davis, R. M. Cothren, P. Quesada, S. B. Hanson, and J. E. Perry, “Frequency content of normal and diabetic plantar pressure profiles: Implications for the selection of transducer sizes,” *Journal of Biomechanics*, vol. 29, no. 7, pp. 979 – 983, 1996. [Online]. Available: <http://www.sciencedirect.com/science/article/pii/S0021929095001166>
- [26] T. C. Pataky, P. Caravaggi, R. Savage, D. Parker, J. Y. Goulermas, W. I. Sellers, and R. H. Crompton, “New insights into the plantar pressure correlates of walking speed using pedobarographic statistical parametric mapping (pspm),” *Journal of Biomechanics*, vol. 41, no. 9, pp. 1987 – 1994, 2008. [Online]. Available: <http://www.sciencedirect.com/science/article/pii/S0021929008001516>
- [27] A. Nagel, F. Fernholz, C. Kibele, and D. Rosenbaum, “Long distance running increases plantar pressures beneath the metatarsal heads: A barefoot walking investigation of 200 marathon runners,” *Gait & Posture*, vol. 27, no. 1, pp. 152 – 155, 2008. [Online]. Available: <http://www.sciencedirect.com/science/article/pii/S0966636207000094>
- [28] M. P. Solano, L. M. Prieto, J. C. Varon, M. Moreno, and A. J. M. Boulton, “Ethnic differences in plantar pressures in diabetic patients with peripheral neuropathy,” *Diabetic Medicine*, vol. 25, no. 4, pp. 505–507, 2008. [Online]. Available: <http://dx.doi.org/10.1111/j.1464-5491.2008.02381.x>
- [29] D. G. Armstrong, E. J. Peters, K. A. Athanasiou, and L. A. Lavery, “Is there a critical level of plantar foot pressure to identify patients at risk for neuropathic foot ulceration?” *The Journal of Foot and Ankle Surgery*, vol. 37, no. 4, pp. 303 – 307, 1998. [Online]. Available: <http://www.sciencedirect.com/science/article/pii/S1067251698800665>
- [30] Tekscan. (Accessed 2011) Tekscan webpage. [Online]. Available: <http://www.tekscan.com/>
- [31] Xsensor Technology Corporation. (Accessed 2011) Xsensor webpage. [Online]. Available: <http://www.xsensor.com/>

- [32] R. Hosein and M. Lord, "A study of in-shoe plantar shear in normals," *Clinical Biomechanics*, vol. 15, no. 1, pp. 46 – 53, 2000. [Online]. Available: <http://www.sciencedirect.com/science/article/pii/S026800339800059X>
- [33] Otto Bock. (Accessed 2011) Otto Bock webpage. [Online]. Available: <http://www.ottobock.com>
- [34] S. Zachariah, R. Saxena, J. Ferguson, and J. Sanders, "Shape and volume change in the transtibial residuum over the short term: Preliminary investigation of six subjects," *Journal of Rehabilitation Research and Development*, vol. 41, no. 5, pp. 683–694, 2004.
- [35] J. Sanders, S. Zachariah, A. Jacobsen, and J. Ferguson, "Changes in interface pressures and shear stresses over time on trans-tibial amputee subjects ambulating with prosthetic limbs: comparison of diurnal and six-month differences," *Journal of Biomechanics*, vol. 38, no. 8, pp. 1566 – 1573, 2005. [Online]. Available: <http://www.sciencedirect.com/science/article/pii/S0021929004003859>
- [36] T. Beil, G. Street, and S. Covey, "Interface pressures during ambulation using suction and vacuum-assisted prosthetic sockets," *Journal of Rehabilitation Research and Development*, vol. 39, no. 6, pp. 693–700, 2002.
- [37] W. J. Board, G. M. Street, and C. Caspers, "A comparison of trans-tibial amputee suction and vacuum socket conditions," *Prosthetics and Orthotics International*, vol. 25, no. 3, pp. 202–209, 2001. [Online]. Available: <http://poi.sagepub.com/content/25/3/202.abstract>
- [38] N. A. Abu Osman, W. D. Spence, S. E. Solomonidis, J. P. Paul, and A. M. Weir, "Transducers for the determination of the pressure and shear stress distribution at the stump—socket interface of trans-tibial amputees," *Proceedings of the Institution of Mechanical Engineers, Part B: Journal of Engineering Manufacture*, vol. 224, no. 8, pp. 1239–1250, 2010. [Online]. Available: <http://pib.sagepub.com/content/224/8/1239.abstract>
- [39] J. Maurer, B. Loitz-Ramage, M. Andersen, *et al.*, "Prosthetic socket interface pressures: Customized calibration technique for the tekscan f-socket system," in *Summer Bioengineering Conference*,(25), vol. 29, 2003.
- [40] A. W. P. Buis and P. Convery, "Calibration problems encountered while monitoring stump/socket interface pressures with force sensing resistors: Techniques adopted to minimise inaccuracies," *Prosthetics and Orthotics International*, vol. 21, no. 3, pp. 179–182, 1997. [Online]. Available: <http://informahealthcare.com/doi/abs/10.3109/03093649709164552>

- [41] J. E. Sanders, A. K. Jacobsen, and J. R. Fergason, "Effects of fluid insert volume changes on socket pressures and shear stresses: Case studies from two trans-tibial amputee subjects," *Prosthetics and Orthotics International*, vol. 30, no. 3, pp. 257–269, 2006. [Online]. Available: <http://poi.sagepub.com/content/30/3/257.abstract>
- [42] J. Sanders, C. Daly, and E. Burgess, "Interface shear stresses during ambulation with a below-knee prosthetic limb," *Journal of rehabilitation research and development*, vol. 29, no. 4, pp. 1–8, 1992.
- [43] J. Sanders, D. Lam, A. Dralle, and R. Okumura, "Interface pressures and shear stresses at thirteen socket sites on two persons with transtibial amputation," *Journal of rehabilitation research and development*, vol. 34, no. 1, pp. 19–43, 1997.
- [44] M. Zhang, A. R. Turner-Smith, V. C. Roberts, and A. Tanner, "Frictional action at lower limb/prosthetic socket interface," *Medical Engineering & Physics*, vol. 18, no. 3, pp. 207 – 214, 1996. [Online]. Available: <http://www.sciencedirect.com/science/article/pii/S1350453395000380>
- [45] M. Gonzalez, F. Axisa, M. V. Bulcke, D. Brosteaux, B. Vandeveld, and J. Vanfleteren, "Design of metal interconnects for stretchable electronic circuits," *Microelectronics Reliability*, vol. 48, no. 6, pp. 825 – 832, 2008, thermal, Mechanical and Multi-physics Simulation and Experiments in Micro-electronics and Micro-systems (EuroSimE 2007). [Online]. Available: <http://www.sciencedirect.com/science/article/pii/S0026271408000760>
- [46] T. Loher, D. Manassis, R. Heinrich, B. Schmied, J. Vanfleteren, J. DeBaets, A. Ostmann, and H. Reichl, "Stretchable electronic systems," in *Electronics Packaging Technology Conference, 2006. EPTC '06. 8th*, dec. 2006, pp. 271 –276.
- [47] F. Bossuyt, J. Guenther, T. L. her, M. Seckel, T. Sterken, and J. de Vries, "Cyclic endurance reliability of stretchable electronic substrates," *Microelectronics Reliability*, vol. 51, no. 3, pp. 628 – 635, 2011. [Online]. Available: <http://www.sciencedirect.com/science/article/pii/S0026271410005226>
- [48] D.-H. Kim and J. A. Rogers, "Stretchable electronics: Materials strategies and devices," *Advanced Materials*, vol. 20, no. 24, pp. 4887–4892, 2008. [Online]. Available: <http://dx.doi.org/10.1002/adma.200801788>
- [49] J. A. Rogers, T. Someya, and Y. Huang, "Materials and mechanics for stretchable electronics," *Science*, vol. 327, no. 5973, pp. 1603–1607, 2010. [Online]. Available: <http://www.sciencemag.org/content/327/5973/1603.abstract>

- [50] P. Valdastri, S. Roccella, L. Beccai, E. Cattin, A. Menciassi, M. Carrozza, and P. Dario, "Characterization of a novel hybrid silicon three-axial force sensor," *Sensors and Actuators A: Physical*, vol. 123-124, pp. 249 – 257, 2005, eurosensors XVIII 2004 - The 18th European conference on Solid-State Transducers. [Online]. Available: <http://www.sciencedirect.com/science/article/B6THG-4FFN4X1-1/2/96e7e452747db1905a27a86570ec5863>
- [51] M. C. Hsieh, Y.-K. Fang, M. S. Ju, J.-J. Ho, and S. F. Ting, "Development of a new contact-type piezoresistive micro-shear-stress sensor," *Design, Test, Integration, and Packaging of MEMS/MOEMS 2002*, vol. 4755, no. 1, pp. 285–295, 2002. [Online]. Available: <http://link.aip.org/link/?PSI/4755/285/1>
- [52] H. Hu, C. Liu, and N. Chen, "A robust tactile shear stress sensor derived from a bio-inspired artificial haircell sensor," in *A robust tactile shear stress sensor derived from a bio-inspired artificial haircell sensor*, oct. 2008, pp. 1517 – 1519.
- [53] K. Noda, K. Matsumoto, and I. Shimoyama, "Flexible tactile sensor sheet with liquid filter for shear force detection," in *Flexible Tactile Sensor Sheet with Liquid Filter for Shear Force Detection*, jan. 2009, pp. 785 –788.
- [54] K. Noda, K. Hoshino, K. Matsumoto, and I. Shimoyama, "A shear stress sensor for tactile sensing with the piezoresistive cantilever standing in elastic material," *Sensors and Actuators A: Physical*, vol. 127, no. 2, pp. 295 – 301, 2006, mEMS 2005 Special Issue - Special Issue of the Micromechanics Section of Sensors and Actuators (SAMM), based on contributions revised from the technical digest of the IEEE 18th International Conference on Micro Electro Mechanical Systems (MEMS-2005). [Online]. Available: <http://www.sciencedirect.com/science/article/B6THG-4HDX6P8-4/2/47ab623290ef434f5e8f1c592e854a85>
- [55] T. Mei, W. J. Li, Y. Ge, Y. Chen, L. Ni, and M. H. Chan, "An integrated mems three-dimensional tactile sensor with large force range," *Sensors and Actuators A: Physical*, vol. 80, no. 2, pp. 155 – 162, 2000. [Online]. Available: <http://www.sciencedirect.com/science/article/pii/S0924424799002617>
- [56] T. Someya, T. Sekitani, S. Iba, Y. Kato, H. Kawaguchi, and T. Sakurai, "A large-area, flexible pressure sensor matrix with organic field-effect transistors for artificial skin applications," *Proceedings of the National Academy of Sciences of the United States of America*, vol. 101, no. 27, pp. 9966–9970, 2004. [Online]. Available: <http://www.pnas.org/content/101/27/9966.abstract>
- [57] Y.-J. Yang, M.-Y. Cheng, W.-Y. Chang, L.-C. Tsao, S.-A. Yang, W.-P. Shih, F.-Y. Chang, S.-H. Chang, and K.-C. Fan, "An integrated flexible temperature and tactile sensing array using pi-copper films," *Sensors and Actuators A: Physical*, vol. 143, no. 1, pp. 143 – 153, 2008, micromechanics Section of

- Sensors and Actuators (SAMM), based on contributions revised from the Technical Digest of the IEEE 20th International Conference on Micro Electro Mechanical Systems (MEMS 2007) - MEMS 2007, IEEE 20th International Conference on Micro Electro Mechanical Systems. [Online]. Available: <http://www.sciencedirect.com/science/article/pii/S0924424707008126>
- [58] J. Castellanos-Ramos, R. Navas-Gonzalez, H. Macicior, E. Ochoteco, and F. Vidal-Verdú, "Tactile sensors based on conductive polymers," in *Society of Photo-Optical Instrumentation Engineers (SPIE) Conference Series*, ser. Society of Photo-Optical Instrumentation Engineers (SPIE) Conference Series, vol. 7362, May 2009.
- [59] M.-Y. Cheng, C.-M. Tsao, Y.-Z. Lai, and Y.-J. Yang, "The development of a highly twistable tactile sensing array with stretchable helical electrodes," *Sensors and Actuators A: Physical*, vol. 166, no. 2, pp. 226 – 233, 2011, 22 nd IEEE International Conference on Micro Electro Mechanical Systems, Sorrento, Italy, 25-29 January 2009 - MEMS 2009. [Online]. Available: <http://www.sciencedirect.com/science/article/pii/S0924424709005354>
- [60] J. Engel, J. Chen, Z. Fan, and C. Liu, "Polymer micromachined multimodal tactile sensors," *Sensors and Actuators A: Physical*, vol. 117, no. 1, pp. 50 – 61, 2005. [Online]. Available: <http://www.sciencedirect.com/science/article/pii/S0924424704003875>
- [61] K. Kim, K. R. Lee, W. H. Kim, K.-B. Park, T.-H. Kim, and J. J. Pak, "Development of polyimide-based flexible tactile sensing module integrated with strain gauges & flexible flat cable," J.-C. Chiao, A. J. Hariz, D. V. Thiel, and C. Yang, Eds., vol. 7269, no. 1. SPIE, 2008, p. 72690P. [Online]. Available: <http://link.aip.org/link/?PSI/7269/72690P/1>
- [62] S. Teshigawara, S. Shimizu, T. Tsutsumi, Y. Suzuki, A. Ming, M. Shimojo, and M. Ishikawa, "High sensitivity slip sensor using pressure conductive rubber for dexterous grasp and manipulation," in *Sensors, 2010 IEEE*, nov. 2010, pp. 570 –574.
- [63] H.-K. Lee, J. Chung, S.-I. Chang, and E. Yoon, "Normal and shear force measurement using a flexible polymer tactile sensor with embedded multiple capacitors," *Microelectromechanical Systems, Journal of*, vol. 17, no. 4, pp. 934 –942, aug. 2008.
- [64] M. I. Tiwana, A. Shashank, S. J. Redmond, and N. H. Lovell, "Characterization of a capacitive tactile shear sensor for application in robotic and upper limb prostheses," *Sensors and Actuators A: Physical*,

- vol. In Press, Accepted Manuscript, pp. –, 2010. [Online]. Available: <http://www.sciencedirect.com/science/article/B6THG-514BPG7-1/2/79a1fa6b18b696528743596bf1341092>
- [65] T. Chase and R. Luo, "A thin-film flexible capacitive tactile normal/shear force array sensor," in *A thin-film flexible capacitive tactile normal/shear force array sensor*, vol. 2, nov. 1995, pp. 1196–1201 vol.2.
- [66] K. Sundara-Rajan, A. Bestick, G. Rowe, G. Klute, W. Ledoux, and A. Mami-shev, "Capacitive sensing of interfacial stresses," in *Sensors, 2010 IEEE*, nov. 2010, pp. 2569–2572.
- [67] K. Sundara-Rajan, G. Rowe, A. Bestick, A. Mamishev, G. Klute, and W. Ledoux, "Capacitive sensing of interfacial forces in prosthesis," in *Medical Measurements and Applications Proceedings (MeMeA), 2010 IEEE International Workshop on*, apr. 2010, pp. 73–76.
- [68] K. Sundara-Rajan, G. Rowe, A. Simon, G. Klute, W. Ledoux, and A. Mami-shev, "Shear sensor for lower limb prosthetic applications," in *Biomedical Science Engineering Conference, 2009. BSEC 2009. First Annual ORNL*, march 2009, pp. 1–4.
- [69] M.-Y. Cheng, C.-L. Lin, Y.-T. Lai, and Y.-J. Yang, "A polymer-based capacitive sensing array for normal and shear force measurement," *Sensors*, vol. 10, no. 11, pp. 10211–10225, 2010. [Online]. Available: <http://www.mdpi.com/1424-8220/10/11/10211/>
- [70] M.-Y. Cheng, X.-H. Huang, C.-W. Ma, and Y.-J. Yang, "A flexible capacitive tactile sensing array with floating electrodes," *Journal of Micromechanics and Microengineering*, vol. 19, no. 11, p. 115001, 2009. [Online]. Available: <http://stacks.iop.org/0960-1317/19/i=11/a=115001>
- [71] S. C. B. Mannsfeld, B. C.-K. Tee, R. M. Stoltenberg, C. V. H.-H. Chen, S. Barman, B. V. O. Muir, A. N. Sokolov, C. Reese, and Z. Bao, "Highly sensitive flexible pressure sensors with microstructured rubber dielectric layers," *Nature Materials*, vol. 9, pp. 859–864, Oct. 2010.
- [72] H.-K. Lee, S.-I. Chang, and E. Yoon, "A flexible polymer tactile sensor: Fabrication and modular expandability for large area deployment," *Microelectromechanical Systems, Journal of*, vol. 15, no. 6, pp. 1681–1686, dec. 2006.
- [73] M. Ohka, H. Kobayashi, J. Takata, and Y. Mitsuya, "Sensing precision of an optical three-axis tactile sensor for a robotic finger," sep. 2006, pp. 214–219.
- [74] F.-G. Tseng and C.-J. Lin, "A high sensitive fabry-perot shear stress sensor employing flexible membrane and double su-8 structures," vol. 2, 2002, pp. 969–972 vol.2.

- [75] W. Wang, W. Ledoux, B. Sangeorzan, and P. Reinhall, "A shear and plantar pressure sensor based on fiber-optic bend loss," *JOURNAL OF REHABILITATION RESEARCH AND DEVELOPMENT*, vol. 42, no. 3, pp. 315–325, MAY-JUN 2005.
- [76] W.-C. Wang, W. R. Ledoux, C.-Y. Huang, C.-S. Huang, G. K. Klute, and P. G. Reinhall, "Development of a microfabricated optical bend loss sensor for distributive pressure measurement," *IEEE TRANSACTIONS ON BIOMEDICAL ENGINEERING*, vol. 55, no. 2, Part 1, pp. 614–625, FEB 2008.
- [77] A. Koulaxouzidis, M. Holmes, C. Roberts, and V. Handerek, "A shear and vertical stress sensor for physiological measurements using fibre bragg gratings," vol. 1, 2000, pp. 55–58 vol.1.
- [78] R. Suresh and S. C. Tjin, "Effects of dimensional and material parameters and cross-coupling on fbg based shear force sensor," *Sensors and Actuators A: Physical*, vol. 120, no. 1, pp. 26 – 36, 2005. [Online]. Available: <http://www.sciencedirect.com/science/article/B6THG-4F1J8SG-2/2/2e2a5108526f459e786de423602c9734>
- [79] J.-S. Heo, J.-H. Chung, and J.-J. Lee, "Tactile sensor arrays using fiber bragg grating sensors," *Sensors and Actuators A: Physical*, vol. 126, no. 2, pp. 312 – 327, 2006. [Online]. Available: <http://www.sciencedirect.com/science/article/pii/S0924424705006084>
- [80] E. Bosman, "Integration of optical interconnections and opto-electronic components in flexible substrates," Ph.D. dissertation, Ghent University, 2010.
- [81] B. Van Hoe, D. Lamon, E. Bosman, G. Van Steenberge, J. Missinne, P. Goethals, P. Krassimir, D. Reynaerts, J. Vanfleteren, and P. Van Daele, "Embedded high resolution sensor based on optical feedback in a Vertical Cavity Surface Emitting Laser," in *PROCEEDINGS OF SPIE - THE INTERNATIONAL SOCIETY FOR OPTICAL ENGINEERING*, K. J. Peters, W. Ecke, and T. E. Matikas, Eds., vol. 7648. SPIE, the International Society for Optical Engineering, 2010. [Online]. Available: <http://dx.doi.org/10.1117/12.847647>



# 2

## Stretchable optical materials

*The sensor technologies described in this dissertation demand materials that are transparent and/or mechanically compliant. The material Polydimethylsiloxane (PDMS) or “silicone” meets these requirements and is commercially available with a range of different properties. This chapter evaluates those material properties that are relevant for establishing the proposed sensor technologies. Next to optical and mechanical, also process related properties are studied.*

### **2.1 Introduction**

---

In the previous chapter, new technological trends were discussed and these trends clearly demonstrate the need for a special category of materials. Stretchable (micro-)systems and wearable electronic applications require packaging materials with dedicated mechanical properties. Typically stretchability and a certain mechanical tear strength are desired. When these applications also involve optical components such as light emitters (displays, light sources, lasers etc.) or sensors (camera, optical detectors etc.), the applied materials require a certain optical behavior: an appropriate (matched) refractive index and generally a low optical loss for a specific wavelength. An additional requirement is the processability of the materials, i.e. they need to allow precise application techniques for creating accurate microsystems.

Silicones are stretchable materials that are ideally suited for micro-optical fabri-

cation since they can be spin-coated, embossed, molded etc., they are tolerant to high optical fluxes and exhibit a thermo-mechanical and environmental stability [1]. Moreover, one of the most commonly used PDMS materials, Sylgard®184 from Dow Corning, is optically transparent for near-UV, visible and near-infrared wavelengths. This type of PDMS has a refractive index of 1.41, but recently, several types of dedicated optically transparent silicones have been developed with refractive indexes tunable from 1.40 to 1.60.

Polyurethane is often used as an alternative material, supplied in liquid form or as thermoplastic sheets. Although this material can be very strong, less materials with suited optical properties were found and therefore, polyurethane is currently not considered.

This chapter gives a brief overview of the most important properties of PDMS that are relevant in the scope of this work but is in no case intended to be complete.

## 2.2 Silicone chemistry

“Silicone”<sup>1</sup> in the most common form is a linear polymer with a -Si-O- backbone (i.e. a chain of siloxane units, see Figure 2.1a) and methyl side groups attached to every silicon atom; the chemically correct name is “Polydimethylsiloxane (PDMS)”, see Figure 2.1b. However, the side groups on the siloxane units can also be substituted by oxygen atoms or different side groups “R” (e.g. methyl, ethyl, phenyl). Depending on the ratio of the oxygen atoms and R groups attached to the backbone, a range of materials with different properties can be synthesized, see Figure 2.2 [2].

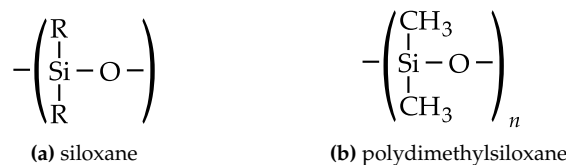


**Figure 2.1** – Formula for “siloxane” and “polydimethylsiloxane” (PDMS): if “R” is “CH<sub>3</sub>” in the basic siloxane unit, then it is named polydimethylsiloxane.

Silica glass is formed when there are no methyl groups. However, when 1 oxygen atom is replaced with an R group, then a resin or silsesquioxane material is obtained. Compared to silica glass, these materials are more flexible, but not

<sup>1</sup>“Silicone” is a historically used term but not chemically correct since the polymer does not contain silicone groups, but a -Si-O- backbone with organic side groups attached to the silicon atoms. Later, the scientifically more correct term “Polydimethylsiloxane (PDMS)” was introduced

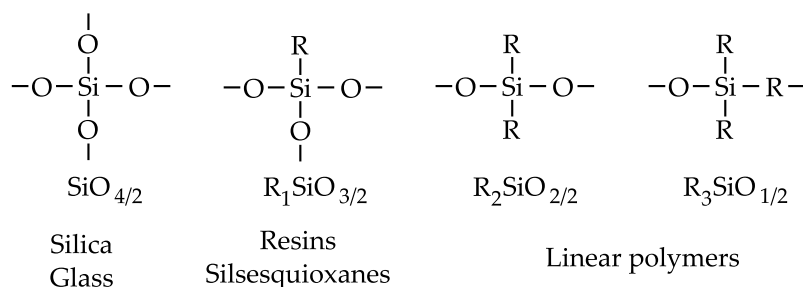


Figure 2.2 – Different Siloxane polymers and corresponding nomenclature.

stretchable. In optical printed circuit boards, these materials are used to create polymer optical waveguides. Examples of such materials are OE-4140 and OE-4141 from Dow Corning [3] and Lightlink from DOW Chemical (formerly Rohm and Haas) [4, 5].

When 2 or 3 oxygen atoms are replaced, linear polymers are obtained. These structures have a very flexible backbone resulting in stretchable materials with a low modulus. As mentioned previously, polydimethylsiloxane is the most common type of these linear polymers.

The types of silicone considered in this dissertation are supplied as 2-component systems consisting of a liquid “base polymer” and a “curing agent” that polymerize by means of an addition-cure reaction. These 2 parts are mixed in a certain ratio (typically 10:1 or 1:1) to initiate the cross-linking or “curing” process that is achieved by reacting vinyl functional polymers (component 1) with oligomers containing Si-H groups (component 2) [6, 2], see Figure 2.3.

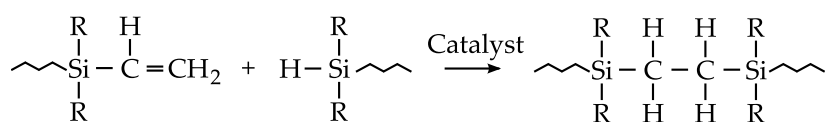


Figure 2.3 – Cure mechanism of a 2-part addition-cure PDMS system.

This reaction is catalyzed by Pt or Rh metal complexes and is initiated at room temperature but can significantly be accelerated with heat.

A study of commercially available silicones was performed. Since this work targets optical applications and more specifically tactile sensors, the search was limited to stretchable silicones that are also optically transparent. The following sections describe the optical, mechanical and processing properties of a set of selected optical silicone materials.

## 2.3 Optical properties

Recently, suppliers have started producing dedicated optical PDMS materials that are transparent in the visible range and exhibit a particular refractive index. These materials are mainly targeting the growing LED industry. A wide range of materials is available and most of them are used for encapsulating LED chips. Another emerging application domain for PDMS is solar energy. To improve durability and performance and reduce costs, researchers are investigating the use of PDMS for embedding silicon based photovoltaic cells.

LEDs emit and photovoltaic cells receive a certain optical power at certain wavelengths. Therefore, the PDMS encapsulant needs to be transparent and stable to tolerate this radiation. Furthermore, LEDs operating at higher power generate a considerable amount of heat resulting in interfacial stresses. Since PDMS is very soft owing to its low mechanical modulus, it is ideally suited to relieve these stresses. Additionally, PDMS is cheap and can easily be processed in large quantities.

In the scope of this dissertation, transparency and refractive index are the most relevant material properties when studying optical structures. For example, 2 types of low optical loss materials are needed to fabricate waveguides as described in Chapter 3, one with a higher refractive index for the core and another with a lower refractive index serving as the cladding. Both properties are dependent on the wavelength. In this dissertation, near infrared light (850 nm) is mainly considered since low-cost miniature optoelectronic components exist to interface at this wavelength.

### 2.3.1 Refractive index

The refractive index of “regular” PDMS such as Sylgard®184 is approximately 1.41, but when substituting methyl groups on the Si atom with other functional groups, this refractive index can be altered. For example, if the ratio of methyl and phenyl groups is varied, the refractive index can be tuned approximately from 1.40 to 1.60 and to decrease the refractive index, fluorinated components such as trifluoropropyl methyl groups can be incorporated [7, 8, 9].

All existing materials are dispersive, meaning that their refractive index  $n_\lambda$  is not constant for every wavelength  $\lambda$ . Therefore, this number is usually specified at a specific wavelength, i.e. 589 nm or the “Sodium D-line” of the spectrum, indicated using the symbol  $n_d (= n_{\lambda=589\text{nm}})$ . However, it is also interesting to know the refractive index at other wavelengths, particularly at the frequently used operating wavelength of 850 nm. Commonly, the relation between the refractive index of a material and the wavelength can be represented using the Sellmeier dispersion curve following a power-law fit of the form:

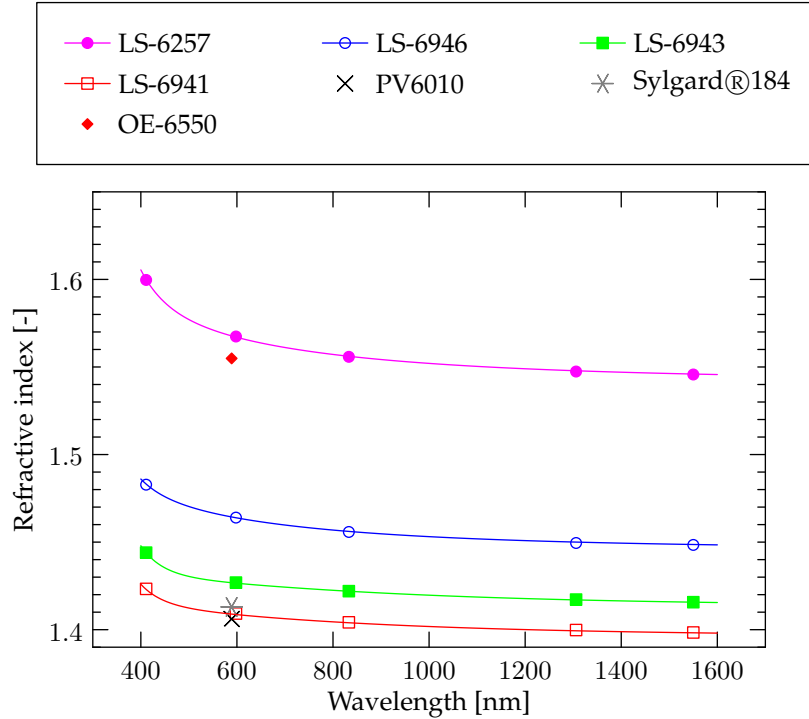


Figure 2.4 – Refractive index vs. wavelength of different optical silicones.

$$n_{\lambda} = A_0 + A_2\lambda^{-2} + A_4\lambda^{-4} + A_6\lambda^{-6} + \dots$$

The Sellmeier dispersion curves for some of the studied materials are displayed in Figure 2.4. The markers in the graph represent measured data and the solid lines are fitted curves. The data for the Nusil materials (LS-6941, LS-6943, LS-6946 and LS-6257) was extracted from the datasheets [10] while the refractive index  $n_d$  of Sylgard®184, PV-6010 and OE-6550 was measured using an Abbe refractometer and added to the graph for comparison. These measurements were performed in Cleanroom conditions ( $21 \pm 1$  °C,  $50 \pm 10$  %RH) and are also summarized in Table 2.1, including own measurements performed on the Nusil materials. Also the curing conditions are mentioned since they slightly influence the final refractive index of the material after cross-linking [11, 12].

An alternative and simpler method to characterize the material dispersion (in the visible part of the spectrum) is using the Abbe-number  $V_D = \frac{n_D - 1}{n_F - n_C}$ . This number compares the refractive indexes of a material corresponding with certain standard wavelengths ( $\lambda_F = 486.1$  nm (blue),  $\lambda_D = 589.3$  nm (yellow),  $\lambda_C = 656.3$  nm (red)) yielding a measure for the wavelength dependency, and is mainly used in

**Table 2.1** – Refractive index  $n_d$  (at 589 nm) of different optical PDMS types, measured using an Abbe refractometer (21 °C).

Material	$n_d$ (21 °C) [-]	PDMS curing conditions
LS-6941	1.411	hotplate: 2 h at 60 °C
LS-6943	1.431	hotplate: 2 h at 60 °C
LS-6946	1.465	oven: 14 h at 80 °C
LS-6257	1.571	oven: 14 h at 80 °C
PV-6010	1.406	hotplate: 2 h at 60 °C
Sylgard®184	1.413	hotplate: 2 h at 60 °C
OE-6520	1.549	oven: 14 h at 80 °C
OE-6550	1.555	oven: 8 h at 60 °C
OE-6351	1.411	hotplate: 2 h at 80 °C

lens optics.

In addition to the wavelength dependency, the refractive index is also depending on the temperature. Since the influence is sufficiently linear in a certain temperature range above the material  $T_g$ , approximately from  $-80$  °C to  $250$  °C, a thermo-optic coefficient  $\frac{dn}{dT}$  can be defined. In Table 2.2, the thermo-optic coefficients of several of the used PDMS materials are compared with other optical materials. It can be noticed that the values for PDMS are significantly larger than for the “traditional” materials such as PMMA, silicon (Si) and  $\text{SiO}_2$ .

The temperature dependency of refractive index is not considered further in this work, although this property is often used to create thermo-optic switches or for sensing applications. Using PDMS for these applications could therefore result in efficient configurations, as a result of the large thermo-optic coefficient.

**Table 2.2** – Thermo-optic coefficient  $\frac{dn}{dT}$  (at 589 nm) of different optical PDMS types compared with traditional optical materials.

Material	$\frac{dn}{dT}  _{\lambda=589\text{nm}}$ [ppm/°C]
LS-6941 [10]	-350
LS-6943 [10]	-390
LS-6946 [10]	-360
LS-6257 [10]	-390
PMMA [13]	-130
Silicon [1]	160
$\text{SiO}_2$ [1]	12

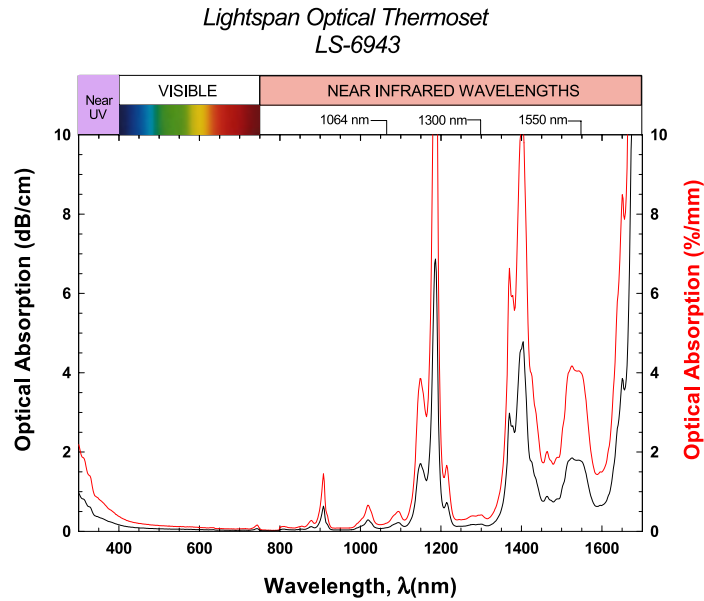


**Figure 2.5** – Optical absorption vs. wavelength (25 °C) of Nusil LS-6943 material. Graph adopted from the datasheet [10].

### 2.3.2 Optical absorption

When optical structures are used to transport optical power, for example using fibers or waveguides, the absorption of the employed materials determines in part the losses in these structures. For long-haul data communication, optical glass fibers with very low losses (typically 0.3 dB/km) are used. Although PDMS has a much higher absorption coefficient (around 0.05 dB/cm at 850 nm), it is very useful for shorter transmission lengths such as on-board or board-to-board optical interconnections [14]. PDMS is also ideally suited for sensing applications, where the distances covered are sufficiently short and the particular mechanical properties of PDMS are beneficial. These combined optical and mechanical properties make PDMS the material of choice for the current research toward unobtrusive optical sensors.

Optical PDMS materials from the Nusil Lightspan series considered in this work (LS-6941, LS-6943, LS-6946 and LS-6257) have specified losses of about 0.05 dB/cm or 0.11 %/mm at 850 nm (interpreted from the datasheet graphs [10]). The optical loss in function of the wavelength is also specified for these materials. Two examples for LS-6943 and LS-6257 are shown in Figure 2.5 and 2.6 respectively. It can be noticed that these types of PDMS are indeed transparent in the visible range,

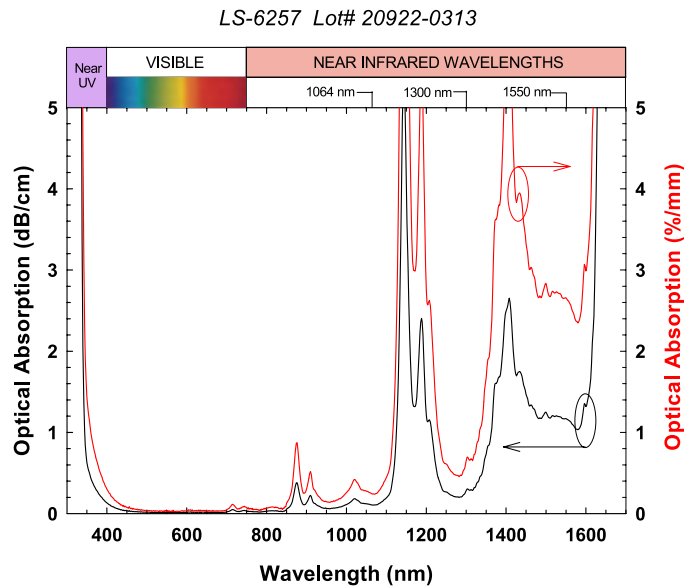


**Figure 2.6** – Optical absorption vs. wavelength of Nusil LS-6257 material. Graph adopted from the datasheet [10].

for near-infrared light and there is also an optical window around the 1300 nm telecom wavelength. The losses associated with the other frequently used telecom wavelength, 1550 nm, are nevertheless higher. The exact optical losses of the PDMS materials supplied by Dow Corning are not precisely mentioned in the datasheet, but comparable loss figures are expected.

Most types of PDMS, such as Sylgard®184 and LS-6943 have additionally significantly low optical losses in the (near-) UV region. This particular property contributed to the development of “Soft Lithography” techniques [15], for patterning materials for example using UV-illumination through a PDMS mold.

Contrarily, optical absorption of UV-light can also be beneficial to pattern materials using (Excimer) laser ablation. This technique has been adopted to create high-quality optical structures in optical polymers [16]. Laser ablation is also a versatile technique to create precise openings in materials such as vias, inlets or outlets for microfluidics etc. Nevertheless, there are also types of PDMS exhibiting high UV-light absorption which is caused by the addition of phenyl groups that are incorporated to increase the refractive index [7]. It is therefore possible to ablate these materials using a UV-laser, as demonstrated in Chapter 3). Examples of highly UV-light absorbing materials are LS-6946 or LS-6257: Figure 2.6 illustrates indeed the high absorption at wavelengths below 350 nm.

## 2.4 Mechanical properties

The glass-transition temperature  $T_g$  is the temperature at which the material transforms from a hard or brittle into a flexible, rubbery state. Compared to other polymers, PDMS exhibits one of the lowest glass-transition temperatures (typically around  $-125^\circ\text{C}$ ) and is therefore a very flexible, even stretchable material at room temperature [2, 17]. PDMS is therefore used as a transducer layer in the construction of the optical tactile shear stress sensor, as described in Chapter 5. Furthermore, the material is used as a skin-like embedding material or base substrate for incorporating the optical sensors, thanks to its mechanical compliance.

### 2.4.1 Elastic properties of PDMS

PDMS is capable of withstanding large deformations and to describe it accurately, a large strain model is needed. Furthermore, PDMS is generally a visco-elastic material meaning that its mechanical properties are time-dependent. However, for several applications, a simplified time-independent behavior can usually be adopted. For example, when PDMS is completely cross-linked, the polymer chains cannot “flow” significantly with respect to each other meaning that the visco-elastic effect will be very limited. As a result, time independent material models can serve as an adequate approximation of the actual behavior.

Following a tensile test, the applied force can be plotted with respect to the length change of the specimen, see Figure 2.7. In [18], several of the widely used mechanical models to describe the mechanical behavior of PDMS during such a test are detailed.

The simplest model to describe the length change of PDMS as a result of an applied force is the linear Hooke model. This model is accurate for extensions below 10-40% (depending on the exact material), which is satisfactory for numerous applications. For this model, the corresponding tensile or Young’s modulus  $E$  is unambiguously defined as the slope of the one-dimensional linear stress-strain curve  $\frac{F}{A} = E \frac{\Delta l}{l_0}$ .

Outside the linear region, higher order terms need to be introduced to describe the material behavior. The Neo-Hookean and Mooney-Rivlin models for example, take these effects into account.

The Neo-Hookean model was constructed based on statistical thermodynamic considerations and the fact that cross-linked polymer chains can initially move relative to each other, but for larger deformations, the chains are completely stretched and the modulus of the material drastically increases. When this model is used to calculate the uni-axial strain situation (force versus extension graph), a non-linear curve is obtained.

An even more accurate model for describing the mechanical PDMS behavior is

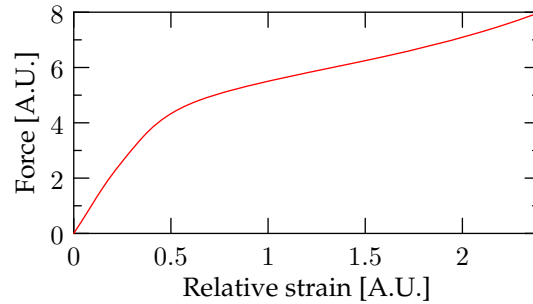


Figure 2.7 – Typical plot of the applied force versus length change of a PDMS specimen following a tensile test.

the Mooney-Rivlin model, allowing to fit the measured data up to 150 % strain [18].

For the sensing applications in this work, small deformations will be considered and it will be assumed that the materials used operate in the linear region and are homogeneous and isotropic. The material behavior is then described by its moduli (Young's modulus  $E$ , bulk modulus  $K$ , shear modulus  $G$ ) and Poisson's ratio  $\nu$ . The bulk modulus is a measure for the material resistance to a uniform (hydrostatic) compression. PDMS is generally considered as nearly incompressible resulting in a Poisson's ratio that is not much smaller than 0.5 and a bulk modulus that is very large. For a homogeneous, isotropic and linear material, the relation between bulk and Young's modulus and Poisson's ratio is given by  $K = \frac{E}{3(1-2\nu)}$ . Correspondingly, the shear modulus expresses the material response to shear strain and is related to the other properties as  $G = \frac{E}{2(1+\nu)}$ , which can be approximated by  $G \approx \frac{E}{3}$  for PDMS ( $\nu \approx 0.5$ ).

The actual Young's modulus of PDMS depends on the specific processing conditions, especially the curing temperature and mixing ratio of the 2 components. Schneider et al. obtained the modulus of Sylgard®184 (standard 1:10 mixing ratio) by performing a standardized tensile test (DIN 53504) on dog-bone shaped samples [19]. The PDMS was prepared following the standard 1:10 mixing ratio and cured for 15 min at 150 °C in an oven. The material behavior was found to be linear up to 40% of elongation and a corresponding modulus of  $1.820 \pm 0.091$  MPa was obtained. However, when an additional hard bake of the PDMS was performed at 200 °C during 4 h, this value increased to 2.60 MPa. In addition to these measurements performed at room temperature, an increase in modulus with temperature of about  $0.01$  MPa °C<sup>-1</sup> was found following measurements performed in a thermo-chamber.

Since the ratio of base and curing agent determines the amount of cross-linking, it

is expected that the Young's modulus increases with the amount of curing agent used to prepare the PDMS. Lee et al. reported that the Young's modulus of Sylgard®184 (cured at 190 °C for 24 h) varies between 0.7 MPa and 3.7 MPa in function of this mixing ratio [20].

In [21], the thickness dependency of the mechanical properties of spin-coated PDMS membranes was investigated. It was found that thinner membranes (30-50 µm thick) fabricated at high spin speed exhibited higher Young's moduli than thicker membranes prepared using low spin speeds. This effect was attributed to the aligning of the polymer chains during the spin-coating process. High spin speeds result in highly aligned chains and hence a stronger cross-linking which results in a higher Young's modulus. Also the ultimate tensile strength at which fracture occurs is up to 4 times higher for thin than for thick membranes. This implies that, depending on the preparation method, the properties of PDMS are not always isotropic which can affect the mechanical, but also the optical properties.

As indicated by the discussion above, simply comparing the exact values of the mechanical properties of different silicones would be misleading and is only meaningful when the same test conditions are strictly enforced for all samples. Therefore, the properties as specified by the provider are not listed here, but the description above is intended to provide a basic understanding of the mechanical behavior of Sylgard®184. Furthermore, the other silicones considered in this chapter exhibit similar mechanical properties, except for PV-6010 and OE-6550: PV-6010 is a much softer material than Sylgard®184 and OE-6550 is considerably harder.

Next to its beneficial optical and mechanical properties, PDMS exhibits good environmental and thermal stability up to 300 °C [7]. Furthermore, the material shows a relatively low moisture absorption and is resistant to a large range of commonly used chemicals [22].

## 2.5 Processing properties

---

For several reasons, it is important to consider the material processing properties. Firstly, it is clear from the previous sections that processing conditions may influence the final material properties drastically. Furthermore, some materials do not cross-link below a certain temperature, have extremely low or high working viscosities or very short working time. Also, adhesion issues related to the use of PDMS are frequently encountered. All these factors influence the fabrication of the final device and therefore materials with the suited processing properties need to be selected, as described below.

### 2.5.1 Material preparation and processing conditions

The types of silicone considered in this dissertation are supplied as 2-component systems consisting of a liquid base and a curing agent that need to be mixed in a certain ratio (typically 10:1 or 1:1) to initiate the cross-linking, see Section 2.2. Afterward, the mixture is degassed in a vacuum chamber to remove the trapped air bubbles. The time needed for this process depends on the type of material and typically increases with the viscosity of the liquid mixture. Typical degassing times range from 1 to 30 min.

Once the 2 components are mixed, cross-linking (curing) is initiated: the viscosity gradually increases until the material is completely hardened. This process can drastically be accelerated by applying heat. The working time is defined as the time needed to increase the viscosity by a factor 2 at room temperature and determines how long the material can be used before it starts hardening. For the used materials, the initial viscosity after mixing and working times are summarized in Table 2.3 to illustrate the large differences that exist for various materials. The curing time depends on the specific material formulation and temperature and varies between a few seconds and several days.

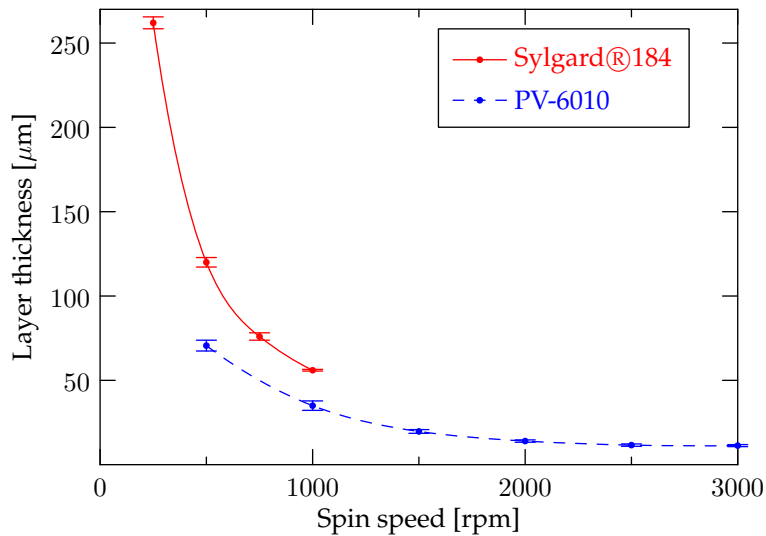


**Figure 2.8** – Layer thickness versus spin speed curves for Sylgard®184 and PV-6010.

The viscosity is an important processing property influencing how the material can be applied: for embossing, molding, cavity filling etc., selecting a material with the appropriate viscosity is critical. Also spin-coating is a widely used microfabrication technique. When the viscosity of a material is higher, the resulting spin-coated layers are thicker and PDMS with very high viscosities (typically

>10 000 mPa s) are not easily spin-coatable. From the silicones listed in Table 2.3, only OE-6550 and LS-6946 were found to be not spin-coatable. For Sylgard®184 and PV6010, layer thickness versus spin speed curves were obtained, see Figure 2.8. Spin-coated layers of Sylgard®184 are used in Chapter 3 and 4 as a base substrate layer for subsequent processing. PV-6010 is a less-viscous material yielding thinner layers and is added to the graph for comparison.

**Table 2.3** – Viscosity and working time of different silicones after mixing the 2 parts (data as provided by the supplier unless otherwise mentioned).

Material	Viscosity [mPas]	Working time
LS-6941	5300	4 h
LS-6943	5500	≈2 h (own experience)
LS-6946	≈37500	>2 h
LS-6257	170	3 days
PV-6010	925	24 h
Sylgard®184	3900	>2 h
OE-6520	1050	8 h
OE-6550	4000	>8 h
OE-6351	2800	not mentioned

## 2.5.2 Microfabrication related properties

As described in Chapter 3, PDMS is ideally suited for microfabrication. Very fine features can be defined using soft lithography techniques since the material has the ability to create a perfect replication of a master mold. When the viscosity is not too high (as a reference, Sylgard®184 is widely used for this purpose), PDMS fills very fine structures completely. Replicated PDMS features smaller than 30 nm [23] and even below 10 nm [15] have been reported. In Chapter 3, the ability to accurately replicate structures is used for the microfabrication of PDMS waveguides.

This “perfect filling property” implies that the quality of the master mold determines the quality of the final PDMS structures upon replication since the inaccuracies in the master mold are also copied in the PDMS.

## 2.5.3 Adhesion related issues

PDMS is a hydrophobic or low surface energy material meaning that a drop of water on its surface does not spread out and has a high contact angle. Therefore,

it is difficult to interact with the surface and materials are typically difficult to adhere with PDMS. This particular property of PDMS has led to several applications such as anti-stick layers, encapsulation, molding etc.

Nevertheless, this also inevitably results in processing and adhesion issues when a material needs to be applied on a PDMS surface. In Chapter 4 it is described that a surface plasma treatment was required to allow a subsequent layer of polymer to adhere to the treated PDMS. Furthermore, PDMS itself does not adhere substantially to most substrates upon curing. Therefore, a dedicated primer was needed when a PDMS layer was applied during the fabrication of the shear sensor, see Chapter 5. Another challenge is to bond 2 layers of PDMS with each other. Since all these issues were encountered during fabrication of prototypes throughout this research, they are discussed in the following paragraphs. The text in this section is mainly focusing on adhesion issues of Sylgard®184 PDMS, but most of the conclusions are also valid for similar types of silicones.

A popular technique to quantify adhesion strength is the “peel test”. To test adhesion of 2 PDMS layers, both layers are fixed for example using a gripper and are then pulled apart while recording the exerted force and displacement.

#### **Adhesion of PDMS after hardening on a substrate**

PDMS is specified to cure in contact with almost any substrate. However, the resulting adhesion with the substrate is usually bad. This problem can be solved by using a primer. For the common, 2 component addition cured silicones, a silane primer is recommended by the manufacturer. Such a primer consists of reactive silanes, a solvent carrier and a condensation catalyst. The silanes have one chemical group that is compatible with the substrate and another that is compatible with the PDMS creating an interface and improving the adhesion of the PDMS with the substrate [6]. These primers need to be applied in a thin layer (ideally a monolayer) on the substrate and are usually activated by atmospheric moisture. After 30-45 min (at 50%RH), the liquid polymer mixture can be applied on the primed surface and can be cured (thermally or at room temperature). Following curing, it was necessary to leave the samples for some days before the final adhesion strength was obtained.

Using such a primer, it was possible to achieve a good adhesion of Sylgard®184 onto metal, glass, SU-8 and polyimide. For this purpose, the OS1200 primer from Dow Corning and MED6-161 primer from Nusil were tested.

There are also silicones available that are self-priming, such as PV-6010 and OE-6351 from Dow Corning. They adhere well to most metals, glass and some polymers without the need for applying an extra primer, but the silicones are slightly sticky even after fully curing.

Nevertheless, it is difficult to quantify this adhesion strength since the bond is much stronger than the bulk PDMS material itself when using a primer. There-

fore, results of “peel tests” are not really meaningful because they only indicate at which stresses the PDMS is torn. It can be concluded, however, that when using a primer to adhere Sylgard®184 onto metal, glass, SU-8 or polyimide, the resulting adhesion strength is higher than the tensile strength of the material.

### Bonding PDMS to PDMS

Unfortunately, a primer is not compatible with any substrate. For example, on some polymers such as polytetrafluoroethylene (PTFE or “Teflon”), polypropylene or PDMS itself, the use of a primer has very little or no effect. However, for the fabrication of PDMS microstructures, applying PDMS onto another PDMS layer that is already cross-linked, is a frequently encountered problem.

In literature, several techniques have been proposed to improve the adhesion of PDMS onto PDMS. An effective technique to obtain a good adhesion is half-curing the layers to be bonded [24]. When these are then brought in contact, cross-linking occurs between the both layers and a strong bond is obtained. However, sometimes it is not possible to leave a layer half-cured, for example when molding or embossing PDMS. In [24], Eddings et al. propose to change the mixing ratio of the 2 components to improve adhesion. One layer of PDMS was prepared with excess base and the other with excess curing agent. After cross-linking the layers and bringing them in contact, the excess base in the first and excess curing agent in the second layer initiate further cross-linking between the layers and create a bond. However, changing the mixing ratio also influences the mechanical behavior of the material [20], which is not desired for (optical) sensing applications. Alternatively, the use of the curing agent as a glue for joining 2 layers of cross-linked PDMS has been reported [25].

Plasma surface treatment is another commonly used technique in polymer processing to improve adhesion of subsequent layers. Unfortunately, in-house experiments with (oxygen) plasma treatment of PDMS did not yield a significant improvement for obtaining a better adhesion of liquid PDMS onto completely cross-linked PDMS. However, when exposing a layer of cross-linked PDMS to an oxygen plasma, reactive silanol groups are formed on the surface and if 2 such layers are then brought in contact, it is believed that a strong covalent Si-O-Si bond is created [26, 27]. This technique is widely used to bond structured layers of PDMS to each other and sometimes named “dry bonding of PDMS” since the layers to be bonded are already cross-linked. It is also employed in Chapter 5 for the fabrication of the shear sensor.

As a conclusion, without the material or processing modifications mentioned above, a strong bonding of PDMS, cured on another cross-linked PDMS substrate, can hardly be obtained. Upon curing of the liquid PDMS, there is always an initial adhesion, but as soon as a delamination occurs at the interface with the substrate, the layers are easily peeled off. Such limited adhesion could be sufficient for sta-

tionary devices (e.g. for bonding of microfluidic channels [28]), but a better adhesion is required when the device needs to withstand severe mechanical stress. Fortunately, by coincidence, we have found one particular silicone, MED-6015 (Nusil) that strongly bonds to a layer of oxygen plasma treated PDMS. Furthermore, this material has similar properties as Sylgard®184 and is transparent so that it can be used for optical applications. For example, MED-6015 was used as top cladding material for covering PDMS waveguides formed using embossing, as described in Chapter 3.

### Adhesion of other polymers onto cross-linked PDMS

Another type of adhesion issue occurs when a liquid (polymer) resin other than PDMS needs to be applied on a cross-linked PDMS substrate. Upon application, the liquid resin usually contracts due to the hydrophobicity or low wettability of the PDMS. It is widely believed that these hydrophobic surface properties of PDMS are determined by the low molecular weight oligomers present at the surface [29, 30, 31, 32]. During a plasma treatment step, these oligomers are removed and the surface is chemically modified rendering the PDMS hydrophilic, i.e. the wettability significantly increases. As a result, liquid resins could be spin-coated subsequently avoiding the contraction compared to untreated, hydrophobic PDMS. For some materials, this plasma treatment also resulted in a good final adhesion of the resin and the PDMS. In Chapter 3, plasma treatment of a PDMS substrate is used to allow subsequent patterning of Truemode and Epocore waveguides on the surface.

Although the application of an oxygen plasma treatment step leads to good adhesion results, there are still several chemical aspects of PDMS unknown. Therefore, as a suggestion for future work, it may be interesting for example to investigate the effect of the amount of PDMS cross-linking on adhesion related issues.

## 2.6 Conclusions

---

PDMS is a very versatile material and ideally suited for a whole range of applications combining good optical, mechanical and processing properties.

A whole range of optically clear PDMS types are available with a low optical absorption in the visible part of the spectrum ( $<0.05$  dB/cm), but also in the near-UV and near-infrared region. Suppliers have tuned the refractive index of PDMS resulting in materials with indexes between roughly 1.40 to 1.60. Light guiding structures can therefore be fabricated by combining 2 materials with a different refractive index. Next to its dispersive behavior as comparable to other materials, PDMS exhibits a relatively large negative thermo-optic coefficient that could be useful for creating thermo-optic switches or sensors.

The glass transition temperature of PDMS is very low (typically around  $-125^{\circ}\text{C}$ ) and therefore the material is very flexible and even stretchable at room temperature. Its Young's modulus is relatively low but the exact value is highly dependent on the processing conditions adopted to fabricate the PDMS. Values ranging between 0.7 MPa and 3.7 MPa have been reported and under typical processing conditions, a value around 1.8 MPa is obtained. The elastic material behavior is sufficiently linear for small displacements but when large deformations beyond 10-40% elongation are considered, more complex material models are needed to describe the material. This rubbery and highly deformable nature of PDMS opened new possibilities for creating sensors, stress relieving structures, deformable encapsulation or conformable substrates etc.

Processing PDMS is very convenient, requires no expensive equipment and basically consists of mixing 2 components. The large number of available formulations with different viscosities and working times allow for a whole range of applications such as micromolding, embossing, injection molding, casting, spin-coating etc. Furthermore, PDMS has the ability to replicate a master mold with very small structures ( $<10\text{ nm}$ ) which has led to a new set of microfabrication techniques known as soft lithography. Its low surface energy allows an easy release from the mold. However, the low surface energy sometimes results in difficulties during processing. The limited adhesion when bonding PDMS to another material can be addressed by using a primer, oxygen plasma treatment or a set of other techniques depending of the specific situation.

## References

---

- [1] A. Norris, J. J. DeGroot, F. Nishida, U. Pernisz, N. Kushibiki, and T. Ogawa, "Silicone materials for optical applications," [http://www.dowcorning.de/de\\_DE/content/publishedlit/rubber\\_tech98.pdf](http://www.dowcorning.de/de_DE/content/publishedlit/rubber_tech98.pdf), no. 75-1007-01, 2003. [Online]. Available: [http://www.dowcorning.de/de\\_DE/content/publishedlit/rubber\\_tech98.pdf](http://www.dowcorning.de/de_DE/content/publishedlit/rubber_tech98.pdf)
- [2] B. Ratner, *Biomaterials science: an introduction to materials in medicine*, ser. Academic Press. Elsevier Academic Press, 2004. [Online]. Available: <http://books.google.be/books?id=Uzmrq7LO7loC>
- [3] N. Bamiedakis, J. B. IV, R. V. Penty, I. H. White, J. Jon v. DeGroot, T. V. Clapp, and D. D. Shazer, "Multimode siloxane polymer components for optical interconnects," *Photonics Packaging, Integration, and Interconnects IX*, vol. 7221, no. 1, p. 72210J, 2009. [Online]. Available: <http://link.aip.org/link/?PSI/7221/72210J/1>
- [4] E. Anzures, R. Dangel, R. Beyeler, A. Cannon, F. Horst, C. Kiarie, P. Knudsen, N. Meier, M. Moynihan, and B. J. Offrein, "Flexible optical

- interconnects based on silicon-containing polymers," *Photonics Packaging, Integration, and Interconnects IX*, vol. 7221, no. 1, p. 72210I, 2009. [Online]. Available: <http://link.aip.org/link/?PSI/7221/72210I/1>
- [5] Rohm & Haas. (Accessed 2011) LIGHTLINK™CLAD AND CORE datasheet. [Online]. Available: [http://www.dow.com/products/product\\_line\\_detail.page?product-line=1120529&application=1120778](http://www.dow.com/products/product_line_detail.page?product-line=1120529&application=1120778)
- [6] K. Peignot, P. Rhodes, "Choosing a silicone adhesive and treatment system." *Medical Device Technology*, vol. 15, no. 3, pp. 22 – 24, 2004. [Online]. Available: <http://search.ebscohost.com/login.aspx?direct=true&db=heh&AN=14301829&site=ehost-live>
- [7] J. Jon V. DeGroot, A. Norris, S. O. Glover, and T. V. Clapp, "Highly transparent silicone materials," *Linear and Nonlinear Optics of Organic Materials IV*, vol. 5517, no. 1, pp. 116–123, 2004. [Online]. Available: <http://link.aip.org/link/?PSI/5517/116/1>
- [8] K. Su, J. Jon V. DeGroot, A. W. Norris, and P. Y. Lo, "Siloxane materials for optical applications," *ICO20: Materials and Nanostructures*, vol. 6029, no. 1, p. 60291C, 2006. [Online]. Available: <http://link.aip.org/link/?PSI/6029/60291C/1>
- [9] B. Riegler and R. Thomaier, "Index matching silicone for optoelectronic applications," *New Developments in Optomechanics*, vol. 6665, no. 1, p. 666508, 2007. [Online]. Available: <http://link.aip.org/link/?PSI/6665/666508/1>
- [10] Nusil. (Accessed 2011) Optical elastomer product datasheets. [Online]. Available: <http://www.nusil.com/products/engineering/photronics/optical.elastomers.aspx>
- [11] D. A. Chang-Yen and B. K. Gale, "Integrated optical glucose sensor fabricated using pdms waveguides on a pdms substrate," *Microfluidics, BioMEMS, and Medical Microsystems II*, vol. 5345, no. 1, pp. 98–107, 2004. [Online]. Available: <http://link.aip.org/link/?PSI/5345/98/1>
- [12] D. A. Chang-Yen, R. K. Eich, and B. K. Gale, "A monolithic pdms waveguide system fabricated using soft-lithography techniques," *J. Lightwave Technol.*, vol. 23, no. 6, p. 2088, Jun 2005. [Online]. Available: <http://jlt.osa.org/abstract.cfm?URI=jlt-23-6-2088>
- [13] Z. Zhang, P. Zhao, P. Lin, and F. Sun, "Thermo-optic coefficients of polymers for optical waveguide applications," *Polymer*, vol. 47, no. 14, pp. 4893 – 4896, 2006. [Online]. Available: <http://www.sciencedirect.com/science/article/pii/S0032386106006367>

- [14] S. Kopetz, D. Cai, E. Rabe, and A. Neyer, "Pdms-based optical waveguide layer for integration in electrical-optical circuit boards," *AEU - International Journal of Electronics and Communications*, vol. 61, no. 3, pp. 163 – 167, 2007. [Online]. Available: <http://www.sciencedirect.com/science/article/B7GWW-4MWPYMN-1/2/ac96bbff8f2adefa730131beed13799d>
- [15] Y. Xia and G. M. Whitesides, "Soft lithography," *Annual Review of Materials Science*, vol. 28, no. 1, pp. 153–184, 1998.
- [16] G. V. Steenberge, N. Hendrickx, E. Bosman, J. V. Erps, H. Thienpont, and P. V. Daele, "Laser ablation of parallel optical interconnect waveguides," *Photonics Technology Letters, IEEE*, vol. 18, no. 9, pp. 1106 –1108, 1, 2006.
- [17] J. C. Lotters, W. Olthuis, P. H. Veltink, and P. Bergveld, "The mechanical properties of the rubber elastic polymer polydimethylsiloxane for sensor applications," *Journal of Micromechanics and Microengineering*, vol. 7, no. 3, p. 145, 1997. [Online]. Available: <http://stacks.iop.org/0960-1317/7/i=3/a=017>
- [18] G. Kofod, *Dielectric Elastomer Actuators*, ser. PhD thesis. The Technical University of Denmark, 2001.
- [19] F. Schneider, T. Fellner, J. Wilde, and U. Wallrabe, "Mechanical properties of silicones for mems," *Journal of Micromechanics and Microengineering*, vol. 18, no. 6, p. 065008, 2008. [Online]. Available: <http://stacks.iop.org/0960-1317/18/i=6/a=065008>
- [20] J. N. Lee, X. Jiang, D. Ryan, and G. M. Whitesides, "Compatibility of mammalian cells on surfaces of poly(dimethylsiloxane)," *Langmuir*, vol. 20, no. 26, pp. 11 684–11 691, 2004. [Online]. Available: <http://pubs.acs.org/doi/abs/10.1021/la048562%2B>
- [21] M. Liu, J. Sun, Y. Sun, C. Bock, and Q. Chen, "Thickness-dependent mechanical properties of polydimethylsiloxane membranes," *Journal of Micromechanics and Microengineering*, vol. 19, no. 3, p. 035028, 2009. [Online]. Available: <http://stacks.iop.org/0960-1317/19/i=3/a=035028>
- [22] J. N. Lee, C. Park, and G. M. Whitesides, "Solvent compatibility of poly(dimethylsiloxane)-based microfluidic devices," *Analytical Chemistry*, vol. 75, no. 23, pp. 6544–6554, 2003. [Online]. Available: <http://pubs.acs.org/doi/abs/10.1021/ac0346712>
- [23] S. R. Quake and A. Scherer, "From micro- to nanofabrication with soft materials," *Science*, vol. 290, no. 5496, pp. 1536–1540, 2000. [Online]. Available: <http://www.sciencemag.org/content/290/5496/1536.abstract>

- [24] M. A. Eddings, M. A. Johnson, and B. K. Gale, "Determining the optimal pdms–pdms bonding technique for microfluidic devices," *Journal of Micromechanics and Microengineering*, vol. 18, no. 6, p. 067001, 2008. [Online]. Available: <http://stacks.iop.org/0960-1317/18/i=6/a=067001>
- [25] B. Samel, M. K. Chowdhury, and G. Stemme, "The fabrication of microfluidic structures by means of full-wafer adhesive bonding using a poly(dimethylsiloxane) catalyst," *Journal of Micromechanics and Microengineering*, vol. 17, no. 8, p. 1710, 2007. [Online]. Available: <http://stacks.iop.org/0960-1317/17/i=8/a=038>
- [26] S. Bhattacharya, A. Datta, J. Berg, and S. Gangopadhyay, "Studies on surface wettability of poly(dimethyl) siloxane (pdms) and glass under oxygen-plasma treatment and correlation with bond strength," *Microelectromechanical Systems, Journal of*, vol. 14, no. 3, pp. 590 – 597, june 2005.
- [27] J. C. McDonald, D. C. Duffy, J. R. Anderson, D. T. Chiu, H. Wu, O. J. A. Schueller, and G. M. Whitesides, "Fabrication of microfluidic systems in poly(dimethylsiloxane)," *ELECTROPHORESIS*, vol. 21, no. 1, pp. 27–40, 2000. [Online]. Available: [http://dx.doi.org/10.1002/\(SICI\)1522-2683\(2000101\)21:1<27::AID-ELPS27>3.0.CO;2-C](http://dx.doi.org/10.1002/(SICI)1522-2683(2000101)21:1<27::AID-ELPS27>3.0.CO;2-C)
- [28] H. Wu, B. Huang, and R. N. Zare, "Construction of microfluidic chips using polydimethylsiloxane for adhesive bonding," *Lab Chip*, vol. 5, pp. 1393–1398, 2005. [Online]. Available: <http://dx.doi.org/10.1039/B510494G>
- [29] D. T. Eddington, J. P. Puccinelli, and D. J. Beebe, "Thermal aging and reduced hydrophobic recovery of polydimethylsiloxane," *Sensors and Actuators B: Chemical*, vol. 114, no. 1, pp. 170 – 172, 2006. [Online]. Available: <http://www.sciencedirect.com/science/article/pii/S092540050500451X>
- [30] J. Kim, M. K. Chaudhury, M. J. Owen, and T. Orbeck, "The mechanisms of hydrophobic recovery of polydimethylsiloxane elastomers exposed to partial electrical discharges," *Journal of Colloid and Interface Science*, vol. 244, no. 1, pp. 200 – 207, 2001. [Online]. Available: <http://www.sciencedirect.com/science/article/pii/S0021979701979093>
- [31] D. Bodas and C. Khan-Malek, "Hydrophilization and hydrophobic recovery of pdms by oxygen plasma and chemical treatment—an sem investigation," *Sensors and Actuators B: Chemical*, vol. 123, no. 1, pp. 368 – 373, 2007. [Online]. Available: <http://www.sciencedirect.com/science/article/pii/S0925400506006113>
- [32] A. Delcorte, S. Befahy, C. Poleunis, M. Troosters, and P. Bertrand, "Improvement of metal adhesion to silicone films: a tof-sims study," *Adhesion aspects of thin films*, no. v. 2, 2005. [Online]. Available: <http://books.google.com/books?id=7x6GPwAACAAJ>

# 3

## Stretchable waveguides for conformable optical sensors

*Optical sensors require optical interconnections, such as waveguides, to guide light to the sensing region where its optical properties are modulated depending on the physical quantity measured. Additionally, waveguides as such can also be used to construct sensors, as described in the next chapter. Whether used for interconnecting or for sensing, these waveguides need to be flexible or even stretchable to obtain the proposed sensor conformability. Therefore, a technology for creating stretchable waveguides and the characterization in terms of optical loss and mechanical deformation is described in this chapter.*

### 3.1 Introduction

---

In stretchable electronics, rigid or flexible islands are embedded in a stretchable matrix and interconnected with copper tracks. In order to make these metal interconnections stretchable, they are implemented as meandering instead of straight lines [1, 2, 3]. A similar technique could be used to obtain stretchable optical interconnections: meandering instead of straight waveguides. Although this is technologically interesting (since established fabrication techniques can be used) and theoretically possible (see simulations on bent waveguides in Section 3.2.2), this technique imposes certain limitations. Compared to the electrical situation,

bending the waveguides will introduce extra losses when not carefully designed. As an alternative, the waveguide core can be made stretchable itself. Therefore, different materials are needed to create the waveguides: next to a stretchable and transparent cladding material, also a stretchable core material with a higher refractive index is required. In Chapter 2, several commercially available stretchable optical materials were presented with different refractive indexes and exhibiting low optical losses (similar as to traditional optical polymers). If such a material with a higher refractive index is combined with a lower refractive index material, stretchable optical waveguides can be obtained as described in this chapter.

This chapter includes both of these approaches. The first section describes how traditional optical polymers can be used to form waveguide cores embedded in PDMS serving as the cladding material. Since these waveguides consist of a stretchable cladding and non-stretchable, but flexible core they are called “hybrid” waveguides in the following. Furthermore, the feasibility of meandering these waveguides is explored.

The remainder of this chapter deals with the fabrication and characterization of straight stretchable PDMS waveguides. The optical behavior of these stretchable waveguides was investigated by characterizing the propagation losses. Furthermore, the effect of mechanical deformation on the waveguides was studied: excess bending and stretching losses were determined. To our knowledge, it is the first time that the losses caused by stretching multimode PDMS based optical waveguides were studied.

## 3.2 “Hybrid” waveguides

---

### 3.2.1 Fabrication of “hybrid” waveguides

Combining optical polymer waveguide technologies and PDMS technologies is not straightforward due to material incompatibilities. PDMS, for example, has a low surface energy which prevents subsequent layers from adhering to it. Furthermore, PDMS is a flexible and even stretchable substrate which makes handling particularly difficult. Therefore, some of the traditional techniques were adapted to obtain a functional and repeatable process. The resulting sequence of process steps is illustrated in Figure 3.1 and described below. Both Epocore and Truemode Dry Film were used to serve as polymer waveguide core material. The exact process parameters corresponding with the description below are listed in Table 3.1 for the Epocore and Truemode based processes.

To facilitate the fabrication of the flexible waveguides on a stretchable substrate, all production steps were performed on a temporary rigid carrier with a release layer. Therefore, a layer of polyvinyl alcohol (PVA) dissolved in DI water was

**Table 3.1** – Process parameters for fabricating  $50\ \mu\text{m} \times 50\ \mu\text{m}$  “hybrid” waveguides with Truemode core (parameters for Epocore waveguides are mentioned between parentheses if different). All process steps are performed on a sacrificial glass substrate.

Step #	Description	Parameters
(0)	Spin PVA solution Evaporate water <i>(Step (0) is not shown in Figure 3.2)</i>	60 s at 1000 rpm 5' at 100 °C on a hotplate
(a)	Spin Sylgard®184 Cure step 1 Cure step 2	60 s at 250 rpm 24 h at 21 °C on leveled surface 60 min at 60 °C on a hotplate
(b)	Plasma treatment	Diener pico device, gas used: air 0.8 mbar, 24 s, 190 W 40 kHz generator
(c)	Dispense Truemode (Epocore) Spin-coat Truemode (Spin-coat Epocore) Remove edge bead Soft bake Truemode  (Soft bake Epocore)	using pipette 60 s at 370 rpm 60 s at 1800 rpm manually with glass substrate 2 min at 95 °C on a hotplate then 10 min at 110 °C on a hotplate 50 min at 85 °C on a hotplate)
(d)	UV-exposure (UV-exposure Post bake Truemode  (Post bake Epocore)	40 s at $10\ \text{mW cm}^{-2}$ 25 s at $10\ \text{mW cm}^{-2}$ ) 3 min at 110 °C on a hotplate then 10 min at 125 °C on a hotplate 10 min at 50 °C on a hotplate then 15 min at 85 °C on a hotplate)
(e)	Development  Hard bake Dissolve PVA to release PDMS	6 min in Mr.Dev 600 developer rinse 30 s in fresh developer rinse 30 s in IPA rinse 30 s in fresh IPA 90 min at 120 °C in convection oven immerse in DI water (1 h)

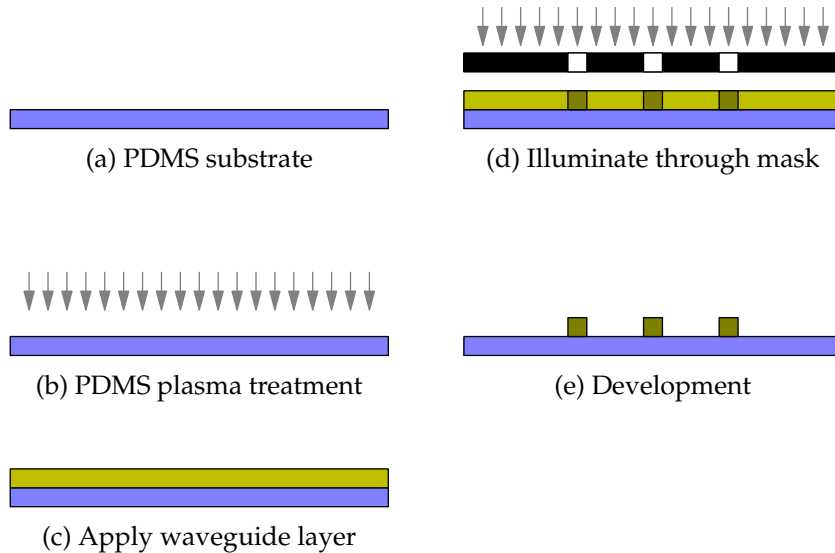


**Figure 3.1** – Process flow for fabricating “hybrid” waveguides. The temporary glass substrate is not show in the picture.

spin-coated on a 2” glass substrate. Then, the Sylgard®184 PDMS cladding layer was spin-coated at 250 rpm for 60 s yielding a thickness of about 250  $\mu\text{m}$  (Figure 3.1, step (a)). Subsequently, the sample was left on a leveled platform for 24 h in order to achieve a maximum layer flatness. Afterwards, a thermal curing step on a hotplate (for 60 min at 60 °C) was performed to further cure the material. A cross-section of an optical profiler scan (WYKO NT3300) of the PDMS top surface is depicted in Figure 3.2. It can be seen that there are no large height variations over the useful, middle area of the substrate.

Since this layer also serves as a cladding, not only the flatness and large-scale uniformity, but also the microscopic roughness is of importance for the optical behavior of the waveguides. As mentioned in Chapter 2, the roughness of spin-coated Sylgard®184 is  $22 \pm 3$  nm when measured on a 1 mm  $\times$  1 mm area and can be considered as sufficiently optically smooth.

On this Sylgard®184 cladding layer, a waveguide core layer needs to be spin-coated. However, because of the low surface energy of cured PDMS, it is difficult for materials to interact with this surface and consequently the adhesion is poor. Furthermore, when spin-coating a layer of optical polymer on top of PDMS, it immediately contracts during the subsequent baking steps due to the poor wettability of PDMS. These problems can be solved by executing a plasma treatment step of the PDMS surface. It is widely believed that the surface properties of PDMS are determined by the low molecular weight oligomers present at the sur-

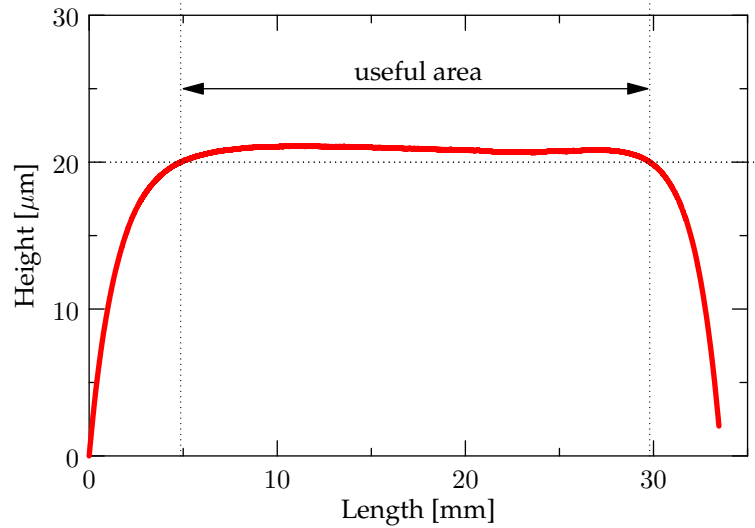


**Figure 3.2** – Cross-section of the profile of a spin-coated layer of PDMS on a 2" square glass substrate.

face [4, 5, 6, 7]. During a plasma treatment step, these oligomers are removed from the surface of the PDMS and the wettability significantly increases. Such a plasma treatment on the PDMS was performed (Figure 3.1, step (b)) using a Diener pico device (0.8 mbar, 24 s, 190 W 40 kHz generator, gas used: air) and this solved the adhesion and wetting problem of the optical polymer material on the PDMS cladding.

These polymer waveguides patterned on a PDMS bottom cladding layer can be covered with an upper cladding layer by spin-coating a final layer of PDMS, using the same parameters as above. However, for sensing applications, the waveguide core is exposed to external influences and therefore they are used without upper cladding layer, as for example in Chapter 4.

After plasma treating the PDMS, a 50  $\mu\text{m}$  thick layer of optical polymer, negative resist, was spin-coated and a soft-baking step was performed subsequently (Figure 3.1, step (c)). The baking step removes the solvent from the material so that the layer hardens. This makes it possible to illuminate the material using contact lithography. To define the waveguides, the negative resist was illuminated with UV light using a dark field mask with openings at the structure locations (Figure 3.1, step (d)). Then, a post-baking step was performed to polymerize the material where exposed to UV-light and finally, the unexposed resist was removed using a solvent developer (Mr.Dev 600).

Throughout the process, the adhesion of the optical polymer layer onto the PDMS

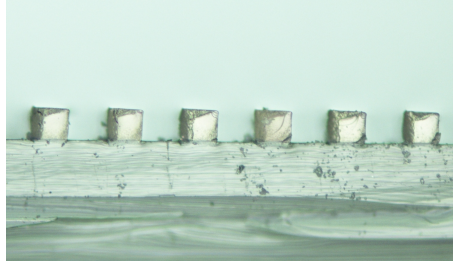


**Figure 3.3** – Cross-section of  $50\ \mu\text{m} \times 50\ \mu\text{m}$  Truemode waveguides patterned on top of Sylgard®184 PDMS cladding. The visible dirt particles were generated when cutting using a razor blade.

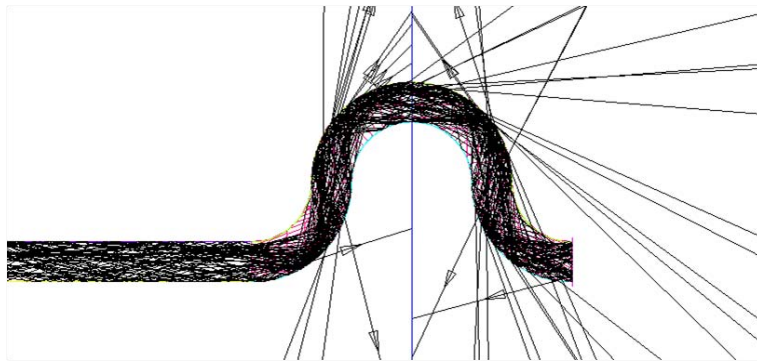


**Figure 3.4** – System geometry for the bend loss simulation: a straight waveguide section is followed by 4 successive  $90^\circ$  bend sections. The collecting efficiency of a detector is analyzed after each section.

cladding is sufficient, but the final adhesion strength depends on the hard bake step performed after the development step. When no hard bake is performed on the samples, the adhesion of the resulting waveguides is poor. However, with a hard bake step during 60 min at  $120^\circ\text{C}$  in a convection oven, the adhesion increased dramatically: when a waveguide was tried to peel off, the PDMS material itself started to rupture, meaning that the adhesion strength is greater than the strength of the PDMS bulk material.

Figure 3.3 shows a cross-section of an array of  $50\ \mu\text{m} \times 50\ \mu\text{m}$  Truemode waveguides patterned on top of Sylgard®184 PDMS cladding layer.

**Table 3.2** – Parameters used for the non-sequential ray tracing simulations.

Parameter	Value
Number of rays	5000
Launching NA	0.73
Refractive index Sylgard®184	1.41
Refractive index Epocore	1.59
Waveguide dimensions	50 $\mu\text{m}$ $\times$ 50 $\mu\text{m}$
Wavelength $\lambda$	850 nm

### 3.2.2 Modeling of waveguide bends

If it is required that not only the substrate, but additionally also the waveguides are stretchable, the design needs to be modified, for example using bends which allow a certain mechanical deformation of the waveguides.

Within the project FAOS, the influence of introducing bends on the propagation in optical waveguides has been studied<sup>1</sup>. The bending losses in function of the bending radius have been investigated by means of non-sequential ray tracing simulations using the Advanced System Analysis Program (ASAP 2009) by Breault Corp.

Two configurations with different materials were studied. The first configuration consisted of a 50  $\mu\text{m}$   $\times$  50  $\mu\text{m}$  Epocore multimode waveguide patterned on top of a Sylgard®184 PDMS cladding layer and surrounded by air on the sides and top. In the second configuration, the 50  $\mu\text{m}$   $\times$  50  $\mu\text{m}$  Epocore multimode waveguide is completely surrounded by a Sylgard®184 cladding. The parameters used for the simulations are summarized in Table 3.2.

The system geometry for the simulation consisted of a 1 mm straight waveguide section followed by four successive 90° bends, as shown on Figure 3.4. First, light was launched in the straight waveguide section to more or less fill the complete numerical aperture of the multimode waveguide. The collecting efficiency of a detector was measured after each section, i.e. at the end of the straight section, after the first 90° bend, after the second bend, ..., and after the fourth bend. A square detector of 60  $\mu\text{m}$   $\times$  60  $\mu\text{m}$  was used, slightly larger than the 50  $\mu\text{m}$   $\times$  50  $\mu\text{m}$  cross-sectional dimension of the waveguide. After the second bend, a large absorbing screen was placed to avoid the light rays from exiting the waveguide at bend number 1 or 2 and propagate further in the waveguide at a later bend and consequently influence the loss after subsequent bends.

To determine the bending loss, the efficiency versus number of bends was calcu-

<sup>1</sup>Simulations performed at B-Phot, VUB

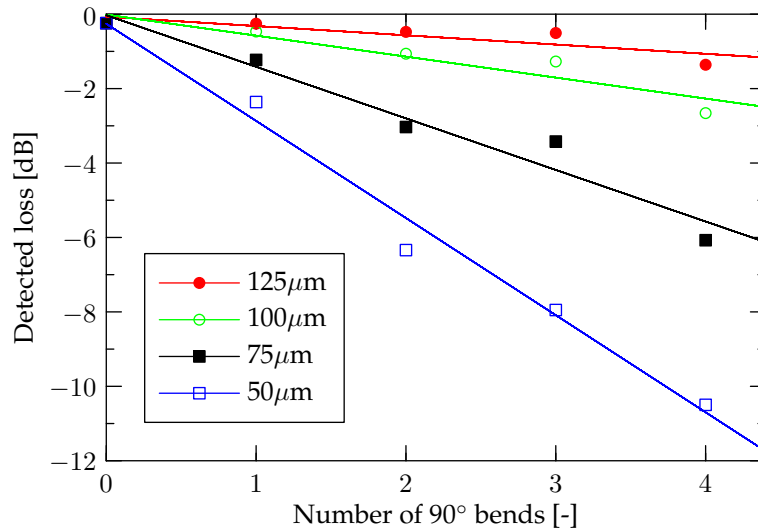


**Figure 3.5** – Collecting efficiency of a detector in function of the number of 90° bends. The slope of the linear regression through these points determines the bending loss per 90° bend. The different curves correspond with different bending radii.

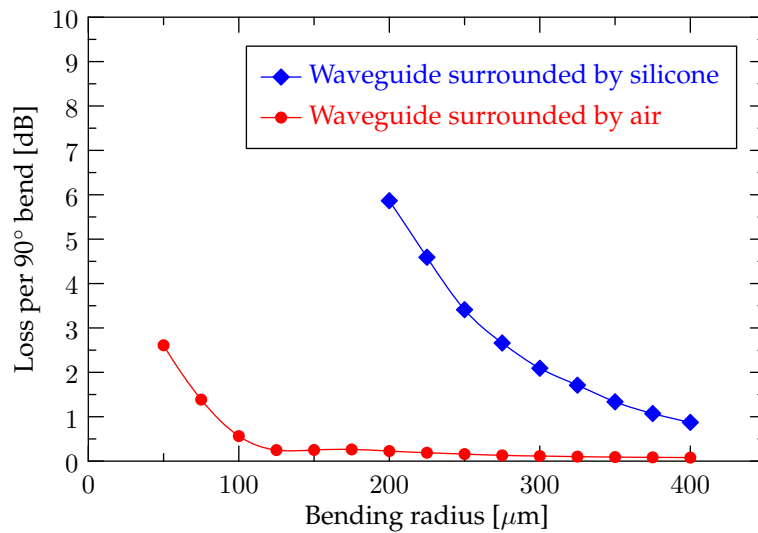


**Figure 3.6** – Bending loss in function of bending radius for Epocore waveguides surrounded by air and by a Sylgard®184 cladding respectively.

lated and a linear regression was performed through those points, for each bending radius, see Figure 3.5. The slope of these linear regression lines determines the bending loss per 90° bend and these values are plotted in Figure 3.6 for different bending radii. For bending radii down to 100  $\mu\text{m}$ , Epocore waveguides exhibit relatively limited bending losses when the waveguide core is surrounded by air (except for the bottom PDMS substrate). However, when the waveguide core is completely surrounded by PDMS, bending radii lower than 500  $\mu\text{m}$  introduce significant extra losses due to the lower numerical aperture of the waveguide.

### 3.2.3 Applicability and Evaluation

As a comparison, a typical design in stretchable electronics consists of meanders with a 350  $\mu\text{m}$  bending radius. When only 90° bends are used, as in Figure 3.4, about 28 bends are required per centimeter of stretchable interconnection. This results in a total extra bending loss of 2.5 dB/cm for the waveguides with air cladding and 37.4 dB/cm for the waveguides fully embedded in Sylgard®184. These bending losses become therefore too high for longer interconnection distances, unless larger bending radii are used.

Furthermore, these values refer to the minimum losses for perfect quality optical structures. The quality of an optical waveguide depends highly on the process accuracy and in particular the surface roughness of the sidewalls. When a waveguide is lithographically defined, this roughness is determined by the quality of the photomask used. On such masks, the structures are typically built-up with transparent and opaque (metal) “pixels” in a matrix. This means that the roughness of bent areas will be much more dependent on the pixel size than for straight sections. Therefore, a much more expensive mask is needed to define bends in waveguides compared to defining straight waveguides.

This effect was experienced when the losses of Epocore waveguides with air cladding and 90° bends (radius 400  $\mu\text{m}$ ) were measured. These waveguides were fabricated using a high-accuracy photomask from Photronics (250 nm structure deviation,  $\approx$ 800 euro) which normally yields high quality straight waveguides with very low sidewall roughness (below 10 nm rms on a 50  $\mu\text{m}$   $\times$  50  $\mu\text{m}$  area) and resulting propagation losses in the order of 0.20-0.30 dB/cm. However, the waveguides with 90° bends showed extra losses of several dB per 90° bend, being considerably higher than the 0.08 dB simulated bend loss. For this reason, this “hybrid” waveguide technology is currently only used for constructing sensors with straight waveguides, as described in the next chapter.

Furthermore, this concept for implementing stretchable waveguides is not ideal from a mechanical point of view. The combination of a harder and more brittle core material embedded in a soft, stretchable cladding material results in poor mechanical strength and reliability of the assembly. Additionally, PDMS has a much larger coefficient of thermal expansion (CTE) than harder polymers. As

a result, combining 2 materials exhibiting significantly different CTE's leads to internal stresses and consequential processing difficulties such as curling of the substrate and adhesion issues. However, when only small polymer structures are patterned onto the PDMS, the influence of the CTE mismatch can be minimized and the technology is usable for low-strain range applications, as discussed in Section 4.5.

In order to reduce optical losses and improve mechanical reliability, the remainder of this chapter focuses on alternative techniques to fabricate stretchable optical interconnections, i.e. using only stretchable PDMS materials and patterning the PDMS itself.

### 3.3 Micro-patterning of PDMS

---

This Section gives an overview of the possible techniques for structuring PDMS to create waveguides. The majority of the available PDMS materials are not suited for photolithographic pattern definition as opposed to the traditional optical polymer materials such as Lightlink, EpoCore, Ormocer, Truemode etc. Therefore other techniques are needed to pattern the PDMS in order to fabricate waveguides. In the following, these techniques are grouped as "traditional techniques" and "soft-lithography" based techniques. With traditional techniques, typically a complete layer of polymer is applied in a first step and then the material is selectively removed using laser ablation, UV-induced polymerization (photolithography), reactive ion etching (RIE) or chemical etching.

Recently, soft lithographic techniques have been investigated [8]. Instead of removing regions from a plain polymer layer, these techniques aim at directly patterning the material by replicating using a mold or stamps. They are called "soft" since the used molds or stamps are typically made from elastomeric materials such as PDMS.

#### 3.3.1 Traditional optical polymer processing techniques

##### Lithographic pattern definition

The commonly available PDMS materials are not patternable using photolithography. However, Dow Corning offers a type of PDMS (WL-5350, WL-5351 or WL-5150) which is photolithographically patternable [9]. Although, since this material is very hard (Young's modulus 160-370 MPa), it is not suited for making stretchable waveguides. However, it has been used for defining microchannels for biological applications [10]. On the other hand, research is being performed to make PDMS materials photopatternable by incorporating UV-sensitive groups that initiate or inhibit polymerization while radiated with UV-light [11, 12, 13,

14, 15, 16]. Developing such a material requires a lot of know-how and process optimization and is therefore more expensive than using commercially available products. Furthermore, several of these reported photopatternable PDMS materials have a limited resolution and exhibit modified mechanical properties due to adapting the curing mechanism.

### Wet chemical etching

Another common patterning technique is “wet chemical etching”: the material to be patterned is covered with a suitable photoresist and subsequently the material in the non-covered areas is removed using a chemical etchant. Since PDMS is resistant to many chemicals, it is not easy to pattern selectively. Garra et al. and Schuettler et al. have reported etching PDMS using a solution of tetrabutylammonium fluoride ( $C_{16}H_{36}FN$ ) in *n*-methyl-2-pyrrolidinone ( $C_5H_9NO$ ), 3:1 (v/v) NMP:TBAF, at room temperature [17, 18], but only a very slow etch rate was achieved. Furthermore, the etching quality was too low for optical applications due to the high isotropy of the etch process and the roughness of the resulting structures.

### Reactive Ion Etching

For reactive ion etching (RIE), a reactive plasma is generated using an electromagnetic field under low pressure. High-energy ions in this plasma attack the substrate and react with it. These ions are mostly vertically incident to the substrate yielding anisotropic etch profiles. Different gas mixtures can be used for reactive ion etching of PDMS. Etching PDMS using an  $O_2$  plasma has been studied by Eon et al. [19]. The resulting surface roughness was high and the etch rates slow (max.  $7 \text{ nm min}^{-1}$ ) due to the surface modification of the material during etching caused by the formation of an  $SiO_x$ -like layer.

A mixture of  $CF_4$  and  $O_2$  in different ratios was used by Garra et al. [17]. An optimum etch rate of approximately  $20 \text{ } \mu\text{m h}^{-1}$  was obtained for a  $CF_4$  to  $O_2$  ratio of 3:1. However, the surface roughness after etching is not acceptable for optical purposes.

Szmigiel et al. [20] achieved high etching rates (up to  $1.2 \text{ } \mu\text{m min}^{-1}$ ) using an optimized  $SF_6 + O_2$  gas mixture plasma. However, a significant morphology change of the PDMS (including surface roughening) was observed and the higher etch rates reduced the etching directionality and hence accuracy. Even higher etch rates ( $4.31 \text{ } \mu\text{m min}^{-1}$ ) were achieved using microwave plasma dry etching techniques [21].

From these reported results, it can be concluded that RIE is a versatile technique for patterning PDMS microstructures, but the resulting surface roughness change of the etched structures is too high to be used for creating low-loss optical wave-

guides in PDMS.

### Laser ablation

Laser ablation is a non-contact technique for structuring layers by removing material using laser irradiation. When a certain minimum amount of optical energy density is delivered to a material, ablation occurs. The wavelength of the laser and the optical absorption characteristics of the material determine how much of the incident light is absorbed and hence contributes to ablation. A material can only be ablated if it absorbs (part of) the laser light. Fogarty et al. have reported CO<sub>2</sub> laser ablation of PDMS for microfluidic channels [22]. In house tests with a 10.6 μm CO<sub>2</sub> laser indicated that this type of laser is not suitable for high quality micro-patterning (e.g. definition of waveguides) due to the high structure roughness caused by the high power and thermal ablation principle. For obtaining good optical structures, an rms roughness below  $\lambda/20$  is required in theory. In a practical situation, a surface roughness in the order of 10 nm (measured over a 50 μm × 50 μm area) or below is desired. Additionally, this type of thermally ablating laser leaves a substantial amount of debris on the surface and ablation of vertical sidewalls is not possible.

For traditional optical polymer patterning, lasers in the UV-range are used (KrF Excimer laser, 248 nm, [23]) yielding high quality optical waveguides with a low sidewall roughness. However, most of the PDMS types exhibit very low absorption for UV-light and therefore these lasers are not ideally suited to pattern PDMS. In [24], the effect of 266 nm irradiation on PDMS was studied. Although ablation of the PDMS was demonstrated, the ablation threshold was high due to the low absorption coefficient resulting in substantial deformation of the material surrounding the ablated region. Tests with the in-house available KrF Excimer laser (248 nm) on Sylgard@184 PDMS resulted in the same conclusions. There are other types of PDMS, however, that exhibit high absorption coefficients in the UV-range, such as LS-6257 and LS-6946 (Nusil, see Chapter 2). Preliminary tests have shown that ablation of these materials is indeed possible using a KrF Excimer laser (see Figure 3.7).

### 3.3.2 Soft-lithography

Soft-lithography refers to a set of microfabrication techniques based on the replication of structures using “elastomeric stamps, molds, and conformable photomasks”. These techniques are particularly interesting since they rely on molding and replication instead of patterning and etching of materials and are therefore potentially very cheap and allow for mass production. Furthermore, they allow patterning of materials (e.g. PDMS) that are difficult to etch or pattern with the traditional techniques. In [8], Y. Xia and G. M. Whitesides have demonstrated

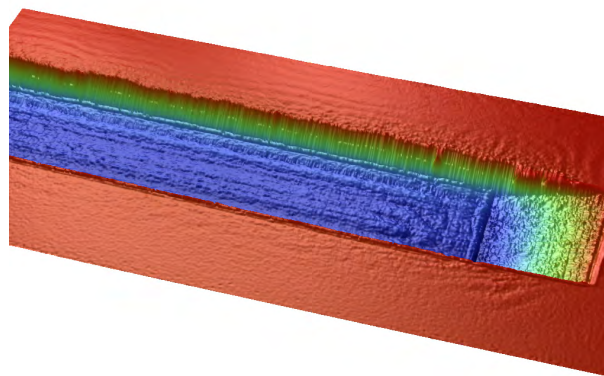


**Figure 3.7** – Preliminary test for laser ablating LS-6946 PDMS using a KrF Excimer laser (wavelength 248 nm): optical profiler scan of an ablated 200  $\mu\text{m}$  wide and 8  $\mu\text{m}$  deep groove.

5 techniques: microcontact printing ( $\mu\text{CP}$ ), replica molding (REM), microtransfer molding ( $\mu\text{TM}$ ), micromolding in capillaries (MIMIC) and solvent-assisted micromolding (SAMIM). For all these techniques, blocks of PDMS with relief structures are used as mold or stamp.

Microcontact printing relies on the transfer of a layer of material from a mold to a substrate by contacting. Therefore, a PDMS mold with desired relief structures is coated with a layer of the material to be patterned. Then, the mold with the liquid material is brought into contact with the substrate and only the material on the top of the mold structures is transferred.

Replica molding simply consist in casting a liquid prepolymer on a mold, subsequently curing it and then peeling it off. However, this simple technique is only usable for creating thick layers. Microtransfer molding is a similar but more advanced technique: a liquid prepolymer is cast on a mold, but the excess material is removed. Subsequently, the structured mold is placed on the substrate with the structures filled with prepolymer facing down. Finally, the material is cured and the mold is peeled off.

For micromolding in capillaries (MIMIC), a mold (e.g. with channels) is placed on a substrate creating closed channels. A drop of liquid prepolymer is then placed at an inlet and fills the channels by capillary forces. Once filled, the prepolymer is cured and afterwards the mold is removed.

Solvent-assisted micromolding (SAMIM) creates structures in a coated layer of material using a solvent which dissolves or softens this material. Therefore, a

PDMS mold is wetted with an appropriate solvent and brought in contact with the layer of material to be patterned. The solvent then dissolves the surface material on the substrate and the resulting liquid fills the structures of the mold. Afterward, when the solvent evaporates, the material hardens. The technique is therefore similar to hot embossing, but instead of using a hard mold, pressure and temperature to pattern a material, this technique uses a soft mold and a solvent for patterning.

An essential step in soft-lithography is the creation of an elastomeric mold or stamp which is typically prepared by casting a liquid PDMS prepolymer on a master mold and subsequently thermally curing the sample and peeling it off. This master mold is a (high-quality) model that can be used multiple times and can be fabricated using photolithography, micromachining, e-beam writing or several other techniques. In this dissertation, the master molds are fabricated using photolithography of an SU-8 polymer layer on a silicon wafer (see Section 3.4.1).

In summary, Table 3.3 compares the most important properties of possible PDMS patterning techniques. The overview table includes a column indicating whether a dedicated type of PDMS is needed for the specific process. When this is the case, own materials have to be developed or only a limited number of commercially available materials can be used. This is for example the case for lithography, requiring a photosensitive material, and for laser ablation, requiring a UV-absorbing material. Furthermore, only the soft-lithography process potentially leaves a residual layer. This means that the structures are connected with a thin layer of the same material after patterning, which can lead to light leakage in an optical waveguide. Finally, for optical applications, the quality of the sidewalls is very important because this directly influences the optical attenuation.

**Table 3.3** – Summary of possible PDMS patterning techniques.

	Finest structures (typical)	Structure sidewall quality	Dedicated PDMS needed?	Processing speed (typical)	Residual layer left?
Lithography	20 $\mu\text{m}$	+	yes	+	no
Chemical etching	100 $\mu\text{m}$	--	no	-	no
RIE	10 $\mu\text{m}$	+	no	--	no
Laser ablation	20 $\mu\text{m}$	-	yes	-	no
Soft-lithography	10 nm	++	no	++	yes

### 3.3.3 PDMS waveguide fabrication in literature

This section presents an overview of the research performed on waveguide fabrication in PDMS. Most of the reported work is based on soft-lithography techniques; the main differences noticed are the varying methods to obtain a refractive index contrast between the core and the cladding of the waveguide and the methods to pattern the waveguide core.

In order to fabricate waveguides, a refractive index contrast between the core and the cladding is required. Chang-Yen et al. use a single material (Sylgard®184, Dow Corning) for core and cladding and introduce different curing conditions of PDMS to obtain a refractive index variation [25, 26]. They have found refractive index variations up to 0.02 when curing is performed at room temperature compared to thermally curing at 150 °C. However, this technique requires precise control of the processing conditions and the refractive index difference might not be stable over time. In [27], Sylgard®184 was also used and a difference in refractive index of 0.01 was obtained by mixing with a silicone oil (200®Fluid, Dow Corning) to increase the refractive index. To obtain a very small difference in refractive index, e.g. for fabricating single mode waveguides, Kee et al. have diluted PDMS with hexane and after complete curing of the PDMS, this solvent was evaporated [28]. The evaporation process leaves small voids and results in a lower refractive index than the pure material, yielding an index contrast of about 0.07%. Finally, the use of 2 different materials obviously results in the required index contrast. In [29], PDMS was modified by incorporating phenyl groups in the side chain of the PDMS-backbone to alter the refractive index. However, similar results can be achieved by using commercially available materials instead of more expensive proprietary solutions. Several optically clear materials with different refractive indexes are commercially available, as presented in Chapter 2.

The second challenge is the fabrication of the waveguide core which is in the ideal case completely surrounded by a cladding material without leaving a residual layer of core material between different waveguide cores. This issue has been tackled in various ways by different research groups. A first technique consists in filling channels in a mold with core material and removing the excess material as much as possible, for example using a razor blade [26]. However, this still results in a substantial residual layer thickness introducing additional optical losses. A precise control of the process is required to find a balance between the presence of a residual layer and the shape of the resulting structures in the channels. Indeed, when traversing the blade, also material below the channel top surface may be removed due to drag, resulting in a concave top surface [30]. Kee et al. have reported using a clean room paper to remove the excess material [28], but due to incomplete removal, this also leaves a residual layer of core material. Kopetz, Neyer et al. have used this mold filling technique in combination with a velocity controlled blading setup and laser cut metal squeegee shims, in order to minimize the residual layer [29].

Another approach consists in fabricating a channel in cladding material and then (capillary) filling it with another material that will form the core. A similar technique was first presented by Xia and Whitesides [8] and has also been adopted to create PDMS waveguides in combination with microfluidics [31, 32]. Using this technique, there is no residual layer between waveguide cores. On the other hand, the usable types of core materials are limited since the viscosity needs to be low enough in order to fill the channel by capillary forces. Furthermore, the design flexibility of the waveguides is limited since the capillary filling process has to be taken into account. Nevertheless, this is an elegant technique to fabricate waveguides which will also be explored in this chapter.

### 3.4 Fabrication of PDMS based waveguides

---

This section describes the fabrication of PDMS waveguides. First, the process for creating a master mold is outlined and then 2 different process flows for patterning the PDMS waveguides (using this master mold) are presented. The first process flow is based on an embossing technique and the second is based on capillary filling of channels fabricated in a PDMS layer.

#### 3.4.1 Fabrication of a master mold

##### Introduction

Micro patterning techniques based on soft-lithography typically require a mold for replicating structures. The type of mold depends on the process and the type of material to be patterned. The goal of this dissertation was to fabricate structures in PDMS directly, in contrast to a typical soft lithographic process where a PDMS mold is used to replicate structures in a different (polymer) material. In any case, a master mold is needed to structure the PDMS material.

For this purpose, a silicon wafer was used as a starting point and on top of the wafer, SU-8 epoxy structures were fabricated. These SU-8 patterns determined the structures to be replicated in the PDMS. Such a type of mold has several advantages. First, the PDMS used for the fabrication of waveguides in a later step does not adhere to both silicon and SU-8, which facilitates the release of the PDMS from the mold once it is cured. Second, silicon is an ideal substrate for fabricating permanent polymer structures in SU-8 and it is very flat and exhibits a very low surface roughness (typically lower than 1 nm) which is desired for producing high-quality optical components.

SU-8 is a spin-coatable, photodefinable epoxy for producing high-aspect ratio (>1:10) and thick (more than 200  $\mu\text{m}$ ) polymer structures, developed by MicroChem. This material is optimized for permanent applications where it is left

on the substrate after processing, making it ideal for creating master molds which can be used multiple times for replicating the structures.

In the course of this research, several new types of SU-8 formations were produced by MicroChem. Each new formulation had slightly different properties compared to the previous version. The “standard” SU-8 series are easy to process but require long baking steps and possibly suffer from bad adhesion and high internal stresses. A new type, the “SU-8 2000 series” material, attempted to solve these mechanical issues and additionally required shorter baking steps, accelerating the fabrication process. However, it was found that this resist was more difficult to process than the previous version since it is fairly sensitive to (micro) air bubble formation while handling. It was therefore difficult to spin-coat a bubble free layer of this type of SU-8. Recently, the “SU-8 3000 series” materials were released. Besides being slightly more expensive, the SU-8 3000 material was found to be very easy to process and a good adhesion with the silicon substrate was obtained, compared to the previous versions.

#### **Fabrication process**

For fabricating a master mold, the SU-8 3050 material was selected to pattern 50  $\mu\text{m}$  thick structures on a silicon wafer. The final process flow is described below and the corresponding parameters are listed in Table 3.4.

The process starts with cleaning the 4” silicon wafer. Typically, a reactive ion etch (RIE) step or piranha wet etch (using  $\text{H}_2\text{SO}_4$  &  $\text{H}_2\text{O}_2$ ) is recommended by the supplier. However, it was found that this time-demanding extra cleaning step could be omitted when using the improved SU-8 3000 formulation. Instead, a degreasing step was introduced and any organic residue was removed by an acetone immersion step. After rinsing in an acetone/IPA bath and subsequently a DI water bath, the silicon wafer was dehydrated on a hotplate at 300 °C for at least 30 min. This baking step was important to ensure a good adhesion of the SU-8 material on the silicon wafer.

After cooling down the dehydrated wafer, SU-8 was deposited by pouring from a small bottle directly since the use of a manual dispensing pipette introduced too many air bubbles in the deposited material. First, the material was spread-out at 500 rpm and then a 50  $\mu\text{m}$  thick SU-8 layer was formed by spin-coating the wafer at a final speed of 2700 rpm for 30 s. Directly after spin-coating, the edge bead was removed manually using a dummy glass substrate. This edge bead is a thicker region of coated material near the edge of the wafer, inherently to the spinning process.

Then, the solvent in the deposited layer was evaporated during a soft bake step on a hot plate. To allow a gradual evaporation and avoid temperature shocks, the substrates were first baked at 65 °C and then at 95 °C. After baking, the substrates were cooled down to room temperature. The resulting layer of SU-8 is now hard

and non-sticky. Subsequently, the wafer was exposed with UV-light through a photomask to define the structures using a contact lithographic aligner system. An optical filter (PL-360-LP from Omega Optical), eliminating UV light with a wavelength shorter than 350 nm was used to obtain vertical sidewalls. Upon illumination of the SU-8, an acid catalyst is formed and cross-linking will be initiated on those locations during the subsequent post baking step. When no filter is used, the light with shorter wavelength is absorbed strongly near the surface, creating an excess amount of catalyst which diffuses laterally and widens the top region of the structures, forming the “T-topping” effect [33].

During a post baking step, polymerization of the material occurs, initiated by the catalyst formed during exposure. The post bake time should be sufficient to cross-link the polymer, but short enough not to let the acid catalyst diffuse laterally and deteriorate the quality of the patterns [34]. Again, a 2-step bake was performed at 65 °C and 95 °C and the wafer was cooled down gradually to minimize excessive internal stress accumulation.

The uncrosslinked material was then removed in SU-8 developer and afterwards a final hard bake step was introduced to further crosslink the structures and improve the final SU-8 properties.

### Characterization of the master mold

Several properties of the fabricated SU-8 mold which were important for replicating optical waveguide structures were characterized using a non-contact optical profiler (WYKO NT3300). The thickness uniformity of the SU-8 layer was measured on 5 different locations on 4 samples and the corresponding results are listed in Table 3.5.

A high-accuracy mask with features of  $50 \pm 0.25 \mu\text{m}$  wide was used to define the waveguide structures. A typical profile scan of such a structure is depicted in Figure 3.8. The structure height can be determined precisely, but it is not possible to accurately measure nearly vertical slopes using the optical profiler since the detected optical signal is not high enough. However, when measuring in the middle of the (interpolated) sidewalls, it can be seen that the structure width does not deviate significantly from the desired  $50 \mu\text{m}$ .

For optical applications, also the roughness of the structure surface is important. The surface roughness of the silicon wafer and the SU-8 structures were also measured with the WYKO optical profiler, using the “phase shifting interferometry (PSI)” mode. The surface roughness of the silicon wafer was measured on 10 different spots of approximately  $100 \mu\text{m} \times 100 \mu\text{m}$ , yielding a rms-roughness value of  $0.7 \pm 0.1 \text{ nm}$ . Similarly, the top surface roughness of the SU-8 structures was  $7.9 \pm 1.1 \text{ nm}$ , when averaged over 10 measurement spots with an area of  $50 \mu\text{m} \times 50 \mu\text{m}$ .

**Table 3.4** – Process parameters for fabricating 50  $\mu\text{m}$  SU-8 structures on a silicon wafer.

Step #	Description	Parameters
(a)	Clean silicon wafer	5' in acetone 5' in acetone+IPA 2' rinse in DI water
(b)	Dehydrate silicon wafer Dispense SU-8 material Spin-coat SU-8 layer	at least 30' at 300 °C on a hotplate pour from a small glass bottle directly ramp-up to 500 rpm at 500 rpm/s hold 10 s at 500 rpm ramp-up to 2700 rpm at 500 rpm/s hold 30 s at 2700 rpm
(c)	Remove edge bead Soft bake	manually with glass substrate 2' at 65 °C on a hotplate 15' at 95 °C on a hotplate
(d)	UV-exposure	35 s at 10 mW cm <sup>-2</sup> using UV-filter
(e)	Post exposure bake	1' at 65 °C on a hotplate 5' at 95 °C on a hotplate
(f)	Development	2' in SU-8 developer rinse 30 s in fresh SU-8 developer rinse 30 s in IPA rinse 30 s in fresh IPA
(g)	Hard bake	90' at 120 °C in convection oven

**Table 3.5** – Tolerances on nominal 50  $\mu\text{m}$  SU-8 layer thickness.

Sample #	1	2	3	4	average
Measurement points	5	5	5	5	20
Avg. layer height [ $\mu\text{m}$ ]	51.5	51.6	53.4	52.3	52.2
Std. Dev. [ $\mu\text{m}$ ]	1.1	2.0	2.6	1.6	1.9

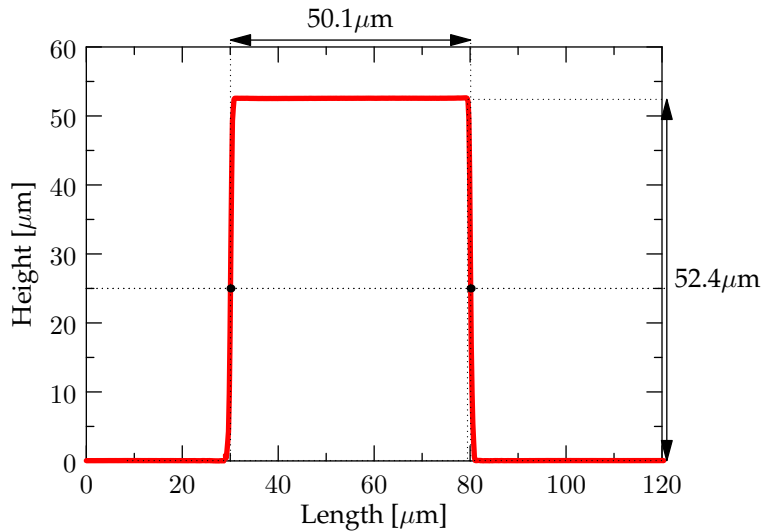


**Figure 3.8** – One dimensional cross-section of an X,Y-WYKO optical profile scan. The structure height is resolved accurately, but the nearly vertical sidewalls cannot be detected precisely by the optical profiler (the data shown is interpolated). However, it can be seen that the structure is approximately 50  $\mu\text{m}$  wide.

**Table 3.6** – Process parameters for fabricating arrays of 50  $\mu\text{m}$   $\times$  50  $\mu\text{m}$  multimode PDMS waveguides using the embossing technique with LS-6943 as core material and Sylgard®184 as cladding. See Figure 3.9.

Step #	Description	Parameters
(0)	Spin-coat Sylgard®184 undercladding layer Thermally cure this layer on hotplate <i>(Step (0) is not shown in Figure 3.9)</i>	1' at 250 rpm 60' at 60 °C
(a)	Apply liquid core material on master mold Distribute by spin-coating	1' at 250 rpm
(b)	Embossing and curing the core material apply pressure + temperature using a press	120' at 1 bar and 60 °C
(c)	Release substrate from mold	manually
(d)	Spin-coat Sylgard®184 uppercladding layer Thermally cure this layer on hotplate	1' at 250 rpm 60' at 60 °C

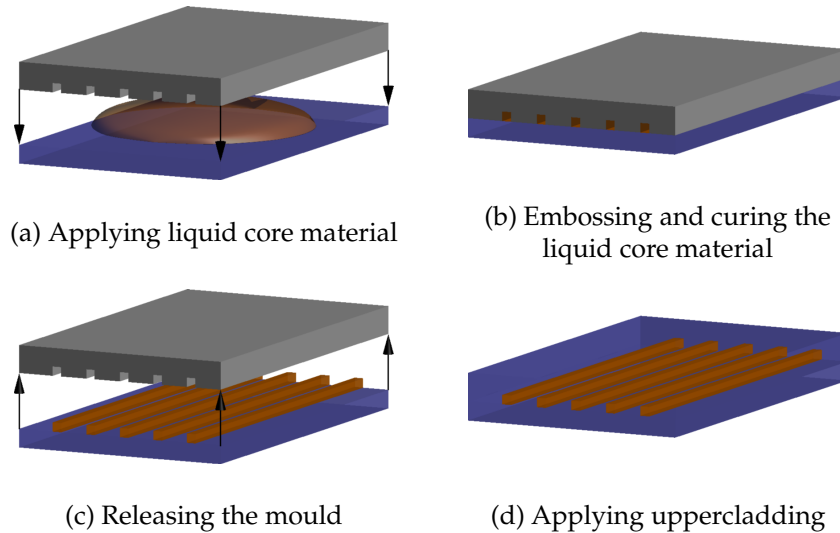
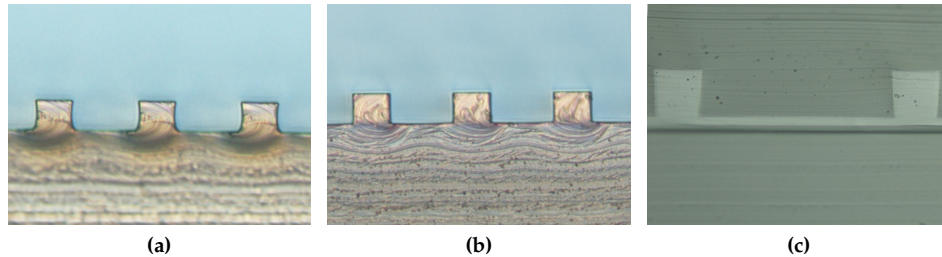


Figure 3.9 – Process flow for patterning PDMS waveguides based on embossing.

### 3.4.2 Process flow 1: embossing based patterning

#### Fabrication Process

Figure 3.9 schematically depicts the process flow for creating PDMS waveguides based on an embossing process; the processing parameters are listed in Table 3.6. The processing was performed on a temporary PET foil. Since PDMS adhesion to this foil is bad, it could be released afterward to obtain the stretchable waveguides. The PDMS material was prepared prior to processing as described in Chapter 2. First, a 250  $\mu\text{m}$  thick PDMS layer with a low refractive index was applied using spin-coating to serve as an undercladding layer (both Sylgard®184 and LS-6941 were used for this purpose, see Chapter 2). This layer was subsequently thermally cured on a hotplate for 60 min at 60  $^{\circ}\text{C}$ . Then, liquid PDMS material with a higher refractive index (LS-6943, see Chapter 2) was pressed between the master mold and this undercladding layer to form the waveguides. Using a Carver press with heated platens (model 12-12H), the liquid LS-6943 material was cured at 60  $^{\circ}\text{C}$  while exerting pressure. Finally, the sample was removed from the press and peeled off from the master mold and a 250  $\mu\text{m}$  thick uppercladding layer was spin-coated on top of the embossed waveguides.



**Figure 3.10** – Importance of a well-controlled embossing process. (a) Deformation due to excessive embossing pressure. (b) Desired structures with optimum embossing parameters. (c) Residual layer is not completely pressed away when too little pressure is applied.

#### Remarks concerning the fabrication process

As is widely known that adhesion of PDMS on a layer of already cured PDMS is very poor, the ideal process as described above was slightly modified to ensure that the embossed waveguides are adhering to the undercladding layer instead of the master mold. Therefore, the undercladding layer was only cured for 60 min, leaving it in a slightly sticky, half-cured state. If a next layer of PDMS is cured on top of such a half-cured layer, the adhesion of both layers is very good (much better than the tensile strength of the bulk PDMS material itself). However, since the undercladding is not fully cured at the time of embossing, the processing parameters are very critical since the half-cured undercladding layer is easily deformed when excessive pressure is applied. Figure 3.10 illustrates the importance of a controlled embossing process: the result of a process with optimized pressure and a process with an approximately 30% increase and decrease in pressure are shown. When the exerted pressure is too high, the undercladding deforms during embossing and the waveguides are not well-formed. However, when too little pressure is exerted, not all the liquid core material is pressed away between the waveguides. Optimum parameters yield waveguides with the intended square cross-section, but without a substantial residual layer between the waveguides in the array.

A similar remark is valid for step (d): the spin-coated Sylgard®184 uppercladding layer will not adhere sufficiently for some applications. However, if needed, another type of PDMS, e.g. MED-6015 (exhibiting similar optical properties as Sylgard®184, see Chapter 2) could be used to obtain a better adhesion and solve this problem.

Additionally, to avoid air bubbles in the embossed waveguide core layer, an optimized process consisted in spin-coating the LS-6943 liquid material on the master mold first (instead of on the undercladding), then degassing this material in vacuum and finally pressing it against the undercladding.



**Figure 3.11** – A cross-section of finished  $50\ \mu\text{m} \times 50\ \mu\text{m}$  PDMS multimode waveguides with Sylgard®184 as cladding and LS-6943 as core material ( $125\ \mu\text{m}$  waveguide pitch).



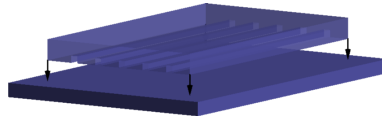
**Figure 3.12** – Light guiding in  $50\ \mu\text{m} \times 50\ \mu\text{m}$  PDMS multimode waveguides with Sylgard®184 as cladding and LS-6943 as core material.

### Evaluation of the process

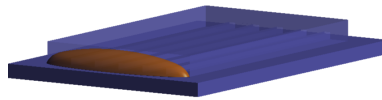
Cross-sections of the fabricated waveguides were produced to evaluate the fabrication process. Therefore, the PDMS was cut perpendicular to the waveguides using a very thin razor blade ( $100\ \mu\text{m}$  thick).

A cross-section of finished PDMS multimode waveguides with Sylgard®184 as cladding and LS-6943 as core material is depicted in Figure 3.11. The waveguides measure  $50\ \mu\text{m} \times 50\ \mu\text{m}$  in cross-section and structure pitches of  $125\ \mu\text{m}$  and  $250\ \mu\text{m}$  were achieved. Figure 3.12 illustrates light guiding in the core of the fabricated waveguides.

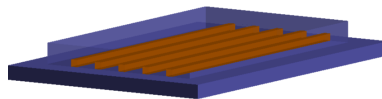
The advantage of this fabrication process is its scalability: the length, size and pitch of the PDMS waveguides can easily be altered by a redesign of the SU-8 master mold. Furthermore, this is a low-cost process; the same master mold can be used repeatedly (the number of uses depends on the allowed amount of possible defects introduced in the mold during embossing). A drawback of the process is the need for optimized embossing parameters. Nevertheless, in an automated and well-controlled (mass-production) environment, this would be feasible.



(a) Bonding of 2 PDMS layers forming covered channels



(b) Applying a drop of liquid core material at the inlet



(c) Curing the core material when the channels are filled

**Figure 3.13** – Process flow for patterning PDMS waveguides based on micro-molding in capillaries. See 3.7 for process parameters

### 3.4.3 Process flow 2: MIMIC based process

A second process flow for fabricating PDMS waveguides is based on “micro-molding in capillaries (MIMIC)” as introduced by Xia and Whitesides as a fabrication technique involving soft-lithography [8]. Based on the capillary effect, small channels can be filled with liquid materials and subsequently (thermally) cured. This process was modified to fabricate PDMS waveguides: first, channels were formed in PDMS (cladding material) and consequently the channels were filled with another type of PDMS (core material) by capillary forces.

#### Fabrication Process

Figure 3.13 illustrates the process and the corresponding parameters are listed in Table 3.7. First, a PDMS layer with channels was fabricated by replica molding against a silicon wafer with waveguide structures in SU-8. The PDMS, serving as the waveguide cladding, was poured onto the wafer, thermally cured and subse-

quently peeled off. This layer with channels was plasma bonded to a plain layer of the same type of PDMS to obtain covered-top channels. Therefore, both PDMS layers were treated using an air plasma (Diener Pico system, 0.8 mbar, 24 s, 190 W, 40 kHz generator) and then brought into contact to obtain an irreversible bond. Finally, to form the waveguide core, a small amount of a different type of PDMS was placed at the inlet of the channel which was then filled with this material by capillary forces. The speed of filling depends mainly on the channel dimensions and the viscosity of the liquid. For the 8 cm long  $50\ \mu\text{m} \times 50\ \mu\text{m}$  waveguides the filling time is about 30 min for the LS-6257 and about 2 h for the OE-6520 liquid core material. When the channel was completely filled, the material was thermally cured to obtain the PDMS waveguides.

#### Remarks concerning the fabrication process

Not all types of PDMS can be used as core material with this process. Only materials that are sufficiently liquid (typically with viscosity below a few 1000 mPas) are filling the channels at a reasonable rate. Furthermore, the working time of the PDMS limits the distance that the liquid PDMS can travel through the channel before hardening. LS-6257 and OE-6520 are low viscosity types of optical PDMS with a long working time and a high refractive index and are therefore ideally suited for this purpose. Using these materials, channels longer than 8 cm can easily be filled by capillary forces. On the contrary, LS-6943 (viscosity 5400 mPas), which was used as core material for the embossing based process, can only fill channels up to 3 cm long due to the shorter working time (the material starts curing at room temperature rather quickly).

**Table 3.7** – Process parameters for fabricating arrays of  $50\ \mu\text{m} \times 50\ \mu\text{m}$  multimode PDMS waveguides using the capillary channel filling technique with LS-6257 as core material and Sylgard®184 as cladding. See Figure 3.13.

Step #	Description	Parameters
(0)	Pour Sylgard®184 on master mold thermally cure this layer on hotplate <i>(Step (0) is not shown in Figure 3.13)</i>	15' at 100 °C
(a)	Bond 2 Sylgard®184 layers plasma treatment of both layers bring treated layers into contact	0.8 mbar, 24 s, 190 W do not apply pressure
(b)	Apply a drop of material (LS-6257) wait	at channel inlet until channel is filled
(c)	Thermally cure the core material	oven, 8 h at 80 °C

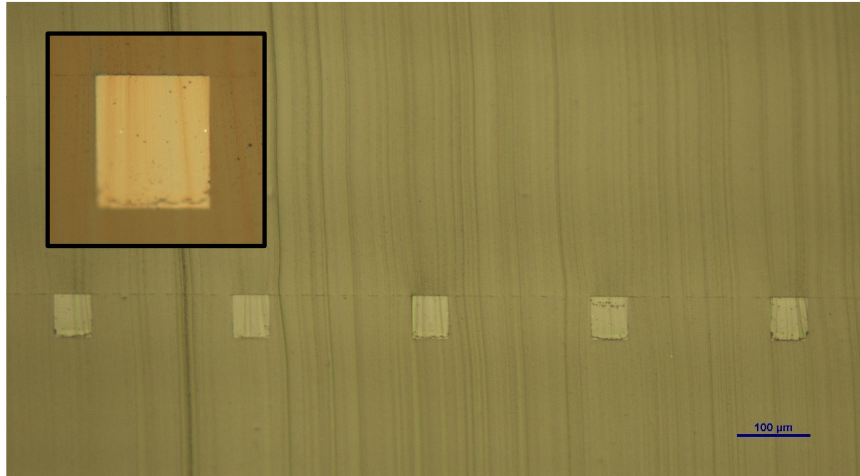


**Figure 3.14** – Cross-section of PDMS waveguides formed by capillary filling of channels (cladding: Sylgard®184 and core: LS-6257). The inset shows a magnified view of the middle waveguide in the array.

When filling Sylgard®184 channels with LS-6257, occasionally a whitening effect of the Sylgard®184 was observed, especially when curing the liquid LS-6257 material at high temperatures and when the channels were not plasma treated. Due to these whitened regions, significant extra optical losses were observed. This effect might be attributed to chemical components in the LS-6257 leaking in the Sylgard®184 material at high temperatures. To avoid this undesirable behavior, a moderate curing temperature (80 °C) was used and the channels were plasma treated, as was already introduced in the fabrication process to obtain bonding (see Table 3.7, step (a)).

It should also be noted that the channels to be filled need to have an inlet and outlet, i.e. need to have an opening on both sides. When the channel is being filled, the excess air needs to escape from the outlet. Nevertheless, PDMS is semi-permeable to air, meaning that small enclosures can also be filled by capillary forces. However, the filling speed of such enclosures is much slower than filling open channels.

### Evaluation of the process

Figure 3.14 shows a cross-section of a waveguide array formed by capillary filling of micro-channels (cladding: Sylgard®184 and core LS-6257). It can be seen that the channels are indeed completely filled with core material and there is no residual layer of core material between the different waveguides.

The PDMS waveguide fabrication process based on capillary filling is straightforward and can easily be applied without considerable parameter tuning. Furthermore, the process can be performed on a large scale and produces almost no waste (only a drop of core material is needed), making it potentially very cheap.

As a drawback, the feasible dimensions are not very scalable: only waveguides of limited length can be fabricated, related to the material used for filling the channels. For example, for the least viscous material used, LS-6257,  $50\ \mu\text{m} \times 50\ \mu\text{m}$  waveguides up to 15-20 cm should be feasible.

## 3.5 Characterization of stretchable waveguides

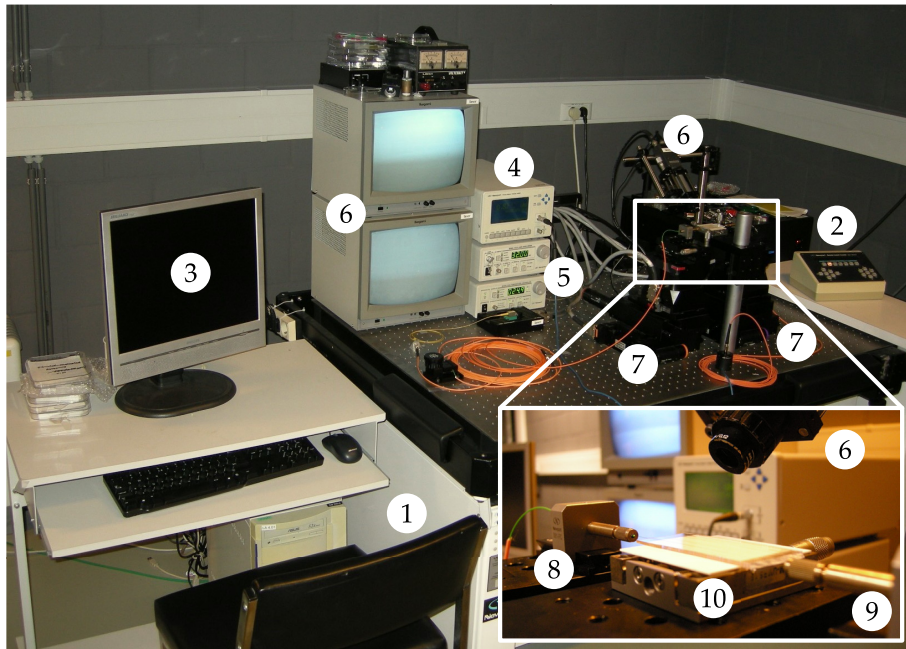
---

### 3.5.1 Introduction

Optical waveguides are typically characterized by their attenuation (at a specific wavelength) which is depending on the waveguide design and fabrication and therefore a measure for the waveguide quality. The total attenuation is determined both by the intrinsic material absorption (see Chapter 2) but is additionally determined by scattering and larger scale phenomena such as surface roughness and voids, related to the fabrication quality. In addition to selecting a low absorption material, it is therefore important to limit the defects (trapped air, contamination etc.) and to minimize the roughness of the waveguide sidewalls in order to reduce the total attenuation.

Flexible waveguides have an additional degree of freedom since they can be bent. These bends in waveguides can introduce extra losses due to the distortion of the electro-magnetic field. Using the ray theory, this phenomenon can be explained by the fact that a number of "light rays" incident on the bent interface exhibit an angle larger than the maximum angle for which total internal reflection (or waveguiding) occurs. These "rays" will therefore not be reflected but escape from the waveguide and result in a so-called bending loss, attributing to the total waveguide attenuation.

Additionally, PDMS based waveguides have the property of being stretchable so that they can be wrapped around irregular surfaces or attached to moving parts. However, stretching the waveguides may also introduce extra attenuation due to the mechanical deformations. Therefore, this section aims at fully characterizing the fabricated PDMS waveguides in terms of their optical attenuation, including effects resulting from bending and stretching.



- |  |                                       |
|--|---------------------------------------|
| (1) Vibration-free working table                   | (6) Camera visualization system       |
| (2) Motion controller                              | (7) 2 x XYZ motorized precision stage |
| (3) PC for automated measurements                  | (8) Input fiber                       |
| (4) Power meter                                    | (9) Output fiber                      |
| (5) Laser diode driver +<br>temperature controller | (10) Sample stage + sample            |

**Figure 3.15** – Setup for performing optical cut-back measurements. Input and output fibers are actively aligned with the sample using high precision motorized stages.

### 3.5.2 Optical propagation losses

#### Measuring setup

Attenuation of the optical power when traveling inside a waveguide is often referred to as “optical propagation loss” and can be determined by calculating the linear attenuation coefficient which is typically expressed in dB/cm. This coefficient (at 850 nm) was obtained using the cut-back technique. Therefore, a sample

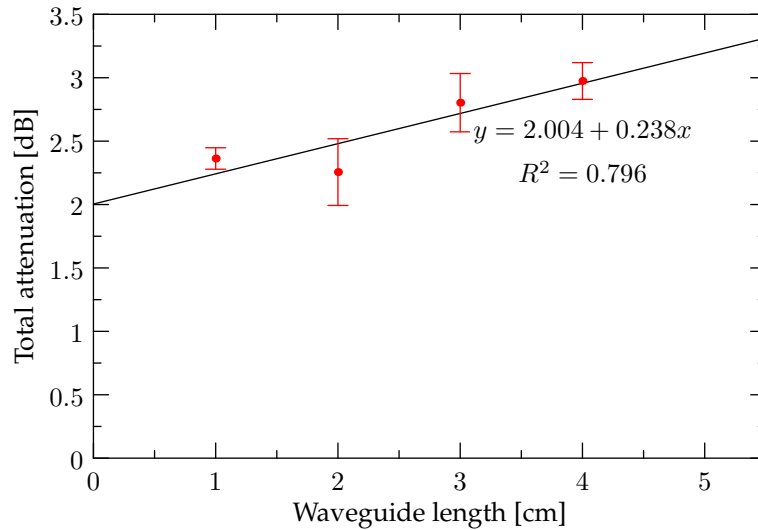


**Figure 3.16** – Optical attenuation of PDMS waveguides based on LS-6943 core and Sylgard®184 cladding (embossing process flow).

with PDMS waveguides of several centimeters long was progressively cut-back in 1 cm increments using a 125  $\mu\text{m}$  thin razor blade to make a clean cross-section of the PDMS sample. At each step, near-infrared laser light (wavelength 850 nm) was launched into the waveguides using a 50  $\mu\text{m}$  multimode fiber (numerical aperture 0.2) which was actively aligned at the input. On this fiber, a mode scrambler was used to obtain a steady mode distribution in the multimode fiber, which is independent of the launching conditions. A power detector was coupled to a 62.5  $\mu\text{m}$  multimode fiber (numerical aperture 0.275) aligned at the output of the waveguides to capture the transmitted optical power. The total attenuation (ratio of the launched optical power to the detected optical power) was then plotted with respect to the waveguide length and a trend line was fitted to determine the linear attenuation coefficient (in dB/cm). This measuring setup is depicted in Figure 3.15.

For all experiments listed in this chapter, it was assumed that a large number of modes propagate in the heavily multimode waveguides so that a continuous, stable mode distribution is obtained.

#### **Sylgard®184 (clad) – LS-6943 (core) 50 $\mu\text{m}$ $\times$ 50 $\mu\text{m}$ waveguides**

The cut-back technique was performed on a 4 cm long sample with an array of 10 50  $\mu\text{m}$   $\times$  50  $\mu\text{m}$  waveguides on a 125  $\mu\text{m}$  pitch (with a numerical aperture of 0.24).

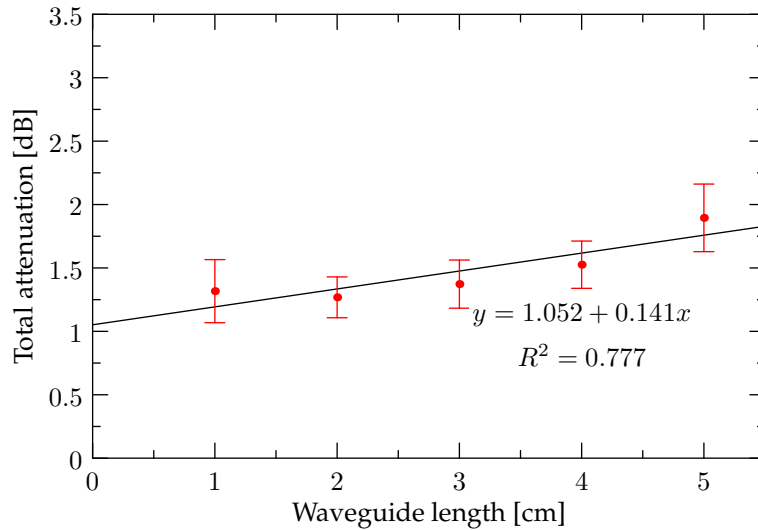


**Figure 3.17** – Optical attenuation of PDMS waveguides based on LS-6257 core and Sylgard®184 cladding (capillary filling process flow).

This sample was fabricated using the embossing technique with Sylgard®184 as cladding material and LS-6943 for the core. Figure 3.16 displays the results, where each measurement point was obtained by averaging the attenuation measured for the 10 waveguides in the array. The standard deviation is also indicated with an error bar. A propagation loss of about 0.24 dB/cm was obtained. The measured propagation loss depends both on the intrinsic material absorption and on the quality of the waveguides. Since the material absorption is very low (see Chapter 2), improving the master mold quality (to obtain a lower sidewall roughness) can further reduce these propagation losses.

#### **Sylgard®184 (clad) – LS-6257 (core) 50 μm × 50 μm waveguides**

Similarly, the cut-back technique was performed on a 5 cm long sample with an array of 10 50 μm × 50 μm waveguides on a 125 μm pitch (with a numerical aperture of 0.69). Since the numerical aperture is rather high, a 100 μm multimode fiber with numerical aperture 0.29 was used at the output instead of the 62.5 μm fiber. This sample was fabricated using the capillary filling technique with Sylgard®184 as cladding material and LS-6257 for the core. Figure 3.17 displays the results, where each measurement point was obtained by averaging the attenuation measured for the 10 waveguides in the array. The standard deviation is also indicated with an error bar. A propagation loss of about 0.14 dB/cm was

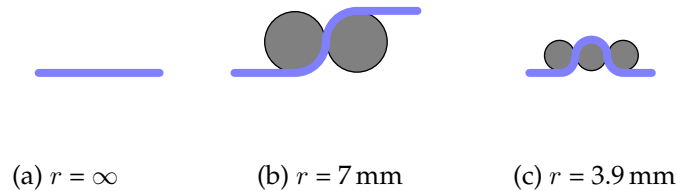


**Figure 3.18** – The different bending loss configurations and corresponding actual bending radius  $r$ .

obtained. Since a higher quality mold was used to fabricate this sample, it can be seen that the propagation loss is lower compared to the values obtained from Figure 3.16. The numerical aperture is different, but the intrinsic material absorption is similar for both samples (about 0.05 dB/cm). Furthermore, the coupling losses appeared to be lower than in Figure 3.16 because of the larger output fiber and possibly because of cleaner waveguide end facets.

The measured propagation loss values are comparable to those found in literature, where values ranging from 0.05 dB/cm to 0.32 dB/cm have been reported for multimode polymer waveguides, depending on the waveguide materials and fabrication methods [29, 35, 36, 37, 38, 39, 40].

### 3.5.3 Optical bending losses

The extra attenuation caused by bending the waveguides or the so-called “optical bending losses” were determined using the same setup (and the same launching conditions) as described in Section 3.5.2. Two bending configurations were compared in order to characterize the losses corresponding with different bending radii. Therefore, the total attenuation was compared for mechanically straight waveguides and subsequently waveguides bent around cylinders with 6.3 mm and 3.18 mm radius, as depicted in Figure 3.18. The measurements were performed on a 1.5 mm thick sample with arrays of  $50\ \mu\text{m} \times 50\ \mu\text{m}$  core multimode waveguides. The samples were prepared using the capillary filling technique

**Table 3.8** – Parameters corresponding with the different bending loss configurations (see Figure 3.18).

Configuration #	(a)	(b)	(c)
Actual bending radius $r$ [mm]	$\infty$	7	3.9
Total bending angle [°]	0	180	360
Length of bent area [mm]	0	22.2	24.7

**Table 3.9** – Measured bending loss for the configurations depicted in Figure 3.18 (average of the population  $\pm$  standard deviation). Both waveguide array samples with LS-6257 and OE-6520 core material were tested (cladding: Sylgard®184)

Configuration #	LS-6257 waveguides		OE-6520 waveguides	
	(b)	(c)	(b)	(c)
Waveguide population	10	10	15	15
Total bending loss [dB]	$0.24 \pm 0.18$	$0.58 \pm 0.38$	$0.13 \pm 0.08$	$0.19 \pm 0.11$
Loss/cm bend [dB/cm]	$0.11 \pm 0.08$	$0.24 \pm 0.15$	$0.06 \pm 0.04$	$0.08 \pm 0.04$

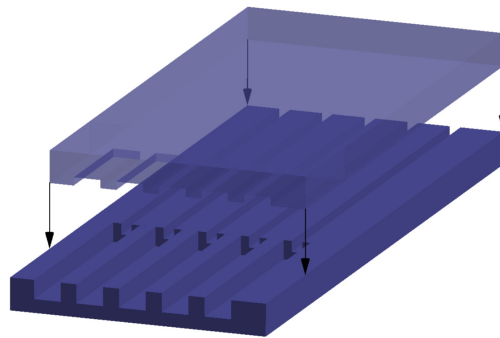
as described in Section 3.4.3. Waveguide array samples with LS-6257 and OE-6520 core material were prepared; the cladding material was Sylgard®184 in both cases. Since the thickness of the samples is not negligible compared to the cylinder radius, this was taken into account for the calculation of the “actual bending radius” of the waveguides which are located in the middle of the 1.5 mm thick sample. The resulting total bending loss and the bending loss per centimeter of bent waveguide length are listed in Table 3.9.

As expected, the bending losses are relatively low since there is a large difference in refractive index between the cladding material (Sylgard®184,  $n=1.41$ ) and core material (LS-6257:  $n=1.57$ ; OE-6520:  $n=1.54$ ). Consequently, the waveguides exhibit a high numerical aperture of 0.69 and 0.62 respectively, meaning that the acceptance angle of the light “rays” incident on the core-cladding interface is large and only a limited amount of “rays” is able to escape from the bent waveguides when the requirement for total internal reflection is not fulfilled. In the PhD of Erwin Bosman [41], bending losses of flexible polymer waveguides as obtained from own experiments and data from literature are mentioned. Compared to these values, both types of samples exhibit similarly low bending losses, but it seems that the bending losses of the OE-6520 based waveguides are lower than those of the LS-6257 based waveguides. On a basis of the numerical aperture, the opposite result is expected meaning that other effects than merely the numerical aperture may have an influence on the measured bending losses. This issue, however, is still under investigation.

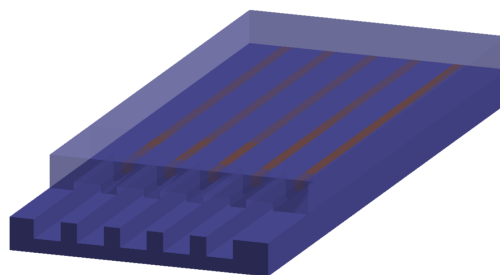
### 3.5.4 Optical behavior under mechanical elongation

#### Coupling of fibers to the waveguides

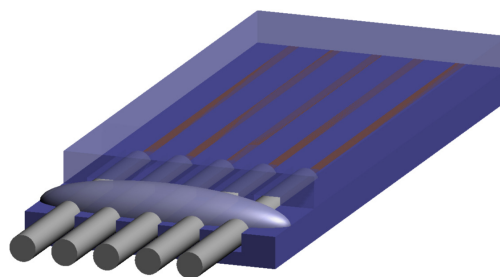
To facilitate optical loss measurements under mechanical elongation, a technique was developed to passively couple fibers to the waveguides. As a consequence, the obtained measurement results are more accurate, since the alignment of the



(a) Aligning and bonding 2 PDMS layers forming covered channels with grooves for butt-coupling fibers



(b) Filling the waveguide channels with liquid core material



(c) Inserting fibers in the grooves and fix with glue

**Figure 3.19** – Process for passively aligning optical fibers in front of the PDMS waveguides formed by capillary filling.

fibers ideally does not change between different measurements.

The capillary filling process flow was adapted for this purpose: instead of merely using straight channels, the master mold was adapted to add extra grooves to passively align the fibers at the channels ends. Since the cross-section of fibers is larger than those of the waveguides –the typical cladding outer diameter of a fiber is  $125\ \mu\text{m}$ –, an extra layer in the SU-8 fabrication process is required to pattern these grooves being larger than the waveguides. To fabricate such a 2-layer mold, the SU-8 process as described in Section 3.4.1 was extended with an extra layer. After UV-exposure and the postbake of layer 1, a second SU-8 layer was directly spin-coated onto this undeveloped first layer. Subsequently, a softbake step was performed for layer 2 and then a second UV-exposure patterned structures in layer 1 and 2 simultaneously, yielding the higher groove structures.

Figure 3.20 shows an optical profiler scan of the fabricated SU-8 structures on the master mold: the waveguides were terminated with structures forming the fiber grooves once replicated in PDMS. Since the fiber cladding outer diameter is  $125\ \mu\text{m}$  and the waveguides are  $50\ \mu\text{m}$  high, the groove structures were ideally  $37.5\ \mu\text{m}$  deeper. With the optical profiler, actual groove depths of  $38\ \mu\text{m} \pm 2\ \mu\text{m}$  were measured.

This mold was used for replicating the bottom cladding layer with channels in PDMS. A similar mold, with only the groove structures, was used to produce a PDMS layer for covering the channels and the fiber grooves. This concept of passively aligning the fibers is illustrated in Figure 3.19.

Both PDMS layers were aligned and bonded following a plasma treatment as described in the section 3.4.3. Then, the channels were filled with the liquid core material and once filled, the fibers were inserted into the grooves and temporarily fixed with tape on the edges. To permanently fix the fibers in the alignment grooves, an acetoxysilicone glue was used, curing in about 12 h at room temperature (ASC Applied Silicone, Part nr. 40064, MED RTV adhesive). When the fibers were finally fixed, the “liquid core” PDMS was thermally cured in an oven, which fixed the fibers in the grooves locally at the input and output of the waveguides, since they are also surrounded by the liquid PDMS material due to the capillary filling phenomenon. Figure 3.21 shows the resulting sample, where fibers are butt-coupled to the waveguides, using the provided grooves.

### Measuring setup

A dedicated setup was built to accurately characterize the PDMS waveguides optically while a mechanical stress is being applied, see Figure 3.23. The stretching mechanism consisted of one fixed and one moving holder on guiding pins. This moving holder was connected with a precision stepper motor using a spindle. The motor speed and direction of movement was addressed by a commercial driving circuit, which was controlled by a programmable microcontroller unit

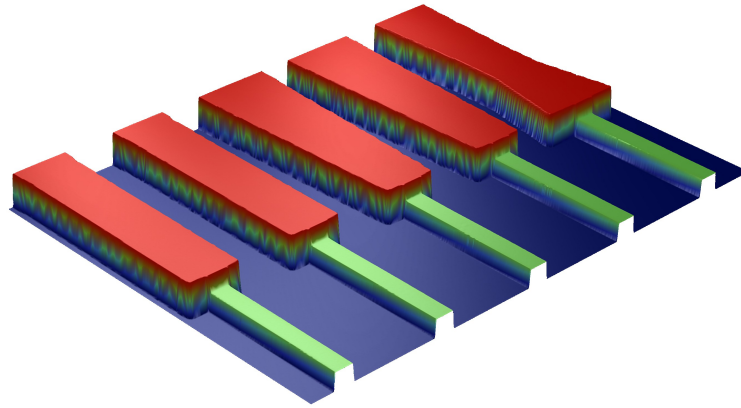


**Figure 3.20** – Optical profiler scan of the 2 layered SU-8 structures: grooves for aligning the fibers passively in front of the waveguides (different designs).

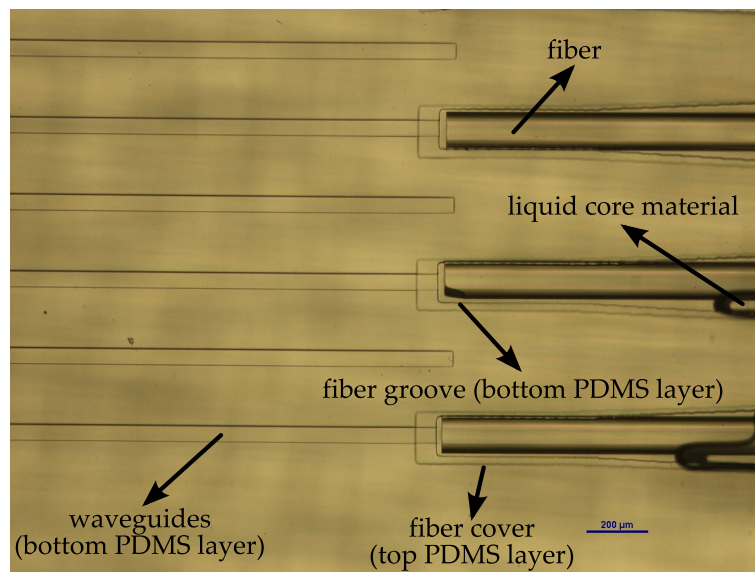


**Figure 3.21** – Optical fibers aligned in front of the PDMS waveguides formed by capillary filling. Since the liquid material surrounding the fibers hardens after thermally curing, the fibers will remain aligned during use.

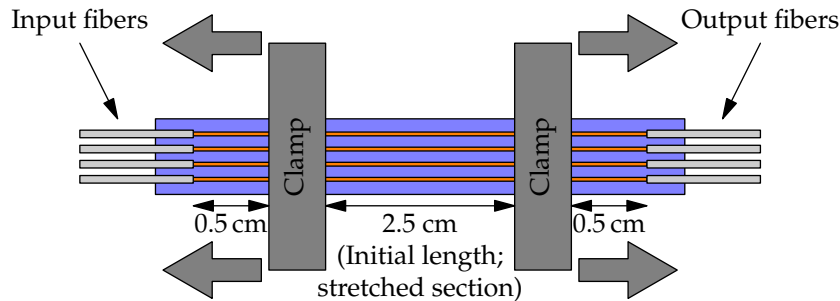


**Figure 3.22** – Configuration for stretching the waveguides: the drawing illustrates how the sample is being clamped and which part of the waveguide section is stretched.

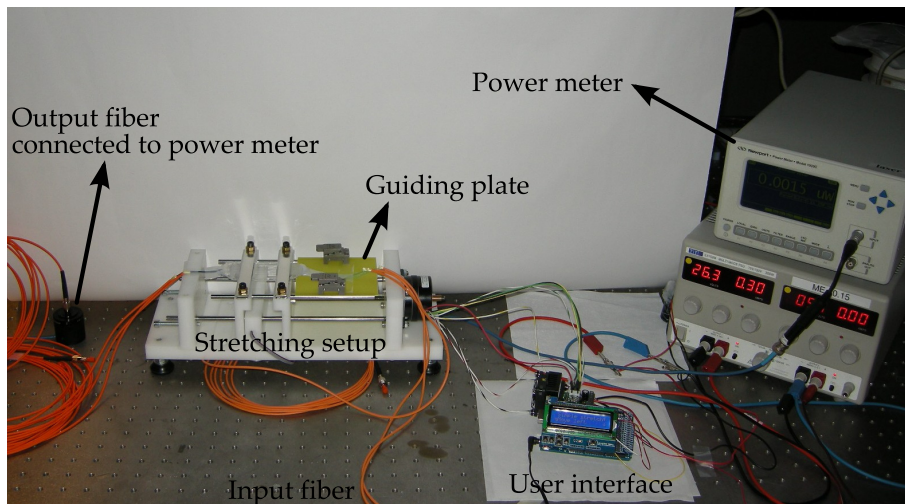


**Figure 3.23** – Custom-built setup for stretching the waveguides: a programmable controller driven stepper motor was used to stretch and relax the sample. Optical power was launched through the butt-coupled input fiber and the butt-coupled output fiber was connected to an optical power meter.

with a user interface.

Since the fibers were fixed to the input and output of the waveguides, no active aligning needed to be performed. To minimize the variations in measured optical power due to movement of the fibers, they were taped at the fixed side of the setup and taped on a moving parallel guiding plate at the “moving” side. To perform the optical measurements, the input 50  $\mu\text{m}$  fiber was connected to an 850 nm laser diode while the 62.5  $\mu\text{m}$  fiber at the output was connected to the power meter.

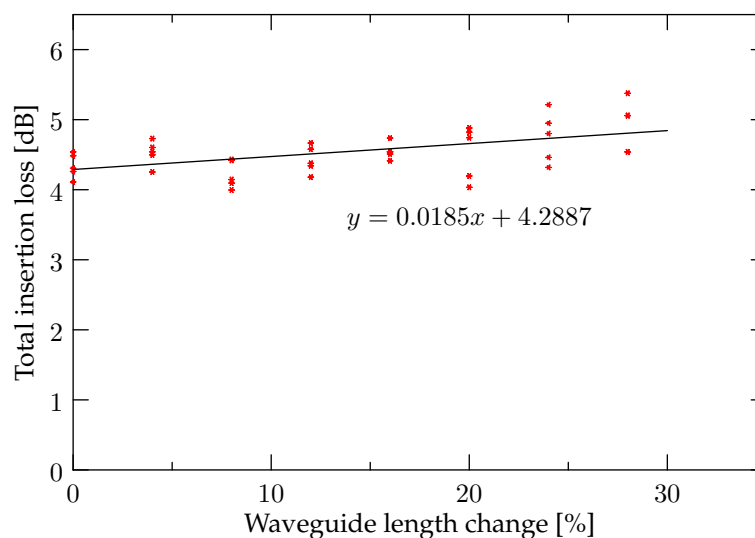


**Figure 3.24** – Influence of waveguide elongation on detected optical power at the waveguide output (5 measurements). A trendline was fitted through the measured values.

The PDMS waveguides were clamped 0.5 cm away from the fiber connections to keep the coupling conditions as constant as possible, see Figure 3.22. One clamp was mounted on the fixed holder and the other clamp on the moving holder, so that only the middle part of the waveguide section is stretched.

#### **Sylgard®184 (clad) – LS-6257 (core) 50 μm × 50 μm waveguides under stretch**

The actual stretched part of the waveguides had an initial length of 2.5 cm and this part was incrementally stretched up to 3.2 cm (28 % elongation) while 2 mW optical power was coupled into the input fiber. Figure 3.24 depicts the influence of waveguide elongation on the optical power measured in the output waveguide during 5 consecutive stretching-relaxing measurements. It can be seen that there is a noticeable decrease in optical power observed as the sample is stretched further. However, little can be concluded about the exact loss values per % elongation due to the considerable variation in optical power measured.

Despite the precautions taken to avoid in- and output fiber movement, it is believed that this variation in measured power can be attributed to the changing coupling conditions at the input and output of the waveguide when the sample is mechanically manipulated. The fluctuation of the optical power emitted by the light source was also evaluated, but measurements showed that these fluctuations were negligible.

Nevertheless, it can be concluded that the total variation measured is limited to 1.5 dB considering all measurements and all elongation values, with an average of 0.19 dB/10% elongation. As a suggestion for future work, this effect of mechanical elongation on the optical attenuation could be modeled, but in order to compare the simulation results with actual measurements, the fluctuations in measured power have to be reduced. This can potentially be achieved by adopting a different coupling strategy to reduce the effect of varying coupling conditions, that are currently being observed using the butt-coupled fibers. Possibly, a light source and detector embedded in a polymer foil [41] could be coupled to the waveguides directly, using a 45° mirror, instead of using fibers. A fabrication technology is currently being developed to test this different coupling approach.

### 3.6 Conclusions

---

Two techniques for obtaining stretchable waveguides were presented in this chapter. The first technique is similar as what is used for creating stretchable electronics: waveguides fabricated in non-stretchable material are patterned in meander-like shapes and embedded in a stretchable matrix (e.g. PDMS). A technology platform for realizing this so-called “hybrid” waveguides was developed and a feasibility study on patterning waveguides in meander shapes was performed. For multimode  $50\ \mu\text{m} \times 50\ \mu\text{m}$  waveguides surrounded by air on 3 sides, the extra bending losses of such meanders are acceptable down to a bending radius of  $100\ \mu\text{m}$ . For waveguides completely surrounded by PDMS, the bending radius needs to be larger than  $500\ \mu\text{m}$  to achieve acceptable bending losses. However, these simulations were performed for ideal, zero roughness waveguide bends. In reality, the fabrication of such bent waveguides requires a very high-quality and expensive photomask. Furthermore, the combination of 2 different (a harder and another, much softer) polymer materials leads to reliability issues.

Another technique to make waveguides stretchable is using stretchable materials for both the cladding and core. The advantage of this technique is that no meanders are needed for stretchability, but instead the straight waveguides can be stretched themselves. Two technology platforms for fabricating such PDMS waveguides were presented: one based on an embossing process and another based on capillary filling of PDMS channels. The propagation losses and bending losses of these waveguides were measured and found to be comparable to losses of polymer waveguides as reported in literature. Furthermore, the effect of stretching the waveguides was investigated. Therefore, a technique to passively couple fibers was developed and the resulting PDMS waveguide sample was tested on a dedicated stretching setup. It was found that stretching the waveguides up to 30% only introduced a small extra optical loss.

*Critical Discussion.* The goal of the research described in this chapter was to develop stretchable optical waveguides for application in conformable sensors. This aim has been achieved as demonstrated by the development of 2 different implementations of stretchable waveguides. In addition, the resulting technology can also be used for optical data transmission, since the stretchable waveguides show similar performance as other rigid or flexible waveguides reported in literature for this application. Furthermore, the proposed stretchable waveguides can be applied in conditions requiring flexible or even stretchable interconnections. For most of these applications, the implementation method using only stretchable PDMS materials is preferred, owing to the higher mechanical reliability. Nevertheless, further research is needed on methods for coupling these stretchable waveguides to light sources and detectors. As discussed in this chapter, it is currently difficult to achieve a stable coupling of for example a hard silica fiber with the much softer and stretchable waveguides.

## References

---

- [1] M. Gonzalez, F. Axisa, M. V. Bulcke, D. Brosteaux, B. Vandeveldel, and J. Vanfleteren, "Design of metal interconnects for stretchable electronic circuits," *Microelectronics Reliability*, vol. 48, no. 6, pp. 825 – 832, 2008, thermal, Mechanical and Multi-physics Simulation and Experiments in Micro-electronics and Micro-systems (EuroSimE 2007). [Online]. Available: <http://www.sciencedirect.com/science/article/pii/S0026271408000760>
- [2] T. Loher, D. Manassis, R. Heinrich, B. Schmied, J. Vanfleteren, J. DeBaets, A. Ostmann, and H. Reichl, "Stretchable electronic systems," in *Electronics Packaging Technology Conference, 2006. EPTC '06. 8th*, dec. 2006, pp. 271 –276.
- [3] F. Bossuyt, J. Guenther, T. L. her, M. Seckel, T. Sterken, and J. de Vries, "Cyclic endurance reliability of stretchable electronic substrates," *Microelectronics Reliability*, vol. 51, no. 3, pp. 628 – 635, 2011. [Online]. Available: <http://www.sciencedirect.com/science/article/pii/S0026271410005226>
- [4] D. T. Eddington, J. P. Puccinelli, and D. J. Beebe, "Thermal aging and reduced hydrophobic recovery of polydimethylsiloxane," *Sensors and Actuators B: Chemical*, vol. 114, no. 1, pp. 170 – 172, 2006. [Online]. Available: <http://www.sciencedirect.com/science/article/pii/S092540050500451X>
- [5] J. Kim, M. K. Chaudhury, M. J. Owen, and T. Orbeck, "The mechanisms of hydrophobic recovery of polydimethylsiloxane elastomers exposed to partial electrical discharges," *Journal of Colloid and Interface Science*, vol. 244, no. 1, pp. 200 – 207, 2001. [Online]. Available: <http://www.sciencedirect.com/science/article/pii/S0021979701979093>

- [6] D. Bodas and C. Khan-Malek, "Hydrophilization and hydrophobic recovery of pdms by oxygen plasma and chemical treatment—an sem investigation," *Sensors and Actuators B: Chemical*, vol. 123, no. 1, pp. 368 – 373, 2007. [Online]. Available: <http://www.sciencedirect.com/science/article/pii/S0925400506006113>
- [7] A. Delcorte, S. Befahy, C. Poleunis, M. Troosters, and P. Bertrand, "Improvement of metal adhesion to silicone films: a tof-sims study," *Adhesion aspects of thin films*, no. v. 2, 2005. [Online]. Available: <http://books.google.com/books?id=7x6GPwAACAAJ>
- [8] Y. Xia and G. M. Whitesides, "Soft lithography," *Annual Review of Materials Science*, vol. 28, no. 1, pp. 153–184, 1998.
- [9] D. Corning. (2011) Information about dow corning brand low-stress patternable silicone materials. [Online]. Available: <http://www.dowcorning.com/applications/search/>
- [10] S. P. Desai, B. M. Taff, and J. Voldman, "A photopatternable silicone for biological applications," *Langmuir*, vol. 24, no. 2, pp. 575–581, 2008, pMID: 18081333. [Online]. Available: <http://pubs.acs.org/doi/abs/10.1021/la702827v>
- [11] K. M. Choi and J. A. Rogers, "A photocurable poly(dimethylsiloxane) chemistry designed for soft lithographic molding and printing in the nanometer regime," *Journal of the American Chemical Society*, vol. 125, no. 14, pp. 4060–4061, 2003. [Online]. Available: <http://pubs.acs.org/doi/abs/10.1021/ja029973k>
- [12] A. Martínez Rivas, S. Suhard, M. Mauzac, A.-F. Mingotaud, C. Séverac, D. Collin, P. Martinoty, and C. Vieu, "Simplified and direct microchannels fabrication at wafer scale with negative and positive photopolymerizable polydimethylsiloxanes," *Microfluidics and Nanofluidics*, vol. 9, pp. 439–446, 2010, 10.1007/s10404-009-0560-0. [Online]. Available: <http://dx.doi.org/10.1007/s10404-009-0560-0>
- [13] J. C. Lötters, W. Olthuis, P. H. Veltink, and P. Bergveld, "The mechanical properties of the rubber elastic polymer polydimethylsiloxane for sensor applications," *Journal of Micromechanics and Microengineering*, vol. 7, no. 3, p. 145, 1997. [Online]. Available: <http://stacks.iop.org/0960-1317/7/i=3/a=017>
- [14] J. Chen, A. R. Vaino, R. L. Smith, and S. C. Collins, "Photomediated crosslinking of cinnamated pdms for in situ direct photopatterning," *Journal of Polymer Science Part A: Polymer Chemistry*, vol. 46, no. 11, pp. 3482–3487, 2008. [Online]. Available: <http://dx.doi.org/10.1002/pola.22653>

- [15] P. Jothimuthu, A. Carroll, A. A. S. Bhagat, G. Lin, J. E. Mark, and I. Papautsky, "Photodefinable pdms thin films for microfabrication applications," *Journal of Micromechanics and Microengineering*, vol. 19, no. 4, p. 045024, 2009. [Online]. Available: <http://stacks.iop.org/0960-1317/19/i=4/a=045024>
- [16] K. Tsougeni, A. Tserepi, and E. Gogolides, "Photosensitive poly(dimethylsiloxane) materials for microfluidic applications," *Microelectronic Engineering*, vol. 84, no. 5-8, pp. 1104 – 1108, 2007, proceedings of the 32nd International Conference on Micro- and Nano-Engineering. [Online]. Available: <http://www.sciencedirect.com/science/article/B6V0W-4MWXPPB-M/2/1679d3a8a39f642b7b898822f5b2d31a>
- [17] J. Garra, T. Long, J. Currie, T. Schneider, R. White, and M. Paranjape, "Dry etching of polydimethylsiloxane for microfluidic systems," *Journal of Vacuum Science Technology A: Vacuum, Surfaces, and Films*, vol. 20, no. 3, pp. 975 –982, may 2002.
- [18] M. Schuettler, C. Henle, J. Ordonez, G. Suaning, N. Lovell, and T. Stieglitz, "Patterning of silicone rubber for micro-electrode array fabrication," in *Neural Engineering, 2007. CNE '07. 3rd International IEEE/EMBS Conference on*, may 2007, pp. 53 –56.
- [19] D. Eon, L. de Poucques, M. C. Peignon, C. Cardinaud, G. Turban, A. Tserepi, G. Cordoyiannis, E. S. Valamontes, I. Raptis, and E. Gogolides, "Surface modification of si-containing polymers during etching for bilayer lithography," *Microelectronic Engineering*, vol. 61-62, pp. 901 – 906, 2002. [Online]. Available: <http://www.sciencedirect.com/science/article/B6V0W-45XXDTY-B/2/7c6e9e598fa8bd51041b4fa8ca223310>
- [20] D. Szmigiel, K. Domanski, P. Prokaryn, and P. Grabiec, "Deep etching of biocompatible silicone rubber," *Microelectronic Engineering*, vol. 83, no. 4-9, pp. 1178 – 1181, 2006, micro- and Nano-Engineering MNE 2005. [Online]. Available: <http://www.sciencedirect.com/science/article/B6V0W-4J79YG1-2/2/02b0569fdcd58b4fae6d90afed91a056>
- [21] S. J. Hwang, D. J. Oh, P. G. Jung, S. M. Lee, J. S. Go, J.-H. Kim, K.-Y. Hwang, and J. S. Ko, "Dry etching of polydimethylsiloxane using microwave plasma," *Journal of Micromechanics and Microengineering*, vol. 19, no. 9, p. 095010, 2009. [Online]. Available: <http://stacks.iop.org/0960-1317/19/i=9/a=095010>
- [22] B. A. Fogarty, K. E. Heppert, T. J. Cory, K. R. Hulbutta, R. S. Martin, and S. M. Lunte, "Rapid fabrication of poly(dimethylsiloxane)-based microchip capillary electrophoresis devices using co2 laser ablation," *Analyst*, vol. 130, pp. 924–930, 2005. [Online]. Available: <http://dx.doi.org/10.1039/B418299E>

- [23] G. V. Steenberge, N. Hendrickx, E. Bosman, J. V. Erps, H. Thienpont, and P. V. Daele, "Laser ablation of parallel optical interconnect waveguides," *Photonics Technology Letters, IEEE*, vol. 18, no. 9, pp. 1106–1108, 1, 2006.
- [24] V.-M. Graubner, R. Jordan, O. Nuyken, T. Lippert, M. Hauer, B. Schnyder, and A. Wokaun, "Incubation and ablation behavior of poly(dimethylsiloxane) for 266 nm irradiation," *Applied Surface Science*, vol. 197-198, pp. 786–790, 2002. [Online]. Available: <http://www.sciencedirect.com/science/article/B6THY-45TTNDS-1P/2/968f2a40cf821ca8da2ce667b81e5a42>
- [25] D. A. Chang-Yen and B. K. Gale, "Integrated optical glucose sensor fabricated using pdms waveguides on a pdms substrate," *Microfluidics, BioMEMS, and Medical Microsystems II*, vol. 5345, no. 1, pp. 98–107, 2004. [Online]. Available: <http://link.aip.org/link/?PSI/5345/98/1>
- [26] D. A. Chang-Yen, R. K. Eich, and B. K. Gale, "A monolithic pdms waveguide system fabricated using soft-lithography techniques," *J. Lightwave Technol.*, vol. 23, no. 6, p. 2088, Jun 2005. [Online]. Available: <http://jlt.osa.org/abstract.cfm?URI=jlt-23-6-2088>
- [27] J. S. Kee, D. P. Poenar, P. Neuzil, and L. Yobas, "Monolithic integration of poly(dimethylsiloxane) waveguides and microfluidics for on-chip absorbance measurements," *Sensors and Actuators B: Chemical*, vol. 134, no. 2, pp. 532–538, 2008. [Online]. Available: <http://www.sciencedirect.com/science/article/B6THH-4SNWW1M-3/2/58e54ab4900ac5626b96e6513c1c9dbe>
- [28] J. S. Kee and D. P. Poenar and P. Neuzil and L. Yobas, "Design and fabrication of poly(dimethylsiloxane) single-mode rib waveguide," *Opt. Express*, vol. 17, no. 14, pp. 11739–11746, Jul 2009. [Online]. Available: <http://www.opticsexpress.org/abstract.cfm?URI=oe-17-14-11739>
- [29] S. Kopetz, D. Cai, E. Rabe, and A. Neyer, "Pdms-based optical waveguide layer for integration in electrical-optical circuit boards," *AEU - International Journal of Electronics and Communications*, vol. 61, no. 3, pp. 163–167, 2007. [Online]. Available: <http://www.sciencedirect.com/science/article/B7GWW-4MWPYMN-1/2/ac96bbff8f2adefa730131beed13799d>
- [30] K. S. Ryu, X. Wang, K. Shaikh, and C. Liu, "A method for precision patterning of silicone elastomer and its applications," *Microelectromechanical Systems, Journal of*, vol. 13, no. 4, pp. 568–575, aug. 2004.
- [31] V. Lien, Y. Berdichevsky, and Y.-H. Lo, "A prealigned process of integrating optical waveguides with microfluidic devices," *Photonics Technology Letters, IEEE*, vol. 16, no. 6, pp. 1525–1527, june 2004.

- [32] V. Lien, K. Zhao, Y. Berdichevsky, and Y.-H. Lo, "High-sensitivity cytometric detection using fluidic-photonic integrated circuits with array waveguides," *Selected Topics in Quantum Electronics, IEEE Journal of*, vol. 11, no. 4, pp. 827–834, july-aug. 2005.
- [33] S. Lee, W. Shi, P. Maciel, and S. Cha, "Top-edge profile control for su-8 structural photoresist," in *University/Government/Industry Microelectronics Symposium, 2003. Proceedings of the 15th Biennial, 2003*, pp. 389–390.
- [34] B. Li, M. Liu, and Q. Chen, "Low-stress ultra-thick su-8 uv photolithography process for mems," *Journal of Microlithography, Microfabrication, and Microsystems*, vol. 4, no. 4, p. 043008, 2005. [Online]. Available: <http://link.aip.org/link/?JMM/4/043008/1>
- [35] G. V. Steenberge, N. Hendrickx, E. Bosman, J. V. Erps, H. Thienpont, and P. V. Daele, "Laser ablation of parallel optical interconnect waveguides," *Photonics Technology Letters, IEEE*, vol. 18, no. 9, pp. 1106–1108, 1, 2006.
- [36] Y. K. Kwon, J. K. Han, J. M. Lee, Y. S. Ko, J. H. Oh, H.-S. Lee, and E.-H. Lee, "Organic-inorganic hybrid materials for flexible optical waveguide applications," *J. Mater. Chem.*, vol. 18, pp. 579–585, 2008. [Online]. Available: <http://dx.doi.org/10.1039/B715111J>
- [37] B. S. Rho, W.-J. Lee, J. W. Lim, G. W. Kim, C. H. Cho, and S. H. Hwang, "High-reliability flexible optical printed circuit board for opto-electric interconnections," *Optical Engineering*, vol. 48, no. 1, p. 015401, 2009. [Online]. Available: <http://link.aip.org/link/?JOE/48/015401/1>
- [38] J. Kobayashi, "Recent progress on polymer optical waveguides," *Organic Photonic Materials and Devices X*, vol. 6891, no. 1, p. 68910O, 2008. [Online]. Available: <http://link.aip.org/link/?PSI/6891/68910O/1>
- [39] K. Hara, Y. Ishikawa, and Y. Shoji, "Preparation and properties of novel silicone-based flexible optical waveguide," *Optomechatronic Micro/Nano Devices and Components II*, vol. 6376, no. 1, p. 63760K, 2006. [Online]. Available: <http://link.aip.org/link/?PSI/6376/63760K/1>
- [40] Y. Ishida and H. Hosokawa, "Optical link utilizing polymer optical waveguides: application in multimedia device," *Photonics in Multimedia II*, vol. 7001, no. 1, p. 70010J, 2008. [Online]. Available: <http://link.aip.org/link/?PSI/7001/70010J/1>
- [41] E. Bosman, "Integration of optical interconnections and opto-electronic components in flexible substrates," Ph.D. dissertation, Ghent University, 2010.



# 4

## Polymer waveguide based sensing

*In this chapter, the feasibility of using fully optical tactile sensors based on waveguides is investigated. Therefore, two principles of light transfer from one waveguide to another are investigated and evaluated as potential techniques to create a tactile sensor. These techniques were also implemented using a modification of the PDMS based waveguide technologies from the previous chapter.*

### 4.1 Introduction

---

“Fully optical” sensors are based on optical fibers, waveguides or free-space optical principles for sensing, and have numerous advantages. The main advantage is that the sensor does not need electrical signals to operate and is therefore insensitive to electromagnetic interference. The presence of electrical currents is furthermore undesirable or may even pose a safety risk for several applications such as sensing inside the human body or in explosive environments. Obviously, optoelectronic light sources and/or detectors are needed to drive the optical sensors, but these can be located away from the sensitive region. Optical sensors are also potentially lighter since no metallic interconnections need to be used and they can rely on very sensitive sensing principles.

Fiber based sensors typically rely on Bragg gratings for sensing and are therefore very sensitive. The measurement value is encoded as wavelength dependent information in the optical spectrum and therefore less susceptible to intensity or

phase noise. Furthermore, several sensors can be incorporated in the same fiber using a wavelength based multiplexing technique. However, fibers are discrete components and therefore need to be embedded in “skin-like” host materials to obtain tactile sensing sheets, which may be challenging and limiting the possible spatial resolution in distributed sensing surfaces. Research is ongoing to overcome this limitation by incorporating the same grating based sensing principle in (polymer) waveguides [1, 2, 3] that can be more easily integrated and patterned in dense arrays, potentially allowing higher resolution sensors. However, to exploit all advantages of Bragg grating tactile sensors, single mode waveguides are preferred. Although some results have already been reported [4, 5], this topic is relatively new as a research domain. In any case, these Bragg grating based sensors require a read-out system that is typically bulky and expensive, e.g. a spectrum analyzer or interrogator.

Other optical sensing principles, i.e. based on detecting changes in intensity could offer a more compact and cheaper solution in exchange for a slightly lower accuracy. Wagner et al. propose a pressure sensor based on a Mach-Zehnder interferometer and a photodiode to record the intensity variations caused by the interference patterns [6]. However, it only allows to record relative pressure changes and the proposed design is not directly suited for tactile sensing. Furthermore, the modulation of the signal caused by the interference phenomena is very small which makes it difficult to detect.

Another intensity based sensing mechanism relies on the changing optical losses in fibers or waveguides caused by bending [7]. The waveguides are organized in a matrix configuration and when exposed to pressure, bending occurs which introduces intensity variations in the optical power transmitted through the waveguides. A similar sensing technique was reported in [8], where the intensity variations are caused by transfer of optical power from a waveguide to a dielectric slab depending on the contact length.

Simultaneously, in the FAOS project [9], a similar idea was investigated in a slightly different configuration, i.e. the pressure dependent coupling change of optical power between arrays of crossing waveguides. Compared to [8], the use of 2 layers of waveguides results in a higher resolution of sensing points. Compared to [7], using the coupling phenomenon instead of the bending loss halves the amount of sources and detectors needed, as explained in the next section. Two physical phenomena are studied in this chapter to investigate the feasibility of this configuration for implementing a tactile sensor: the changing evanescent wave coupling and the pressure dependent change of contact area between 2 crossing waveguides.

## 4.2 Concept for a waveguide based tactile sensor

### 4.2.1 Sensor operation principle

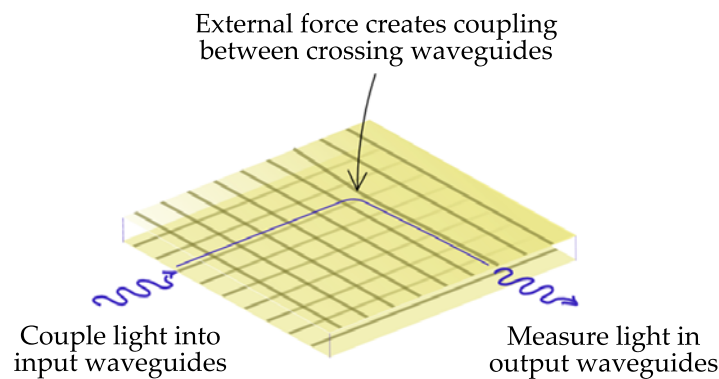


**Figure 4.1** – Illustrated principle of the sensor based on light coupling between crossing waveguides.

The operation of the proposed sensor configuration relies on the changing optical coupling between waveguides crossing in a matrix, see Figure 4.1. The sensor consists of 2 stacked layers, one with input and another with output waveguides, which are separated in the idle situation. The input waveguides are excited with a light source while the optical power in the output waveguides is monitored. When pressure is exerted on a crossing point of 2 waveguides, light from the input waveguide is coupled to the output waveguide. The location of the excited crossing point can be determined by alternately driving the input waveguides while reading the output waveguides in parallel. This configuration results in the minimum optical sources and detectors needed. Only the input waveguides need to be fed with optical power, and the output waveguides monitored since only the coupled power needs to be detected.

Since very small and closely spaced waveguides can be fabricated and arranged in a matrix configuration, this concept has a potential for obtaining a very high density sensor.

### 4.2.2 Optical coupling mechanisms

The characteristics of the sensor are defined by the mechanism for coupling light from input to output waveguides. To achieve a tactile sensor, a pressure depen-

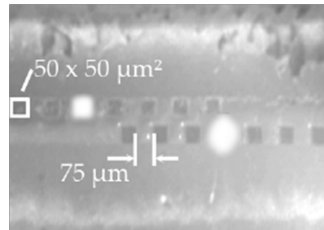


**Figure 4.2** – Evanescent wave optical power coupling proof-of-principle demonstrator. Light is sent into a bottom waveguide and when pressure is exerted on the layer structure, the distance between the 2 waveguide layers decreases and light is coupled to a waveguide in the top layer.

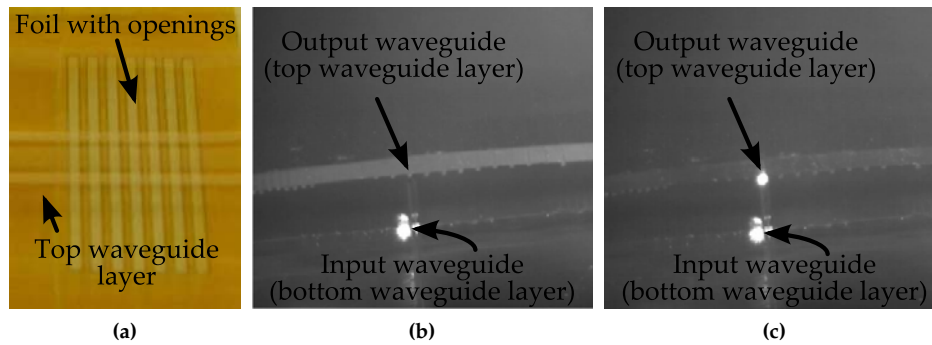


**Figure 4.3** – Optical power coupling through mechanical contact. (a) shows the setup: 2 layers of waveguides separated by a thin foil with openings. The bottom waveguide layer is located under the foil and can therefore not be seen. (b) In rest, no light is coupled but when pressure is exerted (c), light is coupled from the input waveguide to the output waveguide.

dent optical coupling mechanism is required, which can be obtained by several phenomena. A first phenomenon is based on the evanescent wave coupling between 2 waveguides in close proximity. A second phenomenon is based on the pressure dependent contact area between 2 touching waveguides. These 2 methods of influencing the coupled optical power are investigated below. Alternative phenomena rely for example on coupling by means of scattering or micro-fabricated structures such as mirrors, but are not investigated in the scope of this dissertation.

The principle of achieving evanescent wave coupling between waveguides was qualitatively tested by constructing a proof-of-principle demonstrator. Arrays of  $50\ \mu\text{m} \times 50\ \mu\text{m}$  multimode polymer waveguides (Truemode™backplane polymer) were patterned on a layer of Sylgard®184 (see Section 3.2). Then, 2 such

substrates were coated with a thin layer of a very soft, gel-like silicone (Sylgard®527) and then brought into contact and thermally cured to obtain bonding. A cross-section of the resulting layer structure is depicted in Figure 4.2. The soft silicone is highly deformable which was needed to allow bringing the top and bottom waveguide layer close enough upon exerting pressure, since the distance between the waveguides needs to be reduced below about 1  $\mu\text{m}$  to achieve coupling (see Section 4.3.1). To test the principle, light was coupled into a waveguide on the bottom layer using an actively aligned multimode fiber at the input of the sample and the output of the sample was monitored using a CCD camera. In the idle state, only a light spot in the input waveguide was seen, but when pressure was applied on the waveguide sample, the light was partly coupled to an output waveguide on the top layer.

Another proof-of-principle demonstrator was constructed to test the optical coupling caused by changing the contact area of 2 crossing waveguides. Similarly as described in the previous paragraph, polymer waveguides on a Sylgard®184 layer were used as a starting point. Instead of applying a soft silicone between 2 such substrates, a perforated thin polyimide foil was used between 2 waveguide layers, see Figure 4.3a. The top and bottom waveguide layers were aligned so that they cross at the location of the openings in the foil. The same testing setup with CCD camera was used to test the principle. When the sample is unloaded, light is only observed in the input waveguide. However, when pressure is exerted on the stack, the waveguides make contact at the crossing point, through the openings in the foil, see Figure 4.3.

These proof-of-principle tests clearly demonstrate the sensing mechanisms but only provide a qualitative evaluation. Therefore, the potential sensor configurations need to be modeled extensively to obtain a more quantitative characterization, which is the topic of the next section. For both phenomena, it has to be noted that coupling between two waveguides is only possible when their crossing angle is smaller than a certain critical value and for example not possible when waveguides are perpendicularly crossing.

## 4.3 Waveguide based sensor architecture design

---

### 4.3.1 Sensor based on evanescent field coupling

When electromagnetic waves are propagating inside a waveguide, the major part of the power is confined in the core whereas a small part of the power is found as an exponentially decaying field component in the cladding immediately surrounding the core. These so called “evanescent tails” can interact with another waveguide core that is closely spaced so that power is coupled between these

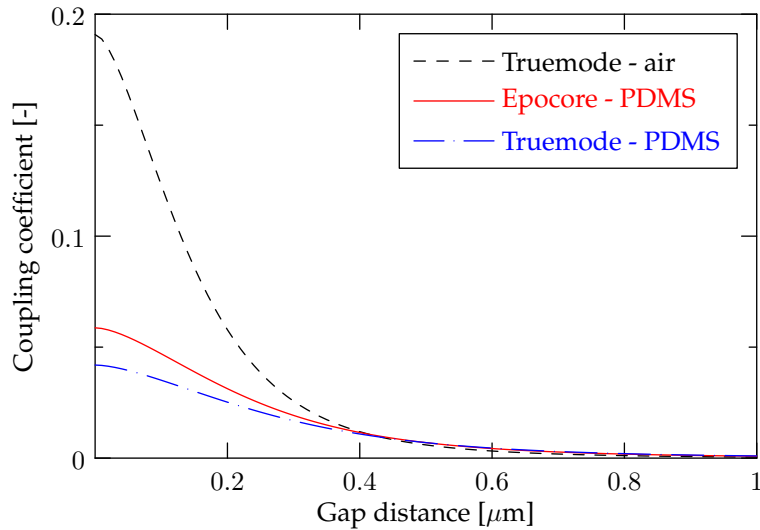


**Figure 4.4** – Coupling coefficient in function of the separation distance for transfer of optical power between Truemode or Epocore waveguides, separated with a PDMS or air gap and crossing under an angle of  $30^\circ$

2 waveguides. This coupling mechanism was extensively studied<sup>1</sup> within the FAOS project and reported in [10]. The main results are briefly described in this section.

The study of the coupling mechanism was simplified by considering transmission of planar waves through a dielectric stack of core-cladding-core material using a one-dimensional transfer matrix approach. This resulted in a general expression for the coupled power in function of the angle of incidence of the planar wave and the thickness of the cladding layer (i.e. separation between the 2 core layers). This general equation was then applied to the specific case of 2 waveguides with a certain separation and crossing under a certain angle. Therefore, the equation was integrated taking into account the dimensions of the waveguides ( $50\ \mu\text{m} \times 50\ \mu\text{m}$ ), their crossing angle and separation and furthermore assuming a large number of modes, evenly distributed in the highly multimodal waveguides.

From this calculations, a “coupling coefficient” was obtained, which is a measure for the fraction of optical power transferred from one waveguide to another. A numerical evaluation of these computations is displayed in Figure 4.4. It shows the coupling coefficient in function of the separation distance for transfer of optical power between Truemode or Epocore waveguides, separated with an air or

<sup>1</sup>The optical modeling was performed at B-Phot, Vrije Universiteit Brussel (VUB).

PDMS filled gap and crossing under an angle of  $30^\circ$ . It is clear that the coupling rapidly decreases with increasing separation distance, which is a direct result of the exponential decline of the evanescent field power in the cladding. A significant coupling is found when the separation is smaller than 500 nm, but at 1  $\mu\text{m}$ , the coupling is reduced below 0.1%. The useful “sensing range”, i.e. the range of distances in which the optical coupling can be modulated, is therefore limited.

Furthermore, it was found to be difficult to fabricate waveguide stacks with such small separation distances so that evanescent coupling could be obtained. In the fabricated proof-of-principle demonstrator shown in Figure 4.2 for example, a highly deformable silicone gel material (Sylgard®527) is used between the waveguides. This material is highly compressible so that the waveguide separation can be reduced below 1  $\mu\text{m}$  while applying pressure. However, it is difficult to apply such materials in a controlled way, meaning that the initial distance between the waveguides cannot be well-defined. Due to these fabrication difficulties, this configuration is not further considered in this chapter and another possible coupling mechanism is studied, as described below. Contrarily, this mechanism relies on the fabrication of accurate mechanical supporting structures so that the separation between the waveguides is highly controllable.

### 4.3.2 Sensor based on coupling through mechanical contact

The second sensing mechanism relies on the changing contact area between 2 initially separated waveguides depending on the pressure [10]. When 2 waveguides are in contact, light can directly propagate from one to another and it is assumed that a larger contact area results in larger coupling. The evanescent coupling is not taken into account here but will not yield a significant contribution once the waveguides are in contact. Controlling the initial spacing between the 2 layers of waveguides was achieved using mechanical support structures or “spacers” defined using lithographic techniques and therefore very accurate. The resulting sensor structure is schematically depicted in Figure 4.5.

To study the operation of the sensor, a theoretical model was constructed. Since it was assumed that the amount of optical power coupled between 2 waveguides depends on the contact area, a purely mechanical simulation was performed to determine this contact area in function of the pressure exerted onto sensor. For these simulation, the actual sensor structure was simplified, and the resulting model is displayed in Figure 4.6<sup>2</sup>. Compared to Figure 4.5, only 2 waveguides from the arrays were modeled for this simulation and the spacers were considered as a complete layer next to the waveguides. The simulation model is therefore mechanically “stiffer” than the fabricated prototype.

The total size of the model was 2 mm  $\times$  2 mm, consisting of five layers: a 0.25 mm

<sup>2</sup>The mechanical modeling was performed at the Katholiek Universiteit Leuven (KUL), Mechanical Department

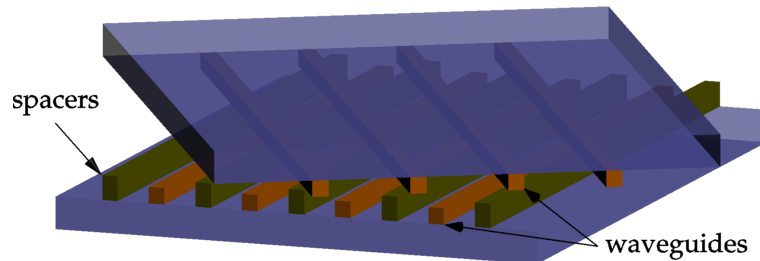


**Figure 4.5** – Schematic representation of the sensor structure based on mechanical contact coupling. Two layers of waveguides patterned on a PDMS substrate are separated by mechanical “spacer” structures and are crossing under an angle.

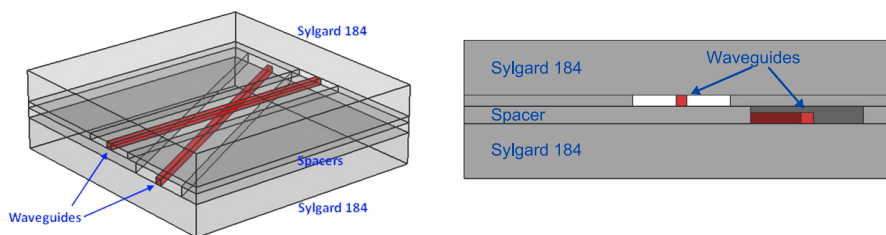


**Figure 4.6** – Simplified geometry adopted for the mechanical simulations. Left: 3D view of the simulation model with 2 waveguides crossing under an angle and separated by an air gap. Right: cross-sectional view of the simulation model.

Sylgard®184 PDMS bottom cladding, a lower waveguide (EpoCore), a spacer layer (Truemode), an upper waveguide (EpoCore) and another 0.25 mm Sylgard®184 top cladding. The two waveguides cross under an angle of  $30^\circ$  and are separated by an air gap of  $30\ \mu\text{m}$ . This was achieved by adding the so-called “spacer layer” with a  $80\ \mu\text{m}$  thickness to provide a mechanical support and spacing between the 2 waveguides.

Two types of optical polymers, EpoCore and Truemode, were used for the fabrication and since these materials are significantly stiffer than PDMS used for the cladding, they were both assigned the material properties of Truemode (Young’s Modulus  $E$  179 MPa, Poisson’s ratio  $\nu$  0.4). The Young’s modulus of PDMS was considered to be 2.37 MPa [11] and the Poisson’s ratio 0.48.

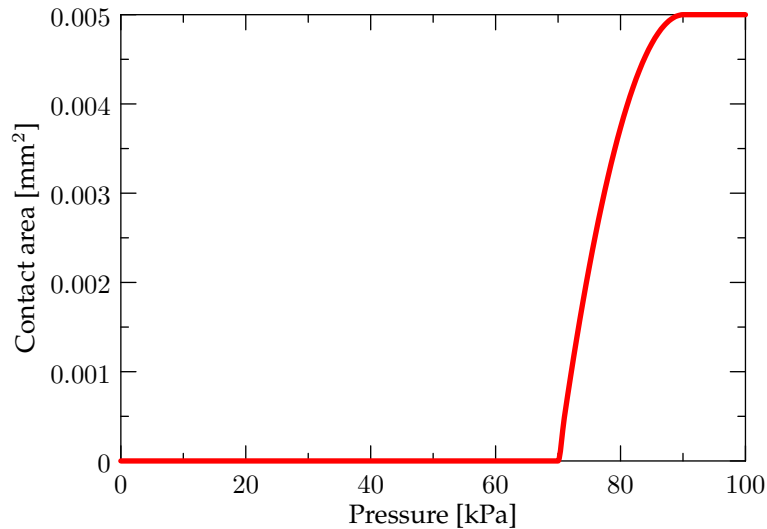


**Figure 4.7** – Result of the mechanical simulation: after a certain threshold pressure is exerted on the sensor, the waveguides are in contact and the contact area increases rapidly with increasing pressure.

An increasing, uniform pressure was applied on the top surface and the resulting change in contact area between the 2 waveguides was determined using finite element simulations in Comsol Multiphysics. The result of this simulation is shown in Figure 4.7 for a spacer height of 80  $\mu\text{m}$  and a waveguide pitch of 500  $\mu\text{m}$ . It can be seen that the waveguides come in contact at a threshold value of about 70 kPa and when the pressure increases, the contact area increases until the maximum contact area is reached at 90 kPa. Therefore, the useful sensing range is between 70 and 90 kPa and within this range, the contact area varies rapidly. Furthermore, the height and pitch of the spacers were varied resulting in similar, but shifted response curves.

It can therefore be concluded that the sensor exhibits an “on/off”, or so-called digital behavior since contact occurs above a certain threshold pressure, and for values of pressure above this threshold, the contact area increases rapidly to the maximum value. This threshold value is shifted to higher pressure values when the spacer height is increased and/or when the waveguide pitch is decreased. In the next section, this digital sensor behavior is verified by performing functional measurements on fabricated prototypes.

## 4.4 Technology platform for waveguide sensors

### 4.4.1 Polymer waveguides on deformable substrates

To fabricate the sensor architecture as simulated in the previous section, deformable waveguides are required in order to modulate the optical coupling depending on deformation caused by pressure. When fabricating polymer waveguide stacks based on the commercially available optical materials such as Truemode, LightLink and EpoCore/Clad, the waveguide core is typically patterned on a layer of cladding material and subsequently covered with another layer of cladding material. This standard process exhibits certain problems when it is to be used for constructing waveguide sensors requiring deformable waveguide substrates. Firstly, such waveguide stacks are fabricated on a rigid substrate, for example FR-4 or a silicon wafer and it is difficult to release the cladding-waveguide-cladding stack afterward which is required for constructing the sensor. However, with appropriate release techniques, releasing seemed possible but rather inconvenient. Secondly, once released, the stack is not very flexible and quite brittle due to the cladding material properties.

Nevertheless, the waveguide cores themselves are somewhat flexible owing to their small size (cross-section  $50\ \mu\text{m} \times 50\ \mu\text{m}$ ). Therefore, deformable waveguide substrates were obtained by combining traditional optical polymer and PDMS fabrication technologies. Waveguide cores were patterned using the traditional optical materials, but instead of the standard cladding materials, PDMS was used serving as both cladding and substrate. This results in very flexible substrates with waveguides. As an alternative, waveguides fabricated completely using PDMS were investigated. Both technologies are described in Chapter 3 and the technology for constructing optical polymer waveguides embedded in PDMS serves as a basis for fabricating the sensors as described in this chapter.

### 4.4.2 Fabrication of mechanical support structures

As explored in Section 4.3.2, both deformable waveguides and mechanical support structures are needed to implement the sensor architecture. The process flow for fabricating these support structures was derived from the process used to pattern polymer waveguides on PDMS, as described in Section 3.2. An extra lithographically patterned layer was added to obtain structures with different heights, as explained in Figure 4.8. After illuminating the waveguide layer through a mask (d), the unexposed material was not removed using a developer but instead, a second "spacer" layer was immediately spin-coated (e) and illuminated through another mask (f). Finally, the material that was not exposed during both the first (d) and the second (f) UV-illumination step, was removed (g) using a solvent developer. This process was implemented using EpoCore for

**Table 4.1** – Process parameters for fabricating  $50\ \mu\text{m} \times 50\ \mu\text{m}$  “hybrid” waveguides with EpoCore as core material and Truemode for the spacer structures (2 layer lithographic process). All process steps are performed on a sacrificial glass substrate.

Step #	Description	Parameters
(0)	Spin PVA solution Evaporate water <i>(Step (0) is not shown in Figure 4.8)</i>	60 s at 1000 rpm 5' at 100 °C on a hotplate
(a)	Spin Sylgard®184 Cure step 1 Cure step 2	60 s at 250 rpm 24 h at 21 °C on leveled surface 60 min at 60 °C on a hotplate
(b)	Plasma treatment	Diener pico device, gas used: air 0.8 mbar, 24 s, 190 W 40 kHz generator
(c)	Dispense Epocore Spin-coat Epocore Remove edge bead Soft bake Epocore	using pipette 60 s at 1800 rpm manually with glass substrate 50 min at 85 °C on a hotplate
(d)	UV-exposure (mask 1)	20 s @10 mW cm <sup>-2</sup>
(e)	Dispense Truemode Dry Film Core Spin-coat Truemode Remove edge bead Soft bake Truemode	using pipette 60 s at 1000 rpm manually with glass substrate 2 min at 95 °C on a hotplate then 10 min at 110 °C on a hotplate
(f)	UV-exposure (mask 2) Post bake Truemode	50 s @10 mW cm <sup>-2</sup> 2 min at 110 °C on a hotplate then 10 min at 125 °C on a hotplate
(g)	Development	5 min in Mr.Dev 600 developer rinse 30 s in fresh developer rinse 30 s in IPA rinse 30 s in fresh IPA
(h)	Hard bake	90 min at 120 °C in convection oven
(i)	Dissolve PVA to release PDMS <i>(Step (h) and (i) are not shown in Figure 4.8)</i>	immerse in DI water (1 h)

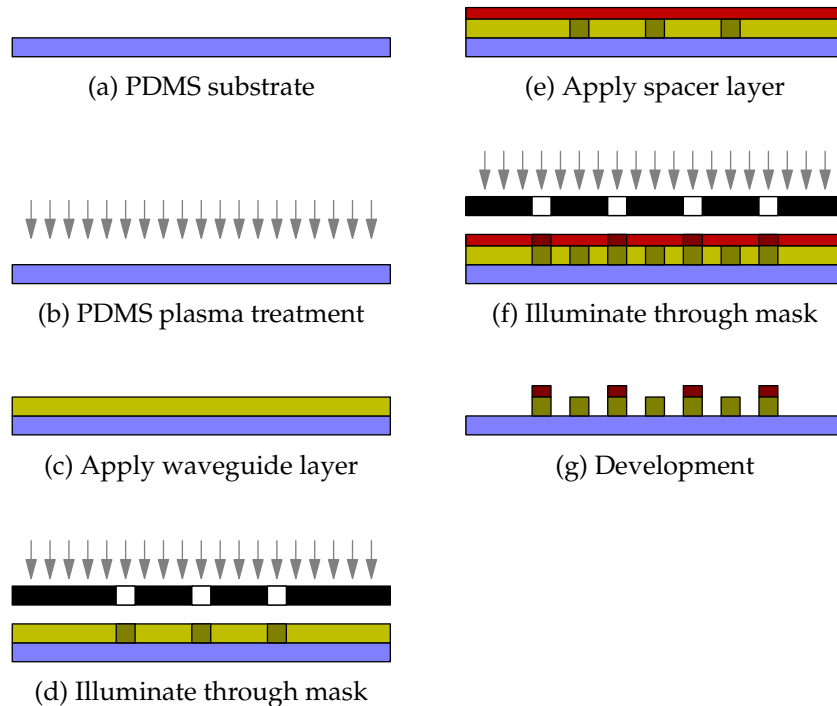


**Figure 4.8** – Schematically illustrated process flow for fabricating waveguides and support structures or “spacers” on a layer of PDMS.

the waveguides and Truemode for the spacer structures and the corresponding simplified process flow is listed in Table 4.1.

It has to be mentioned that an intermediate layer of EpoCore can be applied after patterning the EpoCore waveguide layer and before coating the Truemode layer for the spacers. This extra EpoCore layer is then part of the spacer structures so that higher structures can be achieved. Furthermore, this extra layer facilitates the processing since it acts as a compatibility layer between the EpoCore core layer and the Truemode layer. Without the use of this layer, it was sometimes observed that Truemode residue was left on the EpoCore waveguides after developing, probably due to slight intermixing of both layers during the baking steps. With this extra EpoCore layer, this intermixing is eliminated since the exposed EpoCore waveguides are not in direct contact with the Truemode material.

The appropriate polymer materials (EpoCore for the waveguides and Truemode (Dry Film core) for the spacers) were selected based on their respective refractive indexes. As can be noticed from Figure 4.5, the upper layer of waveguides will permanently be in contact with the spacer structures. In that case, the spacers

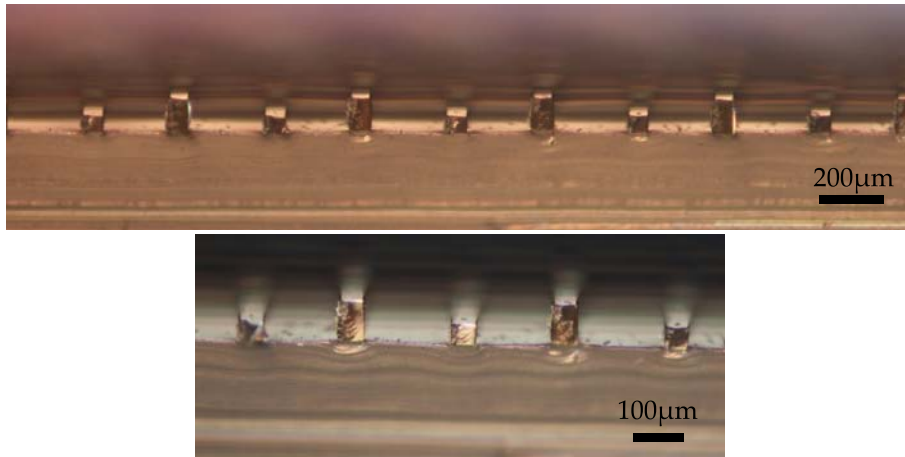


**Figure 4.9** – A microscopic view of the cross-section of a substrate with waveguides and spacer structures.



**Figure 4.10** – Light stays confined and is not escaping into the top part of the spacer owing to its lower refractive index.

need to have a lower refractive index than the waveguides to avoid unintended coupling from these waveguides to the spacers.

EpoClad, with a lower refractive index and usually combined with EpoCore to pattern waveguide stacks, would be a good candidate to use for these spacers regarding refractive index requirements but this material is difficult to pattern using contact lithography due to its tendency to remain sticky after soft bake. Truemode on the other hand comes in 2 varieties, Truemode Dry Film and Wet Film. The Wet Film remains sticky after soft baking and is again not suited for traditional contact lithography. However, only the Dry Film Core and Wet Film cladding material were available and therefore, the Dry film core was selected for patterning the spacers. Although this is the “core”-version of Truemode, it still shows a lower refractive index than the EpoCore material (about 1.54 versus 1.58 @850 nm respectively).

Another optical polymer that was considered, LightLink, was not suited due to

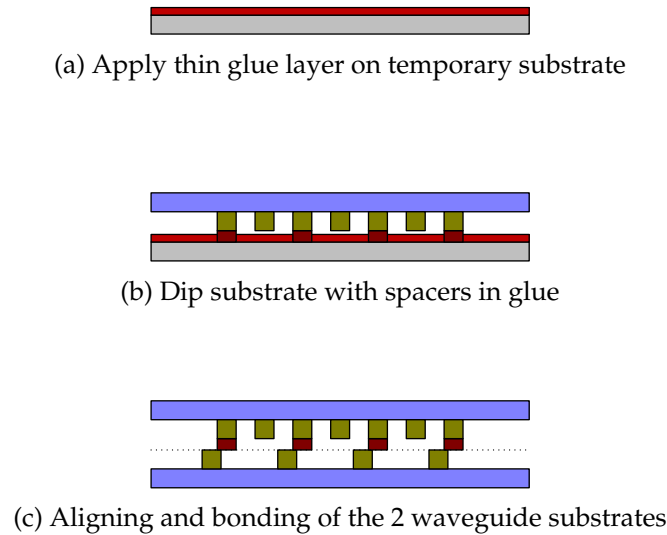


Figure 4.11 – Process flow for micro-bonding 2 waveguide samples.

process incompatibilities since the Mr.Dev 600 developer for EpoCore attacks the LightLink structures. Truemode and EpoCore on the other hand, were found to be process compatible and rely on the same developer.

A microscopic view of the cross-section of a substrate with waveguides and spacer structures is shown in Figure 4.9. On this picture, it is difficult to distinguish between the waveguide and spacer material, however, Figure 4.10 shows the result of an experiment illustrating the lower refractive index of the spacer structures. Light was coupled from 1 side in the “waveguide” under the spacer structures and the other side was observed using a CCD camera. As expected, the light stays confined and is not escaping into the spacer material owing to its lower refractive index.

#### 4.4.3 Micro-bonding techniques

To obtain the proposed sensor, an upper waveguide layer needs to be positioned on a lower spacer layer as illustrated in Figure 4.5. Joining these 2 substrates with waveguides and spacers requires special care. If these layers are not bonded, they can shift which may introduce unwanted behavior. Therefore a “micro-bonding” technique was developed to achieve local fixation between a spacer structure and a corresponding crossing waveguide from the upper layer. This process is illustrated in Figure 4.11.

First, a thin glue layer of about  $10\ \mu\text{m}$  was spin-coated on a temporary glass sub-

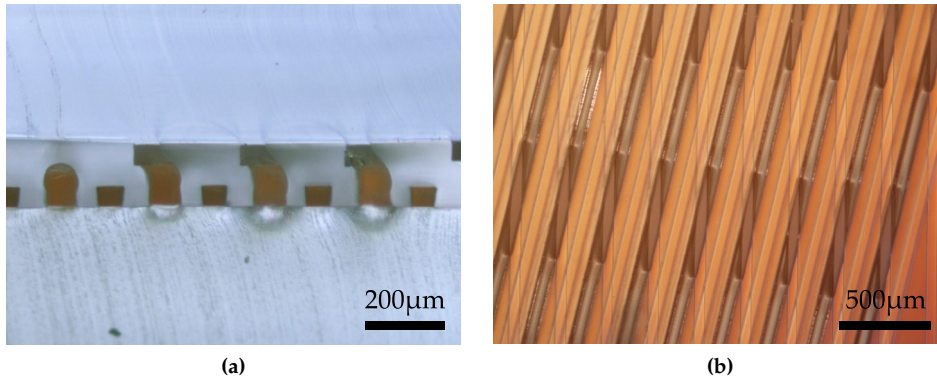


**Figure 4.12** – Result of joining the 2 waveguide layers. (a) Cross-section of top waveguides bonded to spacers. (b) Top view of the 2 layers crossing under an angle. The dark crossing points are locations where top waveguides and spacers are bonded while on the clear crossing points a lower and upper waveguide is crossing.

strate. The same material as the spacer layer, Truemode, was chosen for this purpose because of its low viscosity and UV-curability. Then, the substrate with the spacers was dipped in this layer to transfer a thin layer of glue only onto the spacer structures. Subsequently, the spacer substrate was aligned with another substrate containing only waveguides so that the waveguides on both substrates were crossing under an angle. Therefore, a modified aligner setup was used as described in Section 5.5.2. Once aligned, both substrates were brought in contact and the glue was finally hardened using UV-illumination.

A cross-section and top view of such a final two-layered waveguide stack with mechanical support structures is depicted in Figure 4.12. From the top view it can be seen that waveguides are crossing under a certain angle and the cross-section illustrates that spacers from the lower substrate are bonded with waveguides from the upper substrate resulting in 2 layers of waveguide arrays that are vertically separated by a certain distance.

## 4.5 Functional testing of the fabricated prototype

The sensor was tested and evaluated within the FAOS project [9] and the main results are briefly described in this section. Therefore, a setup was constructed for simultaneous optical and mechanical characterization. The waveguide sample was positioned on a platform while fibers were actively aligned to couple light to the input waveguides and capture light from the output waveguides. A well-defined pressure was applied using a pressing tip with force sensor mounted on

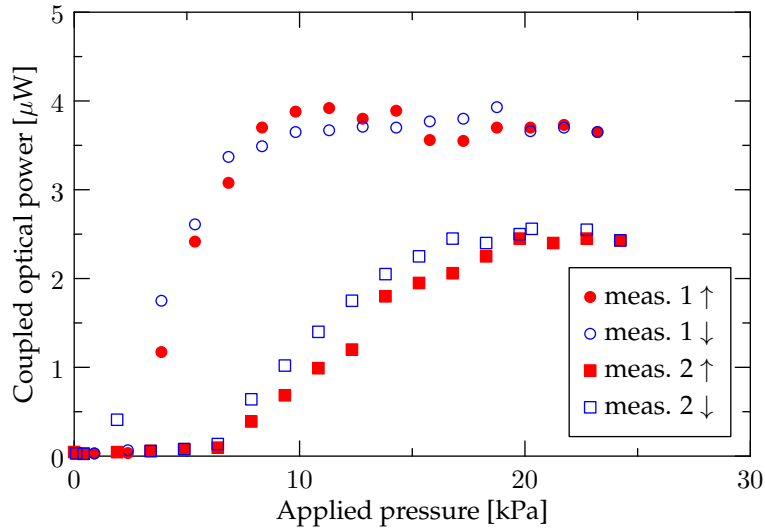


**Figure 4.13** – Coupled optical power in function of applied pressure (increasing  $\uparrow$  and decreasing  $\downarrow$  pressure). For the second measurement, the tip was realigned to test repeatability.

an adjustable mechanical post. At the input and output waveguides, a 50  $\mu\text{m}$  and 100  $\mu\text{m}$  multimode fiber was used, with numerical aperture 0.2 and 0.29 respectively.

The digital behavior of the sensor was tested by increasing the pressure on a certain crossing point of 2 waveguides and recording the corresponding coupled optical power in the output waveguide. Figure 4.13 shows the result of 2 subsequent measurements using 2 mW input power (635 nm wavelength). After the first measurement, the tip was removed and realigned on the same crossing point to evaluate the repeatability of the measurement. As predicted by the simulations described in Section 4.3.2, the coupled power is zero for low pressures and increases rapidly with increasing pressure until full contact of the waveguides is reached and the power coupled to the output waveguides saturates. This results in a non-linear, even digital behavior: the output of the sensor is either zero or the maximum value for pressures lower or higher than a certain threshold pressure. The value of the threshold pressure was found to be lower than simulated which may possibly be attributed to the higher stiffness of the simulation model (a complete spacer layer was used) and the lower PDMS Young's modulus of the fabricated sample. The value of this threshold was found to vary considerably and randomly depending on the exact location of the pressing tip. In addition to the influence of the pressing tip alignment, it is also believed that

the specific way how the waveguides are in contact and deformed may influence the measured characteristics.

After repeated measurements, similar conclusions were found, illustrating the digital behavior as predicted by the simulations. This means that the device is not ideally suited for tactile sensing and therefore it was not further characterized for this purpose. Moreover, this sensor concept is only suited to detect pressure and not for measuring shear stresses.

Nevertheless, from this waveguide sensor demonstrator, much was learned about the coupling mechanism between 2 crossing waveguides and there are numerous other applications that could benefit from this sensor concept. Furthermore, the technology platform established for fabricating the sensor is also available for other purposes. It was found that this technology is less suited for movable or wearable applications (such as tactile sensors) due to the fragility of the waveguides in the stretchable PDMS material and the air gap construction between the 2 waveguide layers. Nevertheless, for stationary or low strain range applications such as microfluidics, the technology could certainly prove to be useful since most of the microfluidic channels are fabricated using PDMS and integrated optical sensing techniques (e.g. employing waveguides) are now increasingly being used.

## 4.6 Conclusions

---

The incentive for using waveguides is that they allow for constructing fully optical sensors without needing electrical signals. In this chapter, waveguide based tactile sensors as reported in literature were evaluated and the feasibility of a proposed new concept was investigated. The main drawback of waveguide based sensors is the need for coupling them to separate light sources and detectors for driving and read-out of the sensors, a challenge that is currently only limitedly tackled.

Sensors based on Bragg gratings in polymer waveguides could provide a very sensitive solution, but this technology is still under development. Most of the other waveguide tactile sensor approaches are based on intensity variations in waveguides caused by bending or light out-coupling. However, such a configuration requires a light source at the input and a detector at the output of every waveguide. Using the concept proposed in this chapter, only the input waveguides require a light source and the output waveguides need a detector, reducing the amount of components by a factor of 2. Therefore, light transfer is considered between 2 crossing waveguides instead of measuring losses in one waveguide. Two different approaches were simulated but showed a non-ideal, "on/off" response. These results were also confirmed by functional tests on fabricated prototypes.

*Critical Discussion.* It can be concluded that the proposed coupling mechanism needs to be improved if used for tactile sensing. Ideally, a linearly increasing signal in function of the applied pressure is desired, but with the current system, a non-linear “on/off”-behavior was obtained. Nevertheless, the design could be useful for other applications requiring an “on/off”-behavior and the established technology platform for the fabrication of flexible polymer waveguides combined with PDMS is available for incorporating in other microsystems such as PDMS microfluidics with optical sensing capabilities.

## References

- [1] G. D. Marshall, M. Ams, and M. J. Withford, “Direct laser written waveguide-bragg gratings in bulk fused silica,” *Opt. Lett.*, vol. 31, no. 18, pp. 2690–2691, Sep 2006. [Online]. Available: <http://ol.osa.org/abstract.cfm?URI=ol-31-18-2690>
- [2] K.-J. Kim and M.-C. Oh, “Flexible bragg reflection waveguide devices fabricated by post-lift-off process,” *Photonics Technology Letters, IEEE*, vol. 20, no. 4, pp. 288–290, feb.15, 2008.
- [3] X. Dai, S. J. Mihailov, and C. Blanchetiere, “Optical evanescent field waveguide bragg grating pressure sensor,” *Opt. Eng.*, vol. 49, no. 2, p. 024401, 2010. [Online]. Available: <http://dx.doi.org/doi/10.1117/1.3319819>
- [4] Y. Ichihashi, P. Henzi, M. Bruendel, J. Mohr, and D. G. Rabus, “Polymer waveguides from alicyclic methacrylate copolymer fabricated by deep-uv exposure,” *Opt. Lett.*, vol. 32, no. 4, pp. 379–381, Feb 2007. [Online]. Available: <http://ol.osa.org/abstract.cfm?URI=ol-32-4-379>
- [5] E. Kim, S. Y. Cho, D.-M. Yeu, and S.-Y. Shin, “Low optical loss perfluorinated methacrylates for a single-mode polymer waveguide,” *Chemistry of Materials*, vol. 17, no. 5, pp. 962–966, 2005. [Online]. Available: <http://pubs.acs.org/doi/abs/10.1021/cm049933a>
- [6] C. Wagner, J. Frankenberger, and P. Deimel, “Optical pressure sensor based on a mach-zehnder interferometer integrated with a lateral a-si:h p-i-n photodiode,” *Photonics Technology Letters, IEEE*, vol. 5, no. 10, pp. 1257–1259, oct 1993.
- [7] W. Wei-Chih, W. Ledoux, H. Chu-Yu, H. Cheng-Sheng, G. Klute, and P. Reinhall, “Development of a microfabricated optical bend loss sensor for distributive pressure measurement,” *Biomedical Engineering, IEEE Transactions on*, vol. 55, no. 2, pp. 614–625, feb. 2008.

- [8] M.-C. Oh, J.-W. Kim, K.-J. Kim, and S.-S. Lee, "Optical pressure sensors based on vertical directional coupling with flexible polymer waveguides," *Photonics Technology Letters, IEEE*, vol. 21, no. 8, pp. 501–503, april15, 2009.
- [9] FAOS Consortium. (2007) Flexible Artificial Optical Skin (FAOS). [Online]. Available: <http://intecweb.intec.ugent.be/faos/>
- [10] J. Missinne, G. V. Steenberge, B. V. Hoe, E. Bosman, C. Debaes, J. V. Erps, C. Yan, E. Ferraris, P. V. Daele, J. Vanfleteren, H. Thienpont, and D. Reynaerts, "High density optical pressure sensor foil based on arrays of crossing flexible waveguides," H. Thienpont, P. V. Daele, J. Mohr, and H. Zappe, Eds., vol. 7716, no. 1. SPIE, 2010, p. 77161G. [Online]. Available: <http://link.aip.org/link/?PSI/7716/77161G/1>
- [11] N. Galler, H. Ditlbacher, B. Steinberger, A. Hohenau, M. Dansachmuller, F. Camacho-Gonzales, S. Bauer, J. Krenn, A. Leitner, and F. Aussenegg, "Electrically actuated elastomers for electrooptical modulators," *Applied Physics B: Lasers and Optics*, vol. 85, pp. 7–10, 2006, 10.1007/s00340-006-2434-4. [Online]. Available: <http://dx.doi.org/10.1007/s00340-006-2434-4>



# 5

## Optoelectronics based sensing: a tactile shear sensor

*Whereas the previous chapter discussed waveguide based pressure sensors, this chapter focusses on the development of optoelectronic sensors. Therefore, light sources and detectors are not used to interface with waveguides, but instead a physical quantity is detected directly using these components. The technology for embedding optoelectronics in very thin flexible foils is applied and evaluated by constructing a tactile sensor sensitive to shear stress variations. A first generation sensor demonstrates the concept, while a second and third generation extend this concept towards a 2-dimensional sensor.*

### **5.1 Introduction**

---

In the previous chapter, the focus was on tactile pressure sensors. However, for the targeted “tactile sensing” applications, shear sensors are also extremely important as described in Chapter 1. For example in prosthetics, they enable measuring the interfacial friction stresses between the amputee’s stump and the prosthetic socket, while in robotics they are indispensable for slip detection to optimize grasping mechanisms. Additionally, Hayward et al. are investigating shear force tactile displays [1] as a means to represent tactile information. Suitable shear stress sensors can therefore be very useful in this research since lateral stretching of the skin is investigated in these displays.

Compared to most types of sensors, tactile sensors demand special requirements since they are used on moving or curved surfaces and may undergo large deformations. Therefore, these sensors need to be thin and flexible or ideally stretchable comparable to the human skin. Furthermore, a certain sensitivity and dynamic range (i.e. the measurement range in which the sensor can produce adequate results) is required and the sensing area should be small so that high-density sensing matrices can be constructed.

For use in prostheses, an optical sensing principle is desirable to eliminate electromagnetic interference that may occur for example when the human body interacts with a capacitive sensor. Furthermore, the sensor needs to be very thin, small, easy to read-out and low-cost. A possible solution could be the use of fiber Bragg grating sensors for this purpose, which cost about 50 EUR each. Although the required read-out unit is rather expensive, the price of a complete setup is comparable to a system using strain gauges. However, Bragg grating sensors fabricated in silica optical fibers are rather fragile and therefore vulnerable in highly dynamic environments when no special mechanical protection is provided. They can therefore be embedded in host materials, such as PDMS, which is an ideally suited material for artificial tactile sensing skins. Unfortunately, the low mechanical modulus of PDMS makes it less compatible with the much harder silica fibers. However, currently work is being performed on fabricating Bragg gratings in polymer optical fibers and embedding these fibers in flexible host materials [2]. Such "plastic" fibers are not brittle, highly flexible but the Bragg grating efficiency still needs to be improved to become a truly alternative to gratings in silica fibers. Furthermore, fiber Bragg gratings are only sensitive to stresses along their axis therefore have to be placed under an angle to measure shear stresses [3, 4], which may complicate the integration process.

To address these challenges, this chapter focuses on using low-cost optoelectronic components for constructing a shear stress sensor. These optoelectronic components are also fragile, but can easily be incorporated in very thin, strong polymer foils and consequently be used to create a sensor, as demonstrated in this chapter. On the other hand, a disadvantage of this technology is that every sensor requires 3 electrical connections. When using a large amount of sensors, the number of connections may become a problem. However, similarly as is used in displays, the sensors can be addressed in a "scanning" matrix to limit the number of interconnections.

## 5.2 Optical sensor principle

---

The sensor operation principle is based on the changing optical power captured by a detector when its relative lateral position to a light source varies. When the light source and detector are perfectly aligned, the detected optical power is

maximum. However, when the light source and detector are increasingly misaligned, the optical power incident to the detector decreases. This is actually an implementation of a displacement sensor. However, shear stresses introduce displacements in materials meaning that a transducer material applied between the light source and detector can be used to convert the mechanical shear stress into displacement. Therefore, the response of the sensor to displacements and to shear stresses are both considered in this chapter, depending on which parameter is most relevant.

### 5.2.1 Selecting a transducer material

The choice of this transducer material determines the sensor response to an applied shear stress. Furthermore, this material needs to be transparent to the light emitted by the source. To measure high stresses, which is for example required in structural mechanics, a “hard” material with a high shear modulus can be used. However, for medical applications and several types of tactile sensors, the shear stresses that occur are limited as described in Chapter 1. Therefore, a soft PDMS (Sylgard®184) transducer material was chosen. Using such a soft material, the sensor dynamic range with respect to shear stress is limited, but correspondingly the sensitivity can be high.

The precise shear modulus of PDMS highly depends on the processing conditions and can easily vary several hundreds of kPa. In literature, a shear modulus value of 250 kPa is found [5], while own experiments indicated a shear modulus of about 400 kPa, see Chapter 2.

### 5.2.2 Implementation of the sensor principle

The presented shear sensor principle can be applied in several ways. The main differences involve the implementation of the actual light source and detector. A physical light source and detector can be used (see Figure 5.1a), but alternatively, an excited fiber or waveguide can be used as light source and another waveguide can be used to capture the light (see Figure 5.1b). Such a fiber optic or waveguide based sensor construction offers several interesting advantages. Firstly, such a type of sensor would be fully optical, meaning that no electrical connections to the sensing point are required; the waveguides can be made long enough so that the active components are placed outside of the sensitive area. This may be extremely useful for sensing applications where electrical signals and the resulting electromagnetic fields are prohibited, for example in radiative environments or for certain biomedical applications. Secondly, several sensing points could be multiplexed, i.e. one actual light source or detector can be connected to a series of waveguides. In such a way, a matrix of sensing points could be implemented using only a limited amount of light sources and detectors. Finally, waveguides

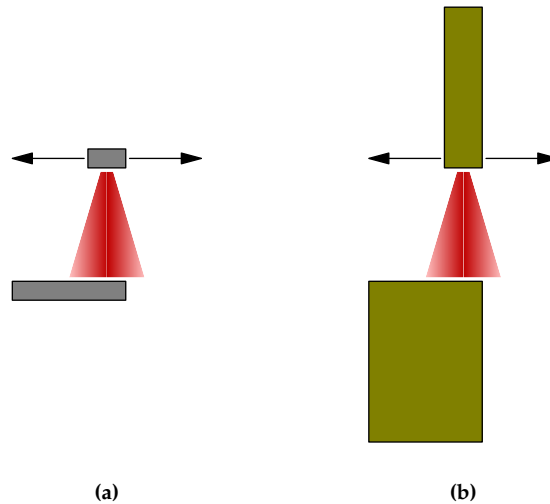


**Figure 5.1** – Schematic representation of different implementations of the shear sensor “light emitter” and “detector”, (a) using a physical light source and detector directly or (b) using a “source” and “detector” waveguide.

can be made very small and therefore a high density of sensing points could be obtained.

Despite these advantages, the implementation becomes more complex since not only the sensor principle itself, but also the waveguiding phenomena need to be taken into account when designing the sensor. Therefore, the process significantly facilitates using optoelectronic light sources and detectors directly. In that case the sensor principle is still optical, but electrical signals have to be provided in order to operate the optoelectronic components. The type of light source and detector determine the sensor operation and characteristics. It can be expected that using a VCSEL with a confined beam yields a very accurate sensor. Contrarily, an LED for example yields a less accurate sensor and since the emitted light beam is broader, a larger detector is needed. However, this may be desired when a sensor with a larger displacement dynamic range is required. These design related considerations are explored in Section 5.3.

### 5.2.3 Ultra-thin flexible shear sensor

The focus of this work was on realizing an easy-to-fabricate miniaturized sensor with the highest possible accuracy, so that it can be made flexible and a high sensor density can be obtained if needed. Therefore, optoelectronic components were used directly and miniature VCSELs were selected as light sources and pho-

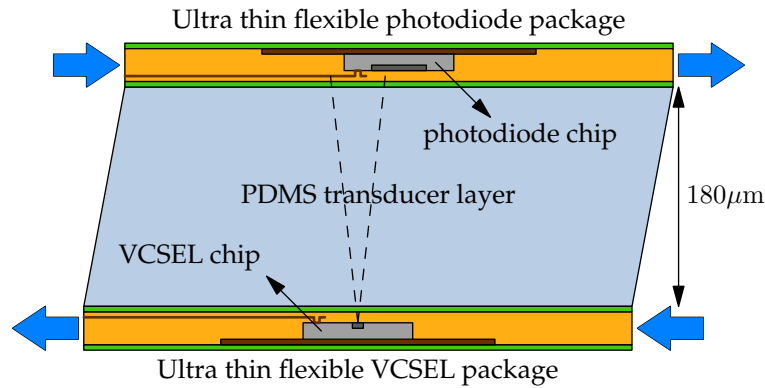


**Figure 5.2** – The principle of the optical shear sensor relies on the changing optical coupling between a light source and a detector depending on the lateral displacement, and hence the shear stress.

todiodes as detectors.

For the projected medical applications, mechanically flexible and thin sensors without protrusions (that could irritate the skin) are required. Typically, (opto)electronics are supplied as packaged components. However, such packaged components are too bulky to be used for a thin and flexible sensor and are certainly not flexible. Therefore, very small active components in bare die form were selected for this purpose. An embedding technology was developed at the Centre for Microsystems Technology within the framework of the PhD of Erwin Bosman [6]. This technique allows to embed optoelectronic chips in very thin flexible polymer layers (down to  $40\ \mu\text{m}$  thin). Therefore, commercially available optoelectronic chips were thinned down to  $20\ \mu\text{m}$  so that they are flexible themselves, making this technology perfectly suitable for constructing the shear sensor. The shear sensor architecture is schematically depicted in Figure 5.2: a photodiode and a VCSEL chip were embedded in a thin polymer packaging foil and separated by the PDMS transducer layer. The total thickness of the sensor is in the order of  $250\ \mu\text{m}$ , depending on the transducer layer thickness, as obtained from the simulations described below. The fabrication of the sensor is described in Section 5.5.

### 5.3 Optical sensor architecture design

Modeling the optical shear sensor can be decomposed into 2 separate parts. In the first set of simulations, the changing optical coupling following a lateral displacement of the light source and detector is determined (“optical behavior”). In

the second set of simulations, the mechanical behavior of the transducer layer is investigated. This links the actual applied shear stress to the relative lateral displacement of the optoelectronic components. This section describes the optical behavior of the sensor, while the next section describes the mechanical behavior.

An analytical model was constructed to predict the optical sensor characteristics. The specific characteristics of the used light source and detector are needed as an input for this model. A 1x4 multimode VCSEL array chip from Ulm-Photonics [7] was used as light source and a 1x4 photodiode array (circular active area;  $\varnothing 100 \mu\text{m}$ ) chip from Enablence as detector [8]. The actual characteristics of these components are detailed in the next chapter, while in this chapter some simplifications were adopted to construct the analytical model.

The photodiode sensitivity was assumed to be uniform and independent of the angle of incidence. This assumption is valid since the incident light originating from the VCSEL beam is very directional and does not diverge significantly from perpendicular incidence.

The VCSEL beam was considered Gaussian with a certain half power divergence angle that was defined as the single sided angle wherein 50% of the optical power is confined. Although this assumption is not completely valid since multimode VCSELs were used for the fabrication of the sensor, it yields an adequate approximation. Furthermore, the divergence angle depends on the driving current and hence the total optical power emitted. The divergence angles and total optical power for different VCSEL driving currents were determined (see next chapter) and taken into account in the simulation model.

To construct an optimum shear sensor, several design parameters need to be selected. Most important is the distance  $d$  between VCSEL and photodiode, determining the thickness of the transducer layer. Another parameter is the VCSEL driving current, and a last parameter is the relative initial misalignment of the VCSEL and photodiode.

The principle of the sensor is based on the relative lateral movement of the VCSEL and photodiode. The general, two dimensional sensor response  $\Psi(x, y)$  for any relative displacement in  $x$ - and  $y$ -direction can therefore be determined by calculating the amount of optical power incident to the photodiode for the specific displacement  $(x, y)$ . For example,  $\Psi(0, 0)$  is the response corresponding with zero relative lateral displacement and a perfect alignment of the VCSEL beam and detector above each other. The response to this lateral movement can be mathematically considered as the convolution of a uniform circular detector area  $PD(x, y)$  with the Gaussian VCSEL beam profile  $\Phi_d(x, y)$  considered at the specified distance  $d$  from the detector, meaning that the general sensor response can be calculated as:

$$\Psi(x, y) = (\Phi_d * PD)(x, y) = \int \int \Phi_d(x', y') PD(x - x', y - y') dx' dy' \quad (5.1)$$

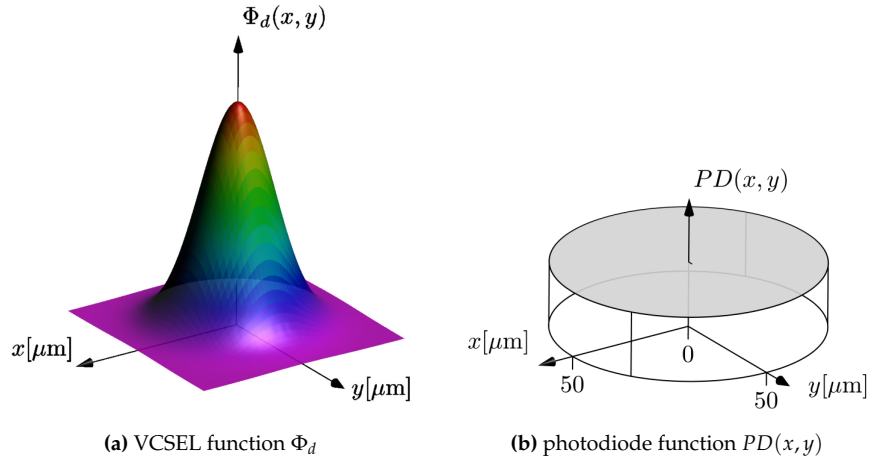


**Figure 5.3** – An example of the 2-dimensional functions  $\Phi_d$  and  $PD(x, y)$  (for an arbitrarily chosen  $d$  and  $\phi$ )

The beam profile  $\Phi_d(x, y)$  is depending on the separation distance  $d$  between the VCSEL and detector since this beam is diverging, determined by a specific divergence angle  $\phi$  (typically 3 - 10° (single sided)). For a given  $\phi$ , the beam profile function  $\Phi_d(x, y)$  is therefore narrow for small  $d$  and broader for larger  $d$ . Since the enclosed volume represents the optical power (being identical for every  $d$ ), the maximum function value is higher for smaller  $d$  and lower for larger  $d$ .

The detector function  $PD(x, y)$  is zero for every  $x, y$  outside the detector active area and evaluates in a constant for every  $x, y$  located inside the detector active area (in this case a circle with 50  $\mu\text{m}$  radius).

An example of the 2-dimensional functions  $PD(x, y)$  and  $\Phi_d$  (for an arbitrarily chosen  $d$  and  $\phi$ ) are shown in Figure 5.3.

Typically, the sensor response for one particular direction of movement is required, which can be obtained by evaluating equation 5.1 along a line in the  $(x, y)$ -plane. In the following sections, the response along the  $x$ -direction will be considered, if not mentioned otherwise, and noted as  $\Psi(x, 0) = \Psi(x)$ . The calculations yielding the sensor response were evaluated numerically using Matlab.

### 5.3.1 One dimensional shear sensor architecture

#### Influence of vertical VCSEL-to-photodiode distance

The influence of the distance between the VCSEL and photodiode can be determined by varying parameter  $d$  in equation 5.1. The sensor response  $\Psi(x)$  (i.e. the

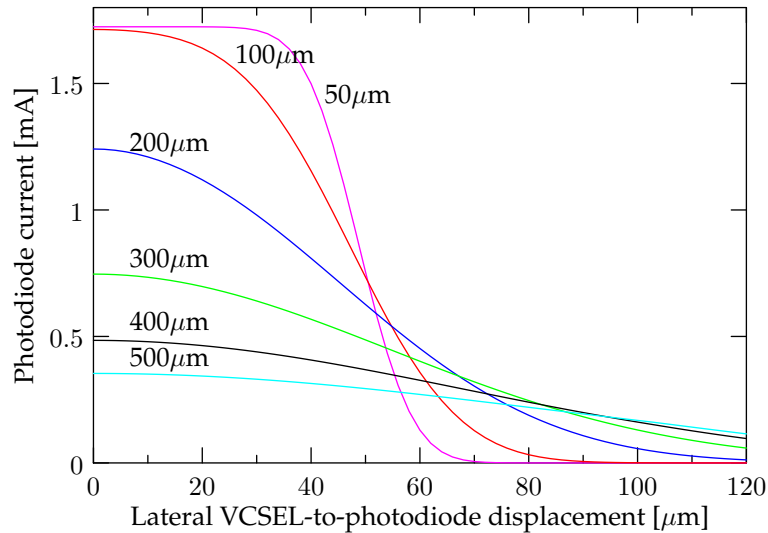


**Figure 5.4** – Simulation showing the influence of the vertical VCSEL-to-photodiode distance on the sensor characteristics.

photocurrent from the photodiode) was calculated for different values of  $d$  ( 50, 100, 200, 300, 400 and 500  $\mu\text{m}$ ) and the result is plotted in Figure 5.4. For these simulations, a typical VCSEL driving current of 5 mA was chosen.

Since the beam diverges, the response will be spread out more when the VCSEL and detector are separated further away. When the distance between source and detector is too small, the laser beam is relatively confined and almost all optical power is captured by the detector when aligned and none is captured when misaligned. In the transition region there is a steep response. It seems that the response improves (in terms of linearity and sensor dynamic range) for higher values of  $d$ . However, the sensitivity is lower, meaning that the sensor reading will be less accurate. Furthermore, the analytical model is based on an ideal Gaussian VCSEL beam behavior. The used light source for constructing the sensor was a multimode VCSEL, meaning that the actual beam is not purely Gaussian, but more irregularly shaped. These effects are averaged out in the sensor response since the optical power is integrated over the complete detector surface, provided that the beam divergence, and hence the distance  $d$  to the detector is limited (see Section 6.2.4).

Therefore, a separation of  $d = 200 \mu\text{m}$  was chosen as a good compromise between sensitivity and dynamic range in terms of displacement.

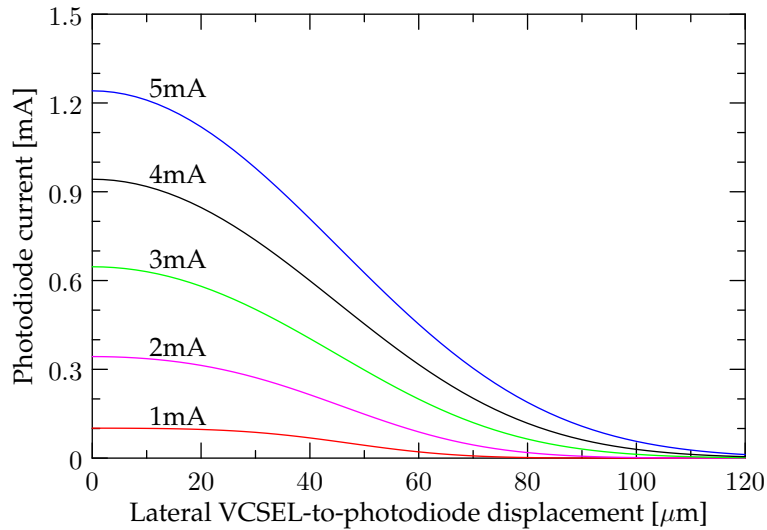


**Figure 5.5** – Simulation showing the influence of the VCSEL driving current on the sensor characteristics.

### Influence of the VCSEL driving current

For the remainder of the chapter, the distance  $d$  was kept fixed at  $200\ \mu\text{m}$ . Since the emitted optical power and the beam divergence angle of the VCSEL depends on the driving current (see Section 6.2.4), this will also have an influence on the sensor characteristics. The half power divergence angle roughly doubles when the driving current is increased from 1 to 5 mA and the emitted optical power increases approximately linearly, starting at the threshold current of 1 mA.

The sensor response was calculated for VCSEL driving currents of 1, 2, 3, 4 and 5 mA (see Figure 5.5). Since the detector behaves as an averaging function for the beam profile of the VCSEL, the response has less variations for small driving currents since the VCSEL beam is almost completely incident to the detector for the largest part of the displacement. Furthermore, the detected optical power and sensitivity is lower. When the divergence angle increases, the detector is not large enough to capture all the light, yielding a more favorable sensor response: for a large dynamic range there will be a significant change in the sensor output.

A secondary effect to be taken into account is that the multimodal behavior of the VCSEL increases for higher driving currents, meaning that the averaging process performed by the detector cannot filter all irregularities in the multimode VCSEL beam (see Section 6.2.4).

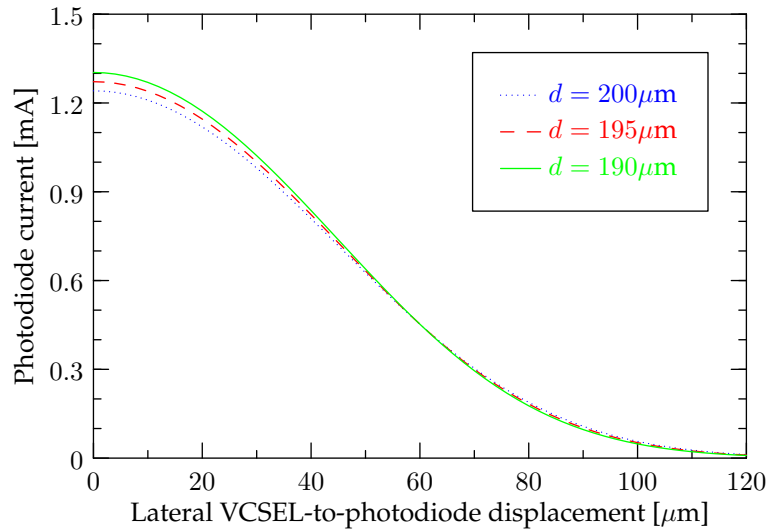


**Figure 5.6** – Simulation showing the influence of the layer thickness change caused by a normal pressure.

### Influence of the normal pressure

The shear sensor should ideally only be sensitive to shear stress and not to normal pressure. However, in reality there is always a certain cross-sensitivity. When exerting a normal force on the sensor, the transducer layer will be compressed and consequently the distance between the VCSEL and photodiode decreases, which influences the sensor characteristics. Following mechanical characterization it was found that the total compression of the layer is less than  $2 \mu\text{m bar}^{-1}$ . The influence is therefore limited, as can be seen in Figure 5.6, showing the effect of a layer compression up to  $10 \mu\text{m}$ .

### Two-dimensional sensor response

The results from the paragraphs above only apply for a 1-directional sensor response, i.e. when the VCSEL and detector are moving along a specific straight line; in the calculations above,  $y = 0$  was chosen. However, in most of the practical cases, shear stresses are not 1-directional but have 2 components in the plane (e.g. an  $x$ - and  $y$ -component). The 2-dimensional response using the optimized parameters as found above ( $5 \text{ mA}$  driving current,  $d = 200 \mu\text{m}$ ) is plotted in Figure 5.7. The color scale represents the photodiode current corresponding with relative VCSEL-to-photodiode displacements in the complete  $(x, y)$ -plane. It is clear that with the current configuration, the sensor is not suitable to distinguish

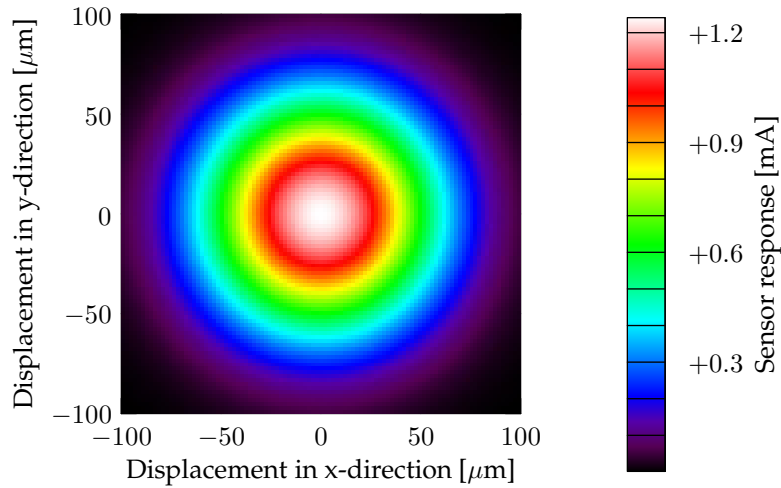


**Figure 5.7** – Two-dimensional sensor response. For  $(0,0)$ , the VCSEL and detector are perfectly aligned.

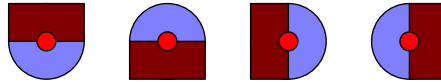


**Figure 5.8** – Configuration of the detector chip with half covered photodiodes in order to obtain an  $(x, y)$ -sensitive sensor topology (large blue circle: detector; small red circle: VCSEL; brown rectangle: metal cover layer).

between displacements in different directions, only the total displacement (magnitude) can be resolved. This limitation is caused by the shape of the round detector that was used: since the configuration is rotationally symmetric with respect to the origin, the sensor response will be independent of the direction of movement away from the origin.

### 5.3.2 Modifications toward an $(x, y)$ -shear sensor design

In order to detect both direction and magnitude of movement, the shape of the detector needs to be modified. Suppose that a sensor sensitive only to variations along the  $x$ -axis is required. First, to distinguish between negative and positive displacements, the initial position of the VCSEL with respect to the detector needs to be changed. Instead of perfectly aligning both components, the VCSEL should initially be positioned above the edge of the detector active area so that the sensor response either increases or decreases, depending on the direction of movement. Second, to make the sensor independent of variations in the  $y$ -direction, the de-

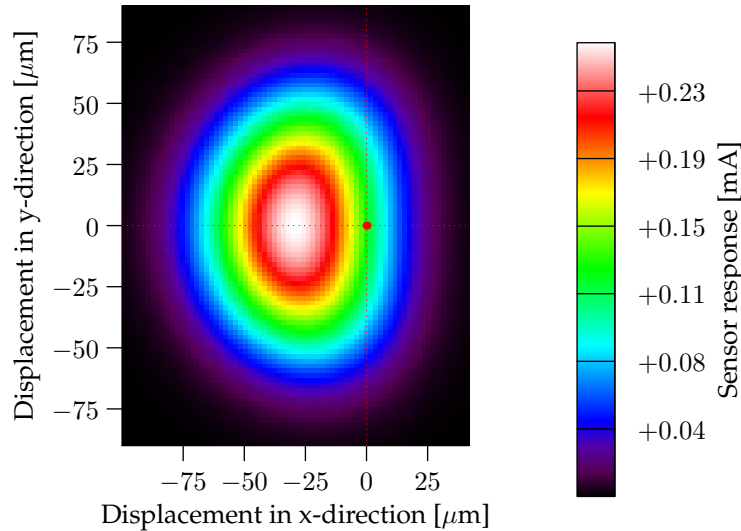


**Figure 5.9** – Two-dimensional sensor response. The red dot indicates the initial VCSEL location,  $(0,0)$ , i.e. when the sensor is not loaded.

tector edge needs to be parallel with the  $y$ -axis.

In a first step toward an  $(x, y)$ -shear sensor, the actual dimensions of the active areas of the in-house available photodiodes were altered by partially covering them with a metal mask. The 4 available photodiodes (PDs) on the detector chip were half-covered in order to pursue the requirements discussed above. Figure 5.8 illustrates this proof-of-principle sensor topology: PD 1 and 2 are sensitive to variations along the  $y$ -axis while PD 3 and 4 are sensitive to variations along the  $x$ -axis. Initially, the VCSELs are perfectly aligned with the photodiodes and consequently aligned with the edges of the metal masks.

The sensor responses corresponding with PD 1-4 can be obtained using formula 5.1, where  $PD(x, y)$  is now a function corresponding with the semicircular detector area. The result corresponding with PD 4 is depicted in Figure 5.9 and the initial VCSEL location,  $(0,0)$ , is indicated with a red dot. When comparing with Figure 5.7, it can be seen that this two-dimensional response is not completely symmetrical anymore. In fact, this sensor configuration is sensitive to variations in the  $x$ -direction and nearly insensitive to variations in the  $y$ -direction. This effect is observed more clearly when plotting a cross-section of the two-dimensional response graph for  $x$ - and  $y$ -directional displacements, as indicated by the dotted lines in Figure 5.9. Figure 5.10 shows the resulting graphs and also indicates the initial VCSEL position with a red dot. In a certain

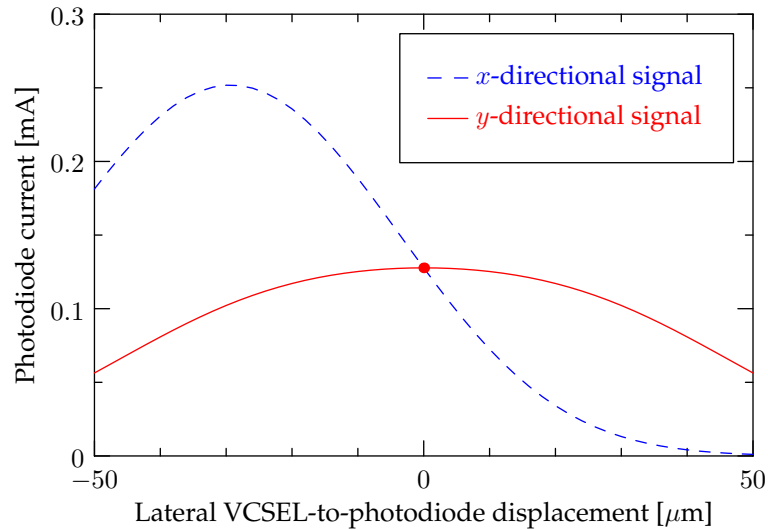


**Figure 5.10** – Cross-section of the graph in Figure 5.9, as indicated by the dotted lines. The cross-sections show the sensor response to lateral displacement in 2 orthogonal directions  $x$  and  $y$ . The red dot indicates the initial VCSEL location.

interval around  $(0,0)$ , the sensor signal increases or decreases when moving in the  $x$ -direction, but remains virtually constant when moving in the orthogonal  $y$ -direction.

Although the principle of an  $(x, y)$ -shear sensor was demonstrated with this sensor design, there are some important restrictions. First, it has to be noted that this configuration only functions with lower VCSEL driving currents. The reason is that the photodiode active areas become too small when covering half of it with a mask. At the optimized 5 mA VCSEL driving current, the size of the VCSEL beam is too large compared to the photodiode surface and therefore this averages out the desired asymmetric effect of the straight edge. As a result, the VCSEL beam size needed to be reduced by lowering the operating current. The unfavorable effects of using this lower operating current can be noticed in Figure 5.9 and 5.10 from the lower maximum sensor response values and consequently lower sensor sensitivity. Obviously, the dynamic range is also smaller because of the smaller beam size. From Figure 5.10, the total dynamic range can roughly be determined as  $40 \mu\text{m}$ , i.e.  $[-20 \mu\text{m}, 20 \mu\text{m}]$ , which is considerably smaller than the first generation technology sensors (e.g. see Figure 5.5). Furthermore, within this dynamic range, the  $y$ -directional signal is not completely constant but shows a certain variation, meaning that the  $x$  and  $y$  sensing points are only approximately decoupled.

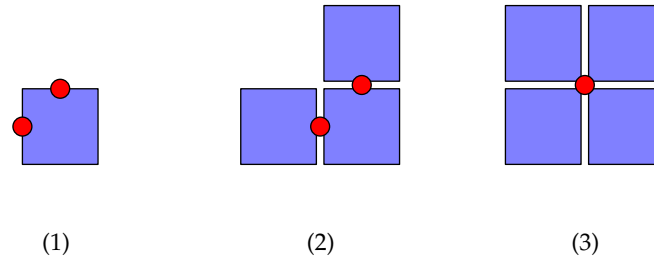


**Figure 5.11** – Different configurations for obtaining a shear sensor sensitive to  $(x, y)$ -variations (large blue square: detector; small red circle: VCSEL).

### 5.3.3 True $(x, y)$ -shear sensor design

To overcome the limitations mentioned in the previous section, larger and preferably square detector chips are needed. Cosemi offers photodiode chips with a square active area (see Section 6.2.3) which are ideally suited for this purpose. Using these photodiodes, introduces a new range of possibilities for constructing shear sensors. Several potential configurations are summarized in Figure 5.11. Each of these configurations allows for constructing sensors capable of detecting shear stresses in the complete  $(x, y)$ -plane. They differ in terms of dynamic range, linearity, number of active components and ability to sense  $x$ - and  $y$ - variations independently.

- (1) The first configuration only uses 2 VCSELs and 1 photodiode.
- (2) The second configuration uses 2 VCSELs and 3 photodiodes.
- (3) The third configuration uses 1 VCSEL and 4 photodiodes

The first 2 configurations share a photodiode for measuring the  $x$ - and  $y$ -component of the signal. Therefore, the  $(x, y)$ -sensor needs to work in a “scanning operating mode”. This means that the VCSELs corresponding with the  $x$ - and  $y$ -direction are turned on alternately at a certain scanning rate and the resulting signals captured by the photodiodes are considered as either  $x$ - or  $y$ -directional information depending on which specific VCSEL is turned on.

Furthermore, it can be noted that the third configuration with 4 photodiodes can be compared to a quadrant photodiode setup that is commonly used for laser positioning and aligning applications. For example, the difference of 2 photodiode currents in different quadrants is used to determine the laser beam location. This configuration can therefore be very accurate, but only operates with laser beam spots having a size comparable to the total photodiode surfaces, since there is always a non-sensitive dead zone between the 4 quadrant photodiodes resulting in

non-linearities when used with small beam size lasers. In the current shear sensor architecture, the VCSEL is placed 200  $\mu\text{m}$  above the photodiode, resulting in a beam spot size of about 100  $\mu\text{m}$  in diameter (see Figure 6.6) being considerably smaller than the total active area of the 4 photodiodes (4 times 250  $\mu\text{m} \times 250 \mu\text{m}$ ). To use this configuration, the sensor design would have to change considerably (e.g. using a different light source) and therefore it will currently not be considered further in this dissertation.

The drawback of these 3 new configurations is that the (currently available) square photodiodes are slightly different and require a modification of the embedding technology. Instead of exhibiting anode and cathode top contacts, these chips have a top anode and bottom cathode contact, meaning that the process for thinning these chips is more complicated. Therefore, the work presented in this dissertation is limited to establishing a proof-of-principle demonstrator, using photodiodes embedded in rigid FR-4 substrates, avoiding the need for thinning down the chips. However, within the scope of the PhD research of Bram Van Hoe, the required processes for thinning down back contacted chips have already been demonstrated and could be implemented for constructing this shear sensor in the future.

Configurations 1 and 2 will be described in more detail in the remainder of this section.

#### Configuration 1: 1 square photodiode and 2 VCSELs

Similarly as performed for the round photodiodes illustrated above, the complete two-dimensional sensor response for this configuration can be obtained using equation 5.1, yielding the result plotted in Figure 5.12. The dashed contour corresponds with the location of the photodiode and the red dot indicates the initial position of the VCSEL on the southern edge of the photodiode, corresponding with the response in (0,0). If the VCSEL is displaced in the  $y$ -direction ( $\chi = \pm 90^\circ$ ) from this initial position, the response increases for positive and decreases for negative angles of  $\chi$  enabling to detect the direction of movement. In contrast, the response remains constant when moving in the  $x$ -direction and is therefore only sensitive to the  $y$ -component of the displacements. Similarly, if another VCSEL is placed for example on the western edge of the photodiode, an  $x$ -directional sensing point is obtained. These 2 sensing points can therefore be combined resulting in the desired  $(x, y)$ -sensitive device provided that both VCSELs are driven alternately.

To compare the performance of the proposed different configurations of sensors, the linearity, dynamic range and sensitivity are investigated. Therefore, a cross-section of Figure 5.12 is made in the direction of interest, i.e. for  $\chi = \pm 90^\circ$  which corresponds with the  $y$ -direction, see Figure 5.13.

The 5% value of the maximum signal,  $\Psi_{max}$ , is used to define the boundaries of

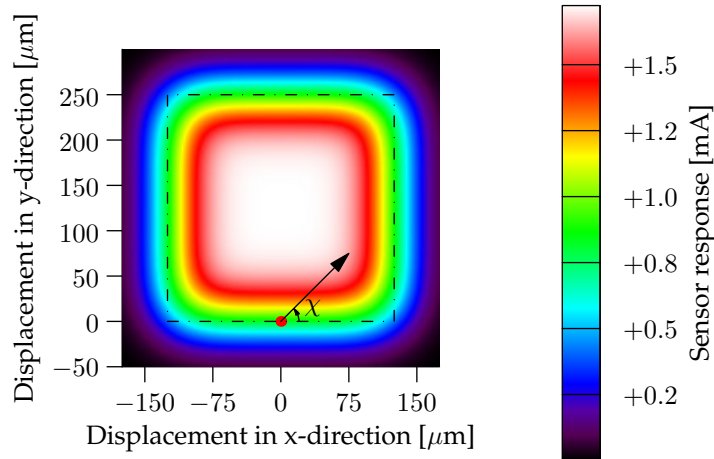


**Figure 5.12** – Sensor response for configuration 1; the dashed contour corresponds with the location of the photodiode and the red dot indicates the initial location of the VCSEL.

the sensor dynamic range (in terms of VCSEL displacements). The resulting dynamic range is then defined as the region where the sensor signal varies between  $0.05 \times \Psi_{max}$  and  $0.95 \times \Psi_{max}$ , as illustrated in Figure 5.13. Within this range, a linear approximation is calculated using the least-squares curve fitting method. A corresponding measure for the linearity of the original curve is given by the coefficient of determination  $R^2$ , while the slope of the linear fit is adopted to define the sensitivity of the sensor. For the current configuration, a dynamic range of  $104 \mu\text{m}$ , a sensitivity of  $17.2 \mu\text{A} \mu\text{m}^{-1}$  and an  $R^2$  value of 0.9963 was found.

### Configuration 2: 3 square photodiodes and 2 VCSELs

The second configuration uses 1 VCSEL aligned between 2 photodiodes to measure displacements in 1 direction. A third photodiode and an extra VCSEL can be added to allow measuring displacements in the other direction. Using this configuration, the sensitivity remains virtually unchanged while the dynamic range is extended by about a factor of 2: instead of monitoring the photocurrent from 1 detector, the current difference of the 2 photodiodes is used as sensor signal. The resulting two-dimensional response is obtained by calculating the response corresponding with  $PD_2$  and subtracting from the response corresponding with  $PD_1$ . These 2 response graphs from the individual photodiodes are identical, except for a horizontal shift. Figure 5.14 shows the resulting two-dimensional response graph for that part of the sensor responsible for detecting the  $x$ -directional dis-

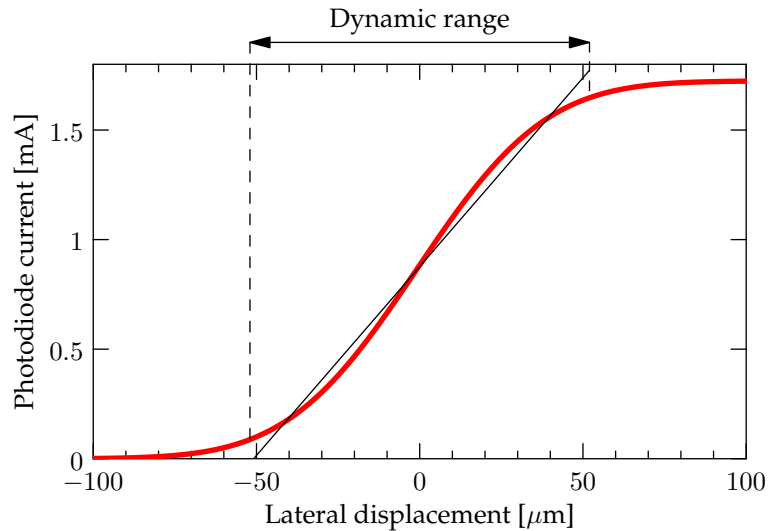


**Figure 5.13** – Cross-section of the sensor response in Figure 5.12 in the direction of  $\chi = \pm 90^\circ$  and the corresponding linear fit within the sensor dynamic range.

placement component (i.e. the two top photodiodes and corresponding VCSEL). It can immediately be remarked that the (color) scale is different due to the larger dynamic range when using 2 photodiodes, compared to for example Figure 5.12. Similarly as for the previous configuration, this part of the sensor is only sensitive to displacements in a single direction (i.e. the  $x$ -direction). The response corresponding with this direction is shown in Figure 5.15.

The resulting linearity, dynamic range and sensitivity of configuration 1 and 2 are summarized in Table 5.1. As a conclusion, configuration 2 requires more components, but also exhibits a larger dynamic range than configuration 1. However, the defined dynamic ranges are only meaningful when the measured  $x$ - and  $y$ -component of the displacement are still independent. As can be estimated from the graph in Figure 5.14 however, the dynamic range in the  $x$ -direction (i.e.  $186 \mu\text{m}$ ) is larger than the range in which the  $x$ - and  $y$ -component of the sensor are independent (i.e.  $144 \mu\text{m}$ , also for configuration 1). Therefore, the smallest of these 2 values has to be considered when specifying the “true” sensor dynamic range for  $x$  and  $y$  displacements. This also means that there is only a limited dynamic range advantage for configuration 2 with the current type of photodiodes. Unless mainly displacements in a specified and single direction need to be measured, it is advisable to use photodiodes with a customly designed layout to take full advantage of this configuration, which is outside the scope of this work. Therefore, configuration 1, using the least components, is selected as proof-of-principle demonstrator and the test results are described in Chapter 6.

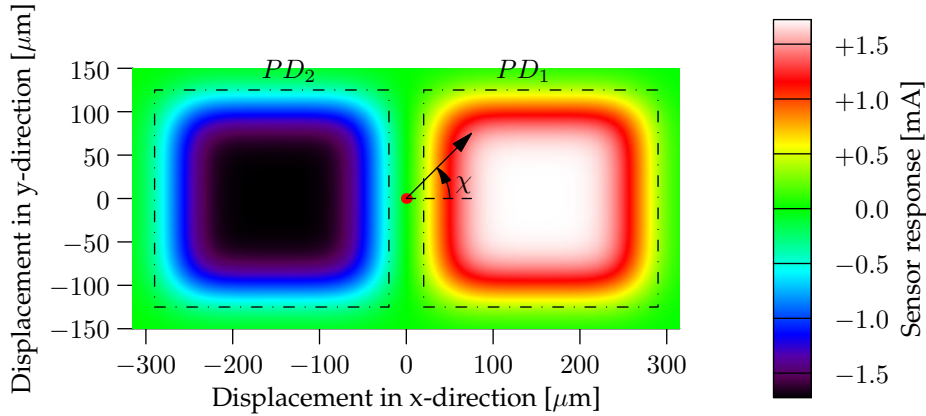


**Figure 5.14** – Sensor response for configuration 2; the dashed contour corresponds with the locations of the photodiodes  $PD_1$  and  $PD_2$  and the red dot indicates the initial location of the VCSEL.

**Table 5.1** – Performance measures for 2 configurations based on square photodiodes.

	Configuration 1	Configuration 2
Dynamic range (single direction) [ $\mu\text{m}$ ]	104	186
True dynamic range (all directions) [ $\mu\text{m}$ ]	104	144
Sensitivity [ $\mu\text{A } \mu\text{m}^{-1}$ ]	17.2	19.9
Linearity measure ( $R^2$ value)	0.9963	0.9960

### 5.3.4 Alternative sensor implementations

The prototypes as described in this chapter were designed to obtain maximum sensitivity, accuracy and miniaturization. Although these proposed sensors have a high sensitivity, they exhibit a limited dynamic range in terms of lateral displacement (an order of magnitude around  $100 \mu\text{m}$  depending on the specific implementation). To cover the desired range of shear stresses, a transducer material with the proper mechanical (shear) modulus can be selected so that the dynamic range of  $100 \mu\text{m}$  displacement is mapped on the required shear stress values.

However, sometimes a larger displacement dynamic range is required, and preferred over a high accuracy. An example is found in limb prostheses where the residual stump can shift laterally in the socket over several centimeter. These larger displacements can be measured by modifying the sensor principle, in exchange for a lower sensitivity or accuracy.

A straightforward method to allow measuring larger displacements is the use of

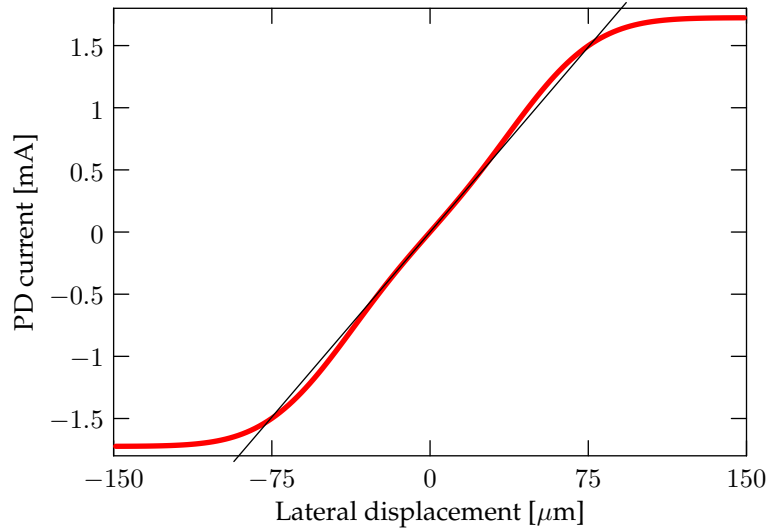


**Figure 5.15** – Cross-section of the sensor response shown in Figure 5.14 in the direction of  $\chi = 0^\circ$  and the corresponding linear fit within the sensor dynamic range.

an additional transducer layer applied on top of the sensor, in addition to the other transducer layer that is already introduced between the light source and detector. This extra transducer layer allows transforming of larger displacements into smaller displacements which can be detected by the sensor.

Alternatively, the optical sensing behavior itself can be adapted. Now that the optical sensing principle has been demonstrated and studied extensively, it is clear that the sensor characteristics can be tuned by changing the  $PD$  and  $\Phi_d$  functions (see equation 5.1). The  $\Phi_d$  function, determined by the characteristics of the VCSEL beam, is not so easy to change although this would be possible for example by employing a certain microlens or filter. However, the  $PD$  function is easily varied by changing the detector surface accordingly. As shown above, the use of round or square detectors results in different sensor behavior. The shape of the photodiode can be changed further by covering it partially, for example with a light absorbing mask.

Figure 5.16a shows a first example of how the sensor dynamic range can be extended. As a first obvious requirement, a larger photodiode is needed. This photodiode active area is covered with strips on a certain pitch preventing the light from hitting the detector on those locations (a “slit mask”). When the VCSEL is displaced laterally, the photodiode detects an oscillating signal depending on the VCSEL position compared to the strips. By counting the number of oscillation periods, the location of the VCSEL can be determined. A drawback of this technique is that the sensor is only able to detect relative displacements since the

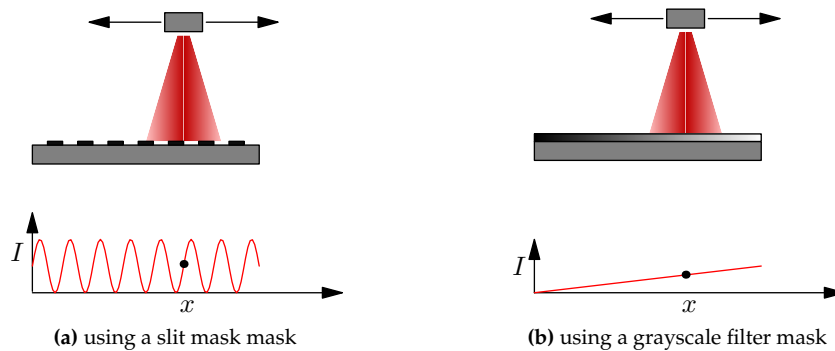


**Figure 5.16** – Schematic representation of alternative shear sensor implementations. The graphs show measured photodetector intensities in function of the light source location.

output signal is periodic and furthermore a second signal in quadrature is needed to determine the direction. This can be compared to an optical position encoder that is used for example in precision motorized stages.

A second example is illustrated in Figure 5.16b: it also employs a large detector and a grayscale filter that linearly allows more light to transmit depending on the VCSEL location. This results in a linear, absolute sensor signal, but in exchange for the larger dynamic range, the sensitivity is reduced. Since the resulting sensitivity and therefore also accuracy is lower anyway, these larger dynamic range sensors could also be constructed using cheaper and more common LEDs (exhibiting a broader beam) instead of VCSELs.

Finally, also other components than photodiodes can be used for detecting the position of the light beam. Position sensitive detectors (PSD), for example, are ideally suited for this purpose. These semiconductor based optical detectors output a signal depending on the location of a light beam incident on the active area and can therefore directly be used as displacement sensors. Using these components for constructing a shear sensor seems much more attractive than using photodiodes, however, they are rather large and currently mainly available as bulky and expensive packaged components. Since an unobtrusive sensor solution is pursued, the physical appearance of the components is of paramount importance for the final product and therefore the commercial PSDs are not considered for use in the flexible shear sensor.

Another possibility is using (printed) organic photodetectors which are currently being developed by several research groups. These optical detectors offer several advantages since they are constructed based on polymer and not on semiconductor processes. Firstly, they can potentially be fabricated cheaply using roll-to-roll techniques and secondly, they can easily be made larger than semicon-

ductor based detectors. These roll-to-roll fabricated components are inherently flexible making them ideally suited for constructing unobtrusive sensors. Similarly, (printed) OLEDs could be used as light sources, so that all steps to fabricate the sensor can be transferred to a roll-to-roll process.

### 5.3.5 Shear sensor implementation in reflection

The shear sensor could also be constructed “in reflection” so that the light source and detector are mounted on the same substrate and a type of mirror is then mounted on top of the transducer layer. This construction makes the fabrication considerably easier since only 1 substrate with active components has to be constructed and consequently only electrical connections are present on 1 side of the transducer material. However, the optical sensor design becomes more difficult since also the reflection of the emitted light has to be considered and an appropriate mirror needs to be designed.

## 5.4 Mechanical sensor architecture design

---

The above-mentioned simulations studied the optical sensor behavior in function of the applied lateral displacement between the VCSEL and photodiode. However, to obtain a shear instead of displacement sensor, the shear stresses applied to the sensor need to be converted into displacements. Therefore, a mechanical transducer layer is needed: a layer of material with the appropriate mechanical properties so that a desired lateral displacement is obtained when a shear stress is applied onto this material. From the simulations above, it can be concluded that lateral displacements in the range between 0 and 100  $\mu\text{m}$  are needed. On the other hand, shear stresses in the order of hundreds of kPa need to be measurable when targeting robotic, biomedical and artificial skin applications. Therefore, the transducer material needs to exhibit a very low shear modulus and furthermore needs to be optically transparent at 850 nm. Rubber-like materials such as PDMS exactly show these requirements. There exists a complete range of commercially available optically transparent PDMS materials with different moduli. This offers the advantage that a PDMS with the required shear modulus can be chosen depending on the application and consequently always obtaining an optimum balance between sensor sensitivity and dynamic range. Using softer materials results in a very sensitive sensor while using harder materials results in a sensor with a large dynamic range with respect to applied shear stress. For the shear sensor prototype, a Sylgard®184 transducer material was selected.

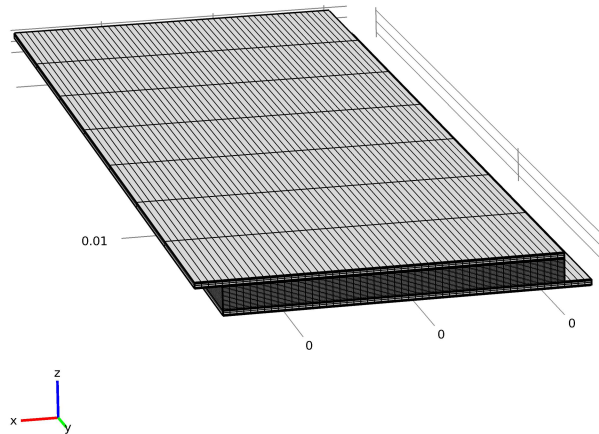


**Figure 5.17** – Meshing of the model: a “mapped” mesh constructed with blocks was used instead of the standard tetraedric mesh, not to disturb the symmetry in the structure.

#### 5.4.1 Mechanical model in Comsol

The mechanical behavior of the sensor was studied using a three-dimensional mechanical model in Comsol Multiphysics, a finite element simulation software program. Figure 5.17 depicts the geometrical model; the adopted dimensions correspond with these of the prototype and are also listed in Table 5.2. As explained in Section 5.2, the sensor consists of 2 flexible foils with the optoelectronics, and a PDMS layer in between. For the mechanical model, the flexible foils were considered to be complete layers of polyimide instead of a polyimide–SU-8–polyimide stack. This is justified since these foils will hardly deform compared to the much softer PDMS material.

The different parts of the model were constructed using rectangular blocks and the meshing strategy was selected accordingly: in order not to disturb the geometrical symmetry of the model, a “mapped” mesh constructed with blocks was used instead of the standard tetraedric mesh, see Figure 5.17. It can be seen that the mesh is coarse in the  $y$ -direction since only  $x$ -directional displacements are studied and hence little variations along the width of the sensor are expected. Along the other dimensions, the mesh is much finer, especially for the highly deformable PDMS material.

**Table 5.2** – Geometrical parameters used for constructing the mechanical model in Comsol Multiphysics. The table also mentions whether the parameter is easily variable without influencing the optical behavior of the sensor.

	Value	Variable in mechanical design?
Thickness PDMS layer $d$	180 $\mu\text{m}$	no
Sensing area length $l$	2.6 mm	yes
Sensing area width $w$	8 mm	yes
OE foil thickness $t$	46 $\mu\text{m}$	no

**Table 5.3** – Mechanical properties of the materials used for the simulation model in Comsol Multiphysics.

	Polyimide	PDMS
Young's modulus	3.1 GPa	1.2 MPa
Poisson's ratio	0.35	0.48
Density	1300 $\text{kg m}^{-3}$	1000 $\text{kg m}^{-3}$

Justified by the relatively small deformations, a linear elastic model was used in Comsol, based on the Young's modulus, Poisson's ratio and density of the materials that are listed in Table 5.3. The Young's modulus of the Sylgard®184 PDMS was adopted from own measurements on the shear sensor (see Chapter 6) while for the polyimide, the built-in Comsol model was used.

As boundary conditions for the physical model, the bottom polyimide foil was kept fixed and all other surfaces were defined as free boundaries. On the top polyimide foil, a uniform shear stress was applied acting in the positive  $x$ -direction.

## 5.4.2 Mechanical simulation results

### Lateral deformation in function of applied shear stress

In a first simulation, the lateral deformation was studied in function of the applied shear stress on the sensor surface. This data, expressing the mechanical behavior of the transducer material, is required to convert the displacement based sensor response (as obtained in Section 5.3) into a shear stress based response.

Figure 5.18 depicts a cross-section showing the deformation in the different sensor layers, caused by an applied  $x$ -directional shear stress of 300 kPa. The color gradations represent the corresponding  $x$ -directional displacement. It can be seen

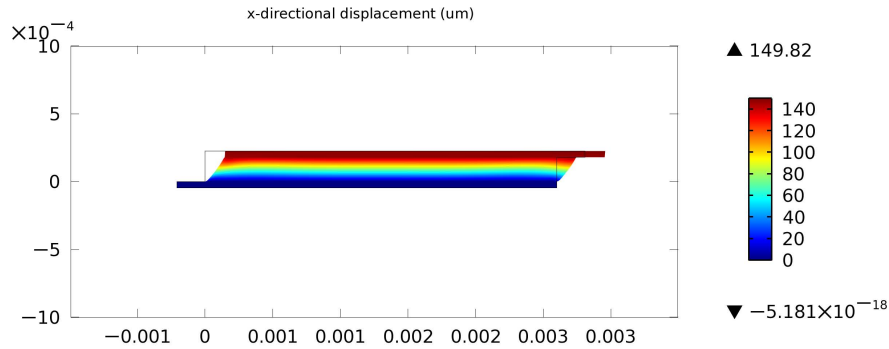


**Figure 5.18** – Deformation of the shear sensor stack (model cross-section). The color scale indicates the  $x$ -directional lateral displacement.

that the polyimide foils do not deform significantly, but instead all the deformations are absorbed in the PDMS material: the maximum lateral displacement in this case was about  $150\ \mu\text{m}$ . For the shear sensor response, the displacements need to be determined in the area where the optoelectronics are located, the “sensing area”, see Figure 5.18. Therefore, the displacement is always evaluated in this point for the following graphs. However, the displacement values at a certain  $z$ -coordinate are never much different than the maximum displacement since this value is very weakly  $x$  and  $y$  dependent and furthermore this dependency only occurs at the edges of the model.

Figure 5.19 shows the lateral displacement in function of the applied shear stress, exhibiting a linear dependency, as a result of the adopted linear elastic model. The obtained lateral deformation values correspond well with the measurements from Section 6.3.1: a dependency of  $22.4\ \mu\text{m N}^{-1}$  or  $0.448\ \mu\text{m kPa}^{-1}$  was measured and the simulations indicate a  $0.492\ \mu\text{m kPa}^{-1}$  dependency.

From this mechanical study of the transducer layer (i.e. its linear relation between shear stress and displacement), it can be concluded that the sensor responses calculated in Section 5.3 only need to be scaled with the factor  $0.492\ \mu\text{m kPa}^{-1}$  when the response in function of applied shear stress is required instead of the response in function of the lateral displacement. Although this linear behavior is a result of the applied simulation model, it was confirmed by actual shear versus lateral displacement measurements (Section 6.3.1).

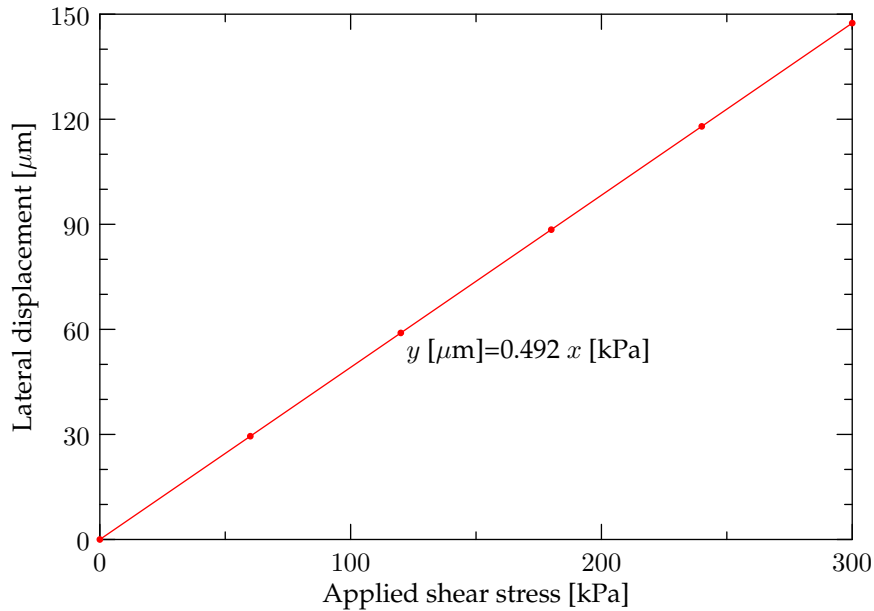


Figure 5.19 – Lateral displacement in function of the applied shear stress.

#### Influence of the normal pressure

In Section 5.3, it was already studied how the (optical) sensor response depends on the compression of the transducer layer. The conclusion was that a layer compression of a few micrometers does not significantly influence the sensor response. This is a desired result since the sensor is ideally only susceptible to shear stress variations to increase the accuracy. For the typical applications, the maximum normal pressure that may occur is not more than a few bar. The following simulation verifies that this normal pressure that may occur does not influence the sensor, which is ideally only sensitive to shear stress. Therefore it is firstly investigated how the lateral displacement of the layer is influenced by a normal force and secondly, how much the transducer layer is compressed by a normal force.

The simulation results depicted in Figure 5.20 show indeed that the lateral displacement as a result of an applied shear force is only very weakly dependent on an extra normal load applied on the sensor (for the considered range of normal pressure). The variation in lateral displacement is only  $1.4 \mu\text{m}$  in the range from 0 to 3 bar.

Furthermore, it was found from this simulation model that the compression of the transducer layer resulting from a normal pressure is only  $1.87 \mu\text{m bar}^{-1}$ , and

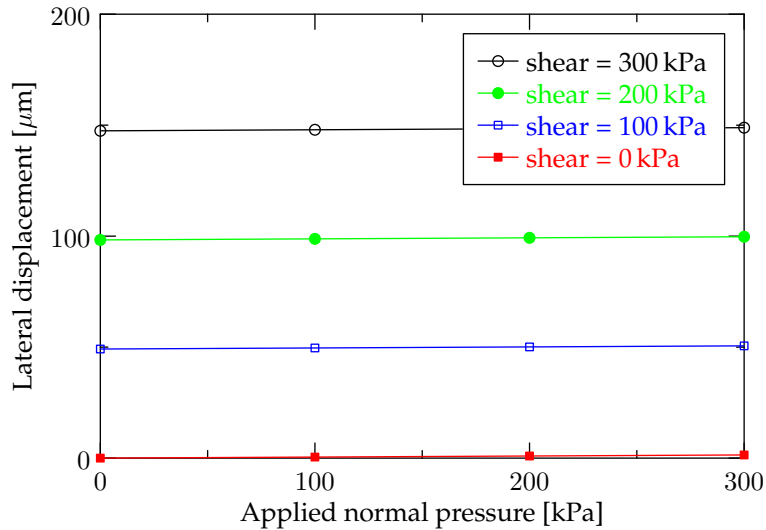


Figure 5.20 – Influence of the normal pressure on the lateral displacement of the transducer layer, for several values of applied shear stress.

this value is nearly independent of the shear stress acting on the sensor.

From these 2 results it can be concluded that the presence of a normal load does not significantly disturb the sensor response to shear stresses.

### Influence of the sensing area dimensions

The in-plane dimensions ( $w$  and  $l$ ) of the transducer layer also have a small influence on the mechanical behavior. The shear modulus  $G$  of a material [9], considering an infinitesimal cube, is defined as:

$$G = \frac{\tau_{xy}}{\gamma_{xy}} = \frac{d \cdot f}{\Delta x \cdot A},$$

where  $\tau_{xy} = f/A$  is the shear stress,  $\gamma_{xy} = \Delta x/d$  is the shear strain,  $\Delta x$  is the infinitesimal transversal displacement and  $d$  is the initial thickness of the cube. For structures with certain finite dimensions, this formula can be integrated and in the ideal case, when the dimensions of the layer are very large in the  $x$ - and  $y$ -direction, compared to its thickness, this yields:

$$G = \frac{d \cdot f}{x \cdot A},$$

where  $x$  is now the total transversal displacement.

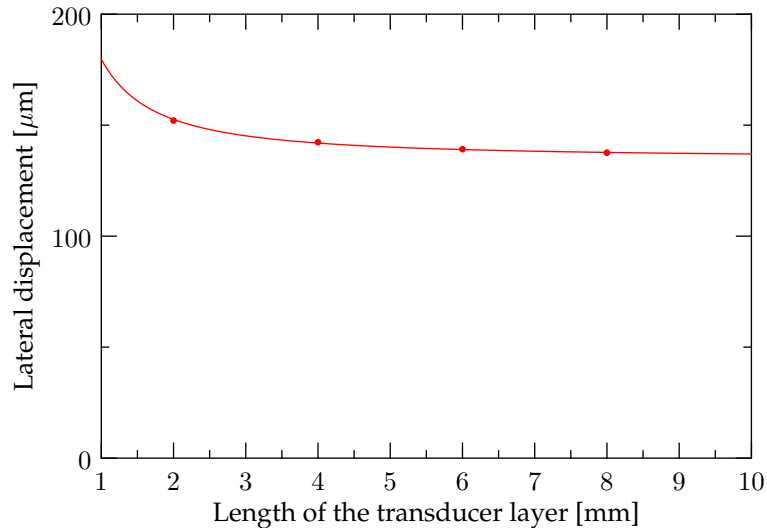


**Figure 5.21** – The influence of the transducer layer length  $l$  on the lateral displacement of the transducer layer (applied shear stress: 300 kPa).

However, the dimensions of the sensor are small and therefore some deviation from this formula can be expected due to boundary effects. In the following simulations, the width of the transducer layer is kept fixed at 8 mm and the length is varied between 2 mm and 8 mm. A shear stress of 300 kPa was applied and the resulting lateral displacement was recorded, see Figure 5.21. This plot shows that for smaller dimensions, the lateral displacement is larger and that for large dimensions, the displacement converges to the theoretical limit as calculated using the formula above (for infinite dimensions).

Adapting the dimensions of the sensor may therefore be useful for obtaining a required mechanical behavior.

#### **Influence of the transducer material properties**

Another technique to tune the mechanical behavior of the sensor is selecting an appropriate transducer material. As discussed previously, the sensitivity and dynamic range with respect to shear stress are determined by the transducer material: a very sensitive sensor is obtained using a soft material and a sensor with a large dynamic range is obtained using a hard material. This influence of the material shear modulus on the lateral displacement of the transducer layer (and hence the lateral displacement of the VCSEL and photodiode) is plotted in Figure 5.22.

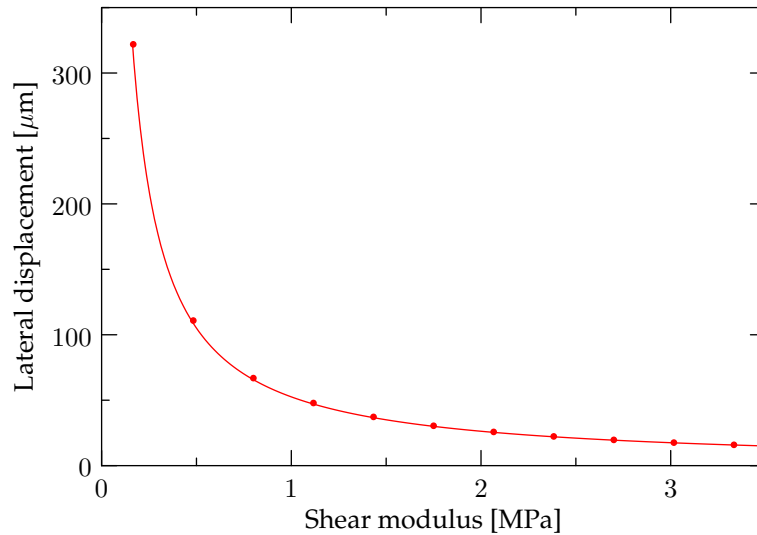
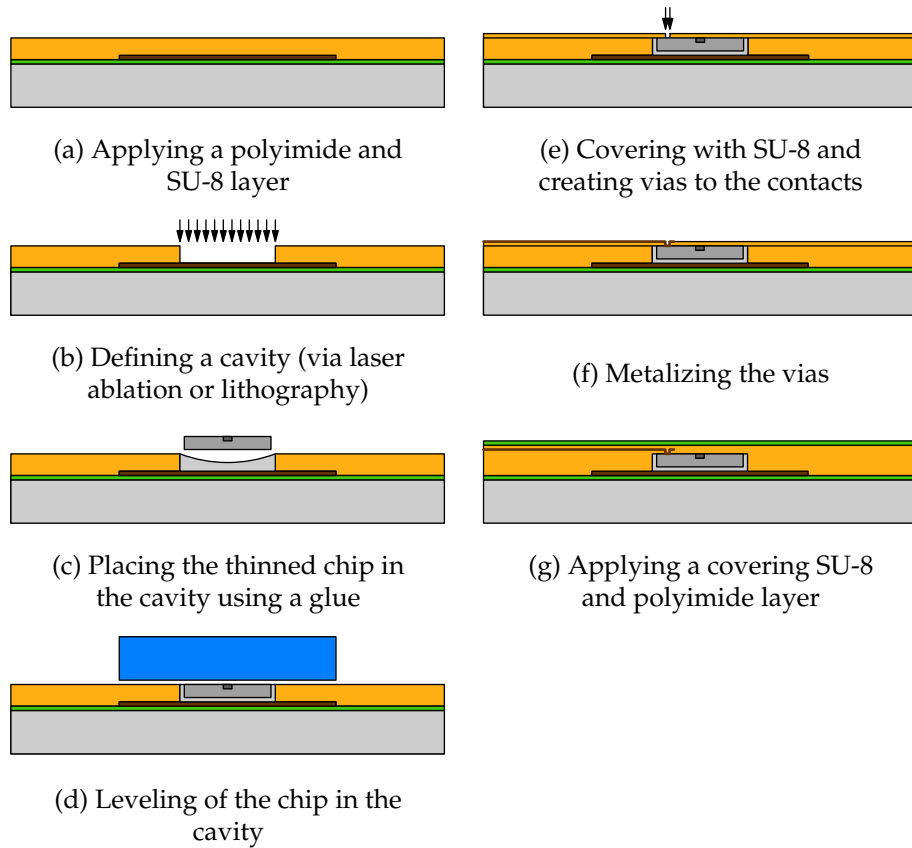


Figure 5.22 – The influence of the material shear modulus on the lateral displacement of the transducer layer (applied shear stress: 300 kPa).

### 5.4.3 Conclusions

From the optical simulations in Section 5.3, the optimum vertical distance between the VCSEL and photodiode, and consequently thickness of the transducer layer was determined to obtain the desired “optical” behavior of the sensor. This vertical distance determines the sensor response to the relative lateral displacements of the VCSEL and photodiode. On the other hand, the mechanical behavior of the transducer layer determines how the shear stress on the sensor is converted in lateral displacement of the optoelectronic components.

From the mechanical simulations above it can be concluded that there is a linear relation between shear stress and lateral displacement in the transducer layer. Furthermore, the influence of a normal pressure on the sensor was found to be negligible. Additionally, the sensor design parameters were explored: there are two possibilities for obtaining a desired mechanical behavior (i.e. lateral displacement in function of shear stress). The most straightforward is selecting a material with an optimum shear modulus. However, when such a material is not available, the flexibility in choosing the sensor dimensions may also be used to tune the mechanical behavior, although its influence on the sensor response is more limited than the influence of using a dedicated material.



**Figure 5.23** – Process flow for embedding optoelectronic components into a stack of polymer layers with a total thickness of 40  $\mu\text{m}$ .

## 5.5 Fabrication process

### 5.5.1 Embedding optoelectronics

The process of fabricating the shear sensor is based on the optoelectronic component embedding technology developed within the framework of the project FAOS (“Flexible Artificial Optical Skin”, funded by the Institute for the Promotion of Innovation by Science and Technology (IWT), Flanders, Belgium) and is described and characterized extensively in the PhD work of Erwin Bosman [6]. The process flow will be described briefly, focusing on the modifications that were adopted to apply this technology for fabricating the shear sensors. A detailed overview of the embedding of optoelectronic chips can be found in [6].

To build the proposed shear sensor, a photodiode and a VCSEL are required, which need to be embedded into very thin foils to obtain the desired mechanical sensor flexibility. The final foil thickness is about 40  $\mu\text{m}$ , implying that the optoelectronic components themselves need to be even thinner. Therefore, bare die chips without package were utilized directly. The used VCSELs were multi-transverse mode emitting at 850 nm (250  $\mu\text{m}$  pitch 1x4 array, ULM Photonics) while the photodiodes were Gallium Arsenide (GaAs) based with an anti-reflection coating for 850 nm and a circular active area of 100  $\mu\text{m}$  diameter (250  $\mu\text{m}$  pitch 1x4 array, Enablence). These optoelectronics are provided as dies with a typical thickness of 150  $\mu\text{m}$ . Therefore, a thinning process was developed to reduce the chip thickness down to 20  $\mu\text{m}$  [6]. These 20  $\mu\text{m}$  thin VCSELs and photodiodes were then used to embed into a thin stack of layers (total thickness 40  $\mu\text{m}$ ).

The embedding process is depicted in Figure 5.23. All steps are performed on a temporary rigid glass carrier from which the flexible layers could be released after the processing. First, a 7.5  $\mu\text{m}$  thick layer of spin-coatable polyimide (PI-2525, HD Microsystems) was applied on the temporary glass substrate. Since there is no adhesion of this layer with the glass carrier, it can easily be released after completing the fabrication. To ensure sufficient adhesion during the process, an adhesion promoter (Pyralin VM652) is applied on the edges of the glass carrier. Then, a copper heatsink was applied by sputtering a 1  $\mu\text{m}$  thick seed layer and electro-plating up to a final thickness of 5  $\mu\text{m}$ . A 20  $\mu\text{m}$  thick SU-8 layer was subsequently spin-coated (a) and a cavity was defined on top of the heatsink (b). Both laser ablation and photolithography were used for this purpose. Laser ablation offers a broad design flexibility during research phase while photolithography allows to define the cavities very accurately (typical precision: 5  $\mu\text{m}$ ). The optoelectronic chip (VCSEL or photodiode) was mounted on the heatsink in the cavity using a thermally conductive glue (U 8449-9, Namics Corporation) (c) and then leveled (d). After thermally curing the glue, the chip was covered with a 5  $\mu\text{m}$  thin layer of SU-8 and via's to the contact pads of the chip were ablated in this layer using a KrF Excimer laser (248 nm) (e). The via's were metalized and an electrical fan-out was provided by sputtering a 1  $\mu\text{m}$  copper layer (f). After lithographically patterning the copper, a thin SU-8 protective layer was applied and finally a 7.5  $\mu\text{m}$  thick layer of PI-2525 polyimide was spin-coated (g).

At this point, the packaging of the electronic chip is finished and the resulting flexible foil is ready to be released. However, for constructing the shear sensor, some additional layers are required which are more easily applied when the flexible foil is still fixed on the temporary processing glass carrier. These extra steps are described in the following section.

Since the chip is placed in a cavity, the resulting optoelectronic packaging foil is completely flat. This is important for the fabrication of the shear sensor using these foils: the deformable PDMS sensing layer is spin-coated on these foils, and

when the chip would stick out, this sensing layer would not be completely uniform. In that case, the stress distribution would also not be uniform and the result from Figure 5.18 is not completely valid.

### 5.5.2 Fabricating the shear sensor

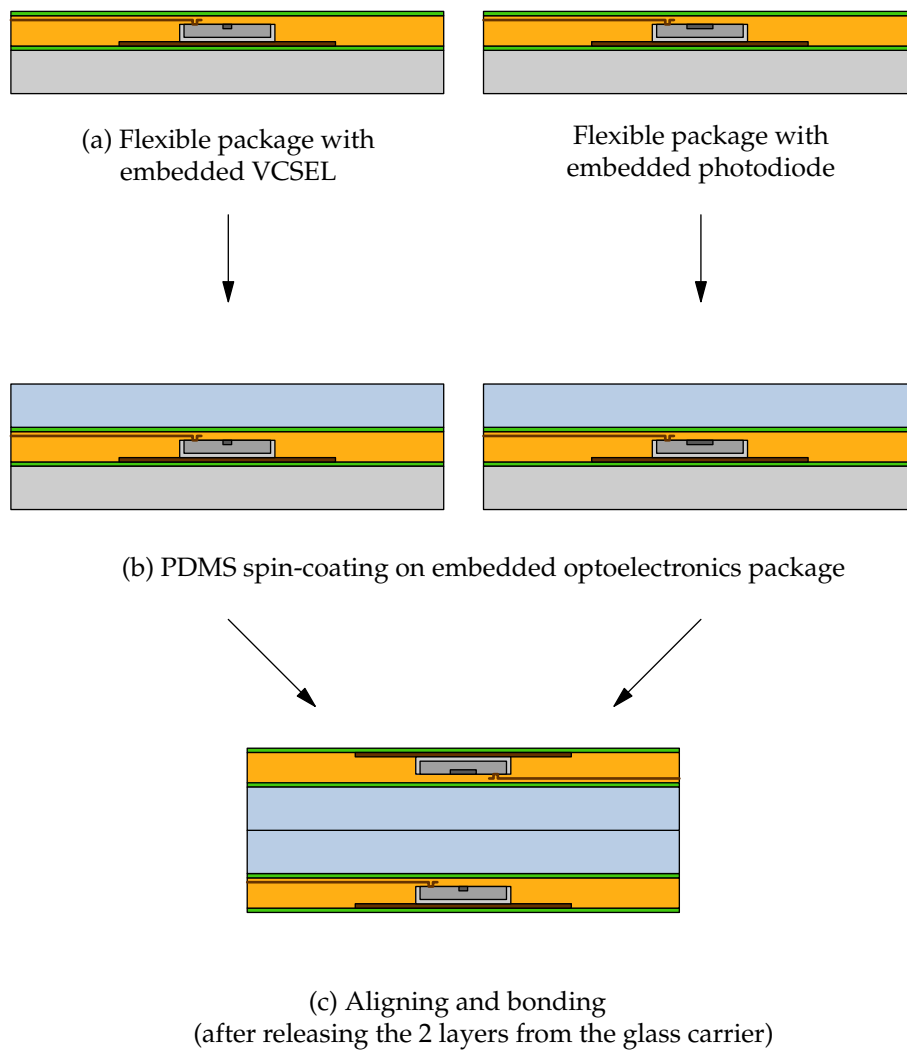


**Figure 5.24** – Additional steps to fabricate the shear sensor, starting from optoelectronics embedded in a thin foil.

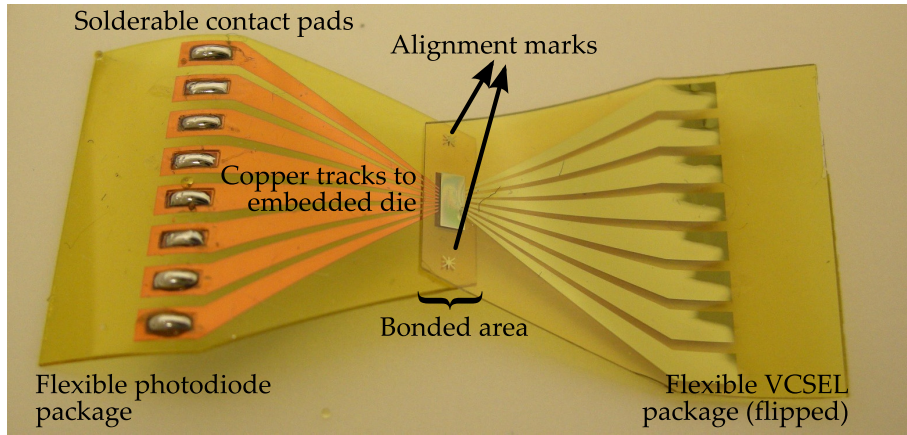


**Figure 5.25** – Finalized flexible shear sensor sample consisting of a flexible photodiode and flexible VCSEL package, separated by a PDMS layer in the bonding area.

### General process overview

Figure 5.24 schematically shows the extra steps needed for fabricating the shear sensor, starting from the embedded optoelectronics in a foil (a). Before releasing the polymer foil with the embedded optoelectronic chips, a polydimethylsiloxane (PDMS) transducer layer was applied first (b). Since PDMS does not adhere to the top layer of polyimide, a primer was used: 1200 OS (Dow Corning). It was applied using a wipe, only leaving a very thin layer. After waiting for 45 min, a 90  $\mu\text{m}$  thick layer of Sylgard®184 was spin-coated on top (by spinning at 700 rpm for 60 s). Both a foil with an embedded VCSEL and a foil with an embedded photodiode were prepared accordingly. The PDMS was cured on a hotplate at 60  $^{\circ}\text{C}$  for 2 h. Then, the electrical contact pads were opened using laser ablation and subsequently the VCSEL and photodiode package were cut-out using a  $\text{CO}_2$  laser so that they could be released from the glass carrier (see Figure 5.27c). Then, the PDMS layers were plasma treated (Diener Pico, 0.8 mbar, 24 s, 190 W 40 kHz generator, gas used: air). Finally, the VCSEL and photodiode package were aligned and the PDMS layers were brought into contact, creating an irreversible bond (c). Figure 5.25 shows the finished shear sensor sample and its flexibility is demonstrated in Figure 5.27d.

In the following paragraphs, more details are provided concerning 2 specific fabrication steps that were outlined in this process overview description: the opening of contact pads and the aligning and bonding of PDMS layers.

### Opening the contact pads and cutting out the flexible package

Copper tracks ending with contact pads are provided to connect the small bond-pads of the embedding optoelectronic chips in the sensor to the electronic driving and read-out circuits. However, this copper layer is deposited before the final polymer protection layers are applied and therefore these pads need to be cleared at the end of the process by removing the polymer layers locally.

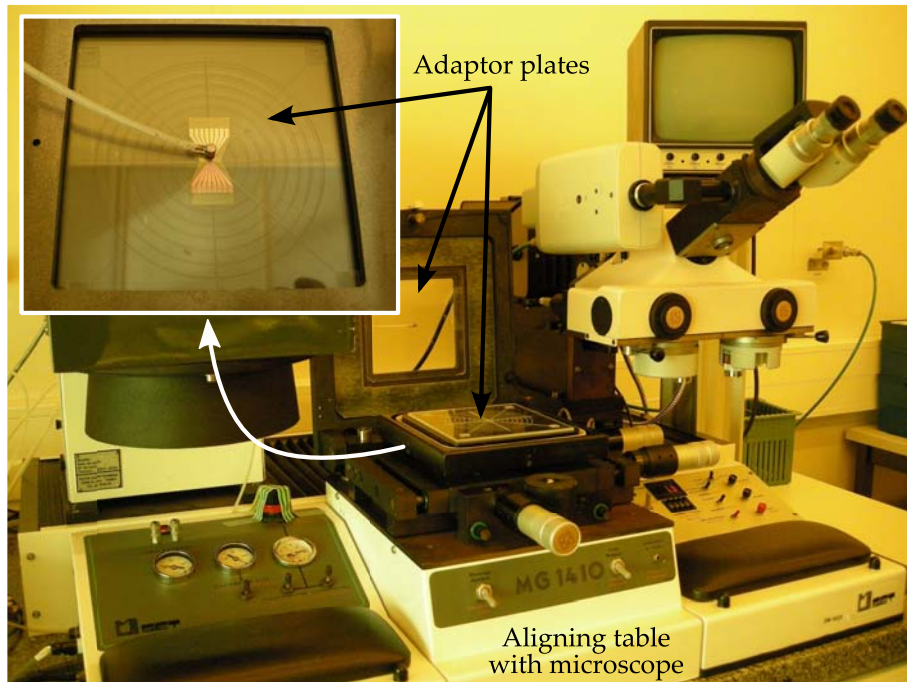
As described previously, the copper contact pads on the package were opened using laser ablation, before releasing the foil from the glass carrier and after applying the PDMS transducer layer. Therefore, an opening needed to be ablated through a layer of PDMS, polyimide and SU-8 selectively without damaging the underlying thin 1  $\mu\text{m}$  copper layer. A CO<sub>2</sub> laser was selected to create this openings since removing Sylgard®184 is only possible using thermal ablation and this laser does not ablate copper.

Since these openings were ablated through PDMS and ablating this material generates a significant amount of debris, a protective layer was spin-coated (4 % PVA powder dissolved in deionized water by weight). In a first ablation step, a CO<sub>2</sub> laser was used to quickly remove the material on top of the copper without damaging the pad. However, a thin layer of polymer (hundreds of nanometer) on top of the pad could not be removed using this laser. Therefore, a KrF Excimer laser was used to remove this residual layer in a second ablation step. The parameters used are summarized in Table 5.4. After the ablation, the protective layer was removed by dissolving in water. Figure 5.27 illustrates the process. Figure 5.27a shows the ablated contact pad before and Figure 5.27b after dissolving the protective PVA layer in water. It can be seen that the amount of visible debris is drastically reduced.

After opening the contact pads, the contours of the resulting flexible VCSEL and photodiode package were cut-out with the CO<sub>2</sub> laser using the same parameters as listed in Table 5.4. Since there was only primer applied on the edge of the glass substrate, the polymer package can be easily peeled off from the glass substrate.

**Table 5.4** – Laser ablation parameters used for opening contact pads by removing polymer layers on top of a 1  $\mu\text{m}$  thin copper layer.

	CO <sub>2</sub> laser	KrF Excimer laser
Energy	level 1, attenuator 90°	200 mJ cm <sup>-2</sup>
Lens demagnification	10x (L1)	10x
Projection mask	3000 $\mu\text{m}$ $\times$ 3000 $\mu\text{m}$	2000 $\mu\text{m}$ $\times$ 2000 $\mu\text{m}$
# pulses/position	8 ( $\approx 3 \frac{\text{mm}}{\text{s}}$ ), 2 times	3 ( $\approx 6.6 \frac{\text{mm}}{\text{s}}$ ), 3 times
Pulse repetition frequency	100 Hz	100 Hz



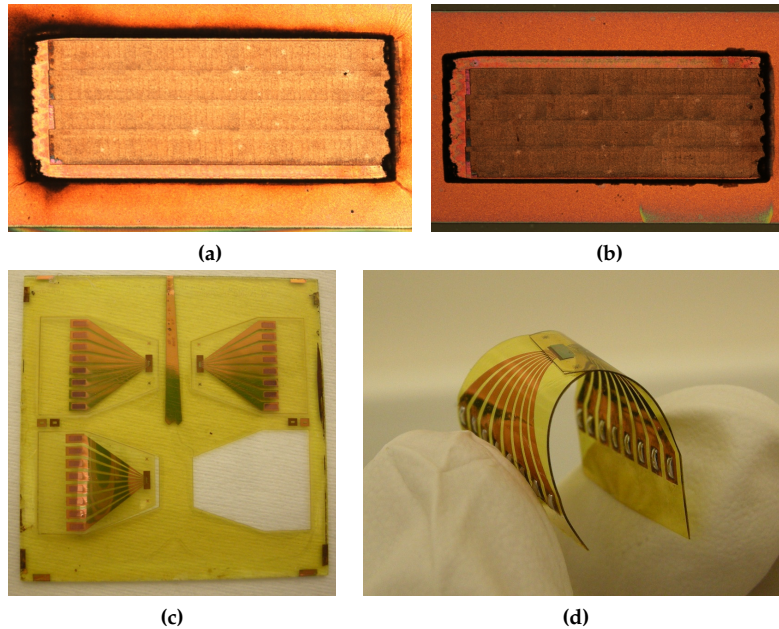
**Figure 5.26** – Aligning two ultra-thin optoelectronic packages using a modified mask aligner setup (close-up: substrate table with aligned flexible optoelectronic packages to be bonded).

Figure 5.27c shows 4 flexible optoelectronic packages processed on a temporary glass substrate and cut-out using the CO<sub>2</sub> laser.

#### Aligning and bonding two PDMS layers

When fabricating the shear sensor, the top PDMS layers on the two flexible substrates with embedded VCSEL and photodiode need to be accurately aligned and bonded (see step (c), Figure 5.24). To bond 2 layers of PDMS, a plasma dry bonding technique is commonly used: 2 smooth PDMS surfaces are plasma treated to create reactive OH-groups [10]. When bringing 2 such treated surfaces in contact, an irreversible bond is created between the PDMS layers.

To accurately apply this procedure, a mask aligner system (SET MG1410) was modified, as depicted in Figure 5.26. An adaptor plate containing an extra vacuum chuck was placed in the mask holder. By providing the extra vacuum connection, this plate was used to hold one flexible embedding package. The other package was fixed in place on the substrate table of the aligner, using another



**Figure 5.27** – Contact pad, opened with CO<sub>2</sub> laser and surface cleaned with KrF Excimer laser (a). After dissolving the protective PVA layer (in water) (b). Releasing the ultra-thin optoelectronic chip package from the temporary carrier (c). Final result: flexible shear sensor consisting of a VCSEL and photodiode package with a PDMS layer in between (d).

adapter plate and the standard vacuum connection. Using the available positioning table and microscope of the aligner system, it was possible to precisely align both flexible embedding packages based on the marks provided on the substrates. Once aligned, the PDMS layers were brought into contact, creating an irreversible bond of the plasma treated layers.

The alignment of the VCSEL and photodiode substrates was performed using alignment marks that were defined along with the pattern definition of the copper tracks. Therefore, these alignment marks were provided in the mask design of the copper pattern so that they are aligned with the active areas of the embedded VCSELs and photodiodes during lithography.

### 5.5.3 Fabrication process evaluation and results

#### Fabricated sensor versions

As described in Section 5.3, the process of implementing an ideal  $(x, y)$ -sensitive shear sensor was performed in 3 phases. First, the technology has been proven

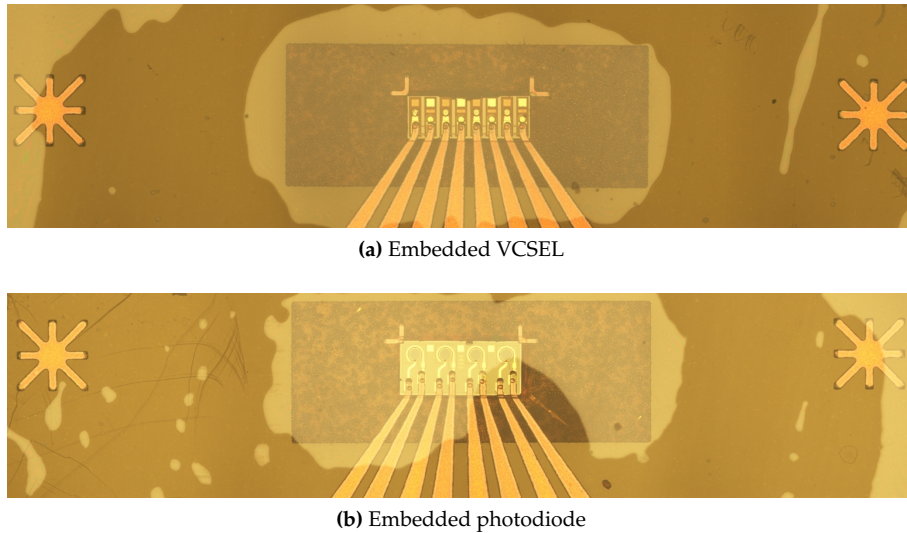


**Figure 5.28** – First generation technology. Top view of the embedded VCSEL and photodiode chips after finishing the process showing the copper contact layer with alignment marks. The spots with different colors on the pictures are caused by imaging through a glass substrate for fixation. Since the substrate is flexible, not all parts were in contact with the glass.

by implementing a one-dimensional, one-directional sensor. Then, the layout of this design was adapted to obtain a proof-of-principle configuration of an  $(x, y)$ -sensitive sensor by covering certain parts of the photodiodes and finally, photodiodes with optimum dimensions were used to construct a truly  $(x, y)$ -sensitive sensor. These generations of prototypes and their differences are described in this section, while the characterization results are reported in the next chapter.

### First generation sensor technology

The first generation technology consists of a one-dimensional, one-directional sensor as obtained by using VCSELs in combination with  $100\ \mu\text{m}$  round photodiodes. Since the used optoelectronic components were available in  $1 \times 4$  arrays, this resulted in 4 VCSEL-PD pairs and hence 4 sensing points per sensor sample. A top view of the embedded components is shown in Figure 5.28. These 2 substrates were then aligned to create the shear sensor shown in Figure 5.25.

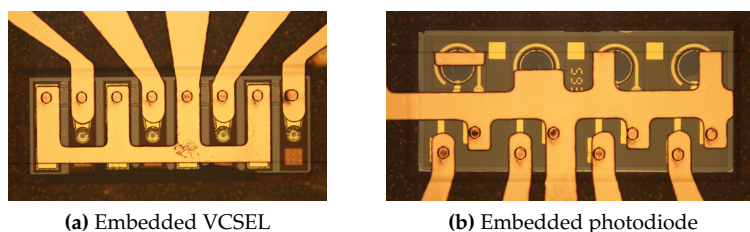


**Figure 5.29** – Second generation technology. Top view of the embedded VCSEL (a) and photodiode (b) chips after finishing the process. Compared to the first generation samples, the photodiodes are now partially covered and the cathode contacts were also connected for the 4 components in the array to reduce the number of copper connections.

### Second generation sensor technology

The second generation sample proves the principle of an  $(x, y)$ -shear sensor using the same embedding technology and components as the first generation. In an attempt to obtain a sensor only sensitive to variations in a certain direction, the photodiodes were partially covered (this concept is depicted in Figure 5.8). The same alignment marks as shown in Figure 5.28 are provided, but this now results in the alignment of the VCSELs above the copper edge in the middle of the photodiode. All the cathodes in the array were also connected in order to reduce the number of copper connections. In any case, the cathodes are connected internally on chip for the VCSEL array chip.

### Third generation sensor technology

The third generation technology aims at a truly  $(x, y)$ -shear sensor design using one or multiple MPD250S  $250\ \mu\text{m} \times 250\ \mu\text{m}$  square detectors from Cosemi Technologies Inc.[11]. The process of thinning down and embedding these components is slightly different since one of the photodiode contacts is provided at the back of the chip compared to the 2 top contacts on the previously employed VCSEL and photodiode components. When thinning down this component, its back-contact is removed and needs to be reapplied. This research is outside the scope of this work and therefore, the third generation technology was evaluated by embedding the detectors in a rigid FR-4 (instead of a flexible) substrate with thick build-up layers avoiding the need for chip thinning. Processing these thick layers on a flexible substrate is not possible due to the excessive stresses that are introduced. However, the thinning of back-contacted chips has recently been demonstrated at the CMST research lab and this technology can therefore be applied for embedding the detectors so that a flexible version of the third generation sensor can also be obtained in the future. This chip-thinning process will be ex-

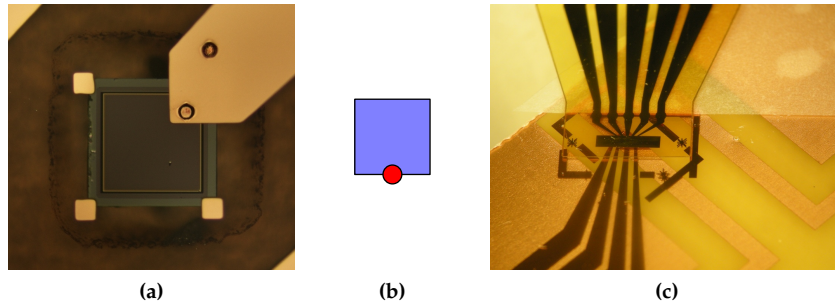


**Figure 5.30** – Third generation technology: (a) square photodiode die embedded in a rigid FR-4 substrate, (b) schematic sensor configuration: a VCSEL initially aligned on the edge of a square photodiode as proposed in Section 5.3.3, (c) a flexible VCSEL package bonded on the FR-4 substrate with an embedded photodiode yielding the proof-of-principle shear sensor.

plained in the PhD thesis of Bram Van Hoe.

Configuration 1 using 1 photodiode and 1 VCSEL for each orthogonal direction was chosen based on the concluding considerations of Section 5.3.3, and this configuration is schematically depicted in Figure 5.30b. Therefore, a square photodiode was embedded in a rigid substrate (see Figure 5.30a) while the VCSEL chip was obviously embedded in a flexible package. Similarly as for the first and second generation technology, both substrates were then covered with a layer of PDMS and subsequently aligned and bonded (see Figure 5.30c).

## 5.5.4 Fabrication process improvements

### Mechanical stress elimination

Due to the different CTE's (coefficient of thermal expansion) of the used materials for embedding the optoelectronic chips, mechanical stresses exist in the flexible substrate. Although these stresses are very limited, resulting in only a slight curving of the foil (see Figure 5.31c), they sometimes introduce problems when aligning the 2 flexible packages to create the shear sensor. The region around the embedded optoelectronic chip exhibited the largest stress due to the presence of various materials with different CTE's (a Gallium Arsenide (GaAs) chip (CTE 6 ppm/°C), a copper heatsink (about 17 ppm/°C) and the PI-2525 (40 ppm/°C) and SU-8 (52 ppm/°C) embedding layers). This local mechanical deformation sometimes results in a small enclosed air bubble at the location of the chip when bonding the 2 PDMS layers (see Figure 5.31a).

This issue was solved by selecting different materials to match all CTE's as closely

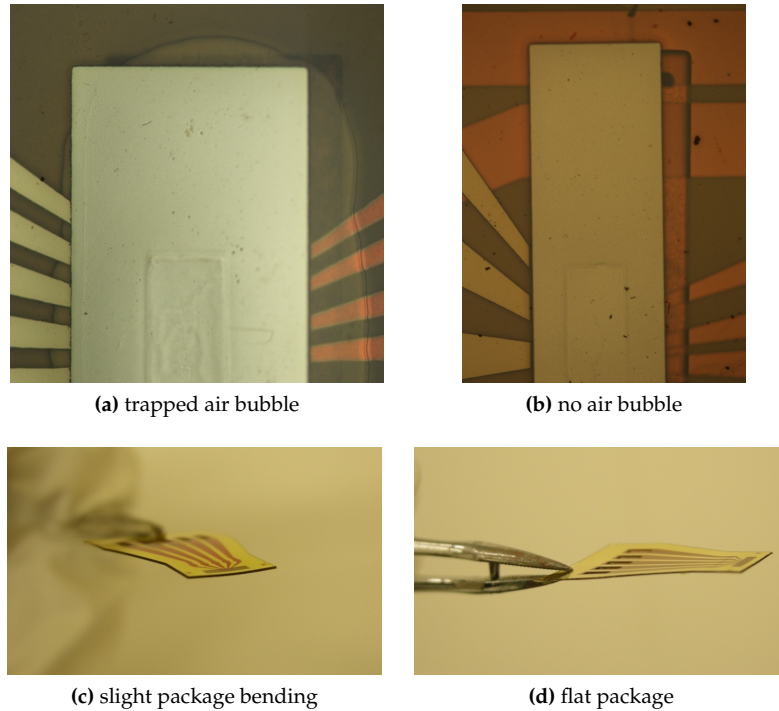


**Figure 5.31** – (a) Air bubble present between the 2 PDMS layers on the photodiode and VCSEL flexible package when using the SU-8+PI2525 embedding process. (b) When polyimide PI2611 was used as embedding material, no trapped air was encountered. (c) SU-8+PI2525 technology: slight bending of the flex in chip region due to stresses. (d) PI-2611 technology: stress eliminated and very flat package.

as possible. Polyimide PI-2611 (HD Microsystems) was finally selected instead of the initial process based on a combination of PI-2525 and SU-8 for embedding the optoelectronic chips. Although the use of this material introduces some extra difficulties in the fabrication process, the resulting flexible foil exhibits considerably less mechanical stress, since the CTE of PI-2611 is very low ( $3 \text{ ppm}/^\circ\text{C}$ ) and hence better matched with the CTE of the GaAs chip. Figure 5.31c shows a thinned VCSEL embedded using the SU-8/PI-2525 based process while Figure 5.31d shows the same type of thinned VCSEL chip but embedded using the PI-2611 based technology. Particularly when considering the region around the embedded chip, it can be noticed that the PI-2611 based package is completely flat while the SU-8/PI-2525 combination shows slight bending of the package due to internal stresses.

More details concerning the use of PI-2611 for embedding optoelectronic chips is

described in the framework of the PhD of Rik Verplancke.

### Electrical connection problem

As illustrated in Figure 5.2, the sensor exhibits electrical connections on both sides of the deformable transducer layer. The bottom layer of the sensor is typically kept fixed, while the top layer of the sensor moves during sensor operation. Therefore, the electrical interconnections on this top layer also need to be movable.

To achieve this, the interconnections on the top layer can be implemented as meandering tracks so that they are able to deform with the transducer layer [12, 13, 14]. Another option is rerouting the top layer interconnections to the bottom layer, through the transducer layer using vias filled with (stretchable) conductive silicone paste. Work is currently being performed to create laser ablated vias through the top and transducer layer, down to the bottom layer. These vias will then be filled with conductive silicone.

Finally, this issue can also be avoided by redesigning the sensor to work in reflection instead of transmission, see Section 5.3.5. In that case, all electrical connections are concentrated on the bottom layer and no connections are needed on the top layer. Solving the electrical connection problem enables to use the sensor in a matrix configuration for artificial skin. Furthermore, the size of the actual sensing area can be very small, when only interconnections need to be provided on the bottom layer of the sensor. Now, the total size of the sensor seems rather large, but this is only due to the electrical interconnections to the active components

## 5.6 Conclusions

---

This chapter described the design and fabrication of mechanically flexible optical tactile shear sensors. The sensor principle is based on the changing optical coupling between a light source and detector depending on their relative lateral position. A deformable transducer layer was used to translate mechanical shear stresses into these lateral displacements. Therefore, the sensor design was split up in an optical and mechanical study. Three generations of technologies were described, where the first generation is a one-dimensional, one-directional sensor and the last generation consists of a fully  $(x, y)$ -sensitive shear sensor able to measure shear force magnitude and direction.

First, the optical architecture was described. Miniature optoelectronic VCSEL and photodiode chips were selected to demonstrate the sensor principle with the smallest possible dimensions. Models of these components and the resulting sensor were constructed and the optimum vertical distance between the VCSEL and photodiode was found to be 200  $\mu\text{m}$ . This results in a transducer layer thickness

of 180  $\mu\text{m}$  since the VCSEL and photodiode are covered with a 10  $\mu\text{m}$  protective polymer covering layer. Furthermore, several concepts for extending the sensor operation to measure shear stress vectors (magnitude and direction) were evaluated. This resulted in a new sensor design based on square photodiodes and 2 “sensing points”, one for measuring the  $x$ -component and another for measuring the  $y$ -component of the shear stress vector.

Then, the mechanical behavior was studied. The selected transducer material, Sylgard®184 resulted in a useful 300 kPa dynamic range for tactile sensing (with the current sensor dimensions) and a shear sensor nearly insensitive to normal pressure. Furthermore, it was shown that the dynamic range and sensitivity with respect to shear stress could be tuned by selecting a different material with optimum mechanical properties (shear modulus).

Finally, the technology for constructing the sensor was described. The process consists of embedding thinned optoelectronic dies in flexible polymer foils. Two foils, one with a VCSEL and one with a photodiode were then cut out using a  $\text{CO}_2$  laser and bonded with their active areas facing each other, separated by the transducer material.

*Critical Discussion.* A tactile shear stress sensor was developed for possible application in prosthetic sockets. Therefore, it was made ultra thin, flat and without protrusions to avoid irritation of the skin. Furthermore, by choosing an optical sensing principle, a miniaturized and highly sensitive sensor was demonstrated. As a suggestion for future work, however, some changes in the sensor design and fabrication process have to be made before becoming a potential commercial product. Firstly, the fabrication of the sensor should be transferred to a lower-cost (roll-to-roll) manufacturing process. Secondly, dedicated optoelectronic components have to be developed (especially photodiodes) to optimize the sensor operation. Finally, a strategy for electrically interconnecting different sensors has to be studied.

## References

---

- [1] V. Hayward and J. M. Cruz-hernandez, “Tactile display device using distributed lateral skin stretch,” 2000, pp. 1309–1314.
- [2] B. V. Hoe, G. V. Steenberge, E. Bosman, J. Missinne, T. Geernaert, F. Berghmans, D. Webb, and P. V. Daele, “Optical fiber sensors embedded in flexible polymer foils,” F. Berghmans, A. G. Mignani, and C. A. van Hoof, Eds., vol. 7726, no. 1. SPIE, 2010, p. 772603. [Online]. Available: <http://link.aip.org/link/?PSI/7726/772603/1>
- [3] A. Koulaxouzidis, M. Holmes, C. Roberts, and V. Handerek, “A shear and vertical stress sensor for physiological measurements using fibre bragg grat-

- ings," vol. 1, 2000, pp. 55 –58 vol.1.
- [4] R. Suresh and S. C. Tjin, "Effects of dimensional and material parameters and cross-coupling on fbg based shear force sensor," *Sensors and Actuators A: Physical*, vol. 120, no. 1, pp. 26 – 36, 2005. [Online]. Available: <http://www.sciencedirect.com/science/article/B6THG-4F1J8SG-2/2/2e2a5108526f459e786de423602c9734>
- [5] J. C. Lotters, W. Olthuis, P. H. Veltink, and P. Bergveld, "The mechanical properties of the rubber elastic polymer polydimethylsiloxane for sensor applications," *Journal of Micromechanics and Microengineering*, vol. 7, no. 3, p. 145, 1997. [Online]. Available: <http://stacks.iop.org/0960-1317/7/i=3/a=017>
- [6] E. Bosman, "Integration of optical interconnections and opto-electronic components in flexible substrates," Ph.D. dissertation, Ghent University, 2010.
- [7] Ulm-Photonics. (Accessed 2011) Products. [Online]. Available: <http://www.ulm-photonics.com/>
- [8] Enablece. (Accessed 2011) Photodiode products. [Online]. Available: <http://www.enablece.com/components/solutions/transmission/photodiodes>
- [9] R. Hibbeler, *Statics and mechanics of materials*. Prentice Hall, 1993.
- [10] S. Bhattacharya, A. Datta, J. Berg, and S. Gangopadhyay, "Studies on surface wettability of poly(dimethyl) siloxane (pdms) and glass under oxygen-plasma treatment and correlation with bond strength," *Microelectromechanical Systems, Journal of*, vol. 14, no. 3, pp. 590 – 597, june 2005.
- [11] Cosemi Technologies Inc. (Accessed 2011) Products. [Online]. Available: <http://www.cosemi.com/gaas.html>
- [12] M. Gonzalez, F. Axisa, M. V. Bulcke, D. Brosteaux, B. Vandeveld, and J. Vanfleteren, "Design of metal interconnects for stretchable electronic circuits," *Microelectronics Reliability*, vol. 48, no. 6, pp. 825 – 832, 2008, thermal, Mechanical and Multi-physics Simulation and Experiments in Micro-electronics and Micro-systems (EuroSimE 2007). [Online]. Available: <http://www.sciencedirect.com/science/article/pii/S0026271408000760>
- [13] T. Loher, D. Manassis, R. Heinrich, B. Schmied, J. Vanfleteren, J. DeBaets, A. Ostmann, and H. Reichl, "Stretchable electronic systems," in *Electronics Packaging Technology Conference, 2006. EPTC '06. 8th*, dec. 2006, pp. 271 –276.
- [14] F. Bossuyt, J. Guenther, T. L. her, M. Seckel, T. Sterken, and J. de Vries, "Cyclic endurance reliability of stretchable electronic substrates," *Microelectronics*

*Reliability*, vol. 51, no. 3, pp. 628 – 635, 2011. [Online]. Available:  
<http://www.sciencedirect.com/science/article/pii/S0026271410005226>



# 6

## Tactile shear sensor characterization

*This chapter deals with the functional characterization of the tactile shear stress sensors as developed in the previous chapter. The actual sensor behavior is compared with the simulated values, for the three generations of sensors.*

### 6.1 Introduction

---

The developed shear sensor is functionally characterized in this chapter. The first part reports on the relevant properties of the used optoelectronic components. Next to the electrical characteristics (the current versus voltage or IV-curve), the optoelectronic characteristics were measured. For the embedded VCSELs, the emitted optical power versus driving current and for the photodiodes, the photocurrent versus incident optical power are described (LI-curves). Furthermore, the actual beam profiles of the VCSELs were measured using a goniometric radiometer. This information was used to validate the proposed simulation model which is based on “ideal” Gaussian beam profiles, as presented in Chapter 5.

The second part of the chapter describes the actual functional testing of the sensor. These measurements are grouped in accordance with the 3 sensor generations as described in Section 5.5.3. For all 3 generations of sensors, the response curve in function of lateral displacement was recorded serving as an easy comparison with the simulated data. The response to actual shear force was also measured on the first generation sensors, to illustrate the linear dependency between

lateral displacement and shear force. The third generation sensor was used to proof the principle of an  $(x, y)$ -sensitive sensor, which was functionally validated by recording the sensor response curves in function of the direction of lateral displacement.

## 6.2 Characterization of embedded optoelectronics

### 6.2.1 1x4 multimode VCSEL array chip

The used chips contain arrays of 4 multi-transverse mode VCSELs on a  $250\ \mu\text{m}$  pitch emitting at  $850\ \text{nm}$ , fabricated by Ulm Photonics [1]. The chip measures  $1\ \text{mm} \times 0.35\ \text{mm}$  and is shown in Figure 6.1. Since the chip contains only top contacts, it is ideally suited for thinning down and embedding in thin flexible polymer layers. The process of thinning down optoelectronic components is described in detail in the PhD thesis of Erwin Bosman [2]; in this dissertation, only the characteristics of these embedded thin chips, as they appear in the constructed shear sensor, are investigated.

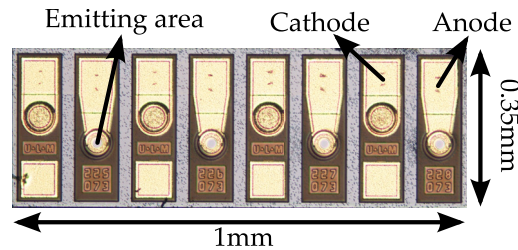


Figure 6.1 – Magnified view of the ULM-Photonics 1x4 multimode VCSEL chip.

#### Electrical and optical characteristics

The electrical characteristics of the VCSELs were measured using a Source Measure Unit (SMU; Keitley Model 2400) while the emitted optical power was captured with a power meter (Newport Model 1930C). Both devices were controlled by a pc in order to automate the measurements.

A first graph (see Figure 6.2) shows the electrical characteristics of the VCSELs, being the current in function of the voltage over the component (the “IV-curve”). Since a typical diode behavior can be noticed, VCSELs are commonly driven with a fixed current source instead of a voltage source.

A second graph, shown in Figure 6.3, depicts the optical output of the VCSEL in function of the driving current (“LI-curve”). The threshold current is about  $1\ \text{mA}$

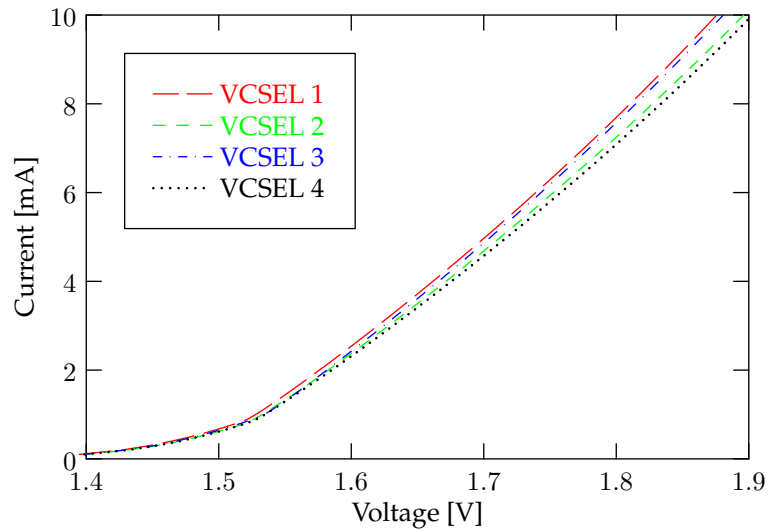


Figure 6.2 – Electrical characteristics of the 4 VCSELs in an embedded array chip: current in function of the voltage over the component (IV-curve).

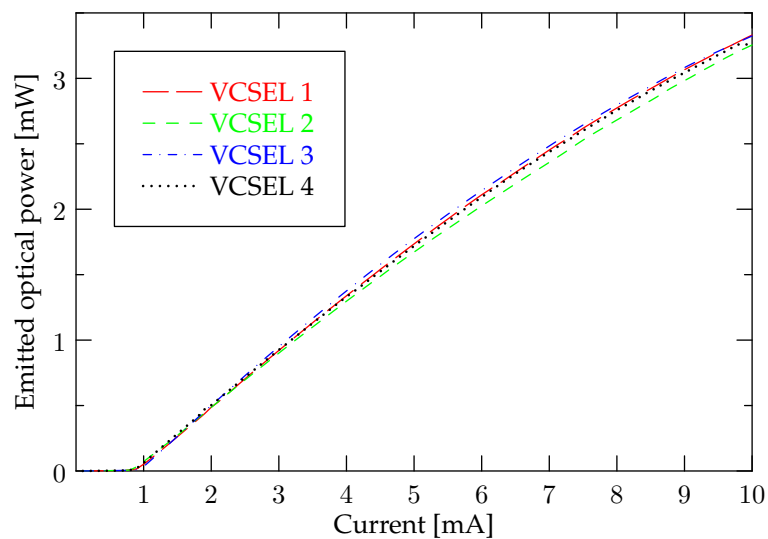
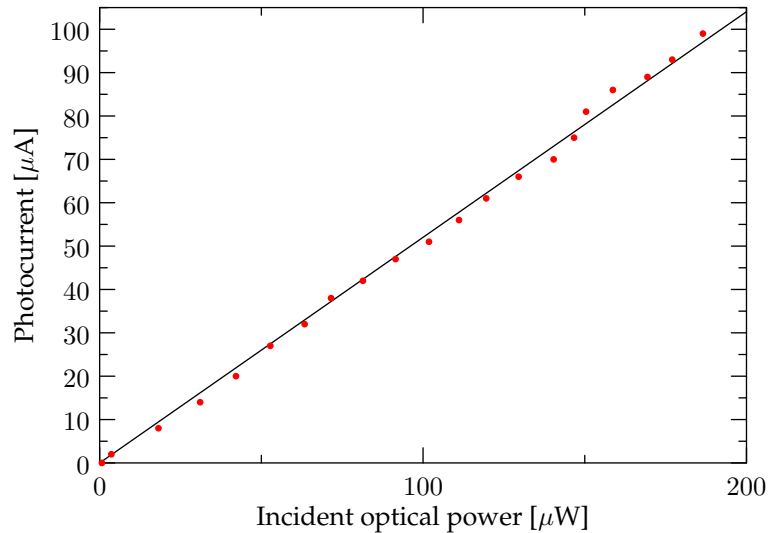


Figure 6.3 – Optoelectronic characteristics of the 4 VCSELs in an embedded array chip: emitted optical power in function of current through the component (LI-curve).



**Figure 6.4** – Optoelectronic characteristics of an embedded PD chip: photocurrent in function of incident optical power (LI-curve).

and the relation between driving current and emitted power is nearly linear, with a small flattening effect for higher currents. This graph shows the total emitted optical power in all directions; the distribution of the power over different directions, the “beam profile”, was also studied and these results are described further on in this chapter (see Section 6.2.4).

## 6.2.2 1x4 100 $\mu\text{m}$ $\varnothing$ photodiode array chip

A first type of used photodiodes consisted of 1x4 arrays of circular 100  $\mu\text{m}$  diameter detectors on a 250  $\mu\text{m}$  pitch, fabricated by Enablence [3]. The chip measures 1 mm  $\times$  0.45 mm and is shown in Figure 6.5a. Since the chip contains only top contacts, it is ideally suited for thinning down and embedding in thin flexible polymer layers, like the VCSEL chip. The component is a p-i-n GaAs photodiode with an antireflection coating for 850 nm wavelength light.

### Optoelectronic characteristics

The optoelectronic response curve of the photodiode was determined by illuminating the photodiode with a calibrated amount of 850 nm laser light, using a 50  $\mu\text{m}$  multimode optical fiber aligned above the photodiode active area. The reverse voltage over the photodiode was kept constant at  $-2\text{ V}$  and the resulting photocurrent was measured as a function of the incident optical power (“LI-

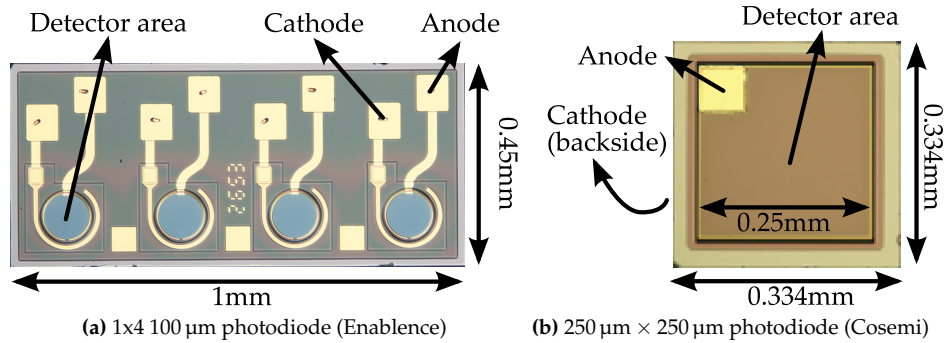


Figure 6.5 – Magnified view on the different bare die photodiodes used.

curve”), see Figure 6.4. This curve was only recorded for low values of the incident power due to limitations of the setup. However, the photodiode also has a linear behavior in the rest of the operating region, i.e. up to a photocurrent of at least a few mA. The slope of this LI-curve determines the responsivity, i.e. the amount of photocurrent generated per unit of incident optical power. For an embedded photodiode, a responsivity of  $0.52 \text{ A W}^{-1}$  was measured.

Although the applied reverse voltage does not significantly affect these (static) response curves, it influences the effective capacitance so that this effect becomes important if a rapidly changing amount of optical power is incident on the photodiode in high-speed dynamic systems.

### 6.2.3 250 $\mu\text{m}$ square photodiode chip

Another type of photodiode used in this dissertation is depicted in Figure 6.5b. The chip contains a single photodiode component with a square active area of approximately  $250 \mu\text{m} \times 250 \mu\text{m}$ . Except for the different active area dimensions, its optoelectronic behavior is nearly identical as for the circular photodiode described above and the analogous discussion is therefore not repeated here.

### 6.2.4 Validation of the sensor simulation model

#### Multimode VCSEL radiation patterns

The actual VCSEL far field angular beam profile was determined using a goniometric radiometer, yielding the optical intensity emitted by the VCSEL in function of a certain direction (solid angle). To represent the pattern, it is convenient to project on a plane perpendicular to the main VCSEL beam direction. Since the

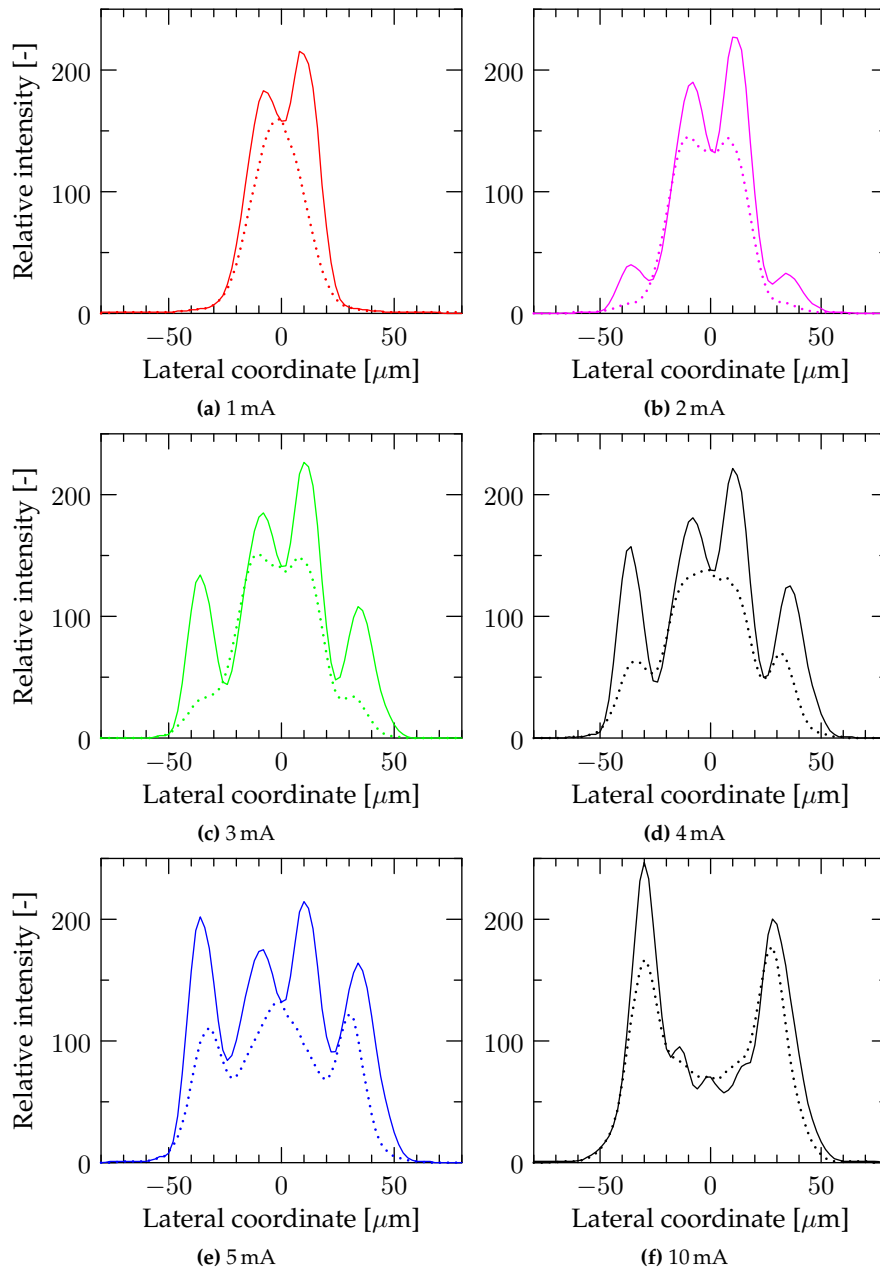


**Figure 6.6** – Measured VCSEL far field beam profile: cross-sections in two orthogonal directions (solid and dotted line), projected on a plane at  $200\ \mu\text{m}$  from the VCSEL, for different VCSEL driving currents. (f) was measured with a different gain, meaning that intensity values cannot be compared with the other graphs.

beam is diverging, this projection is determined by the beam divergence angle (see Table 6.1) and therefore changing depending on the considered distance from the VCSEL. For constructing the shear sensor, the detector is typically placed at 200  $\mu\text{m}$  from the VCSEL, as calculated in the previous chapter. Figure 6.6 shows a cross-section (in 2 orthogonal directions) of this beam profile, projected on such a plane at 200  $\mu\text{m}$  from the VCSEL. It can be seen that, when the current is increased, more modes appear and the beam profile becomes increasingly irregular. Since the width of the separate peaks that appear in the profile are much smaller than the detector area, they will be averaged out. Therefore, the beam width and the total intensity emitted by the VCSEL are the most important parameters considering the sensor characteristics.

The divergence angle of the beam was defined as the single sided angle wherein 50 % of the optical power is confined. This angle depends on the driving current and was calculated from the goniometric radiometer data, see Table 6.1.

#### Sensor response simulation using actual radiation patterns

The actual VCSEL beam profile was used to simulate the influence on the shear sensor characteristics, compared to Section 5.3, where an ideal Gaussian beam was considered (first generation sensor design). The same model (see formula 5.1) was used, but the ideal Gaussian beam function was replaced by the actual measured values. Figure 6.7 shows the sensor response in function of the VCSEL-to-photodiode vertical distance  $d$ , similarly to Figure 5.4, where an ideal Gaussian beam was considered. Both figures show similar sensor behavior: with increasing VCSEL-to-photodiode distance, the sensitivity decreases but the dynamic range increases. However, in Figure 6.7, the influence of the multimodal

**Table 6.1** – Beam divergence angles calculated from the goniometric radiometer data.

Driving current [mA]	divergence angle [°]
1	3
2	4
3	5
4	5.5
5	6
6	6.5
7	7
8	7.1
9	7.4
10	7.8

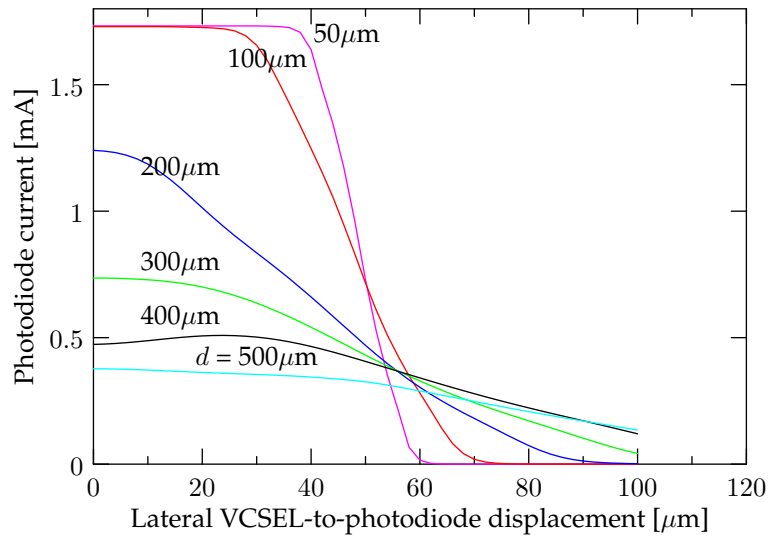


**Figure 6.7** – Simulation showing the influence of the VCSEL-to-photodiode vertical distance  $d$  on the sensor characteristics, using the actual VCSEL radiation pattern as input (VCSEL driving current: 5 mA).

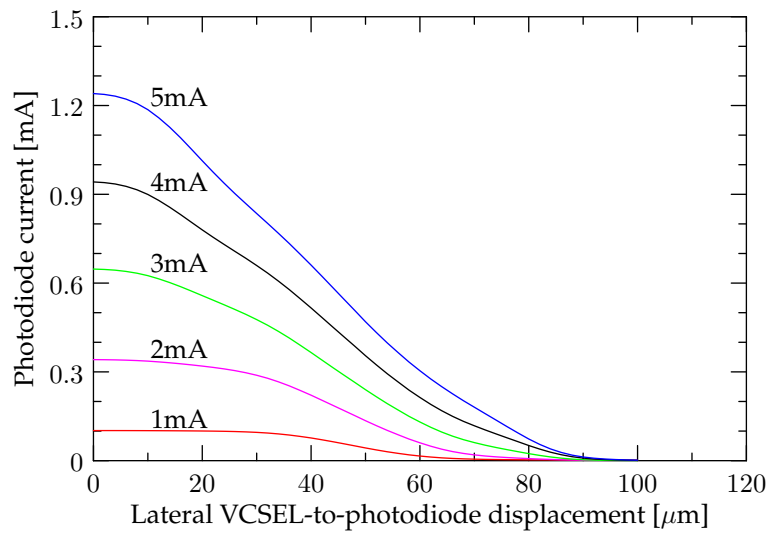


**Figure 6.8** – Simulation showing the influence of the VCSEL driving current on the sensor characteristics, using the actual VCSEL radiation pattern as input (VCSEL-to-photodiode distance: 200  $\mu\text{m}$ ).

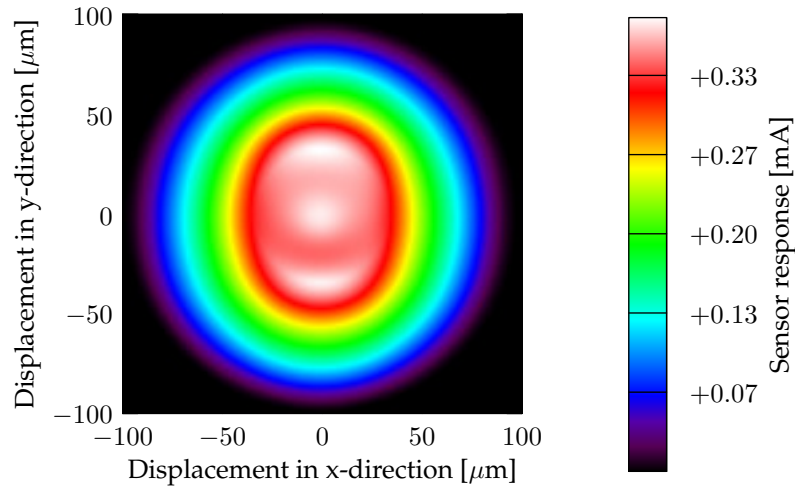


**Figure 6.9** – Simulation showing the two-dimensional shear sensor response, using the actual VCSEL radiation pattern as input (VCSEL driving current: 5 mA, VCSEL-to-photodiode distance  $d=500\ \mu\text{m}$ ).

VCSEL behavior can be observed. For example, the sensor response curve for a VCSEL-to-photodiode distance of  $400\ \mu\text{m}$  is non-monotonous: since the VCSEL beam is wider at larger distances, the intensity variations as seen on Figure 6.6 also appear wider and are not averaged out completely by the photodiode. The fact that the response is monotonous again at  $500\ \mu\text{m}$  is a coincidence. As explained in Section 5.3, the one-dimensional response is obtained by evaluating the two-dimensional sensor response on a line (the  $x$ -axis was chosen therefore). This two-dimensional sensor response for  $d = 500\ \mu\text{m}$  is depicted in Figure 6.9. When moving in the  $x$ -axis direction, the response is monotonous, but this is not the case when moving in the  $y$ -direction. To avoid this undesirable sensor behavior, the detector (acting as an averaging function for the VCSEL beam in the shear sensor) must not be placed too far from the VCSEL. As was already explained in Section 5.3, a distance  $d$  of  $200\ \mu\text{m}$  was therefore chosen, furthermore balancing sensor sensitivity and dynamic range.

### 6.3 Sensor functional testing

This section describes the characterization of the actual sensor prototypes and is subdivided according to the 3 fabricated sensor generations as outlined in Section 5.5.3.

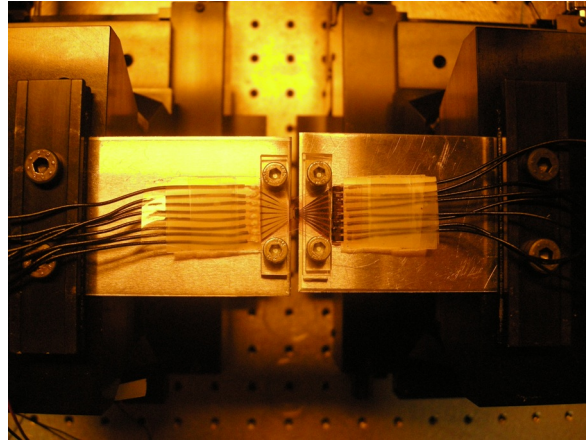


**Figure 6.10** – First setup for testing the sensor response in function of an applied lateral displacement. Both sides of the sample were mounted on a translation stage; the left stage was kept stationary and the right stage was used to induce displacements.

### 6.3.1 First generation sensor

#### Sensor response vs. lateral displacement

**Test setup and conditions** The most straightforward method to test the sensor is applying a known displacement and simultaneously recording the sensor response (i.e. the photodiode current). Therefore, a shear sensor sample was fixed to a stationary platform on one side and fixed to a precision translation stage on the other side (see Figure 6.10). For fixation, the sample was clamped between 2 PMMA blocks on both sides, and tightened with screws. During a measuring cycle, the stage was moved so that the sensor was stretched and subsequently relaxed again. The photodiodes were inversely polarized at  $-2\text{ V}$  and read out using a Source Measure Unit (SMU). Both the translation stages and the SMU were controlled and read out synchronously using a dedicated Labview program.

The advantage of this setup is that the sample can be tested directly, without modification of the sensor as was needed for the second setup using the Dage bondtester. However, the sample needs to be clamped on both sides, which is considerably different as for the actual applications of the sensor.

These measurements were performed on a sensor sample from the first generation technology with an array of round photodiodes and VCSELs initially aligned with the photodiodes (see Section 5.5.3 for an overview of the available samples).

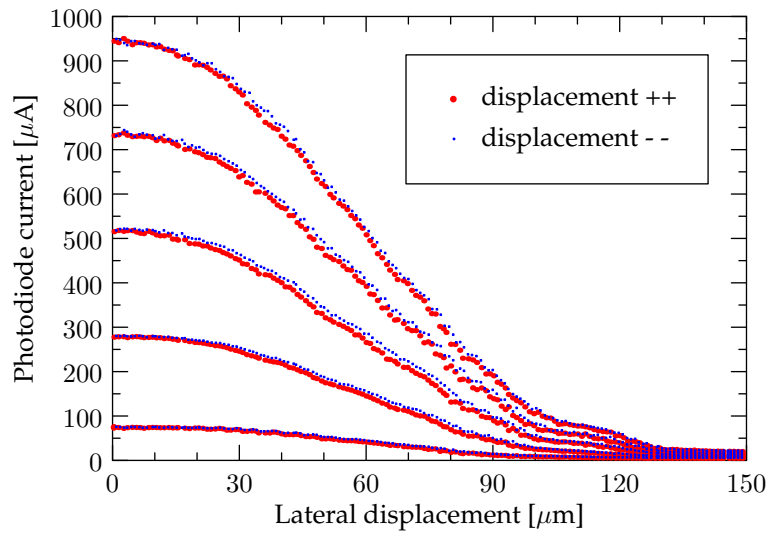


**Figure 6.11** – Sensor response (i.e. photodiode current) versus displacement for different VCSEL driving currents.

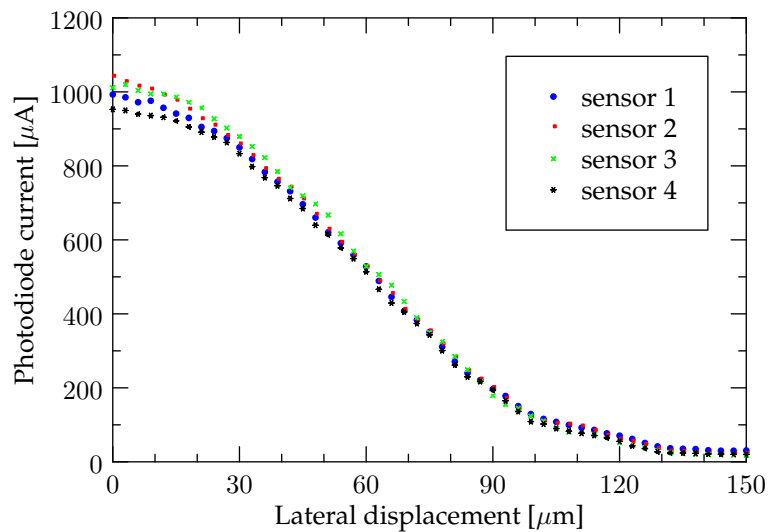


**Figure 6.12** – Sensor response (i.e. photodiode current) versus displacement for different sensor points on the array chip. VCSEL driving current: 5 mA.

**Results and discussion** The results corresponding with different driving currents of one VCSEL in the array are plotted in Figure 6.11. A range of driving currents from 1.5 mA to 5 mA were tested since simulations predicted different sensor behavior corresponding with different VCSEL driving currents.

It can be seen that there is a small difference in response between increasing and decreasing displacement. However, this effect is mainly not due to hysteresis but due to the fact that a perfect rigid clamping of the sensor is not possible. This hypothesis was verified by adapting the clamping conditions of the sample under test and it was clearly seen that the difference in response between increasing and decreasing displacement was changing.

The sensor response is clearly dependent on the driving current through the VCSEL. At lower powers, the beam is less powerful and the opening angle is lower. Compared to higher driving currents, the beam is smaller with respect to the photodiodes and therefore yielding less sensitivity and usable dynamic sensor range. As predicted by the simulations in Section 5.3.1, a driving current of 5 mA yields a better dynamic range and sensitivity. Furthermore, the shape of the sensor response is similar to the corresponding simulated curves from Figure 5.5.

Figure 6.12 shows the responses from the different photodiodes in the array, for a 5 mA driving current of the corresponding VCSEL. There is little variation in the linear part of the range (from 25 to 100  $\mu\text{m}$ ), suggesting that the VCSEL beam is not significantly different between different VCSELs on the same chip. This linear part of the range is the working range that can be used for sensing. As discussed in the previous chapter, an initial misalignment between VCSEL and photodiode needs to be implemented so that the system is usable for sensing. In the case of this experiment, the optimum initial offset in alignment would be about 60  $\mu\text{m}$  yielding the same sensor response as in Figure 6.11 but shifted by 60  $\mu\text{m}$  to the left. When no shear stress or displacement is applied, the photodiode current is about half of the maximum value, while the photodiode current increases or decreases nearly linearly when applying displacements to the left or right respectively.

### Sensor response vs. applied shear force

**Test setup and conditions** In order to characterize the sensor in terms of applied shear force, a different setup was constructed. A Dage Series 4000 bondtester with BS100 cartridge was used to apply a controlled displacement and to measure the resulting shear force. Simultaneously, a Source Measure Unit (SMU) was used to register the sensor response (i.e. the photocurrent from the photodiode, inversely polarized at  $-2\text{ V}$ ). To easily apply the controlled shear force, a cylinder of 2.7 mm diameter was glued on the moving top part of the active sensor area. Furthermore, the flexible sensor sample under test was glued onto a rigid substrate to improve the repeatability of the measurements. The

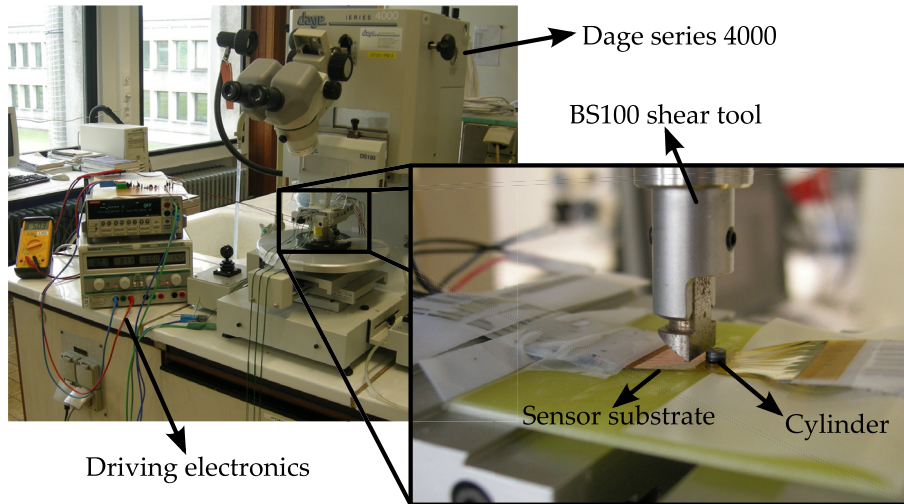


**Figure 6.13** – Setup for testing the sensor response in function of an applied shear force. The sample was clamped in a holder while a shearing tool was used to apply a displacement on the sample by pushing against the cylinder.

Dage setup is depicted in Figure 6.13 with a close-up on the shearing tool and the sample configuration. The experiments were performed for VCSEL driving currents ranging from 1.2 mA to 5 mA.

**Results and discussion** Both the sensor response with respect to displacement and applied shear force was measured. The sensor response to displacement can directly be used to compare with the simulated values, as obtained in Section 5.3.1. Instead, the response of the sensor to shear force is more useful considering the real applications where mainly shear stresses are measured instead of lateral displacements. Nevertheless, the relation between the stress-based and displacement-based sensor response are given by the transducer material (Sylgard®184) mechanical properties, as discussed in the previous chapter.

The measured and simulated curves are plotted in Figure 6.14, showing the photodiode current versus the lateral displacement of the VCSEL and photodiode. To facilitate the comparison between the simulated and measured curves, some minor data processing was performed on the measured values. First, only a limited number of measured data points are shown not to overload the graph. Second, the simulated curves were scaled based on the actual emitted VCSEL power in function of the driving current. Finally, the measured curves were shifted to eliminate the displacement offset resulting from the variation in initial misalignment of the shear tool. Taking these corrections into account, it can be seen that the

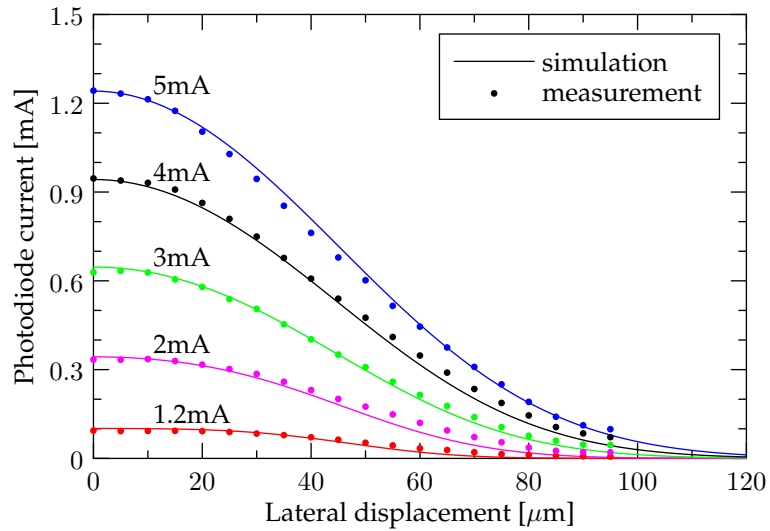


Figure 6.14 – Sensor response (i.e. photodiode current) versus displacement for different VCSEL driving currents: comparison between the simulated and measured data.

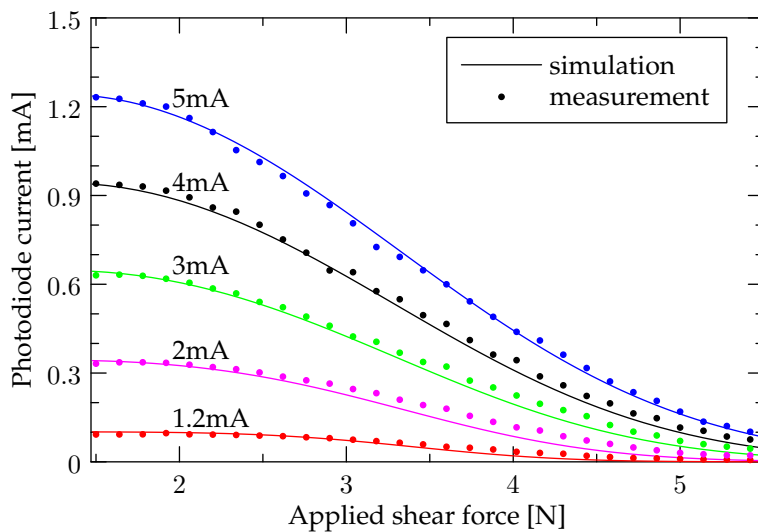


Figure 6.15 – Sensor response (i.e. photodiode current) versus applied shear force for different VCSEL driving currents: comparison between the simulated and measured data.

measured response matches well with the simulated response. The same conclusions can be drawn as in Section 6.3.1: a higher VCSEL driving current results in a higher sensitivity and dynamic range.

Figure 6.15 displays the measured sensor response versus shear force applied by the Dage shear tool. These curves are clearly similar to those of Figure 6.14 since the mechanical relationship between displacement and shear stress is linear for the used Syglard®184 transducer material. Only data points for forces higher than 1.5 N are shown since the Dage software did not record data below this threshold value. The simulated curves shown here are derived from Figure 5.5 by taking into account the relation between lateral displacement  $x$  and force  $f$ , as obtained from the measurements.

Once again, it is interesting to consider the linear part of the graph (between 2 N and 5.5 N) since this is the useful range for sensing. In this part of the graph, the sensitivity was  $-350 \mu\text{A N}^{-1}$  (at 5 mA VCSEL driving current). The relation between lateral displacement  $x$  and force  $f$  was  $22.4 \mu\text{m N}^{-1}$  and the layer of PDMS on the sensor point had a thickness  $d$  of  $180 \mu\text{m}$  with an area  $A$  of  $20 \text{mm}^2$ . Hence, the sensitivity with respect to the shear stress is  $-7 \mu\text{A kPa}^{-1}$  and the shear modulus  $G$  of PDMS can be estimated as:

$$G = \frac{d \cdot f}{x \cdot A} = \frac{180 \mu\text{m}}{22.4 \mu\text{m N}^{-1} \cdot 20 \text{mm}^2} = 402 \text{ kPa}.$$

### 6.3.2 Second generation sensor

The same setup as described above using the Dage shear force tester was adopted to functionally characterize the second generation sensor. This second generation sensor technology demonstrates the principle of measuring shear stress magnitude and direction by measuring its 2 components in the  $x$ - and  $y$ -direction. This sensor prototype design was directly derived from the first generation sensor technology and could therefore be very quickly implemented. However, as indicated by the simulations, the design shows important limitations in terms of sensor dynamic range and sensitivity. Therefore, this second generation sensor technology was mainly intended as a fast-track solution during the research process to demonstrate the  $(x, y)$ -sensing principle, while developing an improved dedicated third generation technology (slow-track).

As a result, this section investigates only the operating principle and no detailed sensor characteristics. This testing was performed by subjecting such a second generation sample, ideally only sensitive to variations in the  $x$ -direction (see Section 5.5.3 for details), to displacements in both the  $x$ - and  $y$ -direction. The resulting sensor output signals are plotted in Figure 6.16 and correspond with the predicted behavior, see Figure 5.10 in Section 5.3.2. In other words, the sensor

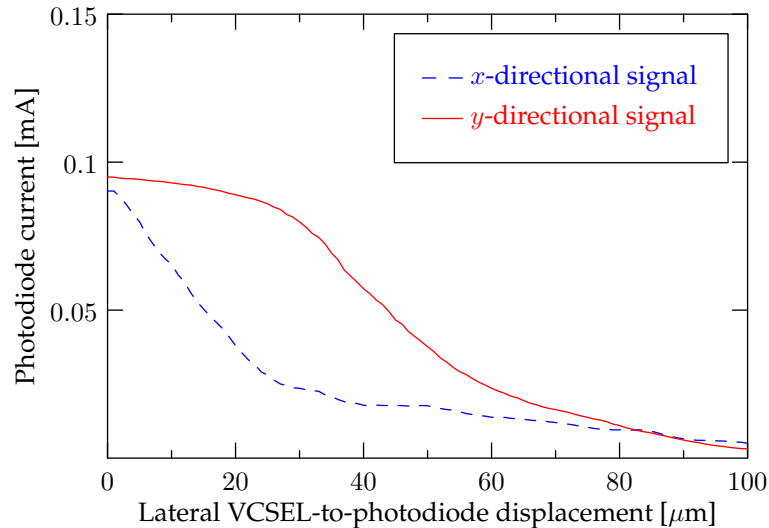


**Figure 6.16** – Measured sensor response to lateral displacement in 2 orthogonal directions  $x$  and  $y$  (second generation sensor).

is able to detect the magnitude and direction of an applied shear stress but the signal levels and dynamic sensor range are low compared to previous generation technology due to the smaller effective photodiode surface and consequently the required lower VCSEL driving current, as described in Section 5.3.2. Furthermore, the 2 orthogonal directional signals are not completely independent. It can be seen that when applying a displacement in the  $x$  direction, the  $y$ -signal is also slightly varying.

### 6.3.3 Third generation sensor

#### Test setup and conditions

For characterizing the third generation of shear sensor which is able to measure both shear magnitude and direction, the application of lateral displacements in a precisely defined direction is required. Therefore, a dedicated setup is constructed as depicted in Figure 6.17. The shear sensor sample is fixed in a holder mounted on a manual high-resolution rotational stage which is used to set the direction of displacement. These displacements were accurately applied using a pressing tip on a computer controlled motorized stage while the photodiode current was recorded simultaneously. A cylinder was glued on the top sensor surface to easily apply the displacements using this tool. This setup was constructed so that every component has a minimum mechanical compliance, so that only the

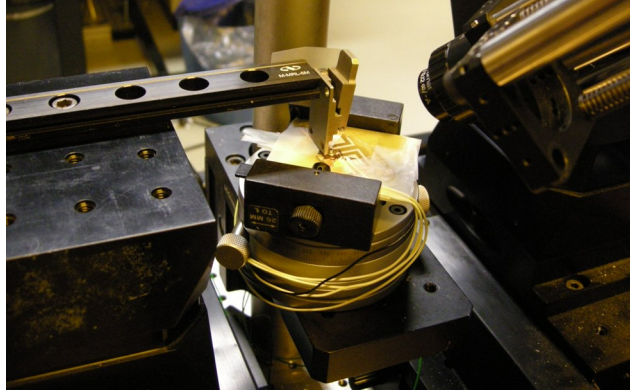


Figure 6.17 – Dedicated setup for testing the third generation,  $(x, y)$ -shear sensor.

actual displacements in the sensor is contributing to the output signal.

In the following paragraphs, the third generation sensor is characterized in terms of displacement only, and not in terms of the actual applied shear force. The reason is that a rigid version of the sensor was fabricated which was not accurately cut out, meaning that the in-plane dimensions of the transducer material are not exactly defined (i.e. the area where top and bottom sensor substrate are bonded through the PDMS). Since the sensor response to shear force depends on these geometric dimensions, it is only meaningful to define the sensor response in terms of displacement. However, a good estimate of the response to shear force can be obtained by merely scaling the displacement based response, as discussed in Section 5.4.

### Results and discussion

The general shear sensing principle and fabrication technology was already verified on the first and second generation sensor prototypes. Therefore, the main purpose of this section is to prove the principle of constructing a true  $(x, y)$ -sensitive sensor design. A sensor prototype using a square detector and a VCSEL, as described in Section 5.5.3 was exposed to lateral displacements under different pushing angles.

As described in Section 5.3.3, the  $(x, y)$  sensor is composed of 2 “sensing points”, which are each only sensitive to either  $x$  or  $y$  variations. To test this principle, the part of the device only sensitive to one direction (either  $x$  or  $y$ ) is characterized since these results are analogous for the other direction owing to the symmetry.

Configuration 1, as presented in Figure 5.11, is evaluated by driving a VCSEL and monitoring the current from the photodiode. The substrate with the photodiode

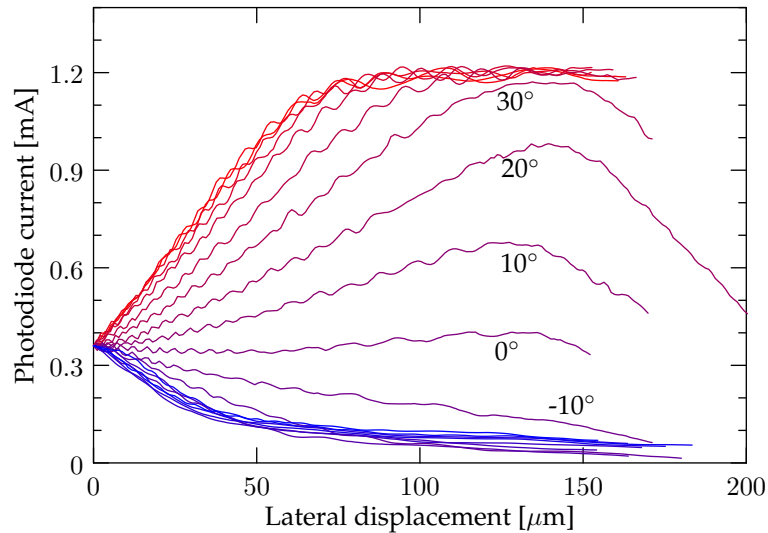


**Figure 6.18** – Sensor response (i.e. photodiode current) in function of displacement for  $\chi$ -values from  $-90^\circ$  to  $90^\circ$  in  $10^\circ$  increments.

was fixed on the rotational stage while the substrate with embedded VCSEL was incrementally displaced by pushing with a tip against the cylinder fixed on the top of the sensor, as displayed in Figure 6.17. These displacements were applied under several angles using the rotational stage to orient the sensor. The angle  $\chi$  in which the displacement is applied, is defined as illustrated in Figure 5.12.

Figure 6.18 shows the resulting photodiode current in function of the applied displacement for  $\chi$ -values from  $-90^\circ$  to  $90^\circ$  in  $10^\circ$  increments.

As expected, the slope of the response curve is largest for displacements in the  $\pm 90^\circ$  direction, while the slope is virtually 0 in the corresponding orthogonal direction, i.e. for  $\chi=0^\circ$ . In this direction there still seems to be a small influence, which is however only caused by the inaccuracy of the initial sensor orientation and not due to the sensor operation.

Since the sensor is only sensitive to  $y$ -directional variations, the slope of the curve is lower when the  $y$ -directional component in the total lateral displacement vector is decreased. The maximum value of the slope,  $(\Delta i_p / \Delta y)_{max}$ , is obtained for  $\chi = \pm 90^\circ$  since there is only a  $y$ -component in the displacement vector. When the value of  $|\chi|$  is reduced, there is also an  $x$ -component present in the total lateral displacement. For the same total displacement amplitude, the  $y$ -contribution will therefore be smaller so that the slope of the curve is reduced. Since the  $y$ -component of a displacement vector  $R$  is obtained as  $\|R\| \sin \chi$  and the curves in Figure 6.18 are plotted in function of the total lateral displacement, their slopes

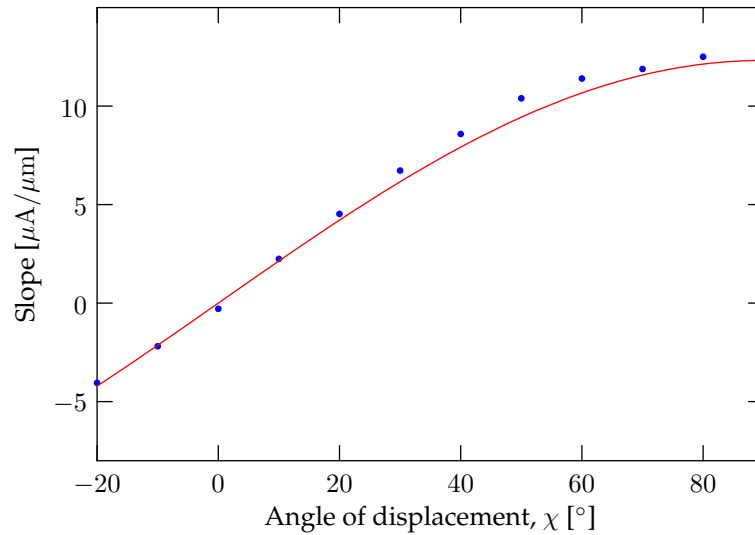


**Figure 6.19** – Slope of the sensor response in function of the direction of displacement, as defined by the value of  $\chi$ .

vary as  $(\Delta i_p / \Delta y)_{max} \sin \chi$ . The measured slopes of these curves are plotted in function of the angle  $\chi$ , see Figure 6.19 (dots). The solid line in this graph depicts the theoretically expected behavior, calculated as  $(\Delta i_p / \Delta y)_{max} \sin \chi$ . It can be seen that the actual measured values indeed follow this expected  $\sin \chi$ -dependent trend.

In Figure 6.20, the sensor characteristics for displacements in the direction of  $\chi=90^\circ$  (“positive  $y$ -direction”) are illustrated. The slope of the curve (i.e. the sensor sensitivity) was found to be  $12.3 \mu\text{A} \mu\text{m}^{-1}$ , which is lower than the simulated value, see Table 5.1. This difference is probably attributed to differences in VCSEL power levels and fabrication inaccuracies. Due to using a rigid substrate for embedding the photodiode, it was much more difficult to align and bond the VCSEL package onto the photodiode substrate. An air bubble was thereby trapped between both substrates which increased the vertical VCSEL-to-photodiode separation distance and also resulted in an alignment error. This inaccuracy can be noticed in Figure 6.18: the origin of the curves does not perfectly coincide with the middle of the dynamic sensor range, which would be the ideal case.

Due to this initial misalignment, it is difficult to rigorously determine the dynamic sensor range. However, in order to compare with the simulated values, the potential dynamic range was estimated by doubling the single sided range as illustrated in Figure 6.20. A photodiode current of  $0.6 \text{ mA}$  was considered to correspond with the middle of the total dynamic range which was estimated to be  $2 \times 42 \mu\text{m}$ , slightly smaller but in the same order as the simulated value.

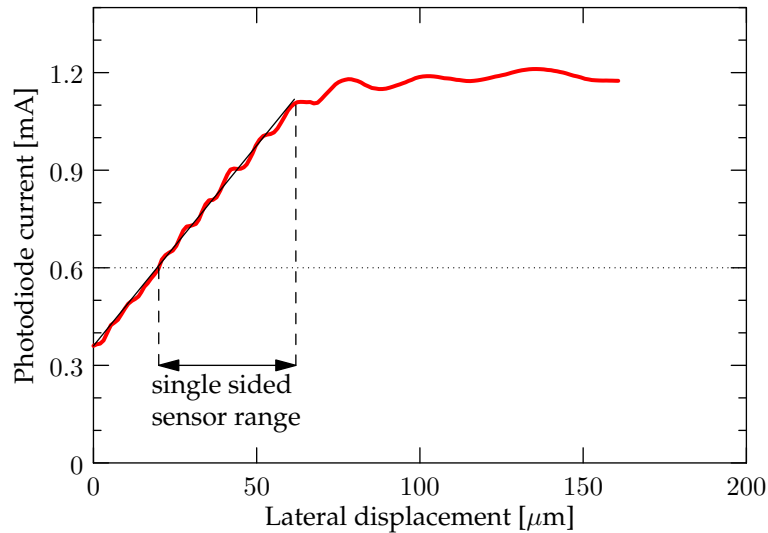


**Figure 6.20** – Sensor response (i.e. photodiode current) in function of displacement for  $\chi=90^\circ$ .

Finally, it can be noticed that for the measured signals, a periodically varying signal seems to be superimposed on the actual sensor response curves. This is probably an interferometric effect caused by reflections of the optical power originating from the VCSEL. Such a behavior is indeed noticed when a mirror above a VCSEL is displaced over nanometer distances [4]. This effect results in a certain decrease of the sensor accuracy. Therefore, it is currently being investigated to limit the amount of reflections in order to improve the sensor accuracy.

### 6.3.4 Parameters potentially interfering with sensor operation

#### Influence of bending the sensor substrate

In the introduction chapter, possible applications and corresponding requirements of artificial skin were discussed and particularly it was stressed that the sensors used in such an artificial skin should be mechanically flexible. Therefore, it can be questioned how much the operation of the proposed shear stress sensor is influenced when it is bent. As discussed in Section 5.5.4, the actual size of the sensing elements can be made very small (in the order of tens of  $\text{mm}^2$ ) when redesigning the electrical connections in the current sensor design. In prosthetic sockets, an application that can benefit from incorporating novel shear sensors, the typical bending radii are in the order of 10 cm. As a result, the bending of the small and thin sensing elements, and the effect on their operation can be

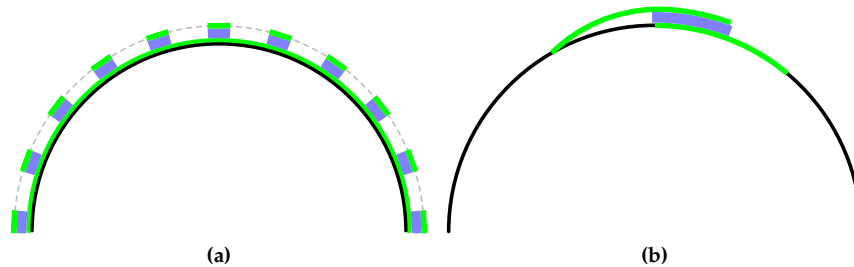


**Figure 6.21** – (a) Sensor configuration for measuring shear stresses: only the bottom part of the sensor is fixed and the top part is kept as small as possible. (b) Sensor configuration for measuring bending of a substrate: bottom and top part of the sensor are fixed to the substrate.

neglected. This configuration is schematically illustrated in Figure 6.21a.

On the contrary, when the influence of bending is maximized, the system could also be used as a bending sensor. In that case not only the bottom foil of the sensor, but also the foil on the top is fixed with a substrate, see Figure 6.21b. Such a configuration, comparable to the operation of a strain gauge, could be useful to measure the bending radius, for example in flexible displays.

### Influence of temperature

As usually occurring with (opto)electronics, it can be expected that changes in temperature will influence the sensor characteristics. These possible effects on the sensor operation can be separated in 2 categories. A change in temperature influences the mechanical properties of the PDMS transducer layer, and also influences the optical properties of the light source and detector used in the sensor. PDMS exhibits a rather large coefficient of thermal expansion (CTE) of around 300 ppm/°C, meaning that the material expands when temperature increases. Furthermore, the Young's modulus increases with about 10 kPa °C<sup>-1</sup> [5].

On the other hand, the wavelength, optical power and opening angle of emitted VCSEL light depend on temperature. The shift in wavelength will typically not influence the sensor operation since the used photodiode has a broadband response, but the optical power and opening angle determine the sensor response and therefore do influence the operation. Furthermore, the sensitivity of the photodiode changes with temperature, meaning that it is not easy to predict how a combination of properties of the different building blocks affect the sensor operation.

To construct an optimum temperature compensation strategy for this sensor, these 2 categories of effects need to be investigated. A rough estimation of the

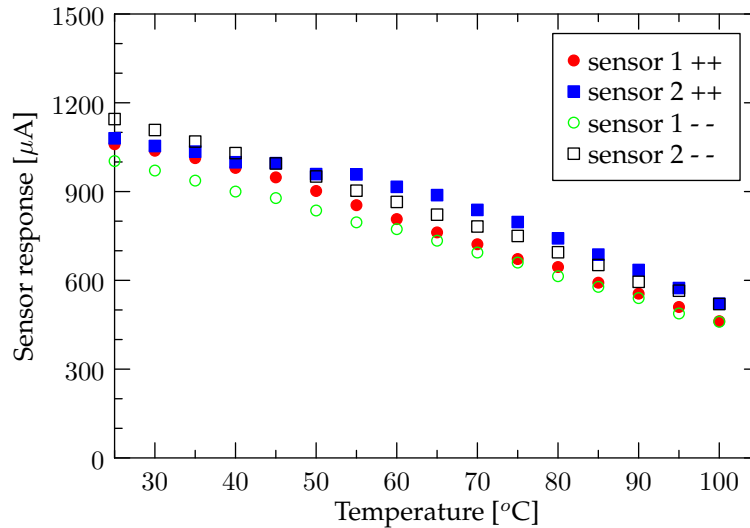


**Figure 6.22** – Measured sensor response (in rest, i.e. no shear stress applied) in function of operating temperature (increasing (++) and decreasing (--) temperature).

effect of rising temperature on the operation of the optoelectronics can be obtained by subjecting the sensor to a varying temperature and simultaneously measuring the sensor response (photodiode current) in rest, i.e. without applying a shear stress. Figure 6.22 shows the result of such a test on a shear sensor sample of the first generation with circular photodiodes. It is clear that the sensor output decreases significantly with temperature (about  $8 \mu\text{A } ^\circ\text{C}^{-1}$ ), originating from combined VCSEL and photodiode effects. Depending on the application, this may or may not significantly affect the sensor operation. For applications where the sensor is in contact with the human body, a more or less constant skin temperature can be expected, but for robotics, this may not be valid.

In any case, it is much more difficult to determine the temperature effects when the sensor is actually subjected to a shear stress. Therefore, the sensor response curves need to be measured for different operating temperatures. This requires a combined mechanical, optical and climate controlled setup which was not available at the time of writing. In the future, the construction of such a setup and an exhaustive study of the sensor operation will be a first step towards the design of a temperature compensation scheme.

---

## 6.4 Conclusions

---

This chapter started with discussing the relevant characteristics of the used optoelectronic components. Then, these actual measured values were used to validate the simulation model as constructed in the previous chapter and finally, the functional characterization of the flexible shear sensor was described.

The development of this shear sensor was performed step by step resulting in 3 generations of sensor technologies, as described in the previous chapter. The first generation technology's aim was validating the fabrication methods and sensor principle, limited to measuring shear stress magnitudes only. The response of the fabricated sensor to both relative lateral displacement of the VCSEL and photodiode and to actual shear stress was recorded. These curves were compared with the simulated values and consistent results were found. A maximum sensitivity of  $-7 \mu\text{A kPa}^{-1}$  and a linear relation between the applied shear force and lateral displacement was recorded.

With the second generation technology, a concept was introduced to develop a sensor which is also able to measure shear force direction in addition to magnitude. It was based on a minor modification of the first generation technology and therefore easily implemented. Although the principle was demonstrated, the used photodiodes were too small to construct a usable sensor.

A third generation sensor technology was therefore introduced to improve the implementation of this  $(x, y)$ -sensitive sensor concept. This technology is based on 2 "sensing points", one for measuring  $x$ - and one for measuring  $y$ -variations. These sensor points were evaluated by recording the influence of the shear stress direction on the sensor response curve. It was concluded that such a sensor point is only sensitive to variations in one direction and that combining two such sensor points in orthogonal directions leads to a sensor capable of measuring the magnitude and direction of an applied shear force.

*Critical Discussion.* Different generations of sensors were functionally tested and it was found that the results are in agreement with the simulations. However, it is clear that further characterization is needed in the future to test other sensor aspects such as sensitivity to temperature variations and pressure and shear stress cross-sensitivity. First measurements have indicated an influence of temperature, whereas simulations have indicated a very limited influence of pressure on the shear sensor operation. Nevertheless, for precisely characterizing all these effects, a dedicated and complex setup needs to be constructed in the future.

---

## References

---

- [1] Ulm-Photonics. (Accessed 2011) Products. [Online]. Available: <http://www.ulm-photonics.com/>

- 
- [2] E. Bosman, "Integration of optical interconnections and opto-electronic components in flexible substrates," Ph.D. dissertation, Ghent University, 2010.
- [3] Enablence. (Accessed 2011) Photodiode products. [Online]. Available: <http://www.enablence.com/components/solutions/transmission/photodiodes>
- [4] B. Van Hoe, D. Lamon, E. Bosman, G. Van Steenberge, J. Missinne, P. Goethals, P. Krassimir, D. Reynaerts, J. Vanfleteren, and P. Van Daele, "Embedded high resolution sensor based on optical feedback in a Vertical Cavity Surface Emitting Laser," in *PROCEEDINGS OF SPIE - THE INTERNATIONAL SOCIETY FOR OPTICAL ENGINEERING*, K. J. Peters, W. Ecke, and T. E. Matikas, Eds., vol. 7648. SPIE, the International Society for Optical Engineering, 2010. [Online]. Available: <http://dx.doi.org/10.1117/12.847647>
- [5] F. Schneider, T. Fellner, J. Wilde, and U. Wallrabe, "Mechanical properties of silicones for mems," *Journal of Micromechanics and Microengineering*, vol. 18, no. 6, p. 065008, 2008. [Online]. Available: <http://stacks.iop.org/0960-1317/18/i=6/a=065008>

# 7

## Conclusions and final remarks

*It's more fun to arrive a conclusion than to justify it.*  
–Malcolm Forbes

### **7.1 Main contributions to the field of tactile sensors**

---

In this section, the main results are discussed based on revisiting the objectives as stated in the introduction. As a summary, it can be reported that the main contribution was the successful implementation of an unobtrusive flexible optical shear sensor. Furthermore, the research initially performed towards a less successful waveguide based sensor led to a significant additional contribution by establishing microfabrication techniques to obtain stretchable optical waveguides which can be used in conformable systems owing to their mechanical compliance.

#### **7.1.1 Objective 1: “Developing unobtrusive sensors”**

Throughout this dissertation, several technologies were described that are needed to eventually obtain unobtrusive sensors. This first objective determines the type of packaging or physical appearance of the sensor: for a sensor to be truly unnoticeable in a typical tactile sensing application, it should be either mechanically compliant or stretchable or small, thin and flexible in order to be embedded as functional islands in a deformable substrate.

Based on the knowledge gained from previous research at the “Centre for Microsystems Technology”, micro-optical embedding technologies were further developed with the purpose to construct tactile sensors. In that respect, this dissertation reports contributions both in the field of deformable optical polymer waveguides and also in the field of optoelectronics embedding. Chapter 3 and 4 report on the work performed towards developing waveguide based sensors. An initial goal of this research (within the scope of the IWT-funded project FAOS) was to construct a flexible or even stretchable high-density waveguide based tactile sensor. However, during the FAOS project, extensive investigations have shown that the requirements for tactile sensing could not be achieved with the proposed waveguide sensor.

Nevertheless, within the scope of working towards this waveguide sensor, technologies were established aiming at unobtrusive systems. A technology platform for microfabrication of optical polymer structures combined with PDMS was established, primarily to construct stretchable polymer waveguides by incorporating a relatively hard polymer core material as meanders in a soft PDMS encapsulant.

Another approach extends this concept of “stretchability” even further and resulted in the development of stretchable polymer optical waveguides based on several commercially available PDMS materials and low-cost replication based processes. The optical loss characteristics of these PDMS based waveguides were found to be comparable to polymer waveguides on rigid substrates. A propagation loss smaller than 0.24 dB/cm was measured for the first generation fabricated samples and about 0.14 dB/cm for the second generation samples. The bending losses of the waveguides were tested down to a radius of 3.9 mm and losses of about 0.08 and 0.24 dB per bent cm were obtained for waveguides with OE-6520 and LS-6257 core material respectively. The cladding material for both types was Sylgard®184. Furthermore, the stretchability was demonstrated by developing a technology for coupling fibers to the PDMS waveguides and recording the optical losses when stretching. It was found that no excessive losses were introduced by elongating the waveguides. However, it was difficult to quantify the actual loss value in function of the elongation since considerable measurement variations were observed, possibly caused by a small movement of the fibers with regard to the waveguides during stretching.

In literature, in the best case flexible polymer waveguides are reported, while the waveguides developed in this dissertation have an additional degree of freedom, i.e. “stretchability”. Owing to this mechanical stretchability, they can be used as unobtrusive components in novel sensor systems or for optical interconnections applied on irregular or moving surfaces. Additionally, the established optical waveguide technology is compatible with microfluidics fabrication technology and can therefore be used for extending microfluidics operation with optical sensing capabilities.

On the other hand, Chapter 5 and Chapter 6 report on the optoelectronic based approach for obtaining tactile sensors. A starting point was the technology for embedding optoelectronic components in flexible polymer foils, as established during the PhD research of Erwin Bosman at CMST. In order to use this concept for obtaining sensors, the technology was slightly modified and extended by combining the flexible foils containing embedded components with PDMS microfabrication technologies. For constructing a tactile shear sensor, thin layers of PDMS (180  $\mu\text{m}$ ) were used as transducer material to convert mechanical stresses into displacements which can then be detected using the embedded optoelectronic components. Since these components are embedded in flexible thin foils of only 40  $\mu\text{m}$  thick, the resulting sensor is also very thin (about 250  $\mu\text{m}$ ) and flexible. Furthermore, the total sensor dimensions are small owing to the use of miniature embedded optoelectronic VCSELs and photodiodes. The largest dimension of the currently used components is 1 mm. These small dimensions and flexibility make the sensor unobtrusive enabling to use it for applications that cannot accept bulky or rigid sensors, such as inside prosthetic sockets.

### 7.1.2 Objective 2: “Exploring optical sensing principles for tactile sensors”

Two optical tactile sensing principles have been investigated during this PhD research. The first was based on changing optical coupling between crossing polymer waveguides and the second based on changing optical coupling between a VCSEL and photodiode. Furthermore, the waveguide based principle was targeting the development of a high-density pressure sensor while with the optoelectronic based sensor it is possible to measure shear stresses.

The optical waveguide coupling principle using multimode waveguides was extensively studied, but the results showed that it is difficult to exploit this principle for constructing a pressure sensor. This was also confirmed with a fabricated demonstrator, indicating that the sensor exhibits an “on/off” behavior, making it possible to detect pressure, but difficult to measure actual values. In this regard, however, the main contribution was the technology platform established when working towards this sensor, as described above.

The proposed second sensing principle is based on a different type of “optical coupling”, i.e. between a VCSEL and photodiode depending on their lateral alignment. Using this principle, a shear sensor was successfully constructed by applying a PDMS transducer layer between a VCSEL and photodiode which were embedded in a thin polymer foil. Consequently, when a mechanical shear stress is applied on the sensor, the PDMS material deforms so that the lateral alignment of the VCSEL and photodiode varies, influencing the photocurrent value.

### 7.1.3 Objective 3: “Focus on the shear stress component in tactile force sensing”

This proposed concept for creating a shear stress sensors was extensively studied since only little research has been reported to detect the “shear” components of the three dimensional tactile forces occurring. Therefore, an analytical model was constructed to predict the sensor characteristics and the model was validated with several generations of fabricated prototypes.

The first generation was only able to measure the magnitude of the shear force due to the symmetrical sensor build-up and the round photodiode used. The dynamic sensor range was about 100  $\mu\text{m}$  displacement or 5 N shear force and the maximum sensitivity was  $-350 \mu\text{A N}^{-1}$  or  $-7 \mu\text{A kPa}^{-1}$ .

The most recent generation shear sensor is capable of measuring along two directions, i.e. both the magnitude and the direction of the shear force can be determined. Therefore, multiple VCSELs and square detectors were used to construct a sensor point only sensitive to  $x$ -directional and another only sensitive to  $y$ -directional variations. This sensor was characterized in function of the angle of lateral displacement and these measurements showed that this design is suited to detect both the shear force magnitude and direction. However, due to the different layout of the photodiodes it is more difficult to embed these components in flexible foils and therefore, some technological development is still needed to make this version of the sensor also mechanically flexible and to fully characterize it.

These sensor characteristics were obtained for a particular design, focusing on maximal miniaturization and sensitivity, to demonstrate the ultimate limits of the technology. Small VCSELs and photodiodes were used since these can be embedded resulting in very small sensors. However, when using other components and slightly different sensor designs, the dynamic range can be largely extended. Obviously, this will imply a compromise in terms of sensitivity and size of the resulting sensor, a trade-off that needs to be made in function of the specific application. In any case, the novel shear sensor technology offers significant opportunities for numerous applications and was therefore also patented.

## 7.2 Outlook and recommendations for future work

Waveguide and optoelectronic based solutions for tactile sensing were investigated. While it was concluded that the waveguide based sensing principle, in the current configuration, is not directly suited for tactile sensing, many interesting results were obtained that could potentially find applications in other fields than tactile sensing.

A first potential application domain is microfluidics where PDMS is frequently

applied as base material. Furthermore, optical sensing techniques are increasingly incorporated in these microfluidic environments requiring optical fibers or waveguides close to the channels for excitation and detection. The PDMS based waveguides developed in this dissertation would therefore be ideal for this application.

Many other (bio-)sensing applications would also benefit from using deformable PDMS waveguides. For example, in the scope of the PhD research of Sandeep Kalathimekkad at CMST, a flexible “optical nose” gas sensor is being developed based on polymer lightguides. PDMS based waveguides and lightguides are currently being investigated as possible solutions for the fabrication of the sensor.

The field of optical interconnections is also increasingly moving from rigid to flexible substrates, comparable to the trend in electronics. PDMS waveguides are a potential solution for applications where waveguides need to be deformable. Examples are high-data rate interconnections between a hinge-based screen and the base module of a mobile phone, or one-time deformable interconnections under the dashboard of a car.

For all these waveguide based applications, a critical aspect requiring further research is the coupling and integration of driving (opto-)electronics with the waveguides. These driving (opto-)electronic assemblies are preferably also flexible not to jeopardize the advantages of mechanical deformability of the waveguides themselves. The thin, flexible optoelectronic packaging foils as used in Chapter 5 could therefore be an ideal solution as starting point for this research.

Furthermore, the developed optoelectronic based tactile shear sensors proved to be very promising, as demonstrated by the development of the flexible shear sensor in this dissertation. Further research could even extend the possibilities of the current sensor prototype. The unobtrusive nature of the sensor was considered as one of the most favorable properties of this shear sensor concept. However, the final sensor design able to detect both shear stress magnitude and direction was not yet implemented on a flexible substrate since no suited photodiode components compatible with the fabrication process were found. Ideally, the required photodiodes should be designed customly so that they can directly be applied using the established fabrication technology.

The focus of this research was on developing individual shear sensors, but to produce a true artificial skin, these sensors need to be incorporated in larger skin-like sensing foils and interconnected in a matrix configuration. In this scope, it would also be beneficial to add pressure sensor points, to obtain a “three-dimensional” stress sensor.

Depending on the requirements of a specific application, the fabrication process of the shear sensor could be adapted. In this dissertation, the focus was on the smallest possible design with a high accuracy. However, when a lower accuracy is acceptable, the sensor could be fabricated using cheaper components such as

LEDs, OLEDs and organic photodetectors. Furthermore, the current spin-coating based fabrication process has the potential to be altered towards a lower-cost foil-based roll-to-roll mass production technology.



## Appendix: Dissemination

### **A.1 Research context and related projects**

---

The research leading to this dissertation was performed within the framework of the following projects:

- A personal grant, supported by the Research Foundation - Flanders (FWO-Vlaanderen) under a Ph. D. fellowship (aspirantschap FWO).
- FAOS (Flexible Artificial Optical Skin) [1]  
SBO project, funded by the Flemish Institute for the Promotion of Innovation by Science and Technology (IWT [2])  
Starting date : January 1, 2007  
Ending date : December 31, 2010  
Project coordinator : Prof. Dr. Ir. Peter Van Daele, IMEC - Ghent University / CMST Microsystems, Technologiepark 914A, B-9052 Zwijnaarde, Belgium

The FAOS-project aims at developing a flexible substrate or foil in which the sensing elements can be integrated and in which also the light sources, detectors and electronic circuitry are embedded or integrated on compact signal processing boards. This artificial and flexible optical sensing foil can then be applied on irregular surfaces (e.g. for distributed sensing applications), on movable surfaces (e.g. in robotics) or can be folded into compact

modules (for portable devices, automotive, etc).

- PHOSFOS (PHotonic Skins For Optical Sensing) [3]  
European ICT-Project, Framework 7  
Starting date : April 1, 2008  
Ending date : March 31, 2011  
Project coordinator : Prof. Dr. Ir. Francis Berghmans, VUB Vrije Universiteit  
Brussel Pleinlaan 2, B-1050 Brussels, Belgium

The PHOSFOS-project aims at developing a flexible and stretchable foil that integrates optical sensing elements and that if necessary, appropriate and relevant to the application, can include optical and electrical powering as well as on-board signal processing and wireless communications. This skin can be wrapped around, embedded in, attached and anchored to irregularly shaped and/or moving objects or bodies and will allow quasi-distributed sensing of mechanical quantities such as deformation, pressure, stress or strain.

## A.2 Research dissemination

---

### A.2.1 Journal papers

- E. Bosman, G. Van Steenberge, B. Van Hoe, J. Missinne, J. Vanfleteren, and P. Van Daele, "Highly reliable flexible active optical links," *IEEE PHOTONICS TECHNOLOGY LETTERS*, vol. 22, no. 5, pp. 287–289, 2010. [Online]. Available: <http://dx.doi.org/10.1109/LPT.2009.2038797>
- J. Missinne, E. Bosman, B. Van Hoe, G. Van Steenberge, S. Kalathimekkad, P. Van Daele, and J. Vanfleteren, "Flexible shear sensor based on embedded optoelectronic components," *IEEE PHOTONICS TECHNOLOGY LETTERS*, vol. 23, no. 12, pp. 771–773, 2011. [Online]. Available: <http://dx.doi.org/10.1109/LPT.2011.2134844>
- E. Bosman, J. Missinne, B. Van Hoe, G. Van Steenberge, S. Kalathimekkad, J. Van Erps, I. Milenkov, K. Panajotov, T. Van Gijseghem, P. Dubruel, H. Thienpont, and P. Van Daele, "Ultrathin optoelectronic device packaging in flexible carriers," *IEEE JOURNAL OF SELECTED TOPICS IN QUANTUM ELECTRONICS*, vol. 17, no. 3, pp. 617–628, 2011. [Online]. Available: <http://dx.doi.org/10.1109/JSTQE.2010.2096407>
- J. Missinne, E. Bosman, B. Van Hoe, R. Verplancke, G. Van Steenberge, S. Kalathimekkad, P. Van Daele, and J. Vanfleteren, "Two Axis Optoelectronic Tactile Shear Stress Sensor," *Submitted for publication in Sensors and Actuators A, Elsevier*, 2011.

### A.2.2 Proceedings of international conferences

- G. Van Steenberge, E. Bosman, J. Missinne, B. Van Hoe, and P. Van Daele, "Flexible optical interconnects," in *Proceedings of the 2nd International Symposium on Photonic Packaging*, 2008.
- F. Axisa, F. Bossuyt, J. Missinne, R. Verplancke, T. Vervust, and J. Vanfleteren, "Stretchable engineering technologies for the development of advanced stretchable polymeric system," in *Proceedings of the 7th International IEEE Conference on Polymers and Adhesives in Microelectronics and Photonics (Polytronic)*, 2008.
- J. Missinne, G. V. Steenberge, B. V. Hoe, K. V. Coillie, T. V. Gijsegheem, P. Dubruel, J. Vanfleteren, and P. V. Daele, "An array waveguide sensor for artificial optical skins," A. L. Glebov and R. T. Chen, Eds., vol. 7221, no. 1. SPIE, 2009, p. 722105. [Online]. Available: <http://link.aip.org/link/?PSI/7221/722105/1>
- E. Bosman, G. Van Steenberge, J. Missinne, B. Van Hoe, and P. Van Daele, "Packaging of opto-electronic devices for flexible applications," in *PROCEEDINGS OF THE SOCIETY OF PHOTO-OPTICAL INSTRUMENTATION ENGINEERS (SPIE)*, A. L. Glebov and R. T. Chen, Eds., vol. 7607. SPIE, the International Society for Optical Engineering, 2010. [Online]. Available: <http://dx.doi.org/10.1117/12.841553>
- B. Van Hoe, D. Lamon, E. Bosman, G. Van Steenberge, J. Missinne, P. Goethals, P. Krassimir, D. Reynaerts, J. Vanfleteren, and P. Van Daele, "Embedded high resolution sensor based on optical feedback in a Vertical Cavity Surface Emitting Laser," in *PROCEEDINGS OF SPIE - THE INTERNATIONAL SOCIETY FOR OPTICAL ENGINEERING*, K. J. Peters, W. Ecke, and T. E. Matikas, Eds., vol. 7648. SPIE, the International Society for Optical Engineering, 2010. [Online]. Available: <http://dx.doi.org/10.1117/12.847647>
- J. Missinne, G. Van Steenberge, B. Van Hoe, E. Bosman, C. Debaes, J. Van Erps, C. Yan, E. Ferraris, P. Van Daele, J. Vanfleteren, H. Thienpont, and D. Reynaerts, "High density optical pressure sensor foil based on arrays of crossing flexible waveguides," in *PROCEEDINGS OF SPIE - THE INTERNATIONAL SOCIETY FOR OPTICAL ENGINEERING*, H. Thienpont, P. Van Daele, J. Mohr, and H. Zappe, Eds., vol. 7716. SPIE, the International Society for Optical Engineering, 2010. [Online]. Available: <http://dx.doi.org/10.1117/12.854578>
- E. Bosman, J. Bauwelinck, K. Panajotov, G. Van Steenberge, J. Missinne, B. Van Hoe, and P. Van Daele, "Characterization of flexible fully embedded optical links," in *Proceedings of SPIE, the International Society for Optical*

*Engineering*, H. Thienpont, P. Van Daele, J. Mohr, and H. Zappe, Eds., vol. 7716. SPIE, the International Society for Optical Engineering, 2010. [Online]. Available: <http://dx.doi.org/10.1117/12.854229>

- B. Van Hoe, G. Van Steenberge, E. Bosman, J. Missinne, T. Geernaert, F. Berghmans, D. J. Webb, and P. Van Daele, "Optical fiber sensors embedded in polymer flexible foils," in *PROCEEDINGS OF SPIE - THE INTERNATIONAL SOCIETY FOR OPTICAL ENGINEERING*, F. Berghmans, A. G. Mignani, and C. A. van Hoof, Eds., vol. 7726, no. Optical Sensing and Detection. SPIE, the International Society for Optical Engineering, 2010. [Online]. Available: <http://dx.doi.org/10.1117/12.854865>
- J. Missinne, E. Bosman, B. Van Hoe, G. Van Steenberge, P. Van Daele, and J. Vanfleteren, "Embedded flexible optical shear sensor," in *IEEE Sensors*. IEEE, 2010, pp. 987–990. [Online]. Available: <http://dx.doi.org/10.1109/ICSENS.2010.5690919>
- E. Bosman, G. Van Steenberge, J. Missinne, B. Van Hoe, S. Kalathimekkad, and P. Van Daele, "Packaging technology enabling flexible optical interconnections," in *Proceedings of SPIE, the International Society for Optical Engineering*, A. L. Glebov and R. T. Chen, Eds., vol. 7944. SPIE, the International Society for Optical Engineering, 2011. [Online]. Available: <http://dx.doi.org/10.1117/12.874959>
- J. Missinne, E. Bosman, B. Van Hoe, R. Verplancke, G. Van Steenberge, S. Kalathimekkad, P. Van Daele, and J. Vanfleteren, "Ultra thin optical tactile shear sensor," *Presented at Eurosensory XXV*, 2011.

### A.2.3 Other international conferences, without proceedings

- G. Van Steenberge, J. Missinne, B. Van Hoe, K. Van Coillie, J. Vanfleteren, and P. Van Daele, "Array waveguide sensor," in *Proceedings NEMO Scientific General Networking Meeting*, 2008.
- J. Vanfleteren, F. Axisa, D. Brosteaux, F. Bossuyt, E. De Leersnyder, T. Vervust, B. Huyghe, J. Missinne, R. Verplancke, and M. Gonzalez, "Elastic electronic circuits and systems using Moulded Interconnect Device (MID) technology," in *MRS Spring Meeting, Abstracts*. Materials Research Society (MRS), 2008.
- J. Missinne, G. Van Steenberge, J. Vanfleteren, and P. Van Daele, "Multimode PDMS waveguides fabricated using a hot-embossing technique," in *International Conference on Micro and Nano Engineering, 35th, Abstracts*, K. Ronse, Ed. IMEC, 2009, pp. P-MEMS-18-P-MEMS-18.

#### A.2.4 Proceedings of national conferences

- J. Missinne and B. Van Hoe, "Array waveguide sensor for artificial optical skin," in *UGent-FirW Doctoraatssymposium, 9e.* Universiteit Gent. Faculteit Ingenieurswetenschappen, 2008, pp. 202–203.
- J. Missinne, "Optical force sensors for smart prostheses," in *UGent-FirW Doctoraatssymposium, 11e.* Universiteit Gent. Faculteit Ingenieurswetenschappen, 2010, pp. 133–133.

#### A.2.5 Other publications

- J. Missinne, B. Van Hoe, "Artificial skin based on flexible optical tactile sensors," in *SPIE newsroom*, Jan 2010. [Online]. Available: <http://spie.org/x38859.xml?ArticleID=x38859>
- J. Missinne, "Flexible miniature shear sensors for prosthetics," in *SPIE newsroom*, Apr 2011. [Online]. Available: <http://spie.org/x47983.xml?ArticleID=x47983>

#### A.2.6 The following patent has been filed

- G. Van Steenberge, J. Missinne et al., "Optical shear sensor and method of producing such an optical shear sensor," *Worldwide patent*, WO 2011/128266 A1, 21 October 2011.

## References

---

- [1] FAOS Consortium. (2007) Flexible Artificial Optical Skin (FAOS). [Online]. Available: <http://intecweb.intec.ugent.be/faos/>
- [2] IWT. (Accessed 2011) Flemisch Institute for the Promotion of Innovation by Science and Technology (IWT). [Online]. Available: <http://www.iwt.be/>
- [3] Phosfos Consortium. (2008) Photonic Skins For Optical Sensing. [Online]. Available: <http://www.phosfos.eu/>



